



University of
Nottingham

UK | CHINA | MALAYSIA

Development of a multi-view fringe projection system for coordinate metrology

Amrozia Shaheen

Faculty of Engineering

University of Nottingham

Thesis submitted to the University of Nottingham for the degree of
Doctor of Philosophy

August 2021

*I would like to dedicate this thesis to my beloved parents
and my niece Hoorain Fatima.*

Abstract

The aim of the thesis is the development of a novel methodology for the characterisation of a multi-view fringe projection system, comparing the developed methodology with the conventional approach, and performing the verification tests on the multi-view fringe projection system. In general, commercially available single-view fringe projection systems struggle to acquire the full form/shape in one acquisition due to multiple occlusions, complex freeform geometries, limited field of view and the line of sight issues. Multi-view fringe projection systems are considered an effective solution to overcome the limitations of existing single-view optical systems. However, characterisation of a multi-view system is challenging due to the complexity involved, the need for defining a global coordinate system for multiple cameras and projectors and the fusion of the data from multiple perspectives.

In order to identify the constraints of the single-view systems, a fringe projection system with a single camera and projector, similar to available commercial systems, has been designed. The system is tested by measuring the three-dimensional shape of different complex additive manufactured artefacts. Additionally, to investigate the error originating from gamma non-linearity, limited depth of field and the environmental noise, commercially available low-cost pico digital light processing and laser projectors are compared for use in fringe projection applications. The outcome reveals that the eye-safe laser projector outperforms the pico digital light processing projector providing a higher quality of sinusoidal fringe patterns, has a much longer depth-of-focus ($\times 10$ that of the pico digital light processing projector) and suitable for measuring large objects. Another case study is performed on the uncertainty evaluation of the form measurement of an industrial test case using contact and non-contact methods.

Multi-view fringe projection systems are considered an active research area. In such systems, characterisation has a decisive influence on the system performance and accurate three-dimensional surface reconstruction. The characterisation of a multi-view fringe projection system relies on finding the intrinsic and extrinsic parameters of the cameras and projectors and bringing them into the global frame of reference. A generic approach is the extension of the methods for characterising the single camera-projector systems, where each camera is characterised with an accurately manufactured target whilst the projector is modelled as an inverse of the camera and needs additional information to develop a one-to-one correspondence between the camera and projector intensity pixels, which is provided in terms of absolute phase map. The relationship between different views is obtained by global optimisation of the extrinsic parameters of all the multiple perspectives.

Two approaches for characterising the multi-view fringe projection system are demonstrated, a conventional one and a novel approach based on stereo rectification of phase maps. In the conventional approach, an automated characterisation method is used, which utilises a checkerboard to characterise the system and determine the intrinsic and extrinsic parameters of all the cameras and projectors. The phase information from the phase-stepped fringes is used to establish the global reference frame by automated image processing and parameter optimisation. The three-dimensional surface reconstructions have been shown to overcome the limitations of the single-view system, mainly associated with occlusions, shading and high slope angles.

In the conventional approach, the transformation from the camera image pixels to the projector image pixels is carried out by a phase-stepped fringe projection technique. However, mapping error induces if the camera pixels are not aligned with the projector pixels, which affects the performance and accuracy of the fringe projection

system. To address this issue, a novel method to characterise a multi-view fringe projection system is introduced, which is independent of projector characterisation and alleviates the influence of mapping error. The proposed method depends on the stereo matching between rectified unwrapped stereo phase maps based on the epipolar constraint, and the matched phase points in the stereo phase maps are triangulated for three-dimensional reconstructions. Furthermore, the developed methodology is used to perform the verification tests on the multi-view fringe projection system.

Acknowledgements

I would like to acknowledge Prof. Richard Leach and Dr Samanta Piano for their supervision and guidance throughout my PhD. I would like to thank Dr Danny Sims-Waterhouse, a trustworthy and friendly adviser, who helped me to enhance my computational skills. I would also like to thank my former supervisor Dr Petros Stavroulakis for familiarising me with the basics of fringe projection technique.

I like to thank my MMT colleagues and friends for their support and technical skills. This includes Teguh Santoso, Mohammed Isa, Patrick Bointon, Nicholas Southon, Shigeru Takushima, George Gaython, Adam Thompson, Mathew Thomas, Shah Karim, Shama Rashid, Kaneez Amna, Rizwana Sadiq and Asma Khalid. A special thanks to Sofia Catalucci for being a lovely friend and teaching me Polyworks and Aditi Thanki for being my travel companion and making me laugh with innocent actions.

I would also like to acknowledge all the members of PAM² (Precision Additive Metal Manufacturing) for their valuable feedback and support throughout the project, specifically during the training workshops. A special thanks to Ann Witvrouw and Kopila Gurung for managing the PAM² project so well. A huge thanks to PAM² colleagues (Marie-Curie Early-Stage Researchers) for giving so many beautiful memories.

I like to especially thank my mentor Prof. Muhammad Sabieh Anwar for giving me an opportunity to get expertise in experimental physics and physics education. My Physlab colleagues for providing me friendly and comfortable working environment. A kind regard to Prof. Harold Zandvliet, Prof. Robert Hicken and Dr Marko Sturm for believing in me and my capabilities.

A very special thanks to my loving parents, grandparents, siblings (Asad Ijaz, Saad Ijaz, Amara Kausar, Aalia Kausar, Muhammad Zain), sisters-in-law (Sobia Nawaz, Samra Ehsan), nephew (Rayan Asad, Muhammad Zayan Ijaz, Muhammad Zaviyar Ijaz), my beloved niece (Hoorain Fatima) and my extended family. Especially, my parents who believed in me and always supported me in all my decisions. Specifically, my father, who went against the norms and allowed me to pursue my higher education and fulfil my dreams, my mother who taught me how to read/write and always there

for me in my cherish/difficult moments of life.

The research was funded by The EU Framework Programme for Research and Innovation - Horizon 2020 - Grant Agreement No. 721383 within the PAM² (Precision Additive Metal Manufacturing) and by the Engineering and Physical Sciences Research Council [EPSRC Grant Nos. EP/M008983/1, EP/L016567/1].

List of Publications

1. **A. Shaheen**, D. Sims-Waterhouse, P. Bointon, S. Takushima, S. Piano, R. K. Leach, *Characterisation of a multi-view fringe projection system based on the stereo matching of rectified phase maps*, Meas. Sci. Technol. 32, 045006, 2021 [Chapter 5]
2. Chapter 10, Post-Process Coordinate Metrology, R. K. Leach, **A. Shaheen**, p 237-268, In: *Precision Metal Additive Manufacturing*, R. K. Leach, S. Carmignato (Eds.) CRC Press. Boca Raton, London, New York. 2021, ISBN 978-1-138-34771-7 [Chapter 2]
3. **A. Shaheen**, D. Sims-Waterhouse, P. Bointon, S. Piano, R. K. Leach, *Automated characterisation of multi-view fringe projection system for three-dimensional measurement of additively manufactured parts* Proc. Euspen/ASPE Advancing Precision in Additive Manufacturing, Nantes, France, September 16-18, 2019 [Chapter 5]
4. P. Stavroulakis, D. Sims-Waterhouse, **A. Shaheen**, S. Catalucci, P. Bointon, R. K. Leach, G. Tzimiropoulos, E. Doyen, Y. Bis Kong, *External shape measurement for industrial applications using artificial intelligence and optimised data fusion*, Proc. IEEE IntelliSys 2018, London, UK, September 6-7, 2018
5. A. Witvrouw, J. Metelkova, R. Ranjan, M. Bayat, D. De, Baere, M. Moshiri, G. Tosello, J. Solheid, A. Charles, S. Scholz, M. Baier, S. Carmignato, P. Stavroulakis, **A. Shaheen**, Thijs L *Precision additive metal manufacturing*, Proc. ASPE/euspen Advancing Precision in Additive Manufacturing, Berkeley, USA, July 18-23, 2018.
6. **A. Shaheen**, D. Sims-Waterhouse, P. Bointon, S. Piano, R. K. Leach, *A flexible method for the geometric characterisation of a multi-view fringe projection system*, 3D Metrology Conference (3DMC), London, United Kingdom, November 5-7, 2019
7. **A. Shaheen**, P. Stavroulakis, R. K. Leach, 2018 *Comparative study of cost effective laser and DLP projectors for fringe projection*, 3D Metrology Conference (3DMC), Hamburg, Germany, October 9-11, 2018 [Chapter 3]
8. P. Stavroulakis, P. Bointon, D. Sims-Waterhouse, **A. Shaheen**, S. Piano, R. K. Leach, *Progress in realising a fast information-enriched complex form measurement system*, 3DMC, Aachen, Germany, October 9-11, 2017

Contents

Abstract	i
Acknowledgements	iii
List of Publications	v
1 Introduction	1
1.1 Motivation	1
1.2 Aims and objectives	3
1.3 The novelty of research work	3
1.4 Overview of the work	6
2 Background - State of the art	8
2.1 Introduction to three-dimensional imaging	8
2.1.1 Time of flight	9
2.1.2 Laser triangulation	10
2.1.3 Photogrammetry	11
2.1.4 Fourier transform profilometry	13
2.1.5 Fringe projection method	15
2.2 Phase unwrapping in fringe projection	19
2.2.1 Spatial phase unwrapping	21
2.2.1.1 Goldstein branch-cut method	22
2.2.1.2 Quality guided maps	25
2.2.1.3 Reliability based quality guided phase unwrapping	25
2.2.1.4 Unweighted least-squares method	27
2.2.1.5 Weighted least-squares method	28
2.2.2 Temporal phase unwrapping	30

2.2.2.1	Multi-frequency phase unwrapping	31
2.2.2.2	Number theoretical phase unwrapping	33
2.2.2.3	Binary coding	35
2.2.2.4	Phase unwrapping by adding a stair pattern	36
2.3	System characterisation in fringe projection	37
2.3.1	Camera characterisation	37
2.3.1.1	Intrinsic parameters	38
2.3.1.2	Extrinsic parameters	40
2.3.1.3	Camera projection model	41
2.3.1.4	Geometric distortion	42
2.3.2	Stereo-camera system	44
2.3.2.1	Epipolar geometry	44
2.3.2.2	Stereo rectification	49
2.3.2.3	Disparity	52
2.3.3	Projector characterisation	54
2.3.3.1	Characterised camera-based method	55
2.3.3.2	Phase-stepping method	58
2.4	Sources of error in fringe projection	61
2.4.1	Optical resolution of the imaging system	62
2.4.2	Error in the phase domain	63
2.4.3	System characterisation error	65
2.4.4	Background illumination	66
2.4.5	Noise	67
3	Single-view fringe projection system	70
3.1	Development of a single-view fringe projection system	72
3.1.1	System design and specifications	73
3.1.2	Methodology for the single-view fringe projection system	76
3.1.2.1	Gamma correction	77
3.1.2.2	System characterisation	78
3.1.2.3	Measurement - 3D reconstruction	79

3.1.3	Experimental results of the single-view fringe projection system	80
3.1.3.1	Gamma correction results	80
3.1.3.2	System characterisation results	81
3.1.3.3	3D reconstruction results	83
3.2	Investigation of sources of error in the single-view fringe projection system	88
3.2.1	Principle of gamma effect and DOF	88
3.2.1.1	Non-linear gamma effect in fringe projection systems .	88
3.2.1.2	Look-up-table approach	89
3.2.1.3	DOF	90
3.2.2	Experiments on gamma correction and DOF	91
3.2.2.1	Non-linear gamma correction	92
3.2.2.2	Experimental results: Gamma correction	93
3.2.2.3	Effect on quality of projected sinusoidal patterns . . .	95
3.2.2.4	DOF: Simulations	96
3.2.2.5	DOF: Experiments	98
3.3	Conclusions	99
4	Uncertainty evaluation of the form measurement of additively manufactured parts	101
4.1	Outline	101
4.2	AM artefacts	102
4.2.1	Mould insert	102
4.2.2	Complex shaped artefact	103
4.3	Measurements	104
4.3.1	Non-contact measurement: Fringe projection	104
4.3.1.1	Methodology for fringe projection	104
4.3.1.2	Uncertainty budget	105
4.3.2	Contact measurement: CMM	112
4.3.2.1	Comparison of fringe projection and CMM measurements	115
4.4	Conclusions	116
5	Multi-view fringe projection system	118

5.1	Introduction to multi-view fringe projection systems	118
5.2	Characterisation approach-1: Triangulation	121
5.2.1	Methods and materials	121
5.2.1.1	Geometric characterisation	122
5.2.1.2	Global frame of reference	124
5.2.2	Experiments on approach-1	125
5.2.2.1	Experimental setup	125
5.2.2.2	Results of the multi-view system	126
5.3	Characterisation approach-2: Stereo rectification of phase maps	127
5.3.1	Methodology of approach-2	127
5.3.2	Experiments on approach-2	132
5.3.2.1	Camera characterisation results	132
5.3.2.2	Rectification of the unwrapped stereo phase maps	134
5.3.2.3	3D reconstruction results	135
5.4	Comparison with the conventional method	141
5.5	Conclusions	145
6	Performance verification of a multi-view fringe projection system	147
6.1	Introduction to performance verification	147
6.2	Multiple view system verification	149
6.2.1	Probing form error	149
6.2.2	Probing size error	151
6.2.3	Sphere spacing error	151
6.3	The methodology of performance verification	152
6.3.1	Artefacts for verification test	152
6.3.1.1	Ball bar	153
6.3.1.2	Ball beam	153
6.4	Experiments on performance verification	154
6.5	Conclusions	160
7	Conclusions and future work	162
7.1	Conclusions	162

7.2 Future work	167
Bibliography	169

List of Tables

- 3.1 System characterisation results for the camera and projector. 83
- 4.1 Features at the front side (top face). FP = Fringe projection, Prob = Probability, dist = distribution, Rect = Rectangular, Norm = Normal, Div = Divisor. 110
- 4.2 Features at the rear side (bottom face). FP = Fringe projection, Prob = Probability, dist = distribution, Rect = Rectangular, Norm = Normal, Div = Divisor. 111
- 4.3 Dimensions of the sample. FP = Fringe projection, Prob = Probability, dist = distribution, Rect = Rectangular, Norm = Normal, Div = Divisor. 111
- 4.4 Complex shaped artefact. FP = Fringe projection, Prob = Probability, dist = distribution, Rect = Rectangular, Norm = Normal, Div = Divisor. 113
- 4.5 Comparison of FP and CMM data for the industrial test case. 116
- 4.6 Comparison of FP and CMM data for the complex artefact. 117
- 5.1 Geometric characterisation results for the cameras and projectors. . . . 122
- 5.2 Dimensional measurements of the complex artefact. 139
- 5.3 Dimensional measurements of a hemisphere shaped AM artefact. Each measurement has three repeats. The hemisphere height measured by CMM (four repeat measurements) is (9.6830 ± 0.0004) mm. 145
- 6.1 Probing form and size errors for a calibrated tested sphere. The diameter of the sphere is 20.00137 mm. 157
- 6.2 Sphere spacing error using a ball beam. The nominal values of sphere-1, sphere-2 and centre-to-centre spacing error are 20.00073, 20.00130 and 120.05509, respectively. 160

List of Figures

1.1	Schema of the measurement pipeline of the stereo matching based characterisation method of the multi-view fringe projection system.	4
2.1	The basic principle of ToF.	9
2.2	Schema for the working principle of laser triangulation. A and B are the intersection points of the laser beam at the measured and the reference surface respectively, A' and B' are the intersection points at the camera sensor, O and O' are the intersection points of the perpendicular lines from points B and B' respectively.	11
2.3	Schema of close-range photogrammetry.	12
2.4	Fourier spectrum of a fringe pattern. (a) Separated spectrum and (b) a single spectrum. Here A and C represent the Fourier spectra, f_0 is the spatial carrier frequency, and f_x is the spatial frequency along the horizontal direction.	13
2.5	Phase-shifted fringe patterns. (a) Fringe pattern with phase 0° (b) fringe pattern with phase 120° and (c) fringe pattern with phase 240°	16
2.6	Schema of the fringe projection system.	17
2.7	The pipeline of a DFP system.	18
2.8	Phase unwrapping in 1D. (a) A sinusoidal signal whose amplitude exceeds the range $[-\pi, \pi]$ and has a continuous phase (b) wrapped phase, the 2π discontinuities in the wrapped phase signal are represented by red circles and removed by adding/subtracting a factor of 2π and (c) the unwrapped phase.	20

2.9	Phase unwrapping in 2D. (a) Original intensity image (b) wrapped phase image (c) unwrapped phase image (d) row-150 of the intensity image shown in (a), (e) row-150 of the wrapped image shown in (b) and (f) row-150 of the unwrapped image shown in (c).	20
2.10	Branch cuts. (a) Positive and negative residues marked by empty and filled circles, respectively (b) the cuts isolate the portions of the image, hence not a good choice and (c) a better option.	23
2.11	Binary coded patterns.	35
2.12	Schema of the pinhole model of the camera.	38
2.13	Schema of geometric distortion. (a) Linear image with no radial distortion (b) image with radial distortion (c) lens and sensor are parallel and (d) the scenario of tangential distortion.	43
2.14	Schema of the epipolar geometry of a stereo-camera system. p_L and p_R are the projections of 3D point P onto the left and right camera images, respectively. L_L and L_R are the epipolar lines, and e_L and e_R epipolar points of the left and right camera images, respectively. O_L and O_R are the left and right cameras centres respectively.	46
2.15	Schema of the stereo rectification process.	49
2.16	Standard stereo-camera system whereby the two cameras are separated by a distance called baseline b . The difference between the horizontal coordinates (x_i^L, x_i^R) of the image points (q_i^L, q_i^R) corresponds to disparity.	53
2.17	Standard targets for camera characterisation. (a) Checkerboard with black and white squares (b) circle pattern with black circles and white background and (c) asymmetric circle pattern with black circles and white background.	56
2.18	Schema of the characterised camera-based method which relies on the pinhole model of the camera and the projector.	57
2.19	The process of generating the projector image coordinate.	59

2.20	Phase unwrapping error. (a) Original image (b) wrapped image and (c) the unwrapped image depicting the error accumulation whereby the high noise area (shadowed) has introduced discontinuities in the unwrapped regions.	64
2.21	Reprojection error. (a) Pinhole camera model depicting the difference between the projected 3D point on the image plane and the point re-projected using camera parameters and (b) a checkerboard pattern illustrating the reprojection error.	65
2.22	Checkerboard image with Gaussian smoothing filter of increasing standard deviations is applied (a) Original image (b) image with $\sigma = 4$ and (c) image with $\sigma = 6$	68
3.1	The CAD design of the fringe projection system. (a) Camera and projector mounted on a baseplate and (b) rotation plate mounted on a rotation stage.	73
3.2	The CAD design of the projector and camera assembly and support to mount the baseplate on a tripod stand.	73
3.3	The CAD design of the single-view fringe projection system. (a) Top view and (b) side view.	74
3.4	The CAD design of the fringe projection system in the assembled form.	75
3.5	Individual components used in the development of a fringe projection system.	76
3.6	Fringe projection system in the acquisition mode. (a) The side view of the developed system when the projector projects fringes on the object and (b) the front view.	76
3.7	The non-linear gamma curve of the DLP projector. The data is shown as blue dotted points and the red line corresponds to the polynomial fitting.	81
3.8	Schema of the system characterisation of the fringe projection system.	82

3.9	Fringes projected on the checkerboard and captured by a camera. (a) Original image and (b) the corresponding phase map with the detected checkerboard points.	82
3.10	Reprojection error per image. (a) Camera and (b) projector.	82
3.11	Extrinsic parameters. (a) Camera and (b) projector.	83
3.12	3D reconstructed results for AM artefacts. (a) Original image with fringes projected (b) unwrapped phase map and (c) a point cloud representing the 3D shape.	84
3.13	3D reconstructed results of a Nylon-12 artefact. (a) Original image with fringes projected (b) unwrapped phase map (c) 3D reconstructed point cloud and (d) zoomed-in view of the data shown in (c).	85
3.14	3D reconstructed results of a jaw shaped artefact. (a) Original image with sinusoidal fringes projected and (b) the unwrapped phase map. . .	85
3.15	Different views of the 3D reconstructed results of a jaw shaped artefact. (a-d) Single-view data acquired from different perspectives and (e) the combined point cloud which is obtained by registering the single-views shown in (a-d).	86
3.16	Flatness deviation of a flat surface measured by the fringe projection system. A colour map for repeat (a) measurement-1 (b) measurement-2 (c) measurement-3 (d) measurement-4 and (e) measurement-5.	86
3.17	The statistical distribution of the data shown in figure 3.16. A histogram showing the signed point-to-point distance between the measured data and fitted flat plane, for repeat (a) measurement-1 (b) measurement-2 (c) measurement-3 (d) measurement-4 and (e) measurement-5.	87
3.18	Gamma correction approach (a) Schema of the relationship between projected and captured intensity and (b) implementation of the LUT approach.	89
3.19	Checkerboard pattern. (a) ROI of 4×4 squares area, (b) FFT spectrum of the ROI and (c) FFT spectrum (2-D view) whereby the red circle denotes the periodicity in 45° axis.	91

3.20	Experimental setup. (a) Schema of the setup to acquire the gamma curve and (b) a photograph of the experimental assembly.	92
3.21	Experimental results. (a) The non-linear gamma curve of a laser projector and (b) gamma curve of a pico DLP projector.	93
3.22	Elimination of non-linear gamma distortion by LUT approach. (a) Laser projector and (b) pico DLP projector.	94
3.23	Non-linear gamma correction. (a) The original intensity image in grayscale for a laser projector (b) cross-section of column-1000 in (a); blue curve (before correction) and red curve (after correction) for a laser projector (c) the frequency spectrum of the centre of the image column-1000 in (a); blue (before correction) and red curve (after correction) (d) the original intensity image for a pico DLP projector (e) cross-section of column-1000 in (d) blue curve (without correction) and red curve (after correction) for a pico DLP projector and (f) FFT spectrum for a pico DLP projector.	94
3.24	Implementation of non-linear gamma correction on laser and pico DLP projectors. (a) Original image as a surface plot (laser projector) (b) original image as a surface plot (pico DLP projector) (c) unwrapped phase image after gamma correction (laser projector) and (d) unwrapped phase image after gamma correction (pico projector).	95
3.25	The RMS phase difference error of column-1000. (a) Laser projector (RMS= 0.087 rad) and (b) pico DLP projector (RMS= 0.19 rad).	96
3.26	The pipeline of the DOF experiment.	97
3.27	Simulated results for DOF. (a) FFT of the ROI (6×6 square) by varying the Gaussian smoothing. The pitch value (14 pixels) remains the same (b) FFT of the ROI (6×6 square) for a very small variation in the Gaussian smoothing ($\sigma = 0.6-0.85$) and (c) FFT of the ROI (6×6 square) when the Gaussian smoothing varies randomly.	97
3.28	Schematic illustration of the DOF setup.	98

3.29	DOF results. (a) Comparison of DOF of the pico DLP and laser projectors (b) laser projector's focused image (c) laser projector's defocused image and (d) pico DLP projector's focused image, and (e) pico DLP projector's defocused image.	99
4.1	Topology optimised mould insert [1]. (a) Top view and (b) bottom view.	103
4.2	Photograph of the complex artefact with labelled features measured by CMM.	104
4.3	Features of interest of the mould insert [1] given in figure 4.1.	105
4.4	A comparison between the fringe projection data of the injection mould and the CAD model. The bottom face of the injection mould (shown in figure 4.1(b)) is chosen to perform the analysis.	112
4.5	Comparison of the fringe projection data of the complex artefact and the CAD model. (a) The difference map and (b) a histogram representing the statistical distribution.	112
4.6	CMM coordinate system.	114
5.1	Multi-view fringe projection system. (a) A photograph of the multi-view fringe projection system with two sets of cameras and projectors and (b) schematic of the Multi-view fringe projection system.	121
5.2	Fringes projected on the checkerboard and captured by two different cameras from different perspectives. (a-b) Original images and (c-d) corresponding phase maps with the detected checkerboard points being projected back.	123
5.3	Extrinsic parameters. (a) Camera 1 (b) camera 2 (c) projector 1 and (d) projector 2.	123
5.4	Reprojection error per image. (a) Camera 1 (b) camera 2 (c) projector 1 and (d) projector.	124
5.5	3D reconstruction results from different perspectives. (a) Projector 1-camera 1 (b) projector 1-camera 2 (c) projector 2-camera 1 and (d) projector 2-camera 2.	125

5.6	3D reconstruction results for a multi-view fringe projection system with four cameras and three projectors.	126
5.7	3D reconstruction results for a hemisphere (60 mm × 60 mm × 20 mm, Nylon-12) artefact. (a) Point cloud from a single-camera projector (b) point cloud from two sets of cameras and projectors and (c) point cloud from four cameras and three projectors.	127
5.8	Schema of the characterisation method of the multi-view fringe projection system.	128
5.9	Schema of the rectification of the stereo-camera phase images. ϕ_L and ϕ_R are the projections of a 3D point P onto the left and right camera phase images, respectively. l_L and l_R are the epipolar lines of the left and right camera phase images, respectively. O_L and O_R are the left and right cameras' optical centres, respectively.	130
5.10	Photograph of the multi-view fringe projection system. The system is comprised of four DSLR cameras and two projectors.	133
5.11	Mean reprojection error per image for the camera characterisation. (a) Camera 1 (b) camera 2 (c) camera 3 and (d) camera 4.	134
5.12	Reprojection error per image for stereo-camera pairs (a) stereo-camera pair 1, (b) stereo-camera pair 2, and (c) extrinsic parameter visualisation of stereo-camera pair 1. The region with coloured squares corresponds to the checkerboard patterns detected by the stereo-camera pair 1, and (d) extrinsic parameter visualisation of stereo-camera pair 2.	135
5.13	Images of a complex shaped object (110 mm × 110 mm × 50 mm) with fringes projected. The images are captured by two cameras in a stereo configuration (a) Camera-1 and (b) camera-2. Filtered unwrapped phase maps of the object for (c) data shown in (a) and (d) data shown in (b).	136
5.14	Rectified unwrapped phase maps. (a) Rectified phase image for the phase map in figure 5.13 (c) and (b) rectified phase image for the phase map in figure 5.13 (d).	136

- 5.15 3D reconstruction results for a complex artefact ($110 \text{ mm} \times 110 \text{ mm} \times 50 \text{ mm}$). On the left side, two point clouds acquired from stereo-camera (a) pair 1 (b) pair 2, respectively and on the right side (c) a consolidated point cloud after combining the two views (a-b). 137
- 5.16 Results for the deviation of two point clouds for the complex artefact. (a) Point cloud showing the ROI as a red box, (b) a colour map indicating the signed point-to-point distance of the two point clouds from stereo-camera pairs 1 and 2, and the distances are determined between a reference point cloud (stereo-camera pair 1) and a target point cloud (stereo-camera pair 2) [2], and (c) a histogram depicting the statistics of the signed point-to-point distance of the two point clouds shown in (b), the standard deviation (St.Dev) of the distribution is $48 \mu\text{m}$ 138
- 5.17 Conventional method. (a) Photograph of the multi-view fringe projector system with two cameras and projectors considered for the conventional approach, (b) schematic diagram of the characterisation of the multi-view fringe projection system. 141
- 5.18 Mean reprojection error per image for the camera characterisation. (a) Camera 1 (b) camera 2 (c) projector 1 and (d) projector 2. 142
- 5.19 3D reconstruction results of a hemisphere shaped AM artefact ($60 \text{ mm} \times 60 \text{ mm} \times 20 \text{ mm}$). Top row: Conventional method. (a-b) Point clouds acquired from camera-projector pair 1 and 2, respectively (c) combined point cloud of the data shown in (a-b). Bottom row: Proposed method. (d-e) Point clouds from two sets of stereo-camera pairs and (f) the combination of two point clouds shown in (d-e). 143

5.20	Results for the deviation of two point clouds of a hemisphere shaped AM artefact. Top row: Conventional method. (a) Point cloud showing the ROI as a red box, (b) colour map indicating the signed point-to-point distance of the two point clouds from camera-projector pairs 1 and 2, and the distances are determined between a reference point cloud (stereo-camera pair 1) and a target point cloud (stereo-camera pair 2) [2] and (c) histogram depicting the statistics of the signed point-to-point distance of the two point clouds shown in (b). Bottom row: Proposed method. (d) ROI shown as a red box, (e) signed point-to-point distance between the two point clouds from stereo-pair 1 and 2 and (f) statistical distribution of the data shown in (e).	144
6.1	Probing error according to VDI/VDE 2634 part-3 [3]. (a) Sensor position for capturing the form of the calibrated test sphere and (b) different orientations of the calibrated test sphere in the measurement volume. .	150
6.2	Different orientations of the ball bar in the measurement volume for sphere spacing error as recommended in VDI/VDE 2634 part-3.	151
6.3	Artefacts used for the verification test. (a) A ball bar and (b) a ball beam.	153
6.4	A dumbbell shaped ball bar with fringes projected. The orientation for one of the measured positions as seen by (a) camera-1 (b) camera-2 (c) camera-3 and camera-4.	155
6.5	Unwrapped phase map for the data shown in figure 6.4 for (a) camera-1 (b) camera-2 (c) camera-3 and camera-4.	155
6.6	3D surface reconstructions for one of the spheres of a ball bar using the stereo matching of unwrapped phase maps approach as mentioned in section 5.3.2. (a) Stereo-camera pair 1 (b) stereo-camera pair 2 and (c) combined point cloud of the data shown in (a) and (b).	156
6.7	Reconstructed point cloud for one of the measured spheres of ball bar. Measured data is fitted with a primitive feature of a sphere.	156

6.8	A ball beam with fringes projected. The orientation for one of the measured positions as seen by (a) camera-1 (b) camera-2 (c) camera-3 and camera-4.	158
6.9	Unwrapped phase map for the data shown in figure 6.8 for (a) camera-1 (b) camera-2 (c) camera-3 and camera-4.	158
6.10	3D surface reconstructions for ball beam using the stereo matching of unwrapped phase maps approach as mentioned in section 5.3.2. (a) Stereo-camera pair 1 (b) stereo-camera pair 2 and (c) combined results of the data shown in (a) and (b).	159
6.11	Reconstructed point cloud for ball beam. Measured sphere points are fitted with a primitive feature of a sphere and the distance between the centres of two spheres is measured.	159

Chapter 1

Introduction

1.1 Motivation

Post-process coordinate metrology imposes a significant challenge due to the complex freeform, occluded, and steep geometries of additively manufactured (AM) objects [4]. In general, coordinate metrology is the science and application of determining the physical geometry/form of an object using a coordinate measuring system [5]. Essentially, metrology is a fundamental tool in manufacturing as it establishes the necessary framework for process and quality control of AM parts, assists in characterising and optimising the AM processes, primarily when new geometries are evolved, and provides guidance for post-process troubleshooting. In general, the inspection process for the verification of geometric dimensions and tolerance (GD&T) specifications regarding the design requirements is necessary for quality assurance. GD&T ensures that the manufactured parts are within the specified tolerance regime, fulfil the functional demands and easily fit within the designed assemblies, reduce the production cost, and help AM manufacturers to optimise the AM processes [6].

Methodologies for the accurate dimensional characterisation of AM parts are primarily categorised as contact and non-contact measurement methods. The field of contact form metrology (coordinate measuring machines, CMMs) is highly accurate (accuracy down to a micrometre [7–10]), well understood and has been used for many years [7, 8, 11–13]. In principle, CMMs use a probe or stylus which comes in contact

with the surface of the object and measures the 3D coordinates of each point. Several discrete points around the object are measured to construct a 3D point cloud of the measured object. However, contact systems are relatively slow, measure a limited number of points, destructive compared to optical form measurement systems and not suitable for in-process monitoring and inspection of the AM processes. In contrast to contact systems, non-contact optical systems such as laser triangulation [14, 15], photogrammetry [16–19], and structured light techniques [19–22] have the benefit of high resolution, full-field acquisition, and fast data processing with a high signal-to-noise ratio.

The digital fringe projection methods have been extensively used in the industrial sector for the post-process characterisation of highly complex AM parts due to their fast acquisition rate, non-contact and non-destructive nature, and cost-effectiveness [20, 21, 23–25]. In practice, significant improvements have been made in the accuracy and precision of commercially available systems which can achieve accuracies up to 10 μm [26] and used for post-process verification of AM parts. However, single-view commercial systems require a rotation table to give the fringe projection system a 360° view for 3D surface reconstructions. In this context, the commercial systems have some limitations due to the frequent existence of occlusions, freeform complex geometries/form of AM parts, shiny surfaces, restricted field-of-view and the multiple views for measuring the full form of the object. In order to overcome the fundamental limitations, multi-view fringe projection systems are considered as a potential candidate, and an active research area [27–30].

In general, multi-view fringe projection systems are highly complex, require characterisation (intrinsic and extrinsic parameters) of all the optical components (cameras and projectors) and a global coordinate system. The complexity involves understanding the structural relationship between multiple sets of optical components, the interaction of light with the object surface and its influence on the accuracy of the multi-view fringe projection system, a key research area for the future of optical form metrology.

1.2 Aims and objectives

This work aims to develop a novel methodology for the characterisation of a multi-view fringe projection system that improves the measurement pipeline, starting from the optics all the way to the algorithms used and to enable an easy and flexible assessment of complex AM objects. The outcome of this work will be,

- Practical demonstration of the proposed novel method for the form measurement of complex AM artefacts
- Manifestation of the multi-view fringe projection system for the conventional characterisation approach
- Comparison between the developed novel and the conventional methods of characterising the multi-view fringe projection system
- Address the practical concerns and limitations of existing single-view fringe projection systems, such as occlusions, limited depth of field, and environmental noise, which generally affect the optical and image processing techniques
- Performance verification of the multi-view fringe projection system using existing verification standards for the optical form measurement system

1.3 The novelty of research work

The novelty of this work relies on developing a methodology for the characterisation of a multi-view fringe projection system that resides on stereo matching between rectified unwrapped stereo phase maps based on the epipolar constraint. The advantage of the method employs in alleviating the mapping error due to its non-reliance on the projector characterisation; therefore, determining the correspondences between the camera and the projector pixels is not required. In general, the dense disparity map is achieved by combining the stereo vision and fringe projection methodologies which further utilises the stereo-camera characterisation information for 3D surface reconstruction [31–34]. In stereo vision, the matching points between multiple images are

determined, and the approach works in the pixel domain. However, the method developed in this work relies on determining the correspondences in the phase domain.

Figure 1.1 depicts the pipeline of the measurement process. The first step, considered as a prerequisite, is the system characterisation which depends on finding the intrinsic and extrinsic properties of all the cameras. Since the developed method does not require projector characterisation, therefore this alleviates the need for multiple characterisations. The camera characterisation is performed by capturing the images of a standard artefact (checkerboard or a dot/circle pattern) which is placed in the field of view of all the cameras. Images of the standard artefact at different orientations are captured by all cameras, and each camera is characterised based on a pinhole camera model [35–38]. The image coordinates of the markers (corners of squares in a

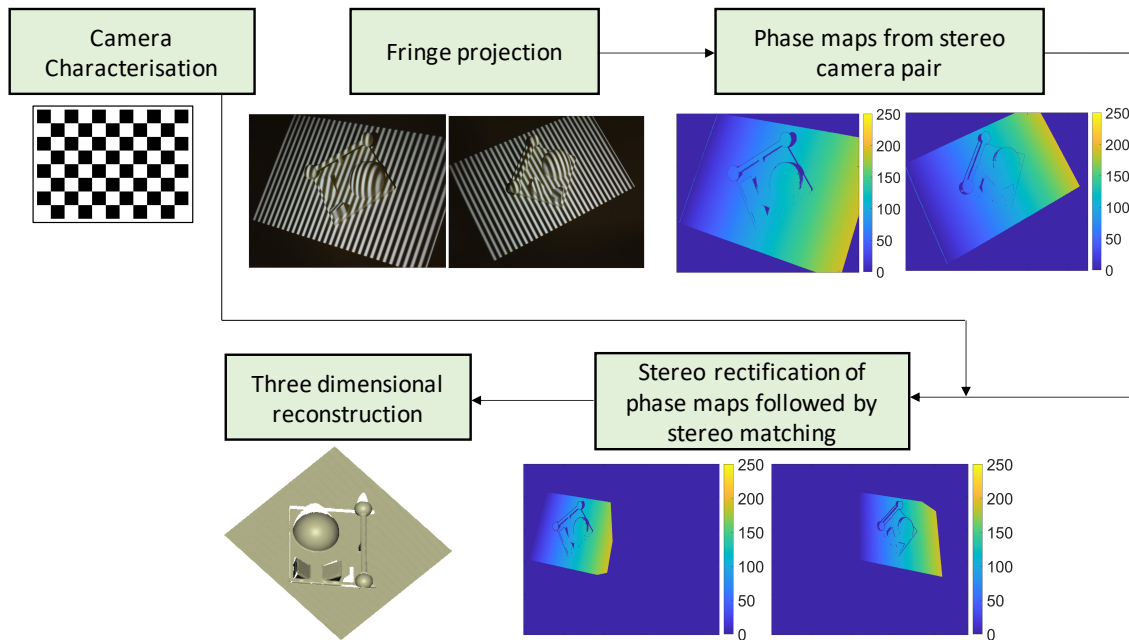


Figure 1.1: Schema of the measurement pipeline of the stereo matching based characterisation method of the multi-view fringe projection system.

checkerboard or circles in a dot/circle pattern) are extracted from the captured camera images, and the camera parameters (intrinsic and extrinsic) of each camera are determined using an image processing algorithm [39]. A global coordinate system is defined by considering the relative orientation and location in each stereo-camera pair with respect to the first checkerboard position, which is in the common field of view of all the cameras; therefore, it represents the same global coordinate system.

The camera characterising follows the generation of the stereo-camera parameters using the characterisation information of individual cameras [40–47]. In principle, the generation of stereo-camera pairs is considered from the perspective of the common field of view and the area illuminated by the structured light pattern (fringes); therefore, the adjacent camera pairs are regarded as stereo-camera pairs, which configures multi-view system as two sets of stereo-camera pairs. After the prerequisite step of system characterisation, phase maps are acquired using the fringe projection method. In general, a fringe projection system can be mathematically modelled as a stereo-camera system (one camera in the stereo pair is replaced with a projector) and utilises common points between the projector and the camera based on the triangulation principle. For that purpose, a set of phase-stepped sinusoidal and binary-encoded fringe patterns [48] are projected onto the surface of the measuring object, and the distorted fringes are captured at each step. The acquired phase has 2π modulation; therefore requires the unwrapped algorithm (a temporal phase unwrapping is applied [49–52]), which eliminates the 2π discontinuities and yields a continuous phase map.

The phase maps captured by the adjacent cameras are considered stereo phase maps. A transformation, called rectification, is applied to stereo phase maps to project them onto the same plane, which accounts for camera distortion and the non-coplanar stereo-camera pair [53, 54]. The benefit of image rectification is that it transforms each image such that the epipolar lines are parallel; therefore, the 2D search problem reduces to a 1D search problem. The rectification follows the stereo matching in which the search for correspondences is established by determining the points at which the phase values match. The output of the stereo matching process is a disparity map. An iterative approach for disparity computation is considered, in which the phase value in the left camera phase image is compared with the corresponding epipolar line of the right camera phase map using the nearest neighbour search. The matched phase points between the rectified phase images are determined and combined with the respective projection matrix of the adjacent cameras (configured as a stereo-camera pair). Ultimately, the 3D world coordinates of the measuring object are determined based on the triangulation principle.

Additionally, a comparison of the developed novel method with the conventional approach (mentioned in chapter 5) of characterising a multi-view fringe projection system is performed. For this purpose, the multi-view fringe projection system is demonstrated for the conventional approach, and the 3D surface reconstructions of AM artefacts are acquired. Furthermore, as there are no specific calibration standards for traceable measurements of 3D optical form measurement systems; therefore, the results are compared with the contact CMM measurements which provide a reference for dimensional measurements.

1.4 Overview of the work

Chapter 2 provides an overview of the existing state-of-the-art three-dimensional imaging techniques with the main focus on the fringe projection method. Extensive background and current research on fringe projection method are presented, and various steps of the fringe projection method such as; phase unwrapping methodologies, system characterisation, especially the camera and projector characterisation methods, stereo-camera system and associated epipolar geometry. Additionally, the factors that affect the measurement accuracy of the fringe projection method are described.

Chapter 3 presents the design and development of a single-view fringe projection system which helps to investigate the fundamental constraints of the existing fringe projection systems. The identification of sources of error in the single-view fringe projection system is established by comparing the commercially available low-cost laser and digital light processing projectors in terms of the non-linear gamma effect and the depth-of-focus. The performance of the two projectors is evaluated from the perspective of their use in the fringe projection applications.

Chapter 4 is related to the uncertainty evaluation of the three-dimensional shape measurement of complex AM metal parts using contact and non-contact instruments. A complete pipeline for the uncertainty evaluation of different features of an AM industrial test case is provided. The measurement uncertainty is determined by considering all types of uncertainties associated with the measurand. Contact method such as

coordinate measuring machine is used which provide a reference for the coordinate measurements.

Chapter 5 covers the development of a multi-view fringe projection system with potential application to address the existing constraints of single-view fringe projection systems. The chapter describes two methods of characterising the multi-view system, one as an extension of the conventional method of characterising a single camera projector systems with the inclusion of a global frame of reference. The second approach is based on the stereo matching of the phase values between the unwrapped stereo phase maps, which does not require projector characterisation. A comparison between the two methods is made by three-dimensional surface reconstructions of complex AM artefacts, which reveals that the second method has attained improved performance by alleviating the mapping error.

Chapter 6 demonstrates the performance verification of the developed multi-view fringe projection system based on the VDI/VDE 2634 part-3 verification standard and evaluates the uncertainty associated with the measurements performed with the multi-view system. The chapter also shed light on the systematic error and their influence on the accuracy of the measurements.

Ultimately, chapter 7 concludes the effectiveness of the multi-view fringe projection system for three-dimensional form measurement of complex AM artefacts, summarises the contribution of the work done in this thesis and purposes future work for further improvement and advancement in the form measurement technology.

Chapter 2

Background - State of the art

2.1 Introduction to three-dimensional imaging

Optical three-dimensional (3D) form measurement is the process of acquiring the information of surface topography by optical means (optical sensors or CCD arrays). It is often referred to as 3D optical metrology, 3D scanning or 3D imaging. In general, with the advent of modern fast computers and reliable image processing software, the accuracy of the optical form measurement systems over the years has been improved. Essentially, the accuracy achievable using optical metrology has made it a useful tool across many engineering and scientific disciplines. The optical methods are non-contact, non-destructive and non-invasive, therefore, highly relevant in various fields including medical science, manufacturing, computer-vision, aerospace and automotive.

Over the last decades, a significant improvement in 3D scanning techniques has been made and numerous methods have been developed including time of flight (TOF) [55, 56], three-dimensional shape from focus and defocus [57, 58], laser triangulation [14, 15], photogrammetry [16–19], Fourier transform profilometry [59–61], and digital fringe projection (DFP) [19–22]. One of the most common and extensively used non-contact measurement techniques is the DFP. In this method, the fringe patterns are demodulated and projected onto the surface of the object to obtain height information. A brief introduction to 3D shape measurement techniques is provided in the following

sections to give a general idea of all the possible options, however the main focus relies on the fringe projection method.

2.1.1 Time of flight

The time of flight (TOF) is a laser scanning method that does not require triangulation. The method calculates the time difference of the round trip of light being emitted and bounced back from the point surface to the sensor [55]. Since the light travels at high speed of 3×10^8 m/s, therefore, in order to resolve a minimal depth change (1 mm), the sensor's resolution should be of the order of 10^{-9} s, which is very difficult to achieve. Rather than directly measuring the time difference, the TOF technique measures the

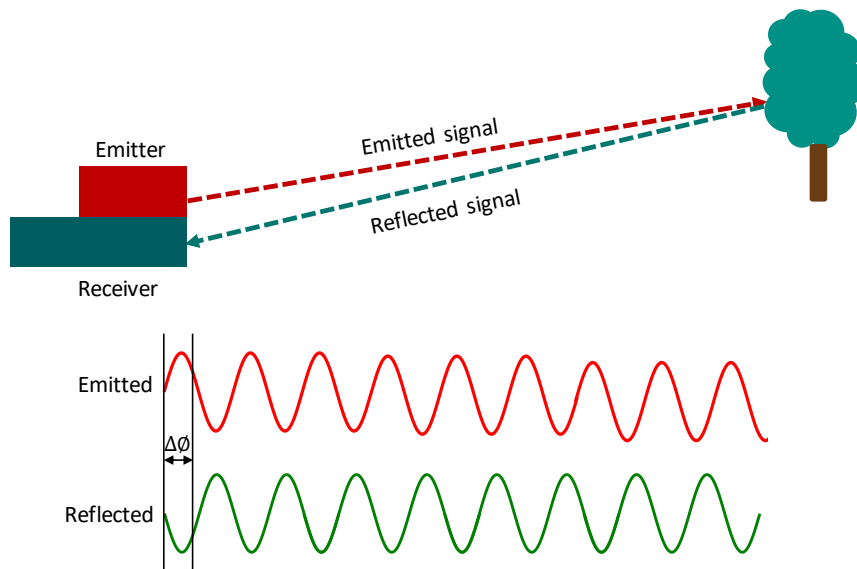


Figure 2.1: The basic principle of ToF.

phase changes for the round trip. A typical TOF assembly consists of a light source and a light sensor, as shown in figure 2.1. A modulated light beam is emitted by the light source, reflected back from the object surface and captured by a sensor. The phase difference between the emitted and reflected light beam is calculated and the height information of the object can be obtained using the speed of light [56], and given by

$$Z = \frac{c\Delta\phi}{4\pi f_m}, \quad (2.1)$$

where c depicts the speed of light (3×10^8 m/s), f_m is the modulation frequency, $\Delta\phi$ is the phase change, and Z is the depth.

Generally, the ToF sensor measures the intensity and phase information simultaneously. The compact design of the ToF laser scanning technology makes it suitable for applications of buildings, robotics and automotive industry. However, the ToF laser scanners are limited by spatial and depth resolution, which is associated with the complexity of manufacturing a sensor.

2.1.2 Laser triangulation

The laser triangulation determines the distance between the laser and the object at each specific point, as depicted in figure (2.2). A typical laser triangulation system comprises a laser source, a detector, and a lens. The lens focuses the laser beam on the photodetector. The laser light shines onto the surface of the object, and the reflected light is sensed by the photodetector. The depth information can be retrieved by the triangular geometry of the laser source point, the reflecting point, and the sensing point on the detector. Mathematically, the distance between the object point and the image point on the CCD is given by [62, 63]

$$h = \frac{ax' \sin \eta}{b \sin \beta - x' \sin(\beta + \eta)}, \quad (2.2)$$

where x' is the image point displacement on the camera sensor, β is the angle between the incident laser beam and the receiving lens, η is the angle between the camera sensor and the optical axis of the lens, a is the distance of the object from the lens, and b is the distance of the image from the lens.

A laser triangulation-based scanner is capable of achieving high spatial and depth resolutions and measuring large objects, such as buildings or ships. However, this method is not robust since a laser spot/line sweeps over the whole surface, which makes the data acquisition process slow and time-consuming; also this technique is less suitable for dynamic object [14]. Another drawback is that the laser light is coherent; therefore, the speckle noise affects the system accuracy.

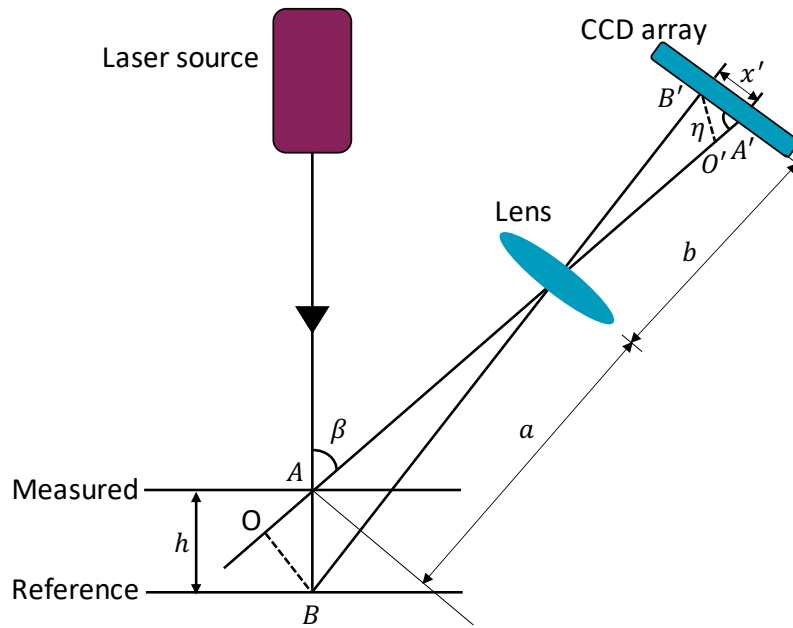


Figure 2.2: Schema for the working principle of laser triangulation. A and B are the intersection points of the laser beam at the measured and the reference surface respectively, A' and B' are the intersection points at the camera sensor, O and O' are the intersection points of the perpendicular lines from points B and B' respectively.

2.1.3 Photogrammetry

Photogrammetry is the science of making measurements from photographs. Photogrammetry incorporates methods of image measurement to retrieve the 3D shape of an object from two or more photographs [64]. In principle, the photogrammetric measurement yields the 3D surface reconstruction of an object either in digital forms such as coordinates and geometric parameters or graphical forms as images, maps, and drawings. Photogrammetry is well-established in topographic mapping; however, in recent years, it is extensively used in the areas of architecture, industrial sector, engineering, medicine, and geology for the generation of precise 3D data.

Photogrammetry, based on the camera position, can be categorised as Ariel photogrammetry and Terrestrial (or close-range) photogrammetry. In Ariel photogrammetry, the camera is placed on the aeroplane and points vertically downward towards the ground. Various overlapping images are taken along the flight path and processed to track the precise path information. In contrast to Ariel photogrammetry, the close-range photogrammetry relies on the camera mounted close to the object usually handheld or on a tripod stand, as shown in figure 2.3. Close-range photogrammetry is

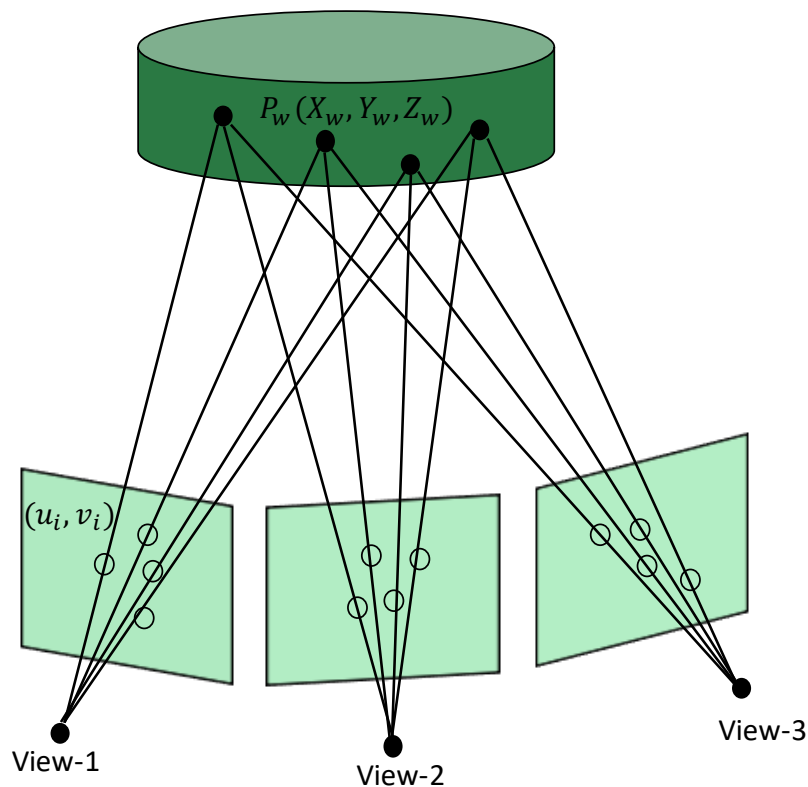


Figure 2.3: Schema of close-range photogrammetry.

preferred for non-topographic purposes, like building measurement, forensic and accident scenes, engineering structures, mines, earthworks and film sets.

The fundamental principle of photogrammetry is based on triangulation, and the typical photogrammetry methods employ the stereo technique [19, 65]. By capturing photographs from different perspectives (at least two different locations) and measuring the same target in each image, a line of sight is defined from each camera to the target. By determining the camera location and orientation, the intersection of rays emerging from the cameras is used to produce the three-dimensional coordinates of the point on the object [17].

The advantages of photogrammetry are cost-effectiveness, achievable resolution, fast acquisition times and suitability for measuring more surfaces using the benefits of diffused light. However, the photogrammetry setups struggle with the low depth-of-field and optics errors associated with camera lens distortion, shot noise, divergence and non-linearities. Surface texture is another constraint, and especially the smooth surfaces require an optical contrast to achieve the 3D information. The slow processing speed

is also a drawback since the 3D reconstruction is dependent on the data processing, which is significantly large for photogrammetry based systems.

2.1.4 Fourier transform profilometry

The Fourier transform profilometry is a well established and extensively used method for obtaining the phase information. This method was first proposed by Takeda et al. who utilised the Fourier transform for fringe pattern analysis and measuring the 3D shape of the objects [59]. Takeda and Mutoh [60], who presented it as an alternative to the Moire contouring method proposed by Idesawa et al. [66]. Takeda and Mutoh aimed to improve the automatic measurement in computer processing by eliminating the associated difficulties with Moire techniques and providing much higher sensitivity. The method involves the projection of the Ronchi grating on the measured object, and the reflected deformed pattern was captured. Takeda et al. also presented a frequency-multiplex Fourier-transform profilometry which yields a single-shot 3D shape measurement of complex discontinuous objects [61]. In general, the intensity of a fringe

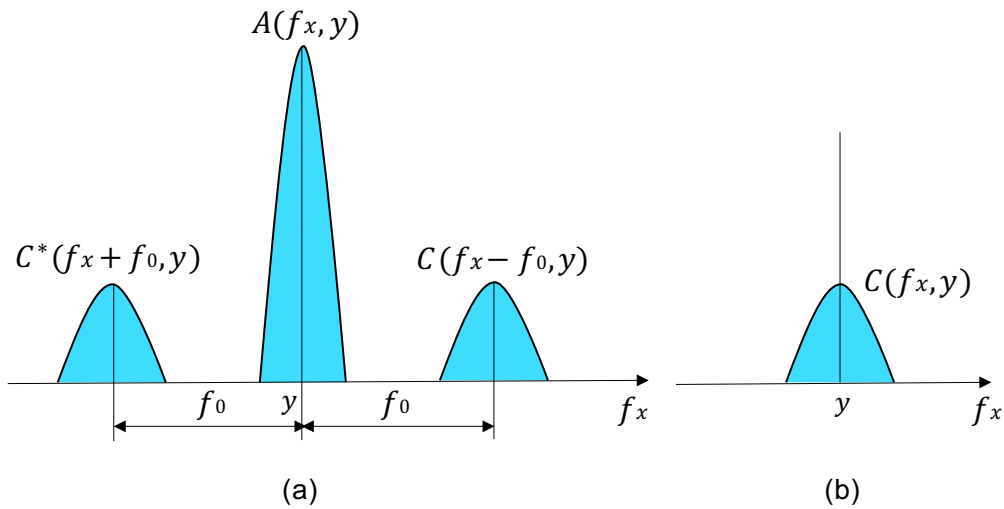


Figure 2.4: Fourier spectrum of a fringe pattern. (a) Separated spectrum and (b) a single spectrum. Here A and C represent the Fourier spectra, f_0 is the spatial carrier frequency, and f_x is the spatial frequency along the horizontal direction.

pattern can be represented as

$$I_g(x, y) = a(x, y) + b(x, y) \cos[\phi(x, y) + 2\pi f_0 x], \quad (2.3)$$

where $a(x, y)$ and $b(x, y)$ represents the object's surface reflectivity, $\phi(x, y)$ is the phase, and f_0 is the spatial carrier frequency [59]. Equation (2.3) can be rewritten as

$$I_g(x, y) = a(x, y) + c(x, y) \exp(2\pi i f_0 x) + c^*(x, y) \exp(-2\pi i f_0 x), \quad (2.4)$$

where

$$c(x, y) = \frac{1}{2} b(x, y) e^{i\phi(x, y)}, \quad (2.5)$$

$$c^*(x, y) = \frac{1}{2} b(x, y) e^{-i\phi(x, y)}. \quad (2.6)$$

Taking the fast Fourier transform of the equation (2.4)

$$G(f, y) = A(f_x, y) + C(f_x - f_0, y) + C^*(f_x + f_0, y), \quad (2.7)$$

where G, A, C represent the Fourier spectra, and f_x is the spatial frequency along the horizontal direction, as shown in figure 2.4. The Fourier spectra is separated by the spatial frequency since the spatial variation of $a(x, y)$, $b(x, y)$ and $c(x, y)$ is slow compared to f_0 . Computing the inverse Fourier transform $C(f_x, y)$ yields the $c(x, y)$, therefore, the complex algorithm can be calculated as

$$\log[c(x, y)] = \log\left[\frac{1}{2} b(x, y)\right] + i\phi(x, y). \quad (2.8)$$

Finally, the phase can be obtained as

$$\phi(x, y) = \arctan\left(\frac{\text{Im}[c(x, y)]}{\text{Re}[c(x, y)]}\right). \quad (2.9)$$

The above equation is a trigonometric arctangent function and ranges between $[-\pi, \pi]$, and gives wrapped phase map; therefore, it requires the unwrapping algorithms to retrieve the absolute phase information.

Fourier transform profilometry has been widely used for high-speed applications

as it requires one (or maximum two) distorted fringe patterns to demodulate the phase information and acquire the 3D shape of the objects. In general, the method is suitable for smooth surfaces but struggles to achieve the correct phase value at the edges (or slopes) of complex freeform objects with discontinuities. This is due to the reliance of the frequency components (in the frequency domain) on the spatial resolution and the existence of high-frequency components (at the edges) in the wrapped phase map that causes ambiguities and inconsistencies in the phase unwrapping. Thus, in order to demodulate the noisy fringe patterns, windowed Fourier transform or wavelet transform are recommended [67, 68].

2.1.5 Fringe projection method

The 3D optical metrology using DFP is extensively used in various fields due to its non-contact and non-destructive nature, fast data acquisition and high sampling density [20, 21]. The DFP system comprises a camera, a projector, and a computer for integration, data acquisition and data processing, as depicted in figure 2.6. The computer-generated fringe patterns (structured light patterns) are projected on the surface of the 3D object through a projector, and a camera captures the distorted fringe patterns (deformed due to the surface profile of the object).

In general, the phase contains the height information of the scanned object that needs to be recovered from the captured fringe images. In the existing methods, phase-shifting techniques are preferred due to their speed and measurement accuracy. Essentially, three fringe images are required to uniquely solve the phase per pixel; therefore, three phase-stepped fringe patterns (shown in figure 2.5) are required for high-speed 3D imaging applications. Mathematically, the three phase-shifted fringes with a phase difference of $(2\pi/3)$ can be expressed as

$$\begin{aligned}
 I_1(x, y) &= I_a(x, y) + I_b(x, y) \cos \phi(x, y) - \alpha, \\
 I_2(x, y) &= I_a(x, y) + I_b(x, y) \cos \phi(x, y) + 0, \\
 I_3(x, y) &= I_a(x, y) + I_b(x, y) \cos \phi(x, y) + \alpha,
 \end{aligned} \tag{2.10}$$

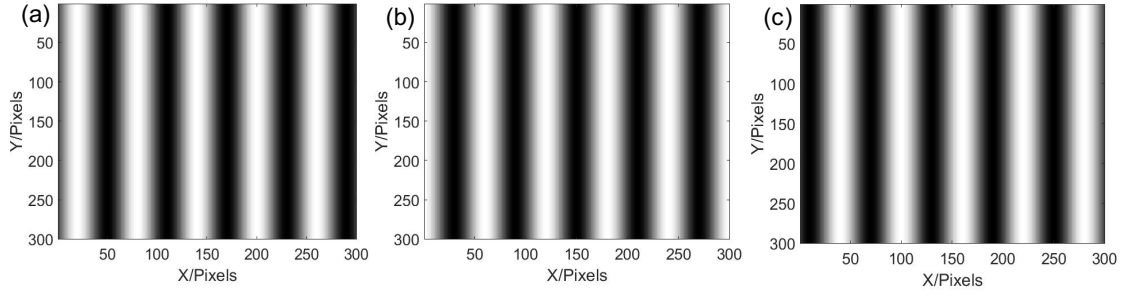


Figure 2.5: Phase-shifted fringe patterns. (a) Fringe pattern with phase 0° (b) fringe pattern with phase 120° and (c) fringe pattern with phase 240° .

where $I_a(x, y)$ is the average intensity while $I_b(x, y)$ is the intensity modulation and $\phi(x, y)$ is the phase. As it can be noticed that there are three unknowns in equation (2.10); therefore at least three modulated images are required for acquiring the phase information. Solving the above equations yields

$$\phi(x, y) = \tan^{-1} \left[\frac{(1 - \cos \alpha)(I_1 - I_3)}{\sin \alpha(2I_2 - I_1 - I_3)} \right], \quad (2.11)$$

$$\gamma(x, y) = \frac{I_b(x, y)}{I_a(x, y)} = \left[\frac{\sqrt{[(1 - \cos \alpha)(I_1 - I_3)]^2 + [\sin \alpha(2I_2 - I_1 - I_3)]^2}}{(I_1 + I_3 - 2I_2 \cos \alpha) \sin \alpha} \right], \quad (2.12)$$

where $\phi(x, y)$ is the phase and $\gamma(x, y)$ is the data modulation that depicts the quality of the fringe data in the range of $[0, 1]$ with 1 indicates the best. For $(\alpha = 2\pi/3)$, the above equations can be simplified as

$$\phi(x, y) = \tan^{-1} \left[\frac{\sqrt{3}(I_1 - I_3)}{2I_2 - I_1 - I_3} \right], \quad (2.13)$$

$$\gamma(x, y) = \frac{I_b}{I_a} = \frac{\sqrt{3(I_1 - I_3)^2 + (2I_2 - I_1 - I_3)^2}}{I_1 + I_2 + I_3}. \quad (2.14)$$

The equation (2.13) indicates that the phase value lies in the range of $[-\pi, \pi]$. The continuous phase map can be obtained by applying a phase unwrapping algorithm. The phase unwrapping is a process of detecting and removing the 2π discontinuities which can be accomplished by adding or subtracting 2π [69–74]. The phase-shifting method (with three phase-step) is reliable for measurement speed and less prone to

harmonic error (for $\alpha = 2\pi/3$) [75, 76]. However, this method is sensitive to camera sensor noise as the averaging effect is insignificant when only three images are used.

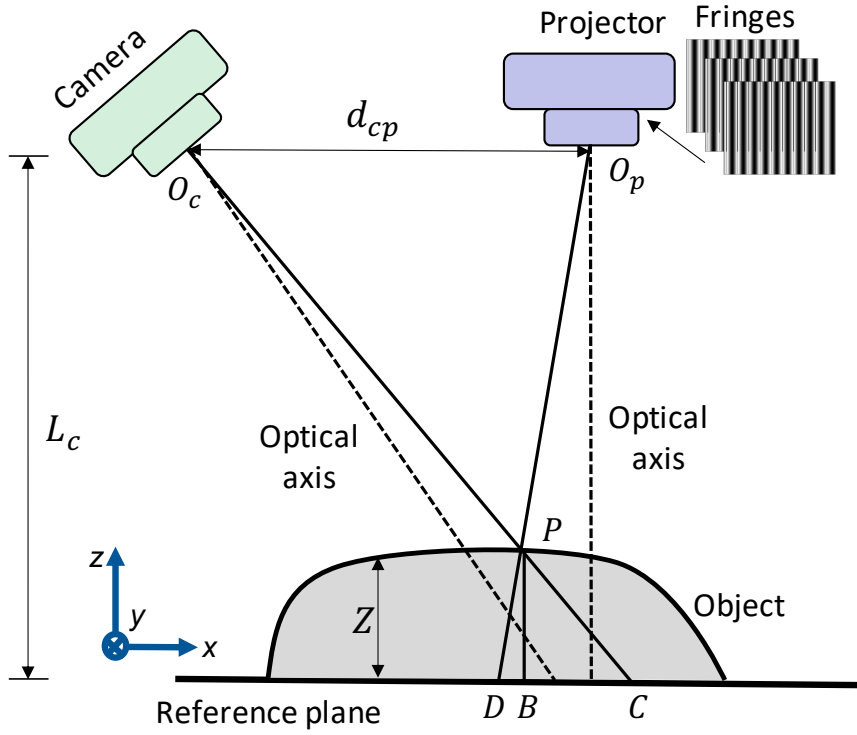


Figure 2.6: Schema of the fringe projection system.

For better measurement accuracy, more fringe images can be used, which help to eliminate the error associated with the non-sinusoidal fringe patterns and the noise effect. Mathematically, for N -step phase-shifted patterns, the intensity of the i^{th} image with a phase shift of δ_i can be represented as

$$I_i(x, y) = I_a(x, y) + I_b(x, y) \cos[\phi(x, y) - \delta_i], \quad (2.15)$$

where $I_a(x, y)$ is the average background intensity, $I_b(x, y)$ is the intensity modulation which represents the surface reflectivity and fringe pattern contrast, $\delta_i = (2\pi i/N)$ is the phase difference, i is the phase stepping index ($i = 0, 1, 2, \dots, N-1$), and $\phi(x, y)$ corresponds to the wrapped phase map and given by

$$\phi(x, y) = \tan^{-1} \left(\frac{\sum_{i=0}^{N-1} I_i(x, y) \sin(2\pi i/N)}{\sum_{i=0}^{N-1} I_i(x, y) \cos(2\pi i/N)} \right). \quad (2.16)$$

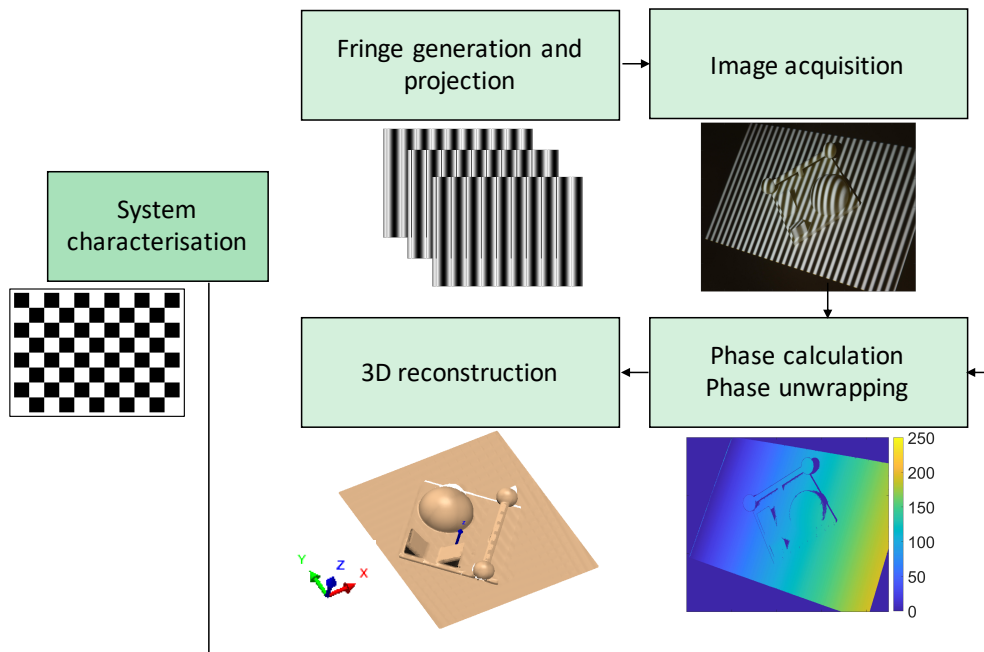


Figure 2.7: The pipeline of a DFP system.

The pipeline of the DFP system is depicted in figure 2.7. DFP method involves a pre-requisite step, called system characterisation, which determines the relationship between image coordinates and the real world 3D coordinates. The measurement process comprises fringe generation and projection, image acquisition at each step, analysis of the captured fringes, which yields the phase information. Since the phase-shifting method encodes in terms of phase, the retrieved phase is usually wrapped between $[-\pi, \pi]$ and needs to be unwrapped to get the absolute phase. Furthermore, by incorporating the system characterisation information and the triangulation principle, the 3D point cloud is acquired.

A schematic diagram of a DFP is shown in figure (2.6). The points O_p and O_c denote the virtual aperture of the optical axis of the projector and camera axis, respectively. A flat plane is measured, which provides a reference and the depth of the object is measured relative to the reference plane. From the projector's point of view, point P on the object surface has the same phase value as the point D on the reference plane ($\phi_P = \phi_D^{\text{ref}}$). Similarly, from the camera's point of view, points D and C have the same pixels for phase map ($\phi_C = \phi_D^{\text{ref}}$). By subtracting the reference phase map from the measured object phase map, the phase difference at this specific pixel is acquired,

and given by

$$\Delta\phi_{PC} = \phi_P - \phi_C^{\text{ref}} = \phi_D^{\text{ref}} - \phi_C^{\text{ref}} = \Delta\phi_{DC}^{\text{ref}}. \quad (2.17)$$

The triangles $\Delta O_p O_c P$ and ΔDCP are similar; therefore the height PB of point P on the object surface relies on the distance between points C and D , and represented as

$$Z(x, y) = \overline{PB} = \frac{\overline{CD} \cdot L_c}{d_{cp} + \overline{CD}}. \quad (2.18)$$

Combining Equations (2.17) and (2.18), and using the assumption $d_{cp} \gg \overline{CD}$ yields the height information $Z(x, y)$ of the object, given by

$$Z(x, y) = \left(\frac{L_c}{2\pi f_m d_{cp}} \right) \Delta\phi_{DC}^{\text{ref}} \approx K_0 \Delta\phi_{DC}^{\text{ref}}, \quad (2.19)$$

where f_m is the spatial frequency of the fringes, L_c is the distance between the optical centre of the camera and the reference plane, K_0 is a constant that can be determined through system characterisation (often called calibration in the fringe projection method), and $\Delta\phi_{DC}^{\text{ref}}$ is the phase containing the depth information. Equation (2.19) provides the depth $Z(x, y)$ based on a relatively simple method called reference-plane-based method. A more accurate, reliable and widely used method of converting the phase information into depth is the system characterisation (details will be discussed in section 2.3) which depends on computing the intrinsic and extrinsic parameters of the camera and the projector.

2.2 Phase unwrapping in fringe projection

In the digital fringe projection system, phase-stepping techniques are highly demanding due to their high speed, measurement accuracy, less sensitivity to surface reflectivity and ambient light. In general, the phase of a signal is acquired through an arctangent function. This mathematical function returns values between $[-\pi, +\pi]$, and values near

2π represent discontinuities in the phase distribution. Unwrapping is the method by which these discontinuities are eliminated, and the desired continuous phase function is achieved for 3D imaging applications.

The concept of phase unwrapping in one and two dimensions is shown in figures 2.8 and 2.9. The two-dimensional phase unwrapping is a well-established field with a huge amount of literature available. Phase unwrapping is not just specific to the fringe projection method; rather, it has been used in various applications. A few examples include interferometry [77], magnetic resonance imaging [78], synthetic aperture radar [79], acoustic imaging [80], and X-ray crystallography [81]. These applications need phase unwrapping to get useful quantities from raw experimental data.

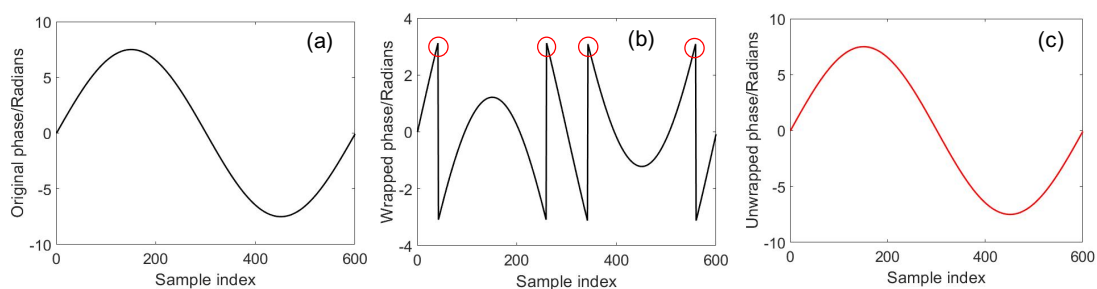


Figure 2.8: Phase unwrapping in 1D. (a) A sinusoidal signal whose amplitude exceeds the range $[-\pi, \pi]$ and has a continuous phase (b) wrapped phase, the 2π discontinuities in the wrapped phase signal are represented by red circles and removed by adding/subtracting a factor of 2π and (c) the unwrapped phase.

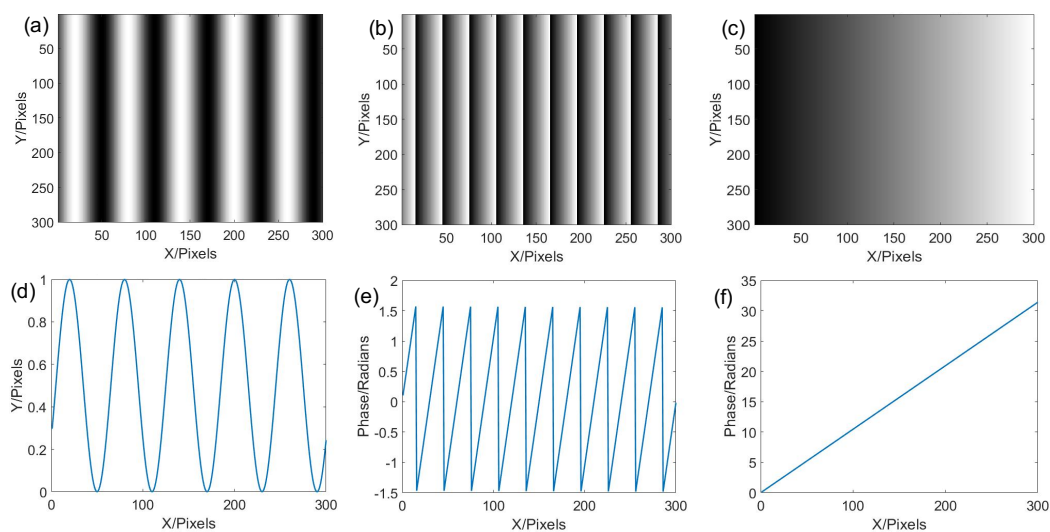


Figure 2.9: Phase unwrapping in 2D. (a) Original intensity image (b) wrapped phase image (c) unwrapped phase image (d) row-150 of the intensity image shown in (a), (e) row-150 of the wrapped image shown in (b) and (f) row-150 of the unwrapped image shown in (c).

Numerous algorithms have been developed, but robustness is by no means assured. In principle, the implementation of phase unwrapping on real images is the most difficult and challenging task. Practical concerns related to discontinuities in the phase wraps, system and environmental noise, variations in signal-to-noise ratio, under-sampling and masked areas make this process complicated. Moreover, the cumulative nature of phase unwrapping imposes very strict conditions on the phase unwrapping algorithms.

Several phase unwrapping methods have been proposed to enhance the noise immunity, robustness and computational efficiency of the unwrapping process [69–74]. These methods can broadly be categorized as spatial and temporal phase unwrapping. The fundamental difference between the two approaches is that the temporal phase unwrapping does not rely on the neighbouring pixel phase information to perform phase unwrapping, therefore appropriate for complex and arbitrarily shaped objects. In comparison, the spatial phase-unwrapping algorithm depends on detecting and removing 2π discontinuities from neighbouring pixels and limited to smooth surfaces. The following sections will elaborate on these protocols in detail.

2.2.1 Spatial phase unwrapping

The spatial phase unwrapping can be further categorized as local and global methods. The local phase unwrapping algorithms calculate the unwrapped phase by integrating over a particular path. They usually follow a specific integration path which covers the entire wrapped phase map [69]. The Schafer and Oppenheim proposed a simple and robust path following the phase unwrapping algorithm. The main idea is to use spiral and multiple scans to locate the sudden and abrupt phase discontinuity in an image and determine the phase offsets. The path-dependent phase unwrapping process can be classified into residue compensation and quality guided methods.

The residue compensation algorithms locate the residues in an image and connect the positive and negative residues through branch cuts [70]. The unwrapping path is identified by the pixels' reliability [71–73]. These algorithms are fast but not robust. In comparison, the quality guided algorithms target the highest-quality pixels and unwrap

them first while the lowest quality pixels are processed at the end in order to avoid error propagation. These algorithms are generally robust and efficient. In contrast to local phase unwrapping algorithms, the global algorithms devise the minimization of a global function. All algorithms that belong to this category are robust but computationally rigorous [69, 74].

The local phase unwrapping algorithms are described as follows.

2.2.1.1 Goldstein branch-cut method

This algorithm detects the *residues* in the wrapped phase map and joins them through branch-cuts. Residues can be positive or negative and appear in the phase map due to noise or discontinuities. The quality of the unwrapped phase map strongly depends on the choice of the branch-cut. A unique unwrapped solution corresponds to the selection of a wrapped gradient integration path that eliminates discontinuities. The algorithm works in three steps: detection of residues, generation of branch-cuts and a flood fill algorithm.

The phase map has grayscale intensity values between [0-255] and scaled to [0-1]. The 2×2 sample-path integral is the smallest closed loop that helps localise the source of each phase inconsistency [82]. Mathematically, the gradient of the wrapped phase can be represented as

$$q = \sum_{i=1}^4 \Delta_i, \quad (2.20)$$

where

$$\Delta_1 = \xi[\phi(i, j+1) - \phi(i, j)], \quad (2.21)$$

$$\Delta_2 = \xi[\phi(i+1, j+1) - \phi(i, j+1)], \quad (2.22)$$

$$\Delta_3 = \xi[\phi(i+1, j) - \phi(i+1, j+1)], \quad (2.23)$$

$$\Delta_4 = \xi[\phi(i, j) - \phi(i+1, j)], \quad (2.24)$$

where $\xi(\cdot)$ is an unwrapping operator, ϕ is the wrapped phase, the non zero q value indicates the inconsistency and considered as a residue, and it can be positive or negative with values 0, +1 or -1. Since the consistency check is a local test, it is not possible for the 2×2 path consistency check to determine if the inconsistency is due to aliasing or noise. This is because phase dislocation is a regional phenomenon. It is assumed that there cannot be more than one half cycle jumps since the data is sampled on Nyquist theorem.

In the Goldstein algorithm, the positive and negative residues are connected by lines which act as barriers during the path integration. The algorithm starts by scanning the phase map to find a residue. Then the residue is enclosed by a 3×3 box and search for another residue continues. When a residue of opposite sign is found, it is connected by a branch-cut, and the scanning continues for finding another residue. If a residue of the same sign appears, the centre of the box is moved to the new location, and the search continues until a residue of opposite sign or no new residue is found. When no residue is found, the box size is increased by (5×5) , and the search continues.

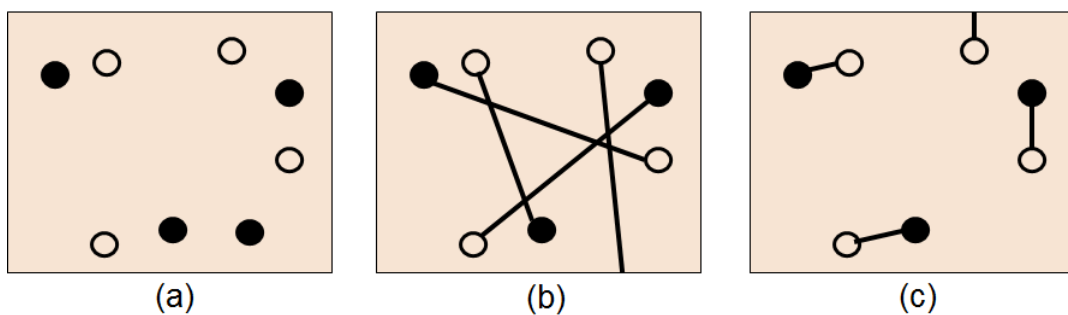


Figure 2.10: Branch cuts. (a) Positive and negative residues marked by empty and filled circles, respectively (b) the cuts isolate the portions of the image, hence not a good choice and (c) a better option.

Principally, the algorithm scans over the entire phase map and finds the unbalanced residues and balance them by placing branch-cuts. However, when border pixels appear during the box search, the residues can be balanced by connecting them with the image border. The branch cuts are based on the nearest-neighbour method that minimises the sum of the cut lengths. Goldstein's algorithm is very fast and effective for generating optimum branch cuts. As a first step, an initial value is chosen at a known location

within the model domain. The four neighbouring pixels are then unwrapped, and the process continues around the location of branch-cut pixels. The unwrapping of the border pixels is done in the end by using the unwrapped value of its adjacent pixels; hence the error can not propagate to other regions of the phase map.

Local phase unwrapping algorithms are usually path-dependent and follow a certain unwrapping path in a specific direction. Algorithms like residue-balancing and quality-guided generate branch cuts and minimise the error propagation by defining the unwrapping path around these branch cuts. In contrast, global phase unwrapping algorithms formulate the phase unwrapping problem in the minimum norm perspective; therefore, referred to as minimum-norm algorithms [82]. Global phase unwrapping algorithms determine the unwrapped phase by minimising the global error function. The gradient of the unwrapped phase is defined as

$$\Delta\psi(x, y) = W[\Delta\phi(x, y)], \quad (2.25)$$

where ψ is the unwrapped phase and ϕ is the wrapped phase. The global phase unwrapping method finds the unwrapped phase whose local x and y gradients matches, therefore, we can write

$$\epsilon^p = \sum_{i=0}^{M-2} \sum_{j=0}^{N-1} \left| \Delta^x \psi(i, j) - \hat{\Delta}^x \phi(i, j) \right|^p + \sum_{i=0}^{M-1} \sum_{j=0}^{N-2} \left| \Delta^y \psi(i, j) - \hat{\Delta}^y \phi(i, j) \right|^p \quad (2.26)$$

where $\Delta^x \psi(i, j)$ and $\Delta^y \psi(i, j)$ are the unwrapped gradients in the x and y respectively, while $\hat{\Delta}^x \phi(i, j)$ and $\hat{\Delta}^y \phi(i, j)$ are the wrapped gradients defined as follows

$$\Delta^x \psi(i, j) = \psi(i+1, j) - \psi(i, j), \quad (2.27)$$

$$\Delta^y \psi(i, j) = \psi(i, j+1) - \psi(i, j), \quad (2.28)$$

$$\hat{\Delta}^x \phi(i, j) = W[\phi(i+1, j) - \phi(i, j)], \quad (2.29)$$

$$\hat{\Delta}^y \phi(i, j) = W[\phi(i, j+1) - \phi(i, j)]. \quad (2.30)$$

Global phase unwrapping algorithms can be categorized into unweighted least-squares, weighted least-squares methods.

2.2.1.2 Quality guided maps

In general, phase-stepped fringe projection technique requires at least three fringe patterns to uniquely determine the phase per pixel. Therefore, in DFP systems, the data modulation value $\gamma(x, y)$ is used to eliminate the background areas and perform the background masking. After alleviating the low-quality phase points through background masking, the second quality map is introduced to unwrap the unmasked data points. Therefore, the quality map is regarded as a maximum of the phase gradient map [83] and can be expressed as

$$Q_g(i, j) = \max \left\{ \Delta x_{(i,j)}, \Delta y_{(i,j)} \right\} \quad (2.31)$$

where $Q_g(i, j)$ ranges between $[0, 1]$ and $\Delta x_{(i,j)}$ and $\Delta y_{(i,j)}$ indicate the maximum values of the partial derivatives of the phase along the x and y directions and represented as

$$\Delta x_{(i,j)} = \max \{ |G\{\phi(i, j) - \phi(i - 1, j)\}|, |G\{\phi(i + 1, j) - \phi(i, j)\}| \}, \quad (2.32)$$

$$\Delta y_{(i,j)} = \max \{ |G\{\phi(i, j) - \phi(i, j - 1)\}|, |G\{\phi(i, j + 1) - \phi(i, j)\}| \}. \quad (2.33)$$

The ϕ is the normalized wrapped phase, and G is the gradient operator. The large quality map $Q_g(i, j)$ value in equation (2.31) corresponds to worse data quality.

2.2.1.3 Reliability based quality guided phase unwrapping

Bone first proposed the quality guided method of phase unwrapping [84]. Bone determined the quality of the phase map by calculating the second-order partial derivative of the individual phase value. The matrix of the quality values is called a quality map. In the unwrapping process, the pixel values with the highest qualities are unwrapped first, while others are not treated until they exceed a specific threshold value. Consequently, many quality guided and path-dependent algorithms were proposed to address

the issue of phase unwrapping [50, 71, 85].

Quality guided algorithms are based on determining the reliability of a point by finding the gradients between a pixel and its neighbours. The points with lowest module 2π gradients with respect to their neighbours are classified as the best points, hence, processed first. The absolute value of the gradient, sometimes, yields an inappropriate measurement for the reliability; therefore, the second difference provides better detection of the potential inconsistencies in the phase map. The second difference is also a measure of the degree of concavity or convexity of the phase map [50]. The second difference D_s of a centre pixel (i, j) can be calculated as

$$D_s(i, j) = \left[H^2(i, j) + V^2(i, j) + D_1^2(i, j) + D_2^2(i, j) \right]^{1/2}, \quad (2.34)$$

where

$$H(i, j) = \xi[\phi(i-1, j) - \phi(i, j)] - \xi[\phi(i, j) - \phi(i+1, j)], \quad (2.35)$$

$$V(i, j) = \xi[\phi(i, j-1) - \phi(i, j)] - \xi[\phi(i, j) - \phi(i, j+1)], \quad (2.36)$$

$$D_1(i, j) = \xi[\phi(i-1, j-1) - \phi(i, j)] - \xi[\phi(i, j) - \phi(i+1, j+1)], \quad (2.37)$$

$$D_2(i, j) = \xi[\phi(i-1, j+1) - \phi(i, j)] - \xi[\phi(i, j) - \phi(i+1, j-1)], \quad (2.38)$$

where $H(i, j)$, $V(i, j)$, $D_1(i, j)$, and $D_2(i, j)$ are the horizontal, vertical, first and the second diagonals of the ROI of the tested image, respectively. $\xi(\cdot)$ is an unwrapping operator which removes the 2π discontinuities in the phase map. The reliability R_s of a pixel is represented as

$$R_s = \frac{1}{D_s}. \quad (2.39)$$

The reliability has an inverse relation with the second difference; therefore, the minimal difference value corresponds to more reliable pixels [50].

The algorithm is very robust, fast, efficient and has been used in constructing a fringe pattern analysis of a complex human body shape measurement. A drawback of

this algorithm is that there is no guarantee that the path will not encircle an unbalanced residue and introduces a spurious discontinuity in the unwrapped solution. The reliability function can be modified by ignoring the intersections with very low reliability. Furthermore, Herraez et al. also proposed a discrete unwrapping path based on finding the qualities of edges, whereby an edge is defined by connecting the adjacent pixels [85]. The algorithm uses the divide and conquers method, such as Quick Sort method which minimises the time of sorting an array of numbers by arranging them either in increasing or decreasing order and yields acceptable results for different types of images [85].

2.2.1.4 Unweighted least-squares method

The unweighted least-squares method was first proposed by Hunt [86]. This algorithm minimises the difference between the unwrapped phase gradients and the wrapped phase gradients based on least-squares method. Therefore,

$$\begin{aligned} \epsilon^2 &= \sum_{i=0}^{M-2} \sum_{j=0}^{N-1} \left| \Delta^x \psi(i, j) - \hat{\Delta}^x \phi(i, j) \right|^2 \\ &+ \sum_{i=0}^{M-1} \sum_{j=0}^{N-2} \left| \Delta^y \psi(i, j) - \hat{\Delta}^y \phi(i, j) \right|^2, \end{aligned} \quad (2.40)$$

where $\Delta^x \psi(i, j)$ and $\Delta^y \psi(i, j)$ are the unwrapped gradients in the x and y respectively, while $\hat{\Delta}^x \phi(i, j)$ and $\hat{\Delta}^y \phi(i, j)$ are the wrapped gradients (given in equations (2.27)-(2.30)). Ghiglia et al. have simplified the above equation [69, 82], as follows

$$\begin{aligned} &[\psi(i+1, j) - 2\psi(i, j) + \psi(i-1, j)] + \\ &[\psi(i, j+1) - 2\psi(i, j) + \psi(i, j-1)] = \rho(i, j), \end{aligned} \quad (2.41)$$

where $\rho(i, j)$ is given by

$$\rho(i, j) = [\hat{\Delta}^x \phi(i, j) - \hat{\Delta}^x \phi(i-1, j)] \quad (2.42)$$

$$+ [\hat{\Delta}^y \phi(i, j) - \hat{\Delta}^y \phi(i, j-1)]. \quad (2.43)$$

Equation (2.43) is similar to the discrete Poisson's equation and can be written as

$$\mathbf{P}\vec{\psi} = \vec{\mathbf{p}}, \quad (2.44)$$

where \mathbf{P} represents the discrete Laplacian operator and equivalent to the L.H.S of equation (2.40), $\vec{\psi}$ and $\vec{\mathbf{p}}$ contains the values of 2-D arrays of $\phi(i, j)$ and $\rho(i, j)$.

In principle, the unweighted least-squares algorithm finds the solution of Poisson's equation. Ghiglia et al. proposed the Gauss-Seidel relaxation method, also shown that this not a practical solution due to very slow convergence [69, 82]. Therefore, they also suggested the technique of Fourier transform to solve Poisson's equation.

2.2.1.5 Weighted least-squares method

In the unweighted least-squares method, all pixels are assigned equal weights in the wrapped phase map. However, when the wrapped phase contains residues and corrupted areas due to noise, the whole unwrapping process is affected, and the error propagates through the rest of the phase map. Weighted least-squares algorithms assign each pixel a certain weight in the wrapped phase map. Noisy pixels and residues are assigned low weights to prevent error propagation. Mathematically, it can be represented as

$$\begin{aligned} \epsilon^2 = & U(i, j) \times \sum_{i=0}^{M-2} \sum_{j=0}^{N-1} \left| \Delta^x \psi(i, j) - \hat{\Delta}^x \phi(i, j) \right|^2 \\ & + V(i, j) \times \sum_{i=0}^{M-1} \sum_{j=0}^{N-2} \left| \Delta^y \psi(i, j) - \hat{\Delta}^y \phi(i, j) \right|^2, \end{aligned} \quad (2.45)$$

where $\Delta^x \psi(i, j)$ and $\Delta^y \psi(i, j)$ are the unwrapped gradients in the x and y respectively, $\hat{\Delta}^x \phi(i, j)$ and $\hat{\Delta}^y \phi(i, j)$ are the wrapped gradients (given in equations (2.27)-(2.30)), $U(i, j)$ and $V(i, j)$ are the gradient weights in the x and y gradients, respectively and defined as follows

$$U(i, j) = \min(q_{i+1, j}^2, q_{i, j}^2),$$

$$V(i, j) = \min(q_{i,j+1}^2, q_{i,j}^2),$$

where $q_{i,j}$ is the quality of each pixel (i, j) . Ghiglia [69, 82] suggested that equation (2.45) can be written as

$$\begin{aligned} & U(i, j)\Delta^x\psi(i, j) - U(i-1, j)\Delta^x\psi(i-1, j) + \\ & V(i, j)\Delta^y\psi(i, j) - V(i, j-1)\Delta^y\psi(i, j-1) = \mu(i, j), \end{aligned} \quad (2.46)$$

where $\mu(i, j)$ is given by

$$\begin{aligned} \mu(i, j) &= [U(i, j)\hat{\Delta}^x\phi(i, j) - U(i-1, j)\hat{\Delta}^x\phi(i-1, j)] \\ &+ [V(i, j)\hat{\Delta}^y\phi(i, j) - V(i, j-1)\hat{\Delta}^y\phi(i, j-1)]. \end{aligned} \quad (2.47)$$

Equation (2.46) can be written in matrix form

$$\mathbf{Z}\vec{\psi} = \vec{\mu}, \quad (2.48)$$

where \mathbf{Z} is the discrete Laplacian operator equivalent to the L.H.S of equation (2.46), μ is the one-dimensional vector that has the values of equation (2.47).

The weighted least-squares method can not be solved by Fourier transform but relies on iterative methods. The Gauss-Seidel relaxation can be applied to the weighted least-squares method, but it is not reliable due to the slow convergence; however, multi-grid can resolve this issue and speeds up the process. Ghiglia et al. also proposed two more methods to find the solution of the unwrapped phase, which are the Picard iteration method and the preconditioned conjugate gradient method (PCG). The Picard method is simple and convenient to apply, but convergence is not guaranteed, however, the benefit of the PCG method is that it yields reasonable good convergence properties [69, 82].

2.2.2 Temporal phase unwrapping

In contrast to spatial phase unwrapping, temporal phase unwrapping methods unwrap the phase of complex objects with large depth variations and discontinuities [87, 88]. In general, this unwrapping process is applied in the temporal realm. The basic concept is to use multiple phase maps or black and white encoded patterns to acquire the absolute value of fringe order. The benefit of temporal phase unwrapping is that it is capable of analysing eminently discontinuous objects because each individual spatial pixel is unwrapped separately from its neighbouring pixels [52, 89] and the chances of error propagation are minimised. Another remarkable feature is that noisy pixels remain distinctive and effectively decreases the error propagation to less noisy areas [89].

In the DFP method, the fringe distortion is associated with phase distribution which can be converted to depth profile of the object by incorporating the system characterisation information. Many methods are used to extract the phase and height information from distorted fringes, and among others, the phase-stepped fringe projection method provides the highest measurement accuracy as it alleviates the ambient light interferences and object's surface reflectivity. In general, sinusoidal fringe patterns with some phase difference are projected on the surface of an object, and the distorted fringes are captured by a camera. The distorted fringes and phase distributions are given in equations (2.15) and (2.16).

The arctangent function in equation (2.16) lies in the range $[-\pi, \pi]$ and depicts discontinuities for the phase data lying outside this range. Therefore, the phase unwrapping procedure deals with adding or subtracting the integer multiple of 2π to eliminate these discontinuities. Mathematically, the unwrapped phase is expressed as

$$\psi(x, y) = \phi(x, y) + 2\pi k(x, y), \quad (2.49)$$

where $\psi(x, y)$ is the unwrapped phase, $\phi(x, y)$ is the wrapped phase (given in equation (2.16)) and k is the unknown fringe order. The key to phase unwrapping algorithm is to determine the fringe order efficiently and adding that (value of fringe order) to the wrapped phase to determine the absolute phase.

The theoretical description seems simple; however, in practical applications, the phase is embedded with noise and other discontinuities which significantly affects the phase unwrapping process. A simple approach to alleviating the phase discontinuities is the grey code temporal phase unwrapping process [48, 49, 88]. The temporal phase unwrapping methods can be implemented by introducing additional (one or more) wrapped phase maps that differ in their fringe period [87, 90–92]. In general, methods such as; multi-frequency [93–95], and number-theoretical approach [60, 96, 97] are extensively used. These methods can effectively resolve the phase uncertainty, which is associated with discontinuous and spatially isolated objects.

2.2.2.1 Multi-frequency phase unwrapping

The concept of multi-frequency phase unwrapping was first proposed by Huntley and Saldner [89]. The method relied on 1D along the time axis by using a set of phase maps and implemented for unwrapping the interferometric phase maps. The approach was simple, which retains the phase error in the high-noise regions and unwraps the global discontinuities. In contrast to Huntley and Saldner, Zhao et al. proposed a relatively simple phase unwrapping algorithm that utilises two-phase maps with different precisions, and the fringe orders are allocated to the low precision phase map [92]. The unwrapping process for each point is performed separately by taking into account the discontinuities. Kinell et al. developed a reduced temporal phase unwrapping as a generalised formulation of the negative exponential sequence, which gives the benefit of using any arbitrary fringe sequence [93]. Peng et al. proposed a modified phase unwrapping algorithm that relies on establishing the initial conditions of the recursive method [94].

Considerable improvements were made by other authors. Tian et al. presented a generalised temporal phase unwrapping method and addressed the constraint on the fringe sequence of the existing classical temporal phase unwrapping methods [95]. The method (proposed by Tian et al.) was robust to noise. Zhang et al. proposed a robust and effective method for the multi-frequency temporal phase unwrapping [98]. The method gives a framework to optimise the three important parameters, i.e., the

highest fringe frequency, the phase-steps and the fringe pattern sequence which results in acquiring the accurate, efficient and reliable measurement in the fringe projection systems. Wan et al. recently developed a hybrid multi-frequency composite-pattern temporal phase unwrapping method to reduce the number of patterns needed in the conventional temporal phase unwrapping method [99]. The approach incorporates a unit frequency ramp pattern with low-frequency phase-stepped patterns to acquire a composite pattern, which is then used with the high-frequency patterns to achieve a reliable and accurate phase map.

In principle, fringe patterns with different fringe frequencies (densities) are projected on the surface of the object and viewed through a different angle using a camera, usually in a triangular geometry. The reference (coarsest) fringe pattern has a phase map with phase values without any 2π discontinuities, which is further used to obtain the useful information for further phase unwrapping. The additional phase maps are unwrapped relying on their frequencies (fringe numbers) and rely on the information the previous phase map contains. The basic idea is that the phase is unwrapped using additional (either one or more) wrapped phase map with various fringe intervals. In general, a large number (> 5) of relative phase maps is required for better measurement accuracy; however, the number of phase maps can be reduced to two in order to shorten the measurement time [51]. The relationship between the two continuous phase maps is given by

$$\psi_h(x, y) = \left[\frac{\lambda_l}{\lambda_h} \psi_l(x, y) \right], \quad (2.50)$$

where $\psi_l(x, y)$ and $\psi_h(x, y)$ are the phase maps for low and high frequency components, respectively, and λ_l and λ_h are the fringe wavelengths [51]. According to equation (2.49), the relationship between the wrapped and unwrapped phase maps can be described as

$$\psi_l(x, y) = \phi_l(x, y) + 2\pi k_l(x, y), \quad (2.51)$$

$$\psi_h(x, y) = \phi_h(x, y) + 2\pi k_h(x, y), \quad (2.52)$$

where $\phi_l(x, y)$ and $\phi_h(x, y)$ are wrapped phase maps and k_l and k_h are the fringe orders for low and high frequency components, respectively. The wrapped phase ($\phi_h(x, y)$) in equation (2.51) can be acquired through the phase-shifting method by using equations (2.15) and (2.16). In two-frequency phase unwrapping method, the low frequency phase map is obtained through a set of unit frequency fringe patterns, therefore no phase unwrapping is needed for ϕ_l (and $\psi_l = \phi_l$). Thus, the fringe order for each pixel can be determined using equation (2.50) and (2.52)

$$k_h(x, y) = \text{Round} \left[\frac{(\lambda_l/\lambda_h)\phi_l(x, y) - \phi_h(x, y)}{2\pi} \right], \quad (2.53)$$

where $\text{Round}[\]$ gives the closest integer value, and by using the above equations, the high frequency phase ϕ can be unwrapped. In the multi-frequency approach, the phase is unwrapped from the reference to the finer layer [51]; therefore, the method is called hierarchical approach, and the two-frequency method is called the reduced hierarchical approach due to the reduction in the number of captured images [100–102].

2.2.2.2 Number theoretical phase unwrapping

The number-theoretical method was first proposed by Gushov and Solodkin, who used two phase maps with different fringe frequencies [103]. The frequencies of these fringes were proportional to relative primes. Significant improvements were made by others. Takeda et al. improved the performance of the Fourier transform profilometry by combining the spatial frequency multiplexing with the Gushov and Solodkin phase unwrapping algorithm [61]. A distinctive feature of the method was to use a single fringe pattern and yielding a single-shot 3D reconstruction of discontinuous objects. Towers et al. presented a modified algorithm for phase measurement in multi-frequency interferometry. The approach was robust to phase error [97]. Zhong also contributed by introducing a convenient look-up-table (LUTs) for fast phase unwrapping using two phase maps [104]. Furthermore, the LUTs based methods were investigated by others [105–108].

The fundamental concept of the number-theoretical method is that for an appro-

appropriate pair of wavelengths λ_l and λ_h (as relative primes), a unique set of phase pairs (ϕ_h, ϕ_l) can be obtained along the phase axis. Generally, this algorithm unwraps the phase value equals to least-common multiple (LCM) of wavelengths (λ_l, λ_h) . The $LCM()$ denotes a function whose output is the least common multiple of input values, precisely a minimum number which is divisible by the wavelengths. The fringe order for the two unwrapped phase maps can be determined as

$$f_h \psi_l(x, y) = f_l \psi_h(x, y), \quad (2.54)$$

where, f_h and f_l are the total number of fringes in the high and low-frequency fringe patterns, respectively [51], and given by

$$f_h = LCM(\lambda_h, \lambda_l)/\lambda_h, \quad (2.55)$$

and

$$f_l = LCM(\lambda_h, \lambda_l)/\lambda_l \quad (2.56)$$

Combining equations (2.54), (2.52) and (2.51) gives

$$\frac{(f_h \phi_l - f_l \phi_h)}{2\pi} = k_h f_l - k_l f_h. \quad (2.57)$$

The wavelength is in pixels (integers); therefore both sides of equation (2.57) should be an integer, and the left-hand side determines the fringe order pair (k_h, k_l) . This process continues unless the entire area of the projected pattern is covered. In general, a look-up-table (LUT) stores all the unique pairs (k_h, k_l) and the fringe order is determined by using the following expression

$$(k_h, k_l) = \text{LUT} \left[\text{Round} \left(\frac{(f_h \phi_l - f_l \phi_h)}{2\pi} \right) \right]. \quad (2.58)$$

Finally, the absolute phase can be determined using equations (2.52) and (2.51). Furthermore, when the low frequency phase map has a unit frequency fringe, the number-

theoretical approach reduces to two-frequency temporal phase unwrapping and can be considered as a generalised version of the two-frequency phase unwrapping [51].

2.2.2.3 Binary coding

Posdamer and Altschular first proposed the method of projecting a sequence of n patterns to encode 2^n stripes using a binary code [109]. The binary coding relies on using two illumination levels (black and white stripes coded as 0 and 1, respectively) to form a series of projection patterns in such a way that each point on the object surface has a unique code (consisting of a sequence of 0s and 1s) that differs from the codes of any other different point. In general, the number of unique codewords depends on 2^n , where n is the number of binary patterns. Specifically, the maximum number of projected patterns depends on the resolution of the projector, and it is preferred to restrict below the maximum number as the camera cannot always see the narrow stripes. For example, we need 6 binary-coded patterns to encode 64 ($2^6, n = 6$) unique areas. The code words lie between 0 to 63 and correspond to the 2π coefficients of phase discontinuities and incorporated to unwrap the phase map.

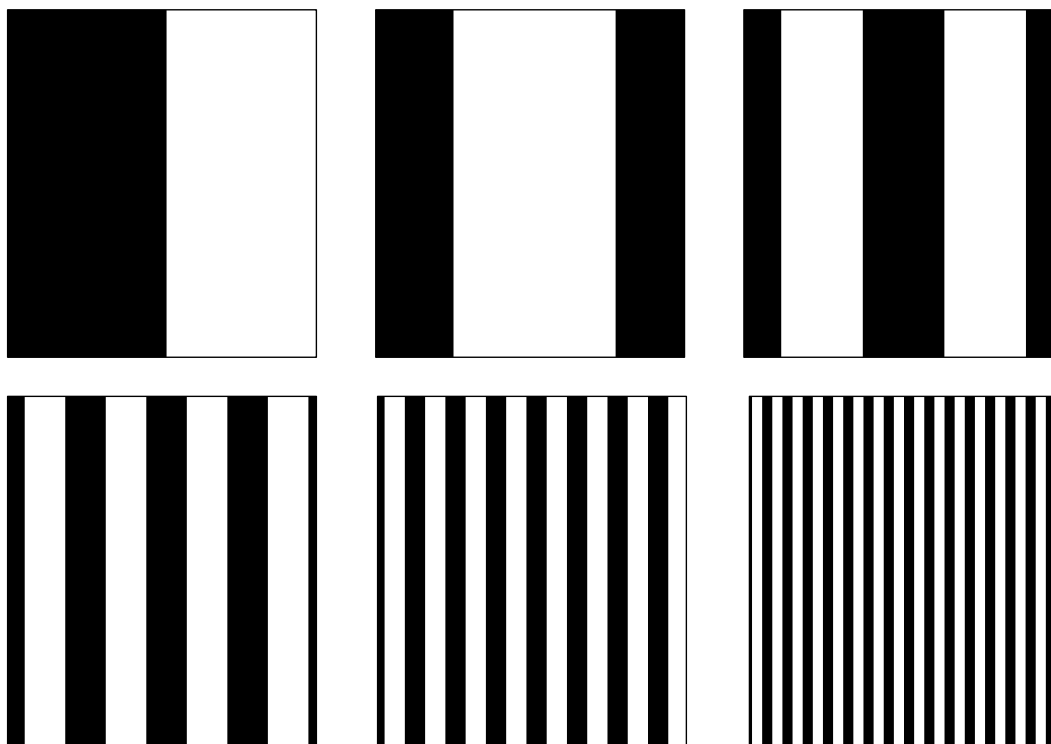


Figure 2.11: Binary coded patterns.

Essentially, it is imperative to use one black and one white pattern to binarize the

grey images. Thus, based on the grey value norm, a threshold value is defined, which plays a decisive role to create unique codewords. In practice, with the inclusion of one black and one white pattern, the total number of binary patterns required will become eight. Figure 2.11 shows the 6 binary-coded patterns. The binary coding method is simple, less susceptible to surface contrast (texture), background light and camera noise, however achieving high spatial resolution is a constraint as a large number of patterns are required, which also affects the speed of the 3D measurement process.

2.2.2.4 Phase unwrapping by adding a stair pattern

Another approach towards temporal phase unwrapping is to add stair image to the phase-shifted patterns. By aligning the stair changes with the 2π phase discontinuities, the fringe order can be calculated from the stair images [110]. For a set of vertical fringes, a stair image can be generated as

$$I_s = \text{Floor} \left[\frac{(x + P_f/2)}{P_f} \right] \times S_t, \quad (2.59)$$

where P_f is the fringe pitch value which is defined by the number of pixels per fringe period, S_t corresponds to the intensity of each stair and $\text{Floor}[\]$ rounds off the integer value. Since the object surface reflectivity is not uniform, therefore, accurately determining the fringe order requires the normalization. The captured normalized stair image (I_s^n) can be represented as

$$I_s^n = \left[\frac{I_s(x, y) - I_{\min}(x, y)}{I_{\max}(x, y) - I_{\min}(x, y)} \right]. \quad (2.60)$$

After normalisation, the wrapped phase is segmented into regions through Canny edge-detection and Wiener filtering. This step helps to identify the 2π discontinuities accurately. The fringe order can be determined as

$$k(x, y) = \text{Round} \left[I_s^n \times \frac{R_c}{S_t} \right], \quad (2.61)$$

where R_c is the computer-generated fringe intensity range. Once the fringe order is determined, the phase can be unwrapped point by point using equation (2.50).

The algorithm performs well in an ideal situation (absence of ambient light and uniform surface reflectivity), however in practice, the captured images are influenced by noise, the surface reflectivity varies over the surface, and the lens defocussing makes the problem complex and challenging, and requires a rigorous computational framework to retrieve the absolute phase information.

2.3 System characterisation in fringe projection

In DFP systems, system characterisation is substantial and significantly affects the performance of 3D optical measurement systems. The system characterisation involves estimating the intrinsic and extrinsic properties of all the optical components (cameras and projectors). In general, the imaging systems accomplish the transformation of the 3D world space to the 2D local space and determining the parameters of such kind of transformation is essential to depicting the imaging system. The camera characterisation explains the transformation of the 3D space to the 2D imaging plane based on a model which relies on the parallel projections or the central perspective projections. The parallel projection is a simple linear method; however, it imposes a constraint that the observed object should be in close proximity of the camera, and approximates what we see in actual cameras. A more appropriate approach to describe the optical systems is using the perspective projective transformation, which is represented by a linear equation in the homogeneous coordinates.

2.3.1 Camera characterisation

A camera is represented by the pinhole model, which encompasses a central projection point (pinhole) and an imaging plane [111–115], as illustrated in figure (2.12). Precisely, the imaging plane is placed in front of the pinhole, which helps to simplify the concept of projection. In order to find the correlation between points in the real world and points on the imaging plane, two coordinate systems are used; the world coordinate

system which is independent of the parameters and the orientation of the camera, and the camera coordinate system. The two coordinate systems are interconnected by the translational and rotational matrices.

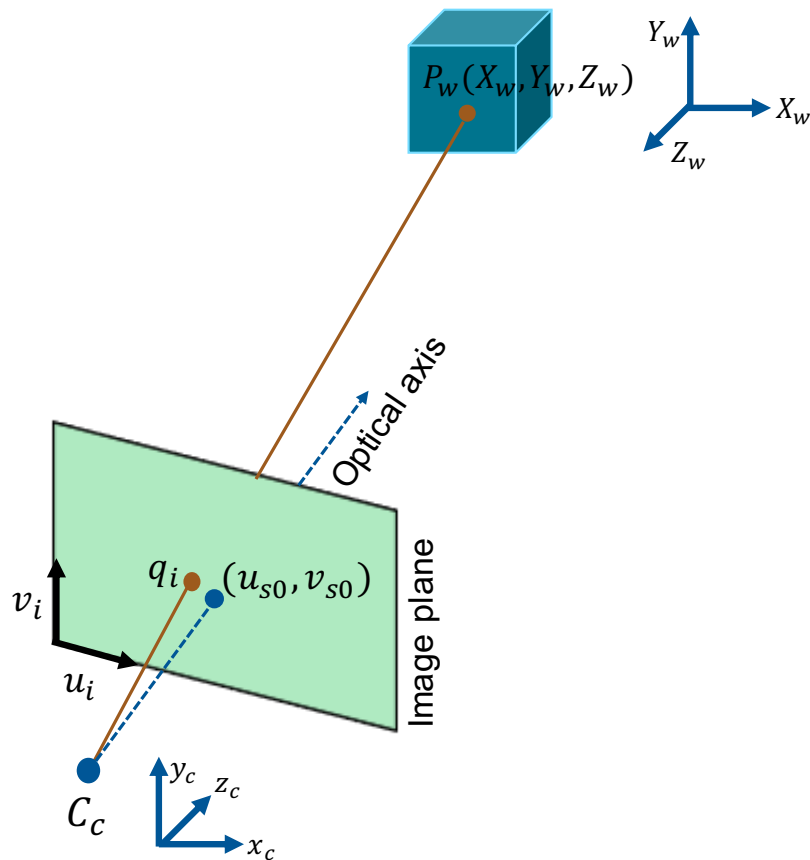


Figure 2.12: Schema of the pinhole model of the camera.

Consider a 3D point P_w in the real world with coordinates (X_w, Y_w, Z_w) and its projection onto the image plane is denoted as q_i with coordinates (u_i, v_i) , as shown in figure (2.12). The point C_c , a central or a focal point along-with the axes (x_c, y_c, z_c) define the camera coordinate system. The projection of camera's central point C_c on to the image plane in the z_c direction estimates the principal points (u_{s0}, v_{s0}) , and the distance from the image plane to the principal point (u_{s0}, v_{s0}) is called the focal length.

2.3.1.1 Intrinsic parameters

The intrinsic parameters transform the camera coordinate system to the image coordinate system and rely on the internal properties of the camera. Consider the projection of the 3D point $P_w = (X_w, Y_w, Z_w)$ on the image plane $q_i = (u_i, v_i)$. The image

coordinates u_i and v_i , based on the similar triangles method, can be represented as

$$u_i = f \left(\frac{X_w}{Z_w} \right), \quad v_i = f \left(\frac{Y_w}{Z_w} \right), \quad (2.62)$$

where f is the focal length which corresponds to the distance between the image sensor and the lens. Using equation (2.62) and the homogeneous coordinates, the relationship of the pinhole camera model can be described as

$$S \begin{bmatrix} u_i \\ v_i \\ 1 \end{bmatrix} = \begin{bmatrix} f_{u_i} & 0 & 0 & 0 \\ 0 & f_{v_i} & 0 & 0 \\ 0 & 0 & 1 & 0 \end{bmatrix} \begin{bmatrix} X_w \\ Y_w \\ Z_w \\ 1 \end{bmatrix}. \quad (2.63)$$

Rearranging the projection matrix

$$= \begin{bmatrix} f_{u_i} & 0 & 0 \\ 0 & f_{v_i} & 0 \\ 0 & 0 & 1 \end{bmatrix} \begin{bmatrix} 1 & 0 & 0 & 0 \\ 0 & 1 & 0 & 0 \\ 0 & 0 & 1 & 0 \end{bmatrix} \begin{bmatrix} X_w \\ Y_w \\ Z_w \\ 1 \end{bmatrix}. \quad (2.64)$$

Thus

$$= K_{\text{int}} \begin{bmatrix} \mathbb{I} & 0 \end{bmatrix} \begin{bmatrix} X_w \\ Y_w \\ Z_w \\ 1 \end{bmatrix}, \quad (2.65)$$

where S is the scaling factor whilst K_{int} is the intrinsic matrix which comprises only one parameter, f_{u_i} and f_{v_i} are the focal lengths (in pixels) along the u_i and v_i axes. The form of K_{int} in the above equation is assumed as an approximation of the real

situation. Practically, the K_{int} comprises of five parameters, and given by

$$K_{\text{int}} = \begin{bmatrix} f_{u_i} & \gamma & u_{s0} \\ 0 & f_{v_i} & v_{s0} \\ 0 & 0 & 1 \end{bmatrix}, \quad (2.66)$$

where u_{s0} and v_{s0} represent the coordinates of the principal point which is the intersection between the optical axis (principal axis) and the image plane, and γ corresponds to the skewness which represents the distortion when pixels along the image axes do not have a perfect square shape.

2.3.1.2 Extrinsic parameters

The mathematical depiction of a scene relies on the defined coordinate system. For 3D points to be described in another coordinate system, a transformation between the desired coordinate system and the coordinate of the camera needs to be accomplished in terms of the rotation and translation, called the extrinsic parameters. The translation denotes the change in the location of the camera and world coordinate centres, while the rotation indicates the difference in the corresponding axes of each coordinate system, represented as an orthogonal matrix of 3×3 dimensions.

The point in the camera and the world coordinate systems are correlated by the following mathematical expression

$$q_c = R(P_w - T), \quad (2.67)$$

where q_c is the point in the camera coordinate system, and P_w is the point in the world coordinate system, R and T are the rotational and translational matrices and given by

$$R = \begin{bmatrix} R_{11} & R_{12} & R_{13} \\ R_{21} & R_{22} & R_{23} \\ R_{31} & R_{32} & R_{33} \end{bmatrix}, \quad T = \begin{bmatrix} T_1 \\ T_2 \\ T_3 \end{bmatrix}. \quad (2.68)$$

Therefore, the extrinsic parameters are all the geometric parameters that transform one coordinate system to the other and play a vital role in determining the accuracy of the system characterisation; therefore, has a significant impact on the performance of optical form measurement systems.

2.3.1.3 Camera projection model

The camera projective model illustrates the mapping of the points from the 3D world space to the points in the 2D imaging plane of an ideal pinhole camera, whereby the camera aperture is considered as a point and does not incorporate a lens and associated geometric distortions. Therefore, the model is regarded as a first-order approximation of the mapping from 3D world coordinate system to the 2D image coordinate system. However, for practical purposes, the geometric distortions are considered in the pinhole camera model and compensated afterwards.

In general, for any arbitrary 3D point P_w , the relationship between a point and its projection on the imaging plane can be represented as

$$\begin{aligned}
 Sq_i &= K_{\text{int}}[R, T]P_w, \\
 &= K_{\text{int}}K_{\text{ext}}P_w, \\
 &= M_{\text{proj}}P_w,
 \end{aligned} \tag{2.69}$$

where S is the scaling factor, $q_i = [u_i, v_i, 1]^T$ is the image point homogeneous coordinate, $P_w = [X_w, Y_w, Z_w, 1]^T$ is the homogeneous point coordinate in the world coordinate system, R and T are extrinsic rotational and translational matrices (given in equation (2.68)) respectively, $K_{\text{ext}} = [R, T]$ is the extrinsic parameter which describes the transformational relationship between the world and camera coordinate systems, and K_{int} is the intrinsic parameter matrix as given in equation (2.66). M_{proj} is the camera projection matrix (3×4 dimensions) which comprises of two parameters; intrinsic

and extrinsic and represented as

$$M_{\text{proj}} = \begin{bmatrix} f_{u_i} & \gamma & u_{s0} \\ 0 & f_{v_i} & v_{s0} \\ 0 & 0 & 1 \end{bmatrix} \begin{bmatrix} \mathbf{R}_1 & -\mathbf{R}_1 \mathbf{T} \\ \mathbf{R}_2 & -\mathbf{R}_2 \mathbf{T} \\ \mathbf{R}_3 & -\mathbf{R}_3 \mathbf{T} \end{bmatrix}, \quad (2.70)$$

where \mathbf{R}_i indicates the i -th row of the rotation matrix R (given in equation 2.68) such as $\mathbf{R}_i = [R_{i1}, R_{i2}, R_{i3}]$ with $i = 1, 2, 3$.

2.3.1.4 Geometric distortion

Equation (2.69) describes the linear model of the camera and assumes that the optical centre, world and image points are collinear. However, in real optical systems, there are imperfections and distortions due to lenses which need to be taken into account in the image acquisitions being acquired under the assumption of the linear camera model. These distortions appear due to non-linearity of the optical components, and reliance of the optical parameters on the properties (wavelength) of the incident light. In practice, these distortions are introduced in the pinhole model to illustrate the non-linear response.

The lens distortion comprises of two components; a radial component which is the predominant deviation, depends on the shape of the lens and becomes more prominent as the focal length of the lens reduces, and a tangential component which is associated with the assembling procedure of the camera where the lens is not parallel to the imaging plane.

A vector representing the distortion components can be written as

$$d_{\text{distort}} = \begin{bmatrix} m_{r1} & m_{r2} & n_{t1} & n_{t2} & m_{r3} \end{bmatrix}^T, \quad (2.71)$$

where m_{r1}, m_{r2} and m_{r3} are the radial distortion coefficients whilst n_{t1} and n_{t2} are the tangential distortion coefficients. The radial distortion is computed by the first few terms of the Taylor expansion at $r = 0$, and the camera coordinates are corrected as

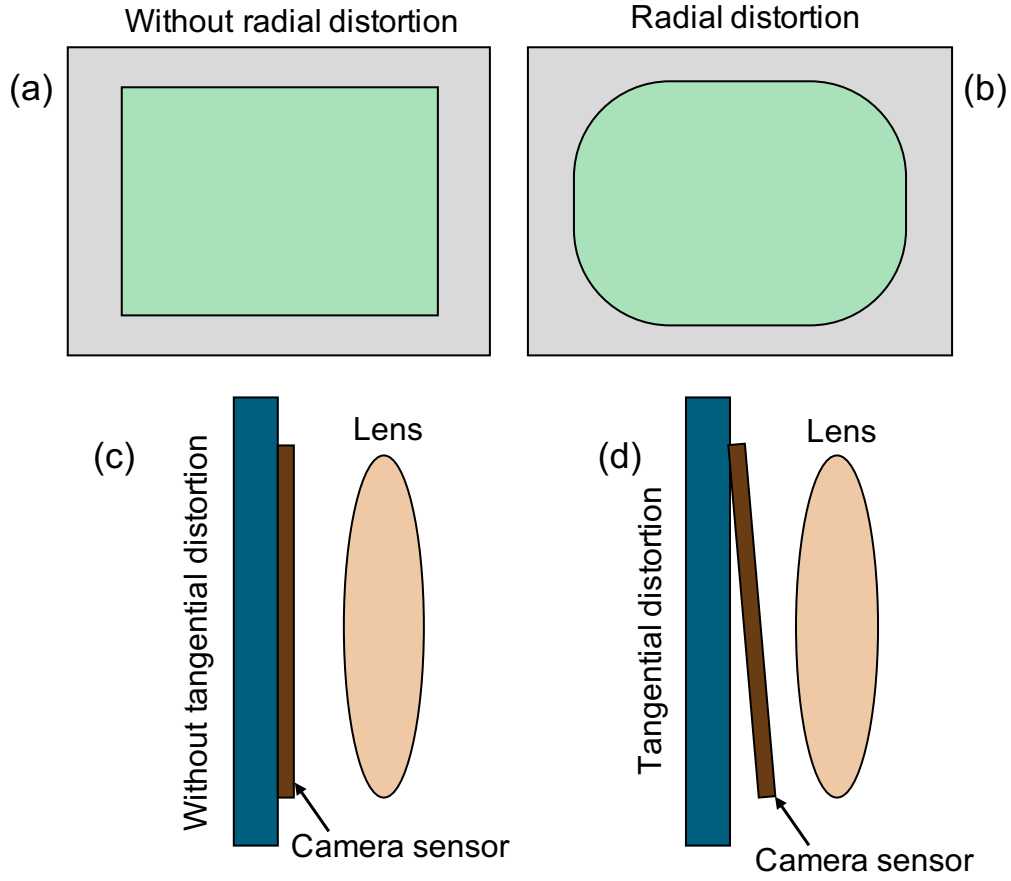


Figure 2.13: Schema of geometric distortion. (a) Linear image with no radial distortion (b) image with radial distortion (c) lens and sensor are parallel and (d) the scenario of tangential distortion.

follows

$$\begin{aligned} x_{\text{corr}} &= x_c(1 + m_{r1}r^2 + m_{r2}r^4 + m_{r3}r^6), \\ y_{\text{corr}} &= y_c(1 + m_{r1}r^2 + m_{r2}r^4 + m_{r3}r^6), \end{aligned} \quad (2.72)$$

where x_{corr} and y_{corr} are the camera coordinates after the correction, and x_c and y_c are the camera coordinates before the correction (for a linear camera model) while $r = \sqrt{x_c^2 + y_c^2}$ indicates the absolute distance between the camera point and the optical centre. Likewise, the tangential distortion coefficients are corrected as

$$\begin{aligned} x_{\text{corr}} &= x_c + [2n_{t1}x_cy_c + n_{t2}(r^2 + 2x_c^2)], \\ y_{\text{corr}} &= y_c + [n_{t1}(r^2 + 2y_c^2) + 2n_{t2}x_cy_c]. \end{aligned} \quad (2.73)$$

2.3.2 Stereo-camera system

A stereo-camera system comprises of two static cameras which are displaced horizontally and observe the scene from two different perspectives. The depth information is retrieved using stereo disparity which relies on determining the relative positions of the object in the two camera images [54, 116, 117]. Specifically, the depth is acquired based on a geometric approach called triangulation. In general, the working principle of the stereo-camera system is analogous to the human binocular system, rather a complex system, in which the brain uses the binocular disparity to compute the depth information from 2D retinal images, as seen by two eyes.

2.3.2.1 Epipolar geometry

The fundamental geometry of a stereo-camera system is described as epipolar geometry. In general, this geometry relies on the two pinhole camera model, epipoles and epipolar lines. We assume a pair of two pinhole cameras with optical centres C_L and C_R in 3D space, as shown in figure 2.14. A line $\overline{C_L C_R}$ that connects the optical centres is the baseline whilst Ψ_L and Ψ_R represent the projective planes with respect to the optical centres C_L and C_R . Points at which the baseline $\overline{C_L C_R}$ crosses the projective planes refer as the epipolar points (e_L, e_R) . In a particular case, when the z -coordinate is zero, the epipolar points lie at infinity as the baseline does not cross the image planes. A plane associated with a 3D point and the optical centres C_L and C_R is called the epipolar plane Ψ_e , and the intersection of the epipolar plane with the image planes Ψ_L and Ψ_R determines the epipolar lines [54, 116, 117].

For a stereo-camera system, the camera projection matrix transforms a 3D point P_w from the world coordinate system to the camera coordinate system. Each camera in the stereo-camera system has a local coordinate system, and it is possible to transform from one coordinate system to the other by determining the translational and rotational matrices [54, 116, 117]. Let $q_i^L = (u_i^L, v_i^L, 1)^T$ and $q_i^R = (u_i^R, v_i^R, 1)^T$ are the projections of a 3D point P_w in the left and right camera images, while $P_w^L = (X_w^L, Y_w^L, Z_w^L)^T$ and $P_w^R = (X_w^R, Y_w^R, Z_w^R)^T$ indicate the 3D point P_w in two separate coordinate systems in which the centre coincides with the camera's optical centre. Assuming the coordinate

is centred on C_L of the left camera, the location of the observed point is P_w^L and the centre of the right camera is at $T = C_R - C_L$ [116, 117]. The two views of a point P_w are related by

$$P_w^R = R(P_w^L - T), \quad (2.74)$$

where P_w^R denotes the point P_w as viewed by the right camera, R and T are the rotation and the translation matrices that bring the right camera coordinate system into the left camera coordinate system and are given by

$$R = R_R(R_L)^T, \quad (2.75)$$

$$T = T_R - RT_L. \quad (2.76)$$

The epipolar plane Ψ_e in the left camera coordinate system comprises of P_w^L , T and a vector $(T \times P_w^L)$ which is perpendicular to both vectors P_w^L and T , therefore all possible points P_w^L passing through the point T would be

$$(P_w^L - T)^T \cdot (T \times P_w^L) = 0, \quad (2.77)$$

According to equation (2.74), we can write $(P_w^L - T) = R^{-1}P_w^R$, and the cross product in equation (2.77) can be described as

$$\begin{aligned} (T \times P_w^L) &= \begin{vmatrix} i & j & k \\ T_1 & T_2 & T_3 \\ P_{11} & P_{12} & P_{13} \end{vmatrix}, \\ &= \begin{bmatrix} 0 & -T_3 & T_2 \\ T_3 & 0 & -T_1 \\ -T_2 & T_1 & 0 \end{bmatrix} \begin{bmatrix} P_{11} \\ P_{12} \\ P_{13} \end{bmatrix} = A_s P_w^L, \end{aligned} \quad (2.78)$$

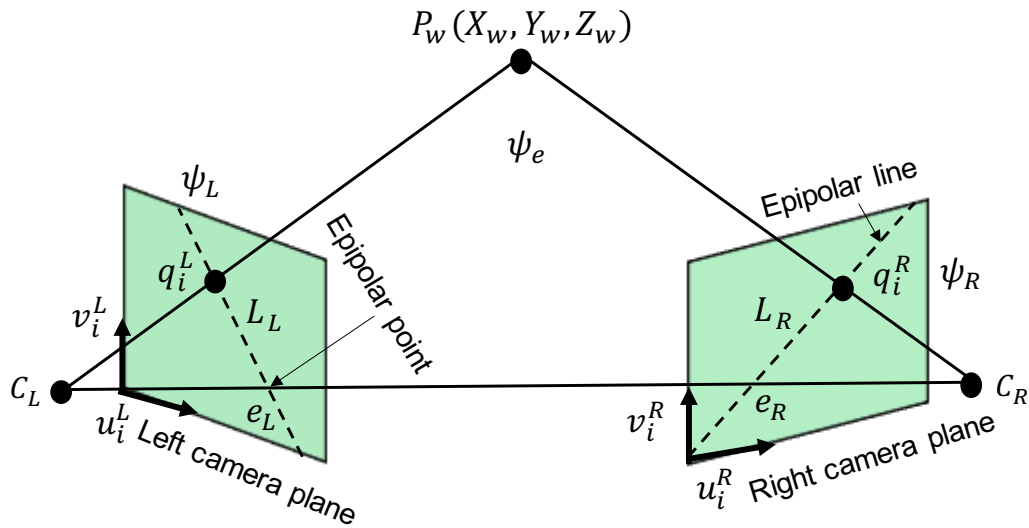


Figure 2.14: Schema of the epipolar geometry of a stereo-camera system. p_L and p_R are the projections of 3D point P onto the left and right camera images, respectively. L_L and L_R are the epipolar lines, and e_L and e_R epipolar points of the left and right camera images, respectively. O_L and O_R are the left and right cameras centres respectively.

where A_s is a skew symmetric matrix. Substituting equation (2.78) into equation (2.77) yields

$$(R^{-1}P_w^R)^T A_s P_w^L = 0,$$

and

$$(P_w^R)^T E P_w^L = 0, \quad (2.79)$$

where $E = R A_s$ is the essential matrix comprising of the rotation and translation and provide information between two cameras in real space. Using equation (2.62), points q_i^L and P_w^L , also q_i^R and P_w^R are correlated, therefore equation (2.79) written as

$$(q_i^R)^T E q_i^L = 0, \quad (2.80)$$

where q_i^R and q_i^L are image point coordinates in the respective image planes. The term $E q_i^L$ denotes the epipolar line on the right image plane (Ψ_R) that passes through the

image point q_i^R [116, 117]. Thus the epipolar lines can be represented as

$$L'_R = E q_i^L, \quad (2.81)$$

and

$$L'_L = E^T q_i^R. \quad (2.82)$$

In general, the essential matrix (E) describes the geometry of the two cameras with respect to each other but no information regarding the cameras. Therefore, to determine the relationship in the pixel domain, one needs to find the correlation between a point (in pixel) on one image and the corresponding epipolar line on the other image and to incorporate the intrinsic parameter information. For this purpose, we will substitute $p_i = K_{\text{int}} q_i$ in equation (2.80)

$$(p_i^R)^T (K_{\text{int}}^{R(-1)})^T E K_{\text{int}}^{L(-1)} p_i^L = 0.$$

Substituting $(K_{\text{int}}^{R(-1)})^T E K_{\text{int}}^{L(-1)} = F$ yields

$$(p_i^R)^T F p_i^L = 0, \quad (2.83)$$

where $[F = (K_{\text{int}}^{R(-1)})^T E K_{\text{int}}^{L(-1)}]$ denotes the fundamental matrix (algebraic illustration of the epipolar geometry) and comprises of camera's intrinsic parameters information along with the extrinsic parameters [116, 117].

Equation (2.83) refers to the epipolar constraint, which is the geometric property of the stereo-camera system and allows to determine the corresponding points between the two images acquired from two different perspectives. The epipolar constraint relies on the coplanarity of the cameras' optical centres (from two-views for a stereo-camera system), 2D image points and the point in the 3D world space. Therefore, for a given fundamental matrix, the corresponding points (p_i^L and p_i^R are the image points of the same 3D point) must satisfy the condition given in equation (2.83). Based on the

fundamental matrix information [54, 116, 117], the epipolar lines (given in equations (2.81) and (2.82)) can be written as

$$L_R = Fq_i^L, \quad (2.84)$$

and

$$L_L = F^T q_i^R. \quad (2.85)$$

Figure 2.14 depicts that one common line (called baseline) exists for all epipolar planes and a common point (called epipole) for all epipolar lines from a specific image plane. As equation (2.83) is true for all the image points on the image plane, thus the left image point is considered the left epipole. Therefore equation (2.83) can be written as

$$(p_i^R)^T F e_L = 0. \quad (2.86)$$

Equation (2.86) satisfies for all image points in the right image plane that exists on the baseline. Therefore, the following must be true

$$F e_L = 0. \quad (2.87)$$

Likewise,

$$F^T e_R = 0. \quad (2.88)$$

The fundamental matrix can also be represented in the form of the camera projection matrices [54, 116, 117] and given by

$$F = [e_R]_x M_{\text{proj}}^R (M_{\text{proj}}^L)^+, \quad (2.89)$$

where e_R is the epipole of the right camera image and can be expressed as $e_R = M_{\text{proj}}^R C_L$ and C_L is the optical centre of the reference camera (left camera), and $(M_{\text{proj}}^L)^+$ is

the pseudo-inverse of the projection matrix of the reference camera (left camera) and satisfies $M_{\text{proj}}^L (M_{\text{proj}}^L)^+ = \mathbb{I}$. Thus, the fundamental matrix represents the projective mapping from points to epipolar lines which forms the basics of epipolar geometry and yields several methods of determining the camera properties.

2.3.2.2 Stereo rectification

In real stereo-camera systems, the two cameras are not precisely coplanar, and the imaging planes are not row-aligned in the horizontal direction. In practice, for stereo images acquired from two perspectives, an image transformation, called rectification in which the image planes are reprojected, is applied that aligns the epipolar lines so that they are parallel with the image rows [42–44, 53]. The purpose of this transformation is to virtually align the cameras of the stereo-camera system which simplifies the computation of stereo disparity as the 2D search problem reduces to 1D search; therefore the process of stereo correspondence becomes well-grounded and computationally identifiable.

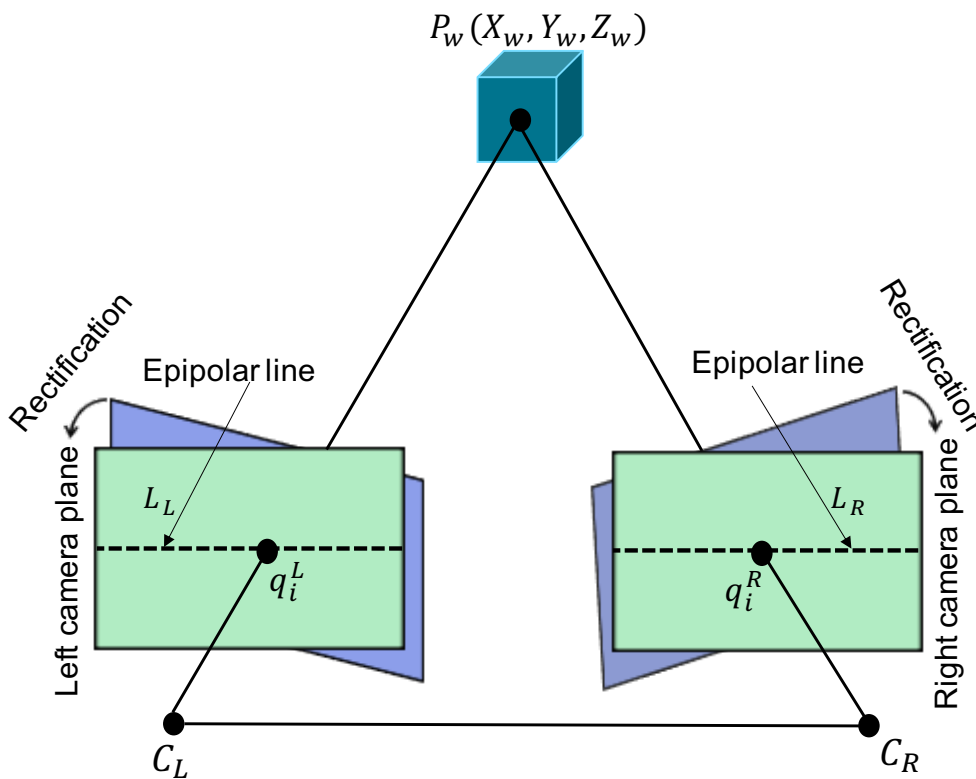


Figure 2.15: Schema of the stereo rectification process.

The first step of the rectification is to remove the distortion by including the radial

and tangential distortion coefficients. This process ensures that the pinhole camera model can be utilised when virtually aligning the cameras. Afterwards, the rectification of the undistorted stereo cameras is performed which is a process of remapping the points from the image planes of unaligned cameras on to the new image planes where a transformation is applied in such a way that the epipoles go to infinity and the epipolar lines are aligned along the image rows (in the horizontal direction). For this purpose, the rotation matrix that rotates the right camera's image plane to the left camera's image plane is equally divided in between the two cameras and represented as r_L, r_R . This rotation brings the two cameras into coplanar (virtual) configuration but not explicitly in the row alignment.

A rotation matrix R_{rect} is computed by taking the epipole of the left camera to infinity and aligning the epipolar lines horizontally [116, 117]. This matrix rotates the reference camera (left camera) about the centre of projection. Furthermore, we take the principal point to be on the reference (left) camera's image origin, the direction of the epipole is along the translation vector T between the two cameras and represented as

$$e_1 = \frac{T}{\|T\|}. \quad (2.90)$$

The second vector must be orthogonal to e_1 and can be computed as a normalised cross product of e_1 with the direction of the optical axis (principal ray), and given by

$$e_2 = \frac{[-T_2 \ T_1 \ 0]^T}{\sqrt{T_1^2 + T_2^2}}. \quad (2.91)$$

The third vector is perpendicular to both e_1 and e_2 and can be written as

$$e_3 = (e_1 \times e_2). \quad (2.92)$$

The rotation matrix R_{rect} can be represented as

$$R_{\text{rect}} = \begin{bmatrix} e_1^T \\ e_2^T \\ e_3^T \end{bmatrix}. \quad (2.93)$$

The row alignment between the left and right cameras is given by

$$R_L = R_{\text{rect}} r_L, \quad (2.94)$$

$$R_R = R_{\text{rect}} r_R. \quad (2.95)$$

By incorporating the rectified camera matrices for the stereo pair, the camera projection matrices can be written as

$$M_{\text{proj}}^L = K_{\text{int}}^{\text{rect-L}} K_{\text{ext}}^{\text{rect-L}} = \begin{bmatrix} f_{u_i^L} & \gamma^L & u_{s0}^L \\ 0 & f_{v_i^L} & v_{s0}^L \\ 0 & 0 & 1 \end{bmatrix} \begin{bmatrix} 1 & 0 & 0 & 0 \\ 0 & 1 & 0 & 0 \\ 0 & 0 & 1 & 0 \end{bmatrix}, \quad (2.96)$$

$$M_{\text{proj}}^R = K_{\text{int}}^{\text{rect-R}} K_{\text{ext}}^{\text{rect-R}} = \begin{bmatrix} f_{u_i^R} & \gamma^R & u_{s0}^R \\ 0 & f_{v_i^R} & v_{s0}^R \\ 0 & 0 & 1 \end{bmatrix} \begin{bmatrix} 1 & 0 & 0 & T_1 \\ 0 & 1 & 0 & 0 \\ 0 & 0 & 1 & 0 \end{bmatrix}. \quad (2.97)$$

The projection matrix projects the 3D point from the world coordinates (homogeneous coordinates) to the 2D point in the image coordinate and given by equation (2.69).

Likewise, 2D point can also be reprojected onto the 3D point by determining the reprojection matrix. Furthermore, if the disparity is known then the 2D point can be

projected into the 3D space and represented as

$$N_{\text{reproj}} \begin{bmatrix} u_i \\ v_i \\ d \\ 1 \end{bmatrix} = \begin{bmatrix} X_w \\ Y_w \\ Z_w \\ S \end{bmatrix}, \quad (2.98)$$

where N_{reproj} is the reprojection matrix which relies on the parameters from the reference camera (left camera) image except for u_{s0}^R which is the principal point in the right camera image. In case when the principal rays (optical axis) intersect at infinity ($u_{s0}^R = u_{s0}^L$) then the term associated with u_{s0}^R becomes zero. The reprojection matrix [116, 117] is given by

$$N_{\text{reproj}} = \begin{bmatrix} 1 & 0 & 0 & -u_{s0}^L \\ 0 & 1 & 0 & -v_{s0}^L \\ 0 & 0 & 0 & f \\ 0 & 0 & -1/T_1 & (u_{s0}^L - u_{s0}^R)/T_1 \end{bmatrix}. \quad (2.99)$$

Whilst the 3D coordinates can be obtained as $(X_w/S, Y_w/S, Z_w/S)$.

2.3.2.3 Disparity

After rectification (described in the above section), the image planes of the two cameras are coplanar with their optical axis being parallel, and the corresponding rows are aligned in the horizontal direction (shown in figure 2.15). A 3D point from the world coordinate system is projected onto the image planes with respective image coordinates q_i^L and q_i^R and the corresponding horizontal coordinates are denoted as x_i^L and x_i^R , respectively. Therefore, in a simple case (shown in figure 2.16), the horizontal points in the stereo camera images are correlated with the depth estimation. Using the characteristics of similar triangles in figure 2.16, we can write

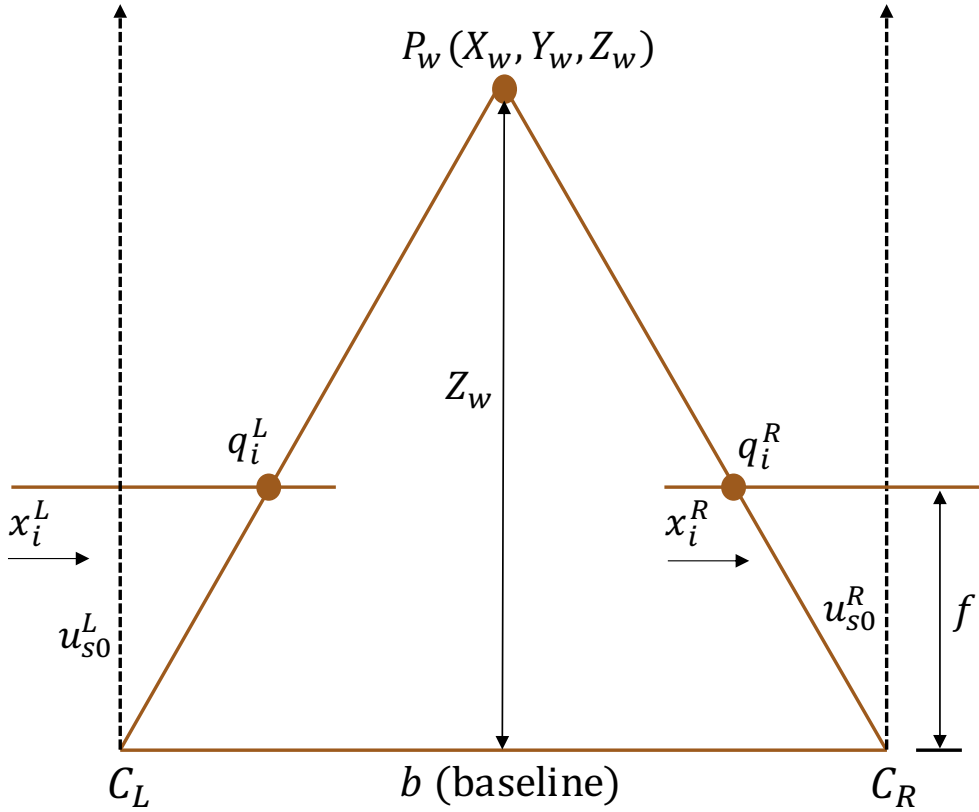


Figure 2.16: Standard stereo-camera system whereby the two cameras are separated by a distance called baseline b . The difference between the horizontal coordinates (x_i^L, x_i^R) of the image points (q_i^L, q_i^R) corresponds to disparity.

$$\frac{b}{Z_w} = \frac{b - (x_i^L - x_i^R)}{Z_w - f},$$

$$Z_w = \frac{fb}{(x_i^L - x_i^R)}, \quad (2.100)$$

where b is the baseline (separation between the cameras' optical centres), f is the focal length which is assumed to be equal for both cameras, $(x_i^L - x_i^R)$ is the disparity, and Z_w is the depth which is inversely proportional to the disparity.

The inverse relationship of depth with disparity generally have non-linear behaviour. Therefore, small disparity (nearly zero) induces large depth variation; however, when the disparity is large, a small difference in the disparity does not affect the depth. Thus, the outcome of this inverse correlation is that the stereo-camera systems have high depth resolution for objects relatively closer to the stereo-camera assembly. The significance of disparity is associated with the stereo correspondence problem, where each pixel in the reference camera (left camera) image is matched with

the corresponding pixel in the right camera image.

2.3.3 Projector characterisation

Digital light processing projectors are an essential part of the fringe projection systems and used to project the structured light patterns onto the surface of the measured object. The benefit of digital light processing projectors is that they are cost-effective and adaptable to programming. In practice, the performance of a fringe projection system depends on the accurate characterisation of the individual components (camera and projector). In general, the camera characterisation (often termed as camera calibration) relies on the pinhole model and a well-studied research area [111–115]. However, the projector characterisation is not simple. A projector can be considered as an inverse of a camera and described as a simple pinhole model. However, a projector cannot see the images projected onto the characterisation board and can be characterised by finding the corresponding relationship between the projected image and its projection onto the characterisation board by using a camera [37] which yields one-to-one mapping and provides the measurement accuracy up to pixel level.

The mapping accuracy of the projector characterisation can be improved by extracting the image coordinates at a sub-pixel level. Huang et al. developed a method to improve the mapping accuracy up to sub-pixel level, and the method applies to a characterisation board with circle patterns [38]. In this method, the circle edges are extracted from the captured images of the characterisation board and then mapped to the projector's pixel; also the locations of the circle centres on the projector are determined by the least-squares fitting technique to acquire the sub-pixel accuracy. Nonetheless, there is considerable eccentricity error related to the projection of circle patterns [118, 119]. Zhang et al. proposed a sub-pixel projector calibration method based on projective geometry and incorporating the projective invariance of the cross-ratio [120]. The method is not limited to any specific pattern type of the calibration target and independent of the camera calibration as a prerequisite of the projector calibration.

Chen et al. proposed a method to improve the characterisation accuracy of the

camera and the projector simultaneously [121]. This approach relies on a sub-pixel edge detection method to improve the detection accuracy of the reference features for coarse characterisation and simultaneously implementing an iterative compensation algorithm for fine characterisation. Gonzales et al. developed a characterisation method for fringe projection system by projecting an adaptive fringe pattern, and the method takes into account the lens distortion effects and eliminates the possible distortions by incorporating an adaptive fringe pattern [122]. Huang et al. also proposed a method for accurately characterising the projector by introducing a coaxial camera, and implemented this method by using a plate beam splitter which helps to treat projector as a true inverse of the camera [123]. The method uses a plate with discrete marked points and utilises the concept of the phase-stepping method of characterising the projector. Furthermore, the effects of lens distortion and projector's non-linearity were also considered to improve the accuracy of projector characterisation in the fringe projection system [124–126].

The methods for projector characterisation can be categorised into two main kinds, such as; characterised camera-based method [124, 127, 128], and phase-stepped method [36–38, 83, 129]. The details of the two methods are given in the following sections.

2.3.3.1 Characterised camera-based method

This method requires a characterised camera as a prerequisite, and the projector parameters are computed by utilising the characterised camera information. In this method, the projector generates an image pattern (a set of circles or checkerboard squares) with their coordinates known (a priori on the projector). The image pattern is then projected onto a flat vacant area and captured by a camera. The image coordinates of the markers (squares in a checkerboard or circles in a dot/circle pattern, as shown in figure 2.17), are extracted from the captured camera images and combined with the camera parameters to determine the marker's coordinates on the characterisation board. Thus, a set of corresponding points are known on the projector image and the characterisation board, which are then used to characterise the projector based on a pinhole model.

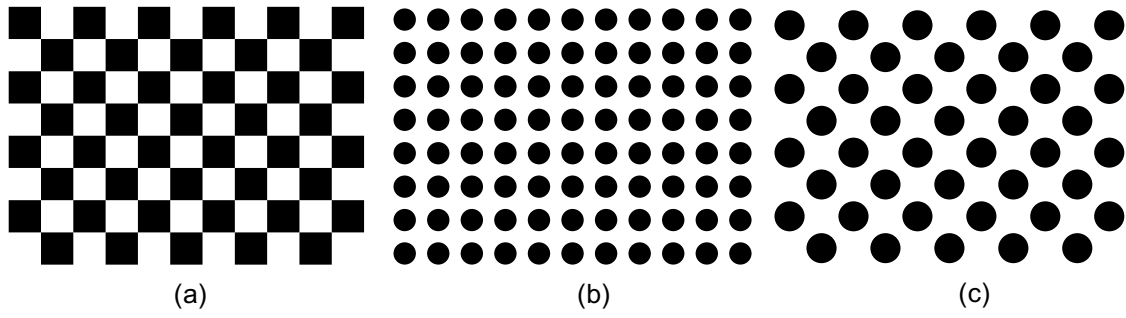


Figure 2.17: Standard targets for camera characterisation. (a) Checkerboard with black and white squares (b) circle pattern with black circles and white background and (c) asymmetric circle pattern with black circles and white background.

A projector (analogous to camera) can also be expressed with a pinhole model based on a non-linear model (including the radial and tangential lens distortion). The pinhole models of the camera (given in section 2.3.1) and the projector with their coordinate systems are depicted in figure 2.18. Let $P_w = [X_w, Y_w, Z_w, 1]^T$ is a corner point of a square of the characterisation board and represents the 3D homogeneous coordinate of the corner point in the world coordinate system, $q_i^p = [u_i^p, v_i^p, 1]^T$ indicate the corresponding 2D homogeneous coordinate of the point in the projector image coordinate system, and $q_i^c = [u_i^c, v_i^c, 1]^T$ denote the corresponding 2D homogeneous coordinate of the point in the camera image coordinate system. The transformational relationship between P_w and q_i^p , also between P_w and q_i^c can be expressed as

$$S^p \begin{bmatrix} u_i^p \\ v_i^p \\ 1 \end{bmatrix} = \begin{bmatrix} f_{u_i}^p & \gamma^p & u_{s0}^p \\ 0 & f_{v_i}^p & v_{s0}^p \\ 0 & 0 & 1 \end{bmatrix} [R^p, T^p] \begin{bmatrix} X_w \\ Y_w \\ Z_w \\ 1 \end{bmatrix}, \quad (2.101)$$

$$S^c \begin{bmatrix} u_i^c \\ v_i^c \\ 1 \end{bmatrix} = \begin{bmatrix} f_{u_i}^c & \gamma^c & u_{s0}^c \\ 0 & f_{v_i}^c & v_{s0}^c \\ 0 & 0 & 1 \end{bmatrix} [R^c, T^c] \begin{bmatrix} X_w \\ Y_w \\ Z_w \\ 1 \end{bmatrix}, \quad (2.102)$$

where S^p and S^c are the scaling factors for the projector and the camera, respectively, $(f_{u_i}^p, f_{v_i}^p)$ are the focal lengths corresponding to the width and height of the projector

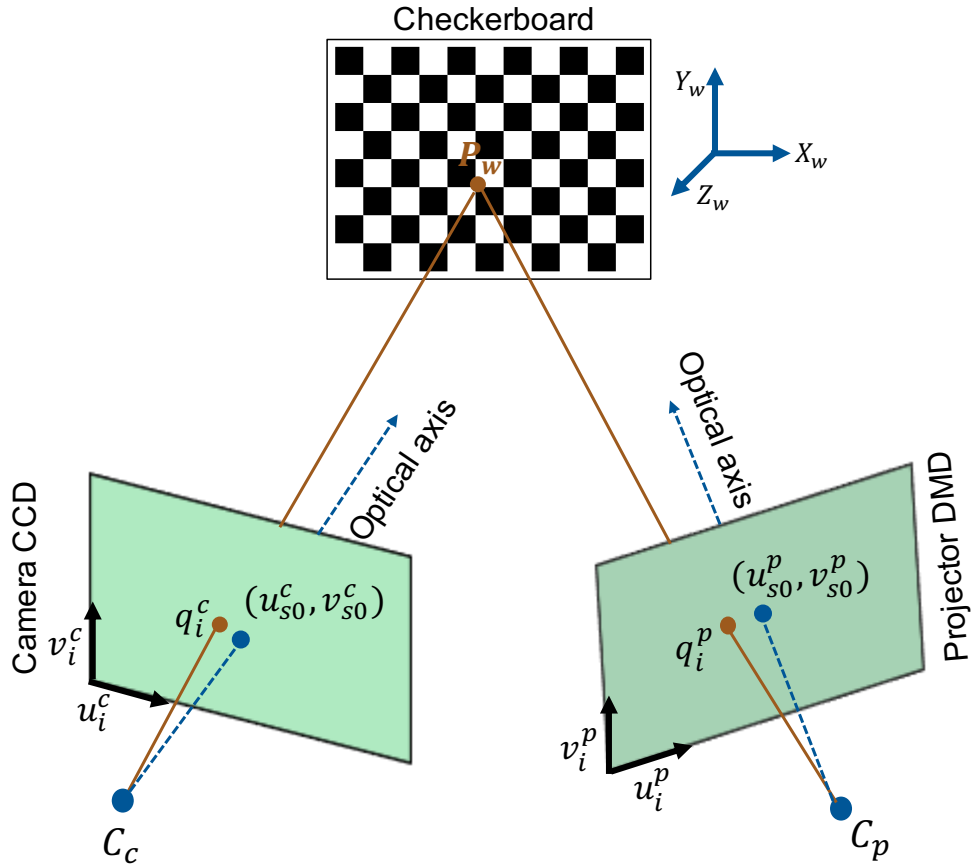


Figure 2.18: Schema of the characterised camera-based method which relies on the pinhole model of the camera and the projector.

pixels, $(f_{u_i}^c, f_{v_i}^c)$ are the camera focal lengths (in pixels) along the (u_i^c, v_i^c) axes, (u_{s0}^p, v_{s0}^p) and (u_{s0}^c, v_{s0}^c) are the coordinates of the principal point of the projector and the camera, respectively, (R^p, T^p) and (R^c, T^c) denote the extrinsic parameters (rotation and translation matrices) for the projector and the camera, respectively.

As the projector is characterised using a pinhole model, therefore it is important to take into account the geometric distortions. By incorporating the radial and tangential distortion coefficients [120], the coordinates of the distorted projector pixel $q_d^p = [u_d^p, v_d^p, 1]^T$ can be computed as

$$q_d^p = q_i^p (1 + m_{r1}r^2 + m_{r2}r^4 + m_{r3}r^6) + \begin{bmatrix} 2n_{t1}u_i^p v_i^p + n_{t2}(r_p^2 + 2(u_i^p)^2) \\ 2n_{t2}u_i^p v_i^p + n_{t1}(r_p^2 + 2(u_i^p)^2) \end{bmatrix} \quad (2.103)$$

where m_{r1}, m_{r2} and m_{r3} are the radial distortion coefficients, and n_{t1} and n_{t2} are the tangential distortion coefficients whilst $r_p^2 = (u_i^p)^2 + (v_i^p)^2$. The accuracy of this method

is associated with the accuracy of the camera characterisation and the extraction of the image coordinates of the markers. Particularly, the error becomes significant if the camera is not characterised well, and this error is inferred to the projector characterisation, affecting the overall measurement accuracy of the fringe projection system.

2.3.3.2 Phase-stepping method

A projector cannot capture images analogous to a camera. Zhang et al. [37] showed that a camera can be used to capture images for the projector by transforming the camera image pixel coordinates into projector image pixel coordinates. The basic idea is to determine a precise one-to-one correspondence between the camera pixels and the projector pixels by phase-stepping fringe projection technique. The absolute phase unwrapping methods, defined as global methods, determine the absolute phase value, which does not change between the fringe pattern projected and the distorted fringes captured, assuming the noise is insignificant. If only horizontal fringes are projected, the absolute phase value can lie anywhere on a line rather than yielding a specific point. This leads to one-to-many mapping, and one camera pixel represents many points on the projector. In order to establish the one-to-one correspondence, the second set of fringe patterns (orthogonal to the horizontal fringes) are used to get another phase line. The two lines intersect at a point which represents the corresponding point of the projector coordinate [83]. The method establishes the one-to-one (pixel-to-pixel) mapping between the camera and the projector, as shown in figure 2.19.

In the phase-stepping method, a set of horizontal and vertical phase-stepped sinusoidally varying fringes are projected onto the surface of the characterisation board (checkerboard, dot/circles pattern), and the images are captured using a camera which are further decoded to acquire the phase map. The intensity of the captured horizontal and vertical fringes is given by

$$I_i^h(u_i^c, v_i^c) = I_a^h(u_i^c, v_i^c) + I_b^h(u_i^c, v_i^c) \cos \left[\phi^h(u_i^c, v_i^c) - \left(\frac{2\pi i}{N} \right) \right], \quad (2.104)$$

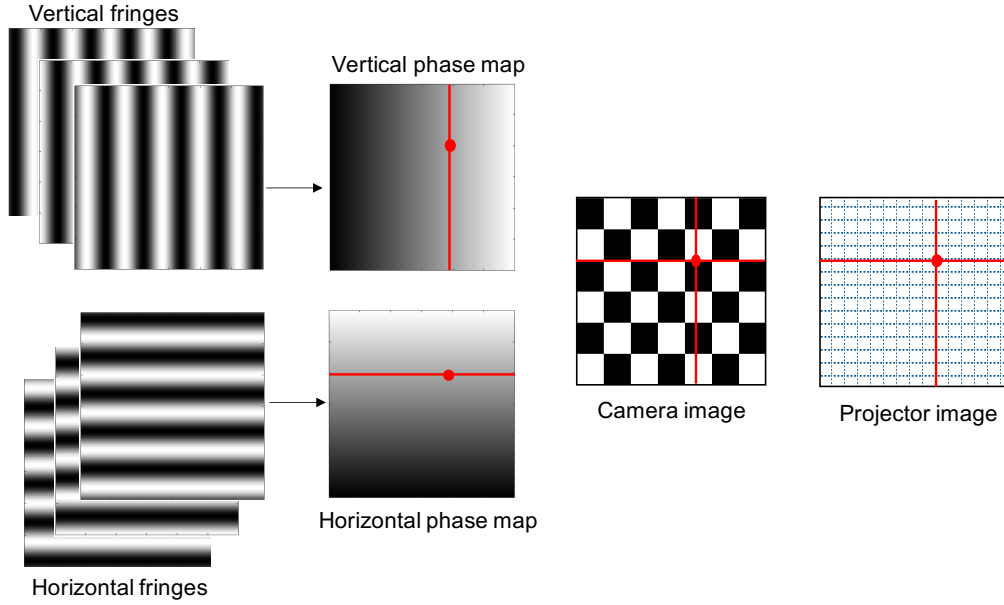


Figure 2.19: The process of generating the projector image coordinate.

$$I_i^v(u_i^c, v_i^c) = I_a^v(u_i^c, v_i^c) + I_b^v(u_i^c, v_i^c) \cos \left[\phi^v(u_i^c, v_i^c) - \left(\frac{2\pi i}{N} \right) \right], \quad (2.105)$$

where $I_a^h(u_i^c, v_i^c)$ and $I_a^v(u_i^c, v_i^c)$ represent the average background intensity for the horizontal and the vertical fringes, respectively, $I_b^h(u_i^c, v_i^c)$ and $I_b^v(u_i^c, v_i^c)$ is the intensity modulation for the horizontal and vertical fringes which represent the surface reflectivity and fringe pattern contrast, i is the phase stepping index ($i = 0, 1, 2, \dots, N-1$), $\phi^h(u_i^c, v_i^c)$ and $\phi^v(u_i^c, v_i^c)$ correspond to the horizontal and vertical wrapped phase maps and given by

$$\phi^h(u_i^c, v_i^c) = -\tan^{-1} \left(\frac{\sum_{i=0}^{N-1} I_i^h(u_i^c, v_i^c) \sin(2\pi i/N)}{\sum_{i=0}^{N-1} I_i^h(u_i^c, v_i^c) \cos(2\pi i/N)} \right), \quad (2.106)$$

$$\phi^v(u_i^c, v_i^c) = -\tan^{-1} \left(\frac{\sum_{i=0}^{N-1} I_i^v(u_i^c, v_i^c) \sin(2\pi i/N)}{\sum_{i=0}^{N-1} I_i^v(u_i^c, v_i^c) \cos(2\pi i/N)} \right). \quad (2.107)$$

Furthermore, an unwrapped phase map is acquired (using a temporal phase unwrapping approach), and a unique one-to-one mapping is established between the camera and projector intensity pixels. The camera characterisation information is retrieved by detecting the specific points (corners of squares of checkerboard or the circle centres in

case of dot/circle pattern) which are further incorporated to map the projector intensity pixels by utilising the established relationship. For this purpose, a set of corresponding points are determined between the projector image and the characterisation board and can further be implemented to characterise the projector similar to the camera characterisation. The accuracy of this method relies on the mapping relationship between the camera and projector intensity pixels.

Figure 2.19 depicts the system for the projector's characterisation based on phase-stepping approach. The world coordinate system is set by considering the XY-plane on the surface of the characterisation board, and thus the coordinates of the markers (squares in a checkerboard or circles in a dot/circle pattern) are known. In practice, a camera is used to capture the images of the characterisation board, and the marker's coordinates are extracted. In general, the mapping relationship between the 2D points (either on the camera and the projector) and 3D points on the characterisation board can be expressed by defining coordinate systems, which in this case, comprises of the camera and projector coordinate system, camera and projector image coordinate system and the world coordinate system.

Let $P_w(X_w, Y_w, Z_w)$ indicate a point in the world coordinate system associated with a 3D point on the characterisation board whilst $q^c(u_i^c, v_i^c)$ and $q^p(u_i^p, v_i^p)$ represent points on the camera and projector image coordinate system, respectively. The relationship between a point on the characterisation board and the camera image coordinate system can be represented by a pinhole camera model; likewise, the pinhole model is used to determine the relationship between the points on the characterisation board and the projector image coordinate system. The image coordinates of the markers (corners of squares in a checkerboard or circle centres in a dot/circle pattern) are determined from the images of the characterisation board (checkerboard, dot/circles pattern). By incorporating the extracted image coordinates information, the absolute phases of the markers can be acquired from the phase maps $\phi^h(u_i^c, v_i^c)$ and $\phi^v(u_i^c, v_i^c)$. Thus, the projector pixel coordinates of the markers can be computed by the transformation

relationship and given by

$$u_i^p = \phi_h(u_i^c, v_i^c) \left(\frac{P_f}{2\pi} \right), \quad (2.108)$$

$$v_i^p = \phi_v(u_i^c, v_i^c) \left(\frac{P_f}{2\pi} \right), \quad (2.109)$$

where (u_i^p, v_i^p) are the image coordinates of the projector, (u_i^c, v_i^c) are the image coordinates of the camera, $(\phi_h(u_i^c, v_i^c), \phi_v(u_i^c, v_i^c))$ are the horizontal and vertical phase values, P_f is the fringe pitch which corresponds to the number of pixels per fringe period.

Equations (2.108) and (2.109) yield the projector coordinates using the absolute phase map information and establishing the one-to-one mapping between the camera and the projector pixels. As the camera and projector utilise the same characterisation board (squares in a checkerboard or circles in a dot/circle pattern), the relationship between the points on the characterisation board and their position on the projector can be established. As the projector pixel coordinates (given in equation (2.108) and (2.109)) are established based on the absolute phase values which rely on the integer pixel values of the captured camera image, thus the projector pixel coordinates are computed with pixel-to-pixel accuracy level. This induces mapping error which affects the accuracy of the projector characterisation and ultimately influences the system characterisation of a fringe projection system.

2.4 Sources of error in fringe projection

In general, optical systems perform the coordinate measurement of the object through the information captured by the optical system, which is processed further to acquire the geometry (form) of the measured object. In principle, the fringe projection methods have been considered one of the most reliable approaches for 3D shape measurement due to the benefits of high-speed and high measurement accuracy. However, like other optical techniques (mentioned in section 2.1), there are some constraints and sources of error associated with the fringe projection method; therefore, it is imperative to take

into account the fundamental limitations. Generally, the fringe projection systems use optical components (camera and projector) to project and capture the fringe patterns, a mechanical assembly to mount the optical components, a computer for integrating the hardware, data acquisition and further data processing. The fringe projection systems have limitations due to the error being inferred from the optical components, such as the optical resolution, camera sensor noise, camera's intensity saturation due to shiny surfaces, mechanical vibration, background illumination, non-linearities, and noise in the phase domain. These factors are significantly important, and extensive research has been going on to address these issues. The fundamental constraints are elaborated here.

2.4.1 Optical resolution of the imaging system

The fringe projection systems comprise a camera and a projector; therefore, the properties of the individual optical components play an essential role in determining the accuracy and the optical resolution of the measurement systems. Optical resolution of an imaging system corresponds to its ability to distinguish the small details of the object, which is imaged, and influenced by many factors such as diffraction limit, aberration and sensor's pixel size. In general, the feedback of an imaging system towards a point source is illustrated as a point-spread function (PSF), also called the impulse response of the system. Precisely, the PSF corresponds to the degree of spreading or blurriness and considered a qualitative measure of the imaging system.

In general, if all parts of the imaging system are assumed to be ideal, then the only constraint on the resolution of the imaging system is diffraction. For a lens, the incoming light from a point source diffracts through the lens aperture and forms a diffraction pattern (Airy pattern). The central region of the diffraction pattern is known as the Airy disk, which indicates the limit of the achievable resolution of an optical system. Generally, two points are considered to be resolved when the angular separation between them is equal to the Airy disk radius (Rayleigh criterion [130]) and

given by

$$\theta_r = 1.22 \left(\frac{\lambda}{D} \right), \quad (2.110)$$

where θ_r represents the angular resolution (in radians), λ is the wavelength of the incident light, and D is the diameter of the lens aperture. The factor 1.22 is derived by computing the location of the first dark circular shaped ring which encompasses the Airy disk of the diffraction pattern. The capability of a system to resolve the details of the object being imaged depends on the ratio of (λ/D) , therefore, for a specific wavelength, a large diameter of the lens aperture yields the fine details in the image. The angular resolution (given in equation (2.110)) can be expressed in terms of spatial resolution by multiplying the angle (radians) value with the distance from the object (focal length) and expressed as

$$R_r = 1.22 \left(\frac{\lambda f}{D} \right) = 1.22 \lambda K_f, \quad (2.111)$$

where $K_f = (f/D)$ is the f-number of the lens and represented as the ratio of the focal length to the aperture diameter [131]. Thus, the optical resolution of an imaging system can be enhanced by minimizing the R_r (Rayleigh criterion) which can be achieved by decreasing the f-number. For example, for incident light with a wavelength of 550 nm, the minimum spatial resolution of 671 nm can possibly be obtained with a ($K_f = 1$) lens configuration. However, it is not feasible to make the f-number very small as reducing the f-number affects the depth of field and image contrast.

2.4.2 Error in the phase domain

In the phase-stepping fringe projection method, the information is encoded in the phase domain, and phase unwrapping algorithms are applied to acquire the absolute phase information. The phase error introduced by the unwrapping algorithms is regarded as the predominant error source. Specifically, spatial phase unwrapping algorithms are liable to error as the unwrapping is performed based on the neighbouring pixels infor-

mation, and the process is considered cumulative [70–73]. Essentially, the cumulative behaviour of phase unwrapping imposes stringent conditions on the phase unwrapping algorithms. Figure 2.20 depicts the phase unwrapping error of a pyramid-shaped artefact. In addition, the phase unwrapping is established through the captured images, and factors such as ambiguities in the phase wraps, noise (camera and background), spiking effect due to the sampling of the camera, and masked areas make this process challenging and complicated. Many phase unwrapping algorithms (spatial and temporal) have been developed to alleviate the potential sources of phase error.

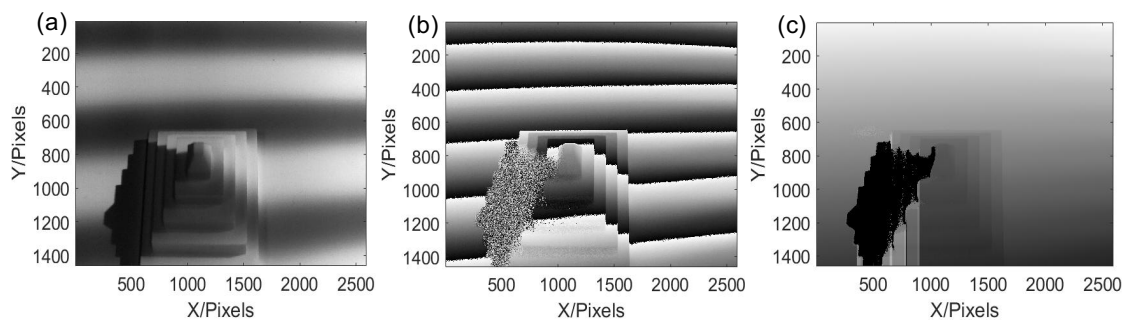


Figure 2.20: Phase unwrapping error. (a) Original image (b) wrapped image and (c) the unwrapped image depicting the error accumulation whereby the high noise area (shadowed) has introduced discontinuities in the unwrapped regions.

Ideally, the projected phase-stepped pattern should have a perfectly sinusoidal waveform, which seems unrealistic as the optical components (camera and projector) have non-linear behaviour. Generally, the non-linear intensity relationship of the digital video projector distorts the projected pattern and deviates them from the sinusoidal pattern (called gamma effect) which induces error in the phase domain. Therefore, it is vital to eliminate the non-linearity. Yao et al. proposed a method to alleviate the phase error caused by gamma non-linearity [132]. Their methodology is based on using four-step phase-shifted patterns four times with an initial offset of 22.5° , and then averaging the four phase maps to obtain the real phase. Song Zhang made a comparative study on the active and passive gamma calibration, which arises due to projector non-linearity. Both approaches are equally efficient and help to eliminate the phase error.

2.4.3 System characterisation error

System characterisation is an essential step which influences the accuracy and performance of the optical system. The process involves the computation of the intrinsic and extrinsic parameters of the camera and projector and establishes the transformational relationship between the 3D world coordinates and the image coordinates. In order to quantify the system's characterisation accuracy, a common approach is determining the reprojection error - a geometric error which denotes the distance between a point detected in the characterisation image (such as checkerboard image) and the respective world point projected onto the same image. In general, the 3D coordinates of a point

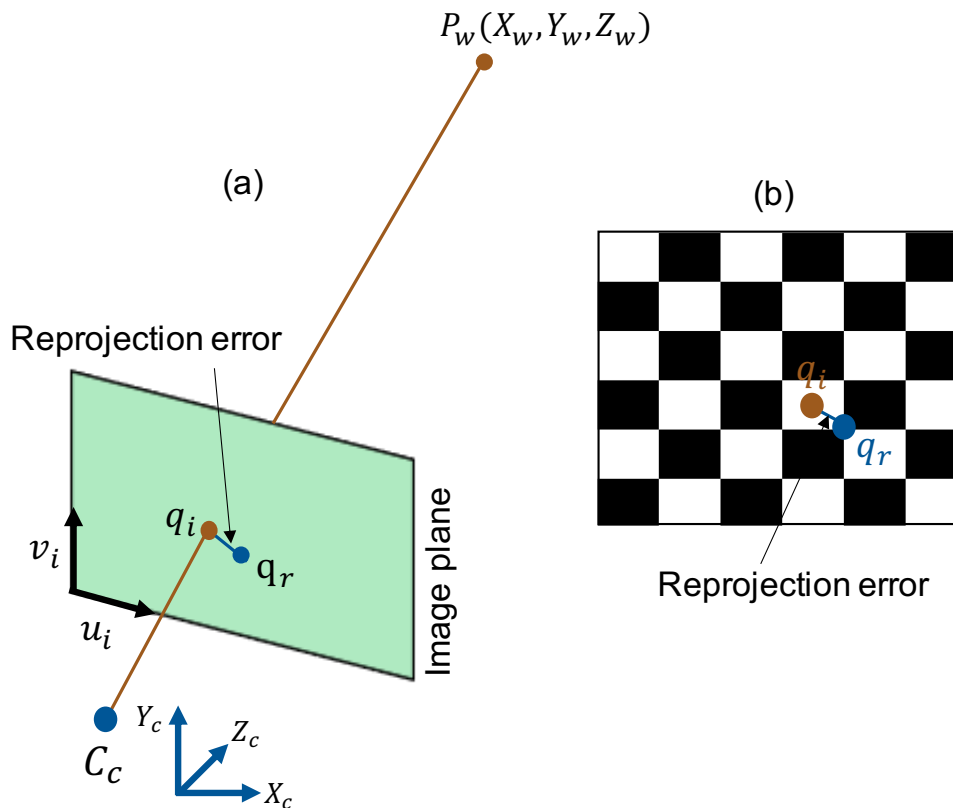


Figure 2.21: Reprojection error. (a) Pinhole camera model depicting the difference between the projected 3D point on the image plane and the point reprojected using camera parameters and (b) a checkerboard pattern illustrating the reprojection error.

are calculated by using the camera parameters (internal and external) and the location of the point in multiple images. After computing the 3D coordinates, the point is reprojected on all the captured images and deviation between the detected and the reprojected point corresponds to the reprojection error. Furthermore, the error relies on the quality of the detected point on the images and the camera characterisation

parameters.

In addition to determining the camera parameters, the system characterisation also involves computing the projector parameters. Generally, the projector works contrary to a camera as it projects images rather than capturing them. Therefore, the projector characterisation needs some additional information (absolute phase) to develop a one-to-one mapping between the camera coordinates and the projector coordinates [36, 37, 129]. The process of establishing the one-to-one correspondences induces mapping error and affects the accuracy of the 3D form measurement optical system.

2.4.4 Background illumination

The background illumination causes interferences and induces biases in the 3D reconstructed results; therefore, it is essential to eliminate the ambient light for achieving high accuracy measurements. In the commercially available systems such as GOM fringe projection system, narrow-band blue light is used to filter out the obstructing ambient light in the image acquisition process [26]. These systems generally use a blue light equaliser which enhances the luminosity of the light source and projects uniform and speckle-free light on the measuring object. In general, different methods have been proposed to reduce the effect of the ambient light, which otherwise affects the accuracy of the 3D form measurements.

Deng et al. proposed an intensity-based fringe projection method which is not influenced by global illumination (such as subsurface scattering and background) and reliable 3D surface reconstructions can be achieved in different environmental conditions [133]. Gupta et al. presented a method of structured light 3D scanning, which is resistive to global illumination [134]. The method utilises a modified structured light coded pattern by using simple logical and mathematical operations. Explicitly, the process does not separate the direct and global components of the target illumination, therefore suitable in situations where the direct component is not strong, and the separation is not feasible.

2.4.5 Noise

In digital imaging systems, such as fringe projection systems, the output signal is the amount of light reflected off the object surface and captured by the camera, in the form of images. In practice, the digital images are discretised (as pixels) and influenced by the noise factor, which usually appears in the image acquisition and processing stages. In general, noise is the undesired information which degrades the image quality, reduces the image contrast and subsequently affects the signal-to-noise ratio (SNR). Therefore, it is necessary to investigate the noise through proper mathematical models and implement the image denoising technique during the characterisation and 3D surface reconstructions in fringe projection systems.

In general, the digital images are distorted due to different types of noise, for instance, Gaussian noise, Brownian noise, salt and pepper noise, speckle noise and Poisson noise. Gaussian noise is considered to one of the most dominant sources of noise and arises during the image acquisition process [135, 136]. This is due to the electrical components (amplifiers and detectors), thermal radiations and vibrations of the camera sensor, which contribute to the noise present in an image. The Gaussian noise is statistical in nature and can be described by a Gaussian distribution (normal distribution) [136], and given by

$$P_G(g) = \frac{1}{\sigma\sqrt{2\pi}} e^{-\frac{(g-\mu)^2}{2\sigma^2}} \quad (2.112)$$

where g indicates the grey values (usually ranging from 0-255), σ is the standard deviation, and μ is the mean value. Gaussian noise generally perturbs the grey values in the captured digital image, and the Gaussian distribution model is considered as a good approximation of the real-world practices. Generally, image denoising is performed for reconstructing the original signal, and Gaussian noise is reduced by applying spatial filters (mean/convolution filter, Gaussian smoothing and median filter) in the digital image processing. Figure 2.22 shows the effect of applying a Gaussian smoothing kernel with different standard deviations.

The digital images are also affected by salt and pepper noise (called impulse noise

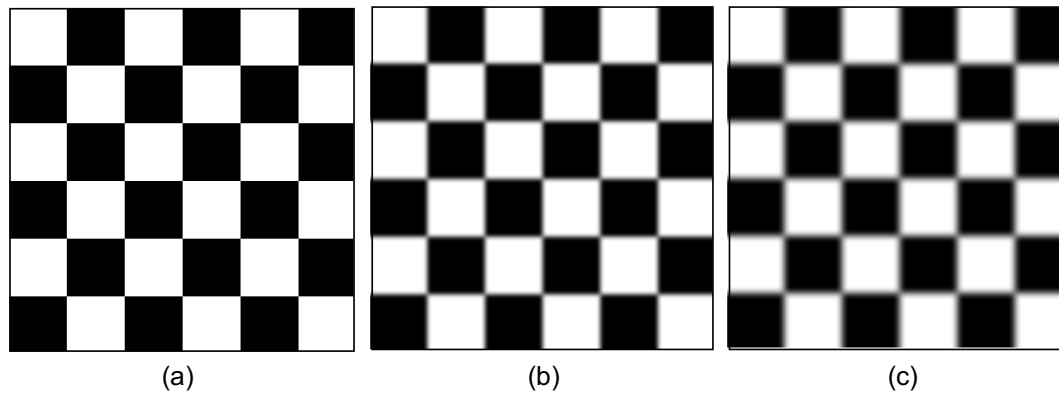


Figure 2.22: Checkerboard image with Gaussian smoothing filter of increasing standard deviations is applied (a) Original image (b) image with $\sigma = 4$ and (c) image with $\sigma = 6$.

or spike noise) which appears due to variations in the image data, the quality of the camera sensor and error in the data transmission. This type of noise degrades the image by introducing bright pixels into dark areas and dark pixels in the bright areas, thus the appearance resembles salt and pepper. For 8-bit images, the colour values range from 0 to 255 and correspond to black and white, respectively on the grey level. The salt and pepper noise perturbs the pixels with bright pixels replaced by 0 and dark pixels by 255.

The salt and pepper noise can be alleviated by using a median filter. Images are affected by shot noise (also called photon noise or Poisson noise) which occurs due to statistical quantum fluctuation and when the number of photons captured by the image sensor changes at specific exposure settings [135, 136]. Images are also influenced by a structured or periodic noise which emerges due to the interference with the camera electronics and appears as a repeating pattern periodically and can be eliminated by applying a notch filter.

Apart from camera noise, there is mechanical noise associated with the vibration of the mechanical parts used to mount the optical components; also the vibration present in the surrounding affects the performance of the optical measurement systems. Bointon et al. investigated the impact of vibration on the measurement accuracy and the repeatability of the fringe projection system [137]. The approach relied both on the theoretical assessment through computational simulation and the experimental investigation and helped to identify the necessary vibration performance parameters of the

fringe projection system. Yu Fu performed the low-frequency vibration measurement by analysing the projected fringe pattern in the temporal domain [138]. The method projects a grating on a vibrating object (vibrating with low-frequency), captures the images with a high-speed camera and analysing them in the time domain. Thus, it is vital to take into account mechanical vibration effects while designing an optical system.

Chapter 3

Single-view fringe projection system

Digital fringe projection (DFP) systems using a projector and camera are popular tools for high-speed 3D form measurement [20, 21, 23–25]. However, commercially available projectors are susceptible to gamma non-linearity, restricted depth of field, system vibration and optical noise, which distort the fringe patterns and introduces significant error in the phase measurement. Any noise or distortion in the phase map during the measurement cycle is manifested as an error to the final 3D measurement. In commercially available DFP systems, one of the main sources of error is the non-linear response of the digital video projector. The deviation of the projected input intensity to the detected output intensity is called the non-linear gamma effect.

Various attempts have been made to eliminate the non-linear errors. Pan et al. investigated that the Fourier analysis is beneficial to decompose the captured images into their harmonics, and the iterative phase compensation algorithm helps to overcome the non-linearity of projected values [139]. Hoang et al. first used the phase-shifting technique to measure the gamma value and pre-encoded it in the fringes before their projection [140]. In principle, the phase error can be alleviated by using more fringe patterns, which could reduce certain harmonics; however, increasing the number of fringes reduces the measurement speed, which is not ideal for high-speed applications [141].

The binary defocusing technique helps to remove the gamma non-linearity, but it certainly has the disadvantage of yielding a lower signal-to-noise ratio [142]. Zhou et al. investigated that the phase error depends both on the non-linear gamma effect and the ratio of intensity modulation; therefore, the ambient light also contributes to the non-linear effects [143]. Zhang et al. proposed a method based on a three-step phase-shifting technique to compensate the phase error using a convenient look-up table approach [144]. This method extracts the full-field error distributions, and it is considered to be a generic approach for any arbitrary phase-stepping technique. Zhang also compared the error compensation methods, mainly active versus passive methods and concluded that both are equally effective and significantly contribute to removing the phase error in DFP systems [145].

Recently, digital light processing (DLP) projection technology has become increasingly popular in the scientific and industrial sectors. In general, projectors are designed with large apertures to reduce the loss of light from the light-emitting source [146, 147]. However, this optical design restricts and narrows down the depth-of-focus (DOF) of commercially available projectors as the large numerical aperture of a lens is inversely related to the focal length ($NA = n \sin[\arctan(D/2f)] \approx (nD/2f)$) [148]. As a consequence, the projected image on the surface of an object with high slopes and large depth variation becomes blurred at short distances and affects the measurement accuracy of the optical systems.

Many methods have been proposed to address the issue of short DOF in optical devices. Kim et al. proposed a novel method of 'Highlighted-depth-of-field (HDOF)' that decreases the brightness of out-of-focus regions in an image by introducing an intensity grid in the z -direction [149]. The method utilises a projector to project the feature pattern onto a specific scene and merges images to acquire the necessary intensity change. Brown et al. introduced a technique that determines a spatially varying point-spread function across the projector image, and then applies the Wiener filter to acquire the desired pre-processed image to be projected [150]. The technique reduces the image blurriness caused by the out-of-focus regions in the projected image. Nonetheless, the technique uses an off-axis projector and can be applied to any surface

form if the captured camera image of the displayed constituents is rectified back into the projector coordinate system.

Zhang et al. proposed an approach to enhance the DOF by reducing the spot size on the marginal depth plane and acquired by utilising a negative lens array that does not have a diffuser [151]. Daisuke et al. suggested and practically implemented the method of the fast focal sweep, which can extend the DOF of DLP projectors [152]. Grosse et al. suggested the concept of the coded aperture to sustain the high-frequency components in the image correction process [153]. Cossairt and others utilise the concept of the coded aperture to extend the depth of field in the photography domain [154–156]. In recent years, the miniaturisation of projector display technology has led to small and powerful light sources, and significant efforts have been made to improve the resolution, and colour replication of projectors [157].

The aim of this chapter is to understand how fringe projection systems work and what are the limitations associated with the optical components used. The chapter is divided into two parts. The first part (section 3.1) addresses the design and development of a single-view fringe projection system. A complete pipeline with the inclusion of non-linear gamma correction, system characterisation and the 3D form measurement is presented. In the second part (section 3.2), the sources of error are investigated, and two projectors (a miniaturised mobile laser projector and commercially available cost-effective pico DLP projector) are compared. Their performance will be assessed with regards to their suitability to fringe projection applications by comparing the non-linear gamma response and the DOF.

3.1 Development of a single-view fringe projection system

An in-house cost-effective single-view fringe projection system using a single camera and projector is designed. The system utilises the basic principle of the fringe projection method and helps to investigate the limitations associated with the single-view fringe projection systems. The details are provided in the following sections.

3.1.1 System design and specifications

The experimental setup comprises of a machine vision camera (Basler Ace acA4024-29 um USB 3.0 monochrome camera with 12 mm C series fixed focal length lens, 4024×3036 pixels) and a digital light processing projector (DLP LightCrafter 4500 Texas Instruments, 912×1140 pixels). In the single-view fringe projection system, the camera and projector are mounted on a rectangular aluminium plate, which is fixed on a tripod stand with a $1/4''$ threaded screw. The tested object is placed on a rotation plate (20 mm diameter) which is mounted on a rotation stage (8MR151- Motorized Rotation Stages).

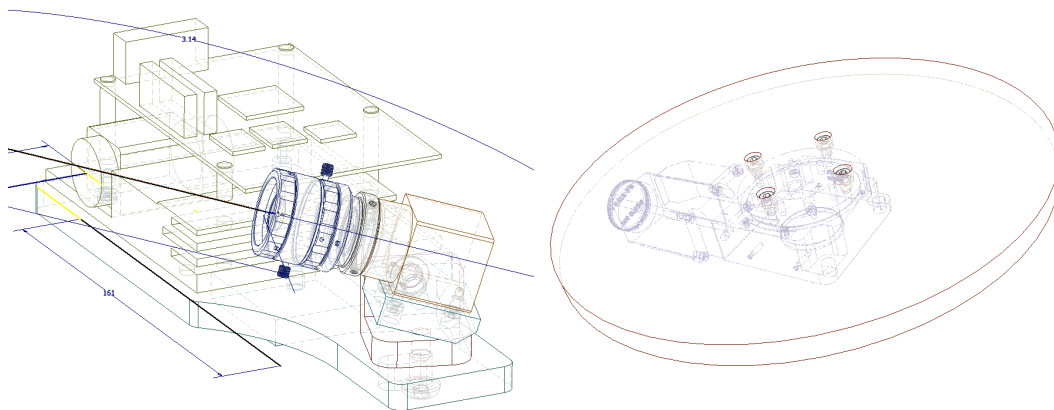


Figure 3.1: The CAD design of the fringe projection system. (a) Camera and projector mounted on a baseplate and (b) rotation plate mounted on a rotation stage.

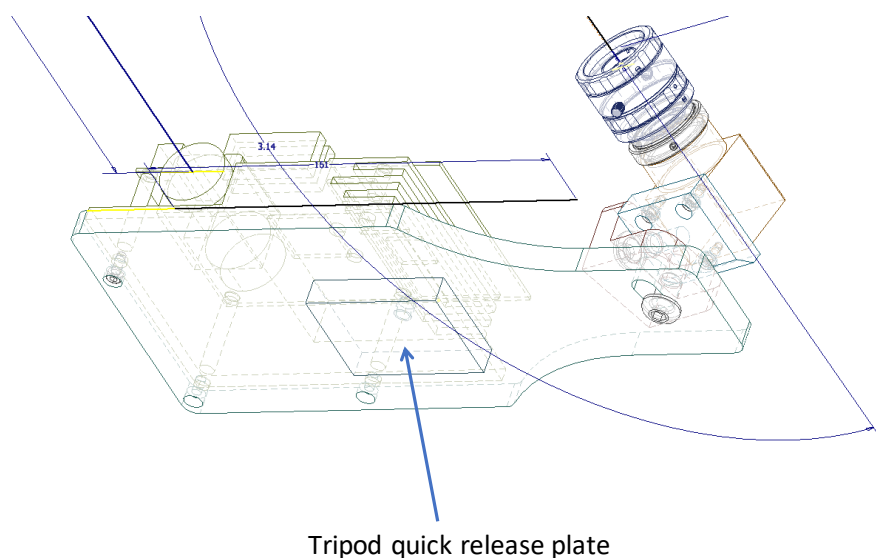


Figure 3.2: The CAD design of the projector and camera assembly and support to mount the baseplate on a tripod stand.

The projector's HDMI interface is used to project images onto the object. Specifically, the distance between the optical centres of the camera and the projector is 161 mm and the distance between the object and the projector's optical centre is 500 mm. The camera is lifted up by an angle of 17.28° so that its optical axis aligns with the centre of the chosen field of view ($400 \text{ mm} \times 400 \text{ mm}$). The computer-aided design (CAD) of the fringe projection system is shown in figures 3.1-3.4.

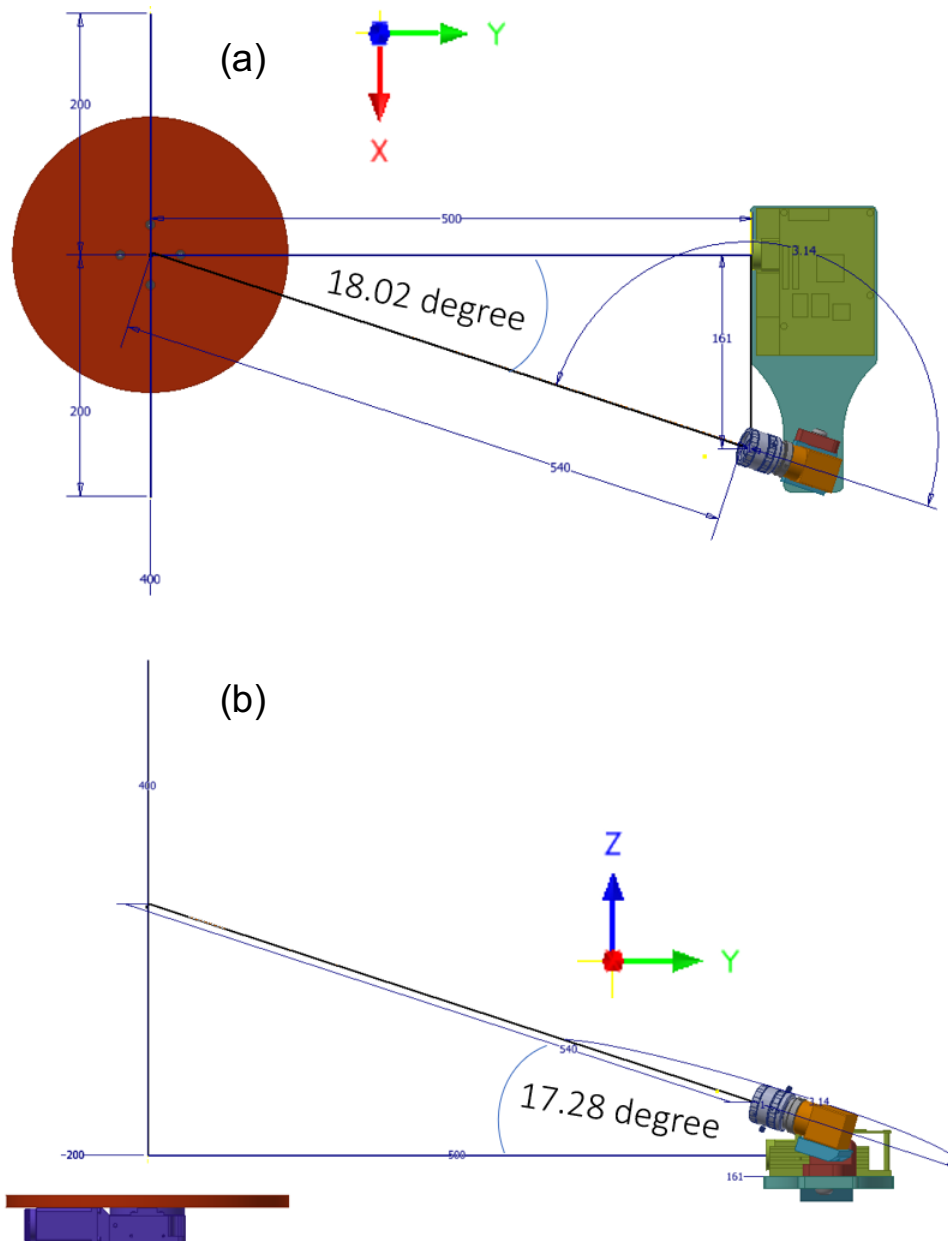


Figure 3.3: The CAD design of the single-view fringe projection system. (a) Top view and (b) side view.

The developed fringe projection system is capable of acquiring the form of complex AM parts of $< (200 \text{ mm} \times 200 \text{ mm} \times 100 \text{ mm})$. Figure 3.5 shows the individual

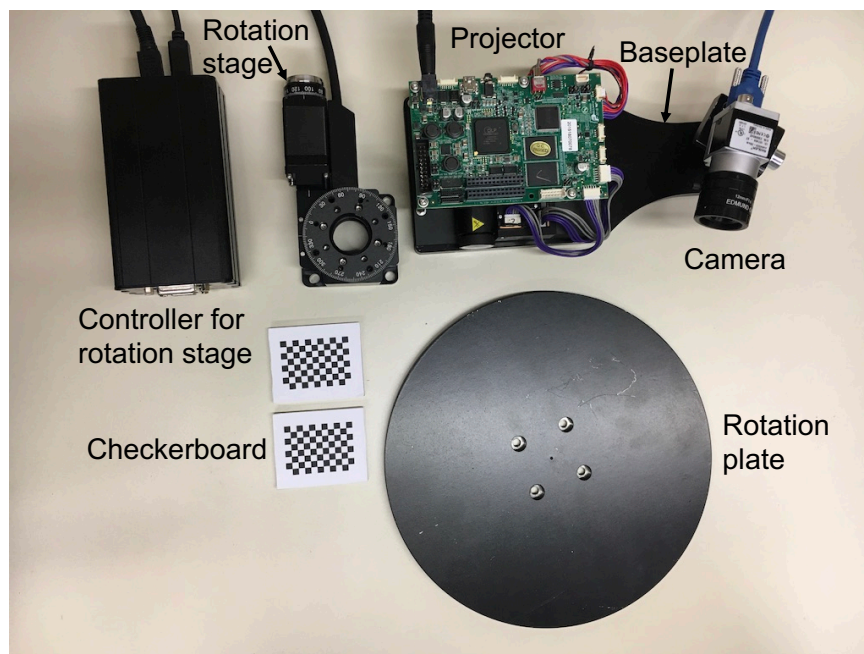


Figure 3.5: Individual components used in the development of a fringe projection system.

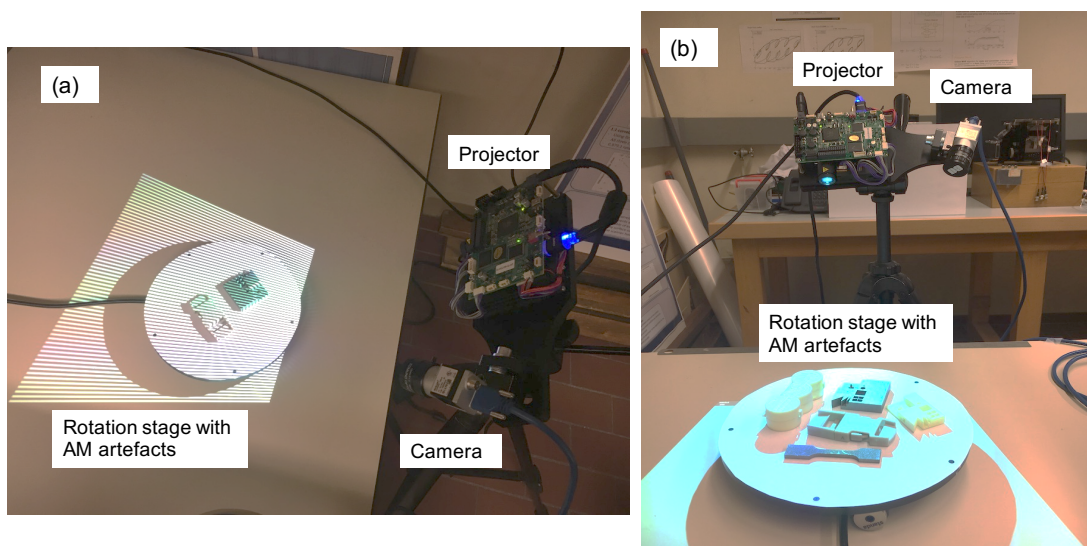


Figure 3.6: Fringe projection system in the acquisition mode. (a) The side view of the developed system when the projector projects fringes on the object and (b) the front view.

3.1.2 Methodology for the single-view fringe projection system

The methodology of the developed single-view fringe projection system relies on three main steps: *Gamma correction*, *system characterisation and measurement - 3D reconstruction*. The detail of these steps is given in the following sections.

3.1.2.1 Gamma correction

The fundamental principle of the fringe projection method is to project periodic fringe patterns onto the surface of the object and capturing the distorted fringe patterns which are yielded by the depth change of the measured surface. In practice, the periodic fringes are acquired by projecting a grating slide. However, the main limitation associated with the fabrication of the sinusoidal grating is the inconvenience of varying the phase and frequency of the fringe patterns.

Generally, in order to overcome these constraints, the digital fringe projection method is used, which utilises a digital video projector (digital light processing or liquid crystal display) as an enlightening device. The upside is its high speed for the phase-stepping method, which yields variable grating frequency and less affected by the surrounding disturbance. However, the downside is the non-linear illuminance of the video projector, which significantly affects the measurement accuracy. In general, the projector's gamma response [145] can be mathematically represented as

$$I_{\text{out}} = a(I_{\text{in}})^{\gamma} + b, \quad (3.1)$$

where I_{out} is the output intensity in grayscale while I_{in} is the given input intensity value, a and b are the constants that can be optimized effectively by altering the camera settings. The γ value can be estimated through harmonic analysis [158–160], statistical models [161], and least-squares fitting methods [162–164].

The non-linear gamma response of a projector varies from one projector to another for the same model, also from one model to another. The gamma correction requires to pre-distort the sinusoidal fringe patterns before their projection so that the final output is sinusoidal fringe patterns. For this purpose, the inverse gamma curve is acquired and fitted with the seventh order polynomial function [145], given by

$$I_{\text{in}} = a_0 + a_1(I_{\text{out}}) + \dots + a_6(I_{\text{out}})^6 + a_7(I_{\text{out}})^7, \quad (3.2)$$

where a_k , [$k = 0, 1, 2, 3, \dots, 7$] are the constants which can be determined from the

experimental data.

3.1.2.2 System characterisation

The system characterisation is the foremost important step on which the system performance relies. The process involves determining the intrinsic and extrinsic parameters of the optical components by establishing the transformational relationship between the 3D world coordinates to the camera and projector coordinates. A camera is described as a pinhole model, and the intrinsic parameters (given in equation (2.66), see section 2.3.1) including focal length, principal point, pixel skew factor, and pixel size are determined by taking multiple images of a high-precision characterisation artefact (checkerboard) from different orientations, and then extracting the image coordinates of the specific features (square corners of the checkerboard) using the Matlab based image processing algorithm.

For a 3D point with coordinates (X_w, Y_w, Z_w) and (x_c, y_c, z_c) in the real world coordinate system and the camera coordinate system, respectively, the relationship between a point on the object and its projection on the imaging plane can be determined based on the camera projection model (mentioned in section 2.3.1 and equation (2.69)). The extrinsic parameters (given in equation (2.68)) include the rotation and translation matrices and describe the transformation of a 3D point from the real world coordinate system to the camera coordinate system. The extrinsic parameters of the camera and projector are determined by projecting periodic phase-stepped fringes and acquiring the absolute phase map information.

A phase map for the fringe projection system can be obtained by different methods; however, we have utilised a set of sinusoidal phase-stepped (10 phase-shifted patterns with a phase shift of $\delta_i = (2\pi i/N)$, where, the phase stepping index is $i = 0, 1, 2, \dots, N-1$, and given in equations (2.15) and (2.16)) and binary fringe patterns. The images are captured at each step and analysed in the phase domain to retrieve the continuous phase information acquired using a temporal phase unwrapping method. For that purpose, the binary fringes are used to evaluate the fringe order. If the fringe order for each fringe stripe/line is uniquely determined, the phase is considered as an absolute

phase, and this a key parameter in the temporal phase unwrapping process [88].

In order to determine the projector coordinates, a set of horizontal and vertical phase-stepped patterns (10 phase-shifted patterns for each direction) are projected onto the checkerboard and images are captured at several different orientations by moving the checkerboard manually in the measurement volume (mentioned in section 2.3.3). For each characterisation pose, the projector coordinates are established from the camera coordinates using the one-to-one correspondence accomplished through the absolute phase maps [37, 83, 114]. The transformational relationship for establishing the projector coordinates is provided in equations (2.108) and (2.109). Furthermore, the absolute phase maps are retrieved for the measured object and further utilised in 3D surface reconstruction using the geometrically characterised parameters for coordinate calculations.

3.1.2.3 Measurement - 3D reconstruction

The system characterisation (mentioned in section 3.1.2.2) establishes the intrinsic and extrinsic parameters for the optical components (camera and the projector). The transformation from the image coordinates to the three-dimensional world coordinates can be acquired based on the triangulation principle. For this purpose, the camera and the projector pair is considered a stereo pair, and the relationship is given by

$$S^c q_i^c = K_{\text{int}}^c [R^c, T^c] P_w, \quad (3.3)$$

$$S^p q_i^p = K_{\text{int}}^p [R^p, T^p] P_w, \quad (3.4)$$

where q_i^c and q_i^p are the homogeneous coordinates of the image point in the image coordinate system of the camera and projector respectively, P_w is the homogeneous point coordinate in the world coordinate system, $(K_{\text{int}}^c, K_{\text{int}}^p)$ are the intrinsic parameters, (R^c, R^p) are the rotational and (T^c, T^p) are the translational parameters for the camera and the projector, respectively. The homography matrices (H^c and H^p for the camera and projector [83]) correspond to the projection matrices given in equations

(3.3) and (3.4) and represented as

$$H^c = K_{\text{int}}^c [R^c, T^c] = \begin{pmatrix} h_{11}^c & h_{12}^c & h_{13}^c & h_{14}^c \\ h_{21}^c & h_{22}^c & h_{23}^c & h_{24}^c \\ h_{31}^c & h_{32}^c & h_{33}^c & h_{34}^c \end{pmatrix}, \quad (3.5)$$

$$H^p = K_{\text{int}}^p [R^p, T^p] = \begin{pmatrix} h_{11}^p & h_{12}^p & h_{13}^p & h_{14}^p \\ h_{21}^p & h_{22}^p & h_{23}^p & h_{24}^p \\ h_{31}^p & h_{32}^p & h_{33}^p & h_{34}^p \end{pmatrix}, \quad (3.6)$$

where h_{ij}^c and h_{ij}^p are the homography matrix elements for the camera and the projector, respectively, while the indexes $\{i = 1, 2, 3\}$ and $\{j = 1, 2, 3, 4\}$. The real world coordinates can be acquired based on the triangulation equation [83] and given by

$$\begin{pmatrix} X_w \\ Y_w \\ Z_w \end{pmatrix} = \begin{pmatrix} h_{11}^c - u_i^c h_{31}^c & h_{12}^c - u_i^c h_{32}^c & h_{13}^c - u_i^c h_{33}^c \\ h_{21}^c - v_i^c h_{31}^c & h_{22}^c - v_i^c h_{32}^c & h_{23}^c - v_i^c h_{33}^c \\ h_{11}^p - u_i^p h_{31}^p & h_{12}^p - u_i^p h_{32}^p & h_{13}^p - u_i^p h_{33}^p \end{pmatrix}^{-1} \begin{pmatrix} u_i^c h_{34}^c - h_{14}^c \\ v_i^c h_{34}^c - h_{24}^c \\ u_i^p h_{34}^c - h_{14}^p \end{pmatrix}. \quad (3.7)$$

The above equation holds when the horizontal fringes (u_i^p is the projector image coordinate in the x-direction) are projected onto the surface of the measured object.

3.1.3 Experimental results of the single-view fringe projection system

3.1.3.1 Gamma correction results

The experimental assembly of a single projector-camera is depicted in figure 3.6(a-b). The gamma curve of the projector can be acquired by projecting multiple grayscale images (0–255) onto a flat surface and then capturing the images by a camera. Matlab software is used to generate an image with a resolution of (912 × 1140) pixels which is sent to the digital projector (DLP LightCrafter 4500 Texas Instruments, 1280 × 800

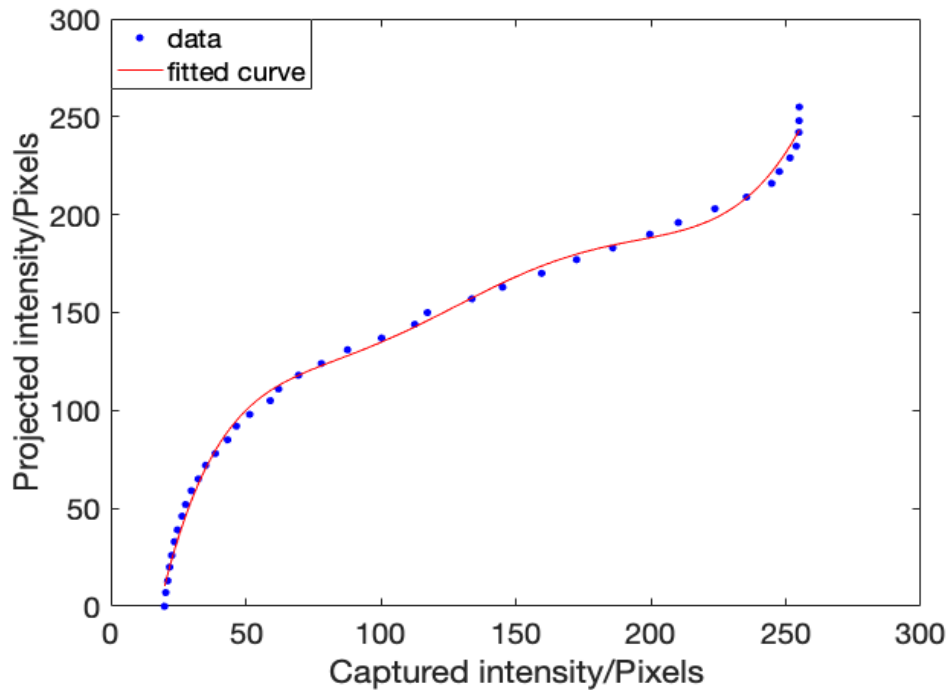


Figure 3.7: The non-linear gamma curve of the DLP projector. The data is shown as blue dotted points and the red line corresponds to the polynomial fitting.

pixels) for projection. A machine vision camera (Basler Ace acA4024-29, 4024×3036 pixels) is used to capture the images. The pixel intensities from a specific region-of-interest ROI (100×100 pixels) is averaged in the captured image and the output intensity value is acquired. The gamma curve is obtained and fitted with a polynomial, as shown in figure 3.7.

3.1.3.2 System characterisation results

The geometric characterisation of the fringe projection system is performed by using a printed checkerboard (checker size 4 mm) and capturing images at 20 different orientations as discussed in section 3.1.2.2. The schematic of the geometric characterisation is shown in figure 3.8. The camera is characterised using a pinhole model and the intrinsic parameters of the camera are listed in table 3.1.

For the projector characterisation, additional information is provided in terms of the phase maps to determine the one-to-one correspondence between the projector and the camera intensity pixels. Figure 3.9 shows the fringes projected onto the checkerboard pattern and the corresponding phase maps with square corners detected for one orientation of the checkerboard.

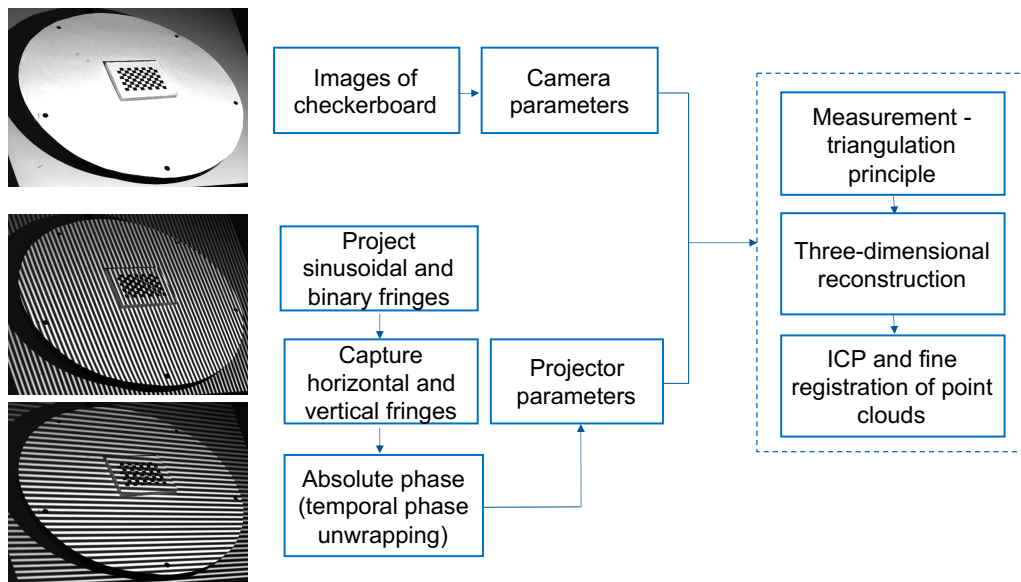


Figure 3.8: Schema of the system characterisation of the fringe projection system.

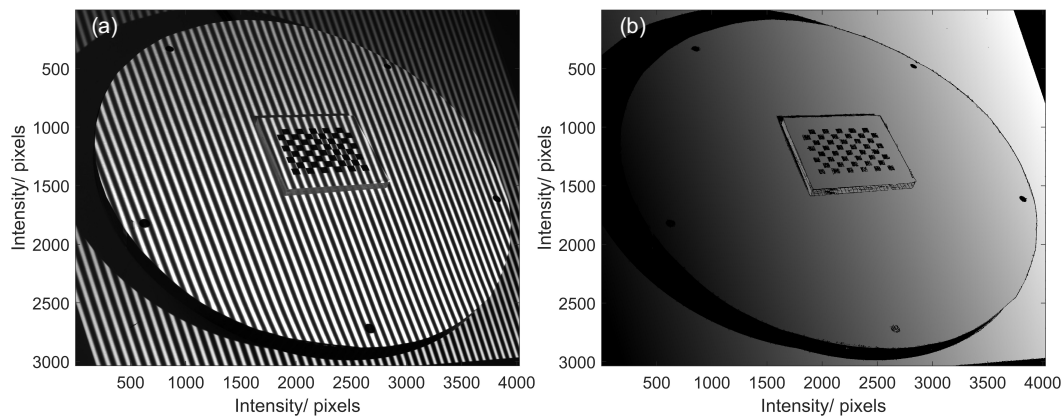


Figure 3.9: Fringes projected on the checkerboard and captured by a camera. (a) Original image and (b) the corresponding phase map with the detected checkerboard points.

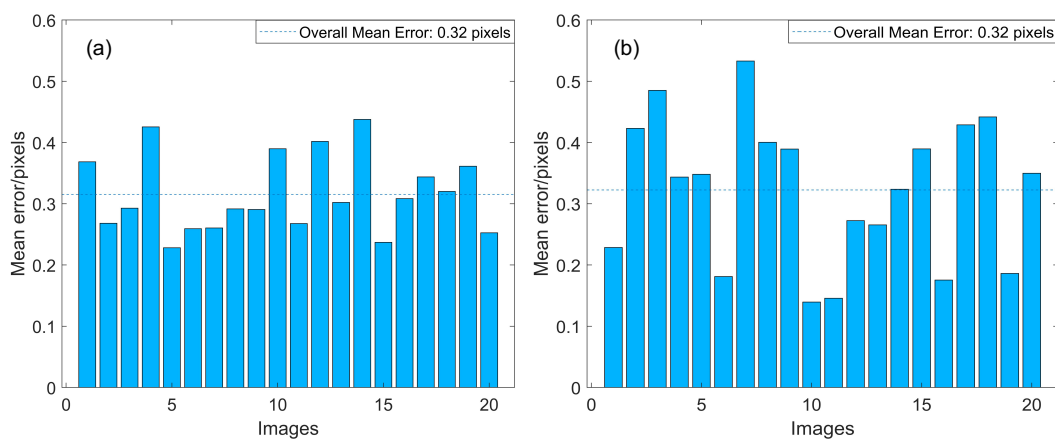


Figure 3.10: Reprojection error per image. (a) Camera and (b) projector.

To evaluate the accuracy of the system characterisation quantitatively, the reprojection error for the camera and the projector are determined as shown in figure 3.10.

Table 3.1: System characterisation results for the camera and projector.

Optical component	Intrinsic parameter
Camera	$\begin{bmatrix} 6838.0 & 0 & 2370.0 \\ 0 & 7116.3 & 1529.1 \\ 0 & 0 & 1 \end{bmatrix}$
Projector	$\begin{bmatrix} 2618.9 & 0 & 557.2 \\ 0 & 8732.2 & 1439.3 \\ 0 & 0 & 1 \end{bmatrix}$

The mean reprojection error per image is less than half a pixel which can further be improved by using a high-precision checkerboard. The 3D visualisation of the extrinsic parameters of the camera and projector is another measure of the system accuracy. Figure 3.11 shows the extrinsic parameters in 3D space which displays the orientation of the detected checkerboard patterns relative to the camera and the projector.

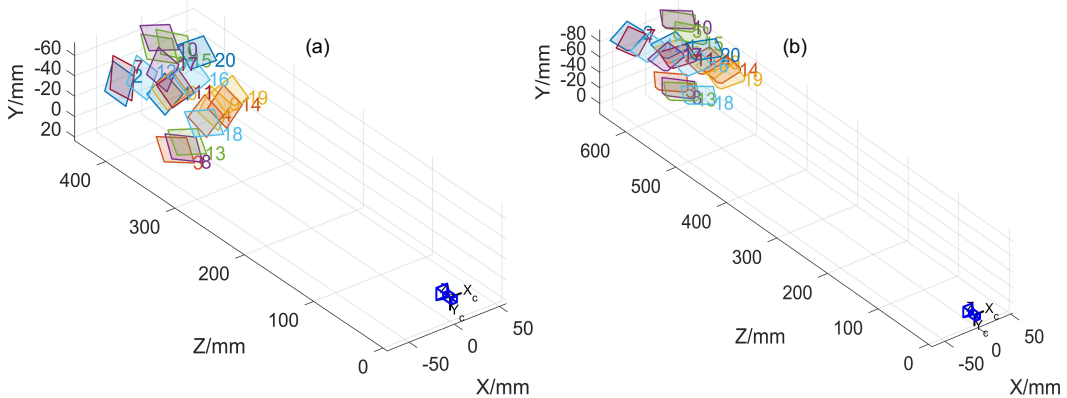


Figure 3.11: Extrinsic parameters. (a) Camera and (b) projector.

3.1.3.3 3D reconstruction results

The system's characterisation accuracy is further evaluated by the 3D form/shape measurement of complex AM artefacts of different materials (polymer, metal and plaster) with certain depth variations. A set of phase-stepped sinusoidal fringes (equation 2.15) and binary coded fringes are projected onto the surface of the measured object and the distorted images are captured by the camera. In this experiment, we have used 20 phase-stepped sinusoidal fringes with the fringe period of 20 pixels and 8 binary codes patterns. Figure 3.12(a) shows the image of the AM artefacts with sinusoidally varying

fringes projected onto the objects.

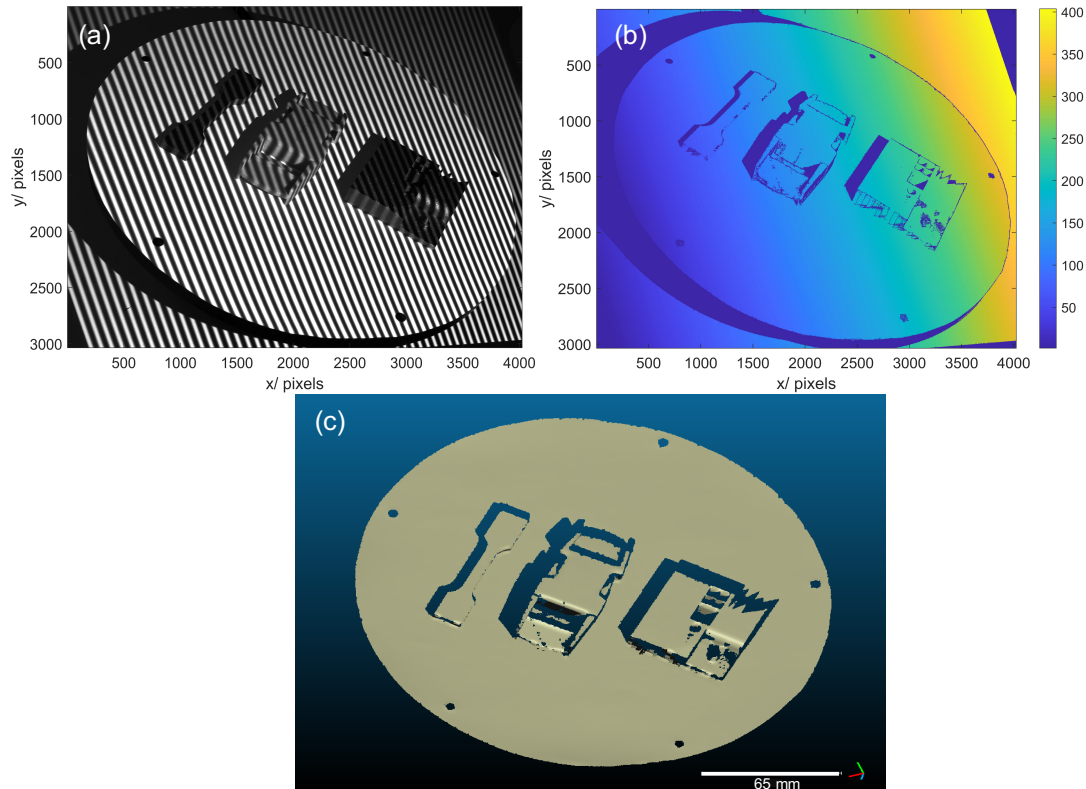


Figure 3.12: 3D reconstructed results for AM artefacts. (a) Original image with fringes projected (b) unwrapped phase map and (c) a point cloud representing the 3D shape.

The phase map is acquired using equation (2.16). Since the acquired phase map has 2π modulation and is trapped between $[-\pi, \pi]$, therefore it needs the removal of the 2π discontinuities in order to obtain a continuous phase map. For this purpose, the temporal phase unwrapping [49–52] is used to produce an absolute phase map. In the temporal unwrapping, the fringe order is encoded into binary fringes and projected onto the object, and an absolute unwrapped phase map is acquired.

A modification to the binary fringes is introduced by converting the binary values to greyscale values, which simplifies the search for 2π discontinuities in the phase map with respect to the neighbouring pixels. The unwrapping errors in the acquired phase maps are corrected using a filtering algorithm that convolves the unwrapped phase map with a Sobel edge kernel and removes the random spikes and dips in the phase map. The unwrapped phase map is depicted in figure 3.12(b). By incorporating the system characterisation information and triangulating the common points between the camera and the projector, the 3D reconstructed results for AM complex parts are acquired as

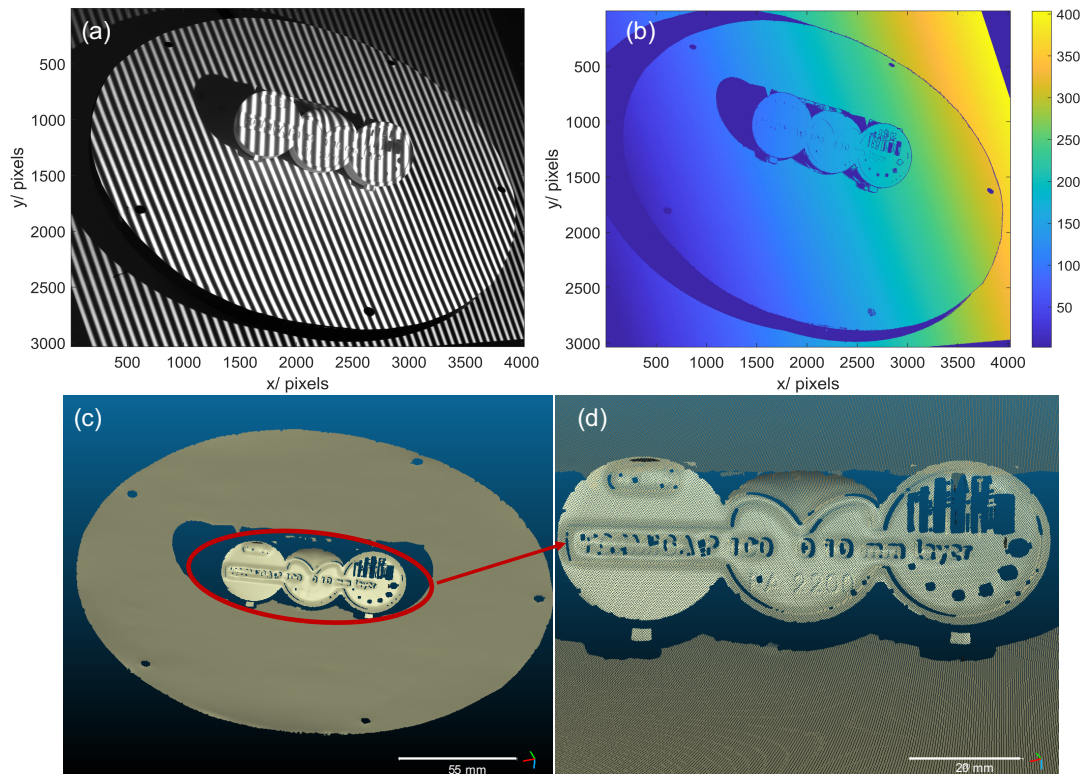


Figure 3.13: 3D reconstructed results of a Nylon-12 artefact. (a) Original image with fringes projected (b) unwrapped phase map (c) 3D reconstructed point cloud and (d) zoomed-in view of the data shown in (c).

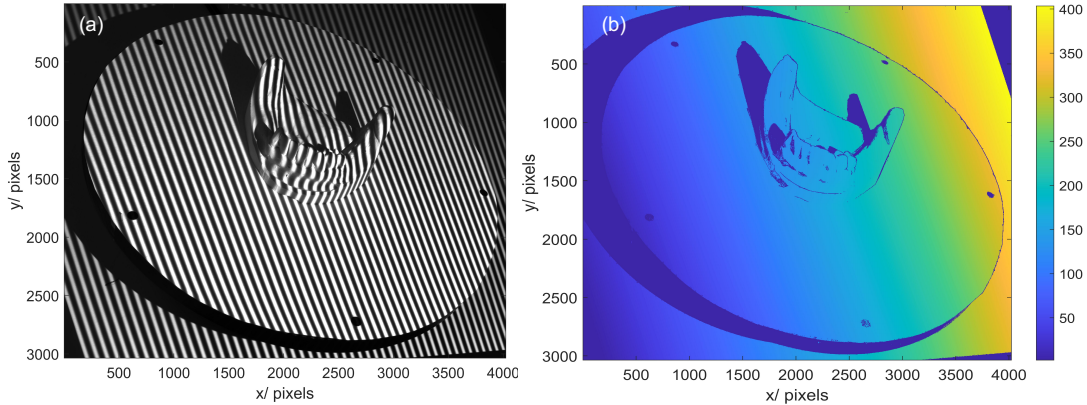


Figure 3.14: 3D reconstructed results of a jaw shaped artefact. (a) Original image with sinusoidal fringes projected and (b) the unwrapped phase map.

shown in figure 3.12(c).

Another Nylon-12 calibration artefact is measured using the methodology in section 3.1.2. Figure 3.13(a) shows the artefact with fringes projected whilst figure 3.13(b) depicts the unwrapped phase map. A small region is zoomed-in which shows the spatial resolution of the 3D reconstructed results of the calibration box and depicted in figure 3.13(c-d). The reconstructed results do not represent any non-linearities which usually

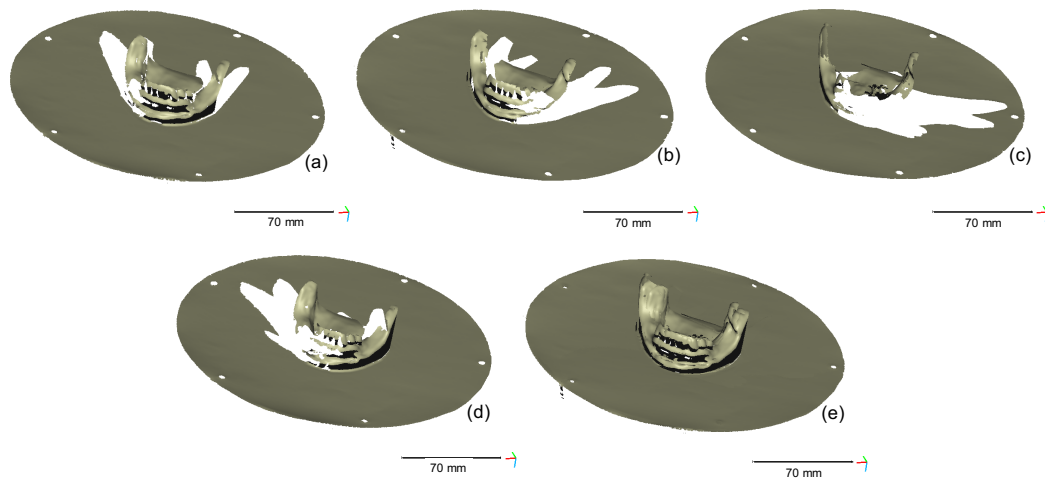


Figure 3.15: Different views of the 3D reconstructed results of a jaw shaped artefact. (a-d) Single-view data acquired from different perspectives and (e) the combined point cloud which is obtained by registering the single-views shown in (a-d).

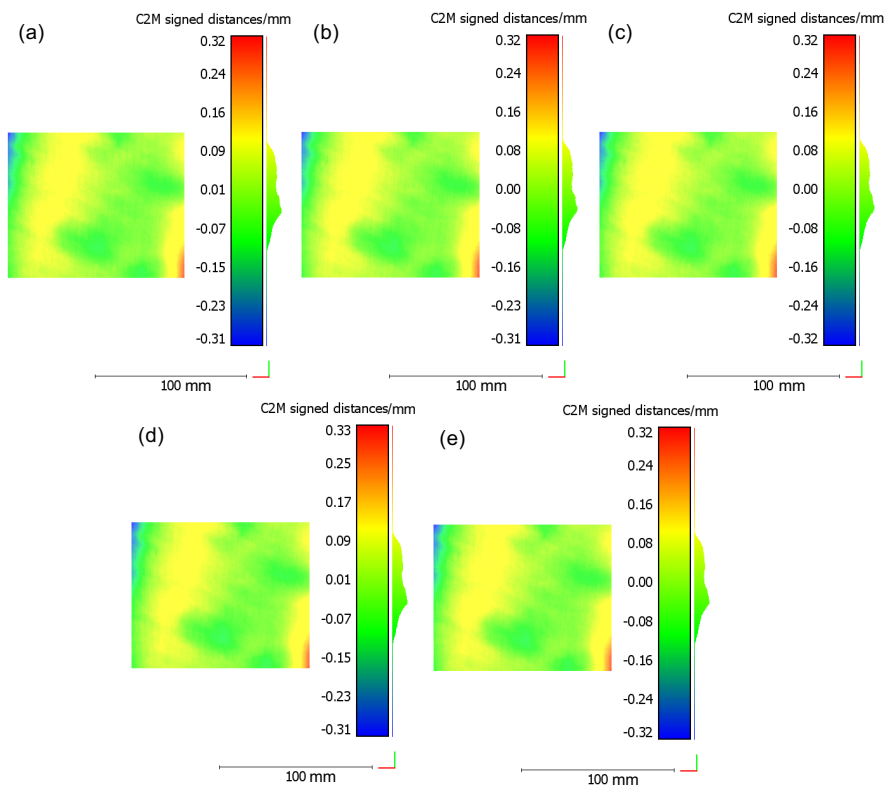


Figure 3.16: Flatness deviation of a flat surface measured by the fringe projection system. A colour map for repeat (a) measurement-1 (b) measurement-2 (c) measurement-3 (d) measurement-4 and (e) measurement-5.

create waviness or structured pattern in the acquired point clouds.

A jaw shaped plaster artefact is also measured as shown in figures 3.14 and 3.15. Figure 3.14(a) displays the image of the measured artefact with phase-stepped sinusoidally varying fringes projected onto the object and figure 3.14(b) depicts the un-

wrapped phase map. Figure 3.15(a-d) shows the different views of the acquired 3D shape. The single-views (figure 3.15(a-d)) are registered together using an iterative-closest-point (ICP) approach. The combined point cloud which is a combination of all the single-views is depicted in figure 3.15(e). There are some registration errors seen in figure 3.15(e) which are the outcome of the manual registration. This error can be reduced by introducing marker (circles or dots) detection approach, automating and optimising the point cloud registration ICP algorithm.

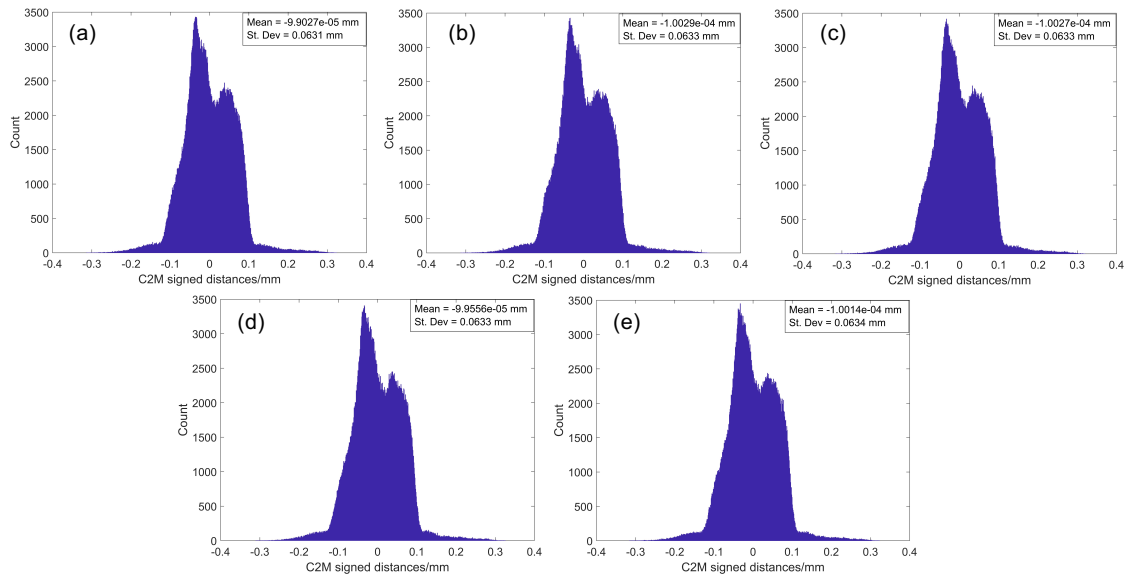


Figure 3.17: The statistical distribution of the data shown in figure 3.16. A histogram showing the signed point-to-point distance between the measured data and fitted flat plane, for repeat (a) measurement-1 (b) measurement-2 (c) measurement-3 (d) measurement-4 and (e) measurement-5.

In order to evaluate the flatness deviation, a region of interest of (119 mm \times 99 mm) is chosen and fitted with a primitive feature of a flat plane. The colour map shows the signed point-to-point distances between the measured data and the primitive feature, the measurement was repeated five times and the results are shown in figure 3.16(a-e). Figure 3.17(a-e) shows the statistical distribution for flatness deviation of the data shown in figure 3.16(a-e). The histograms depict the statistics of the signed point-to-point distance of the scanned data from the fitted primitive feature of a flat plane. The flatness deviation for a region of (119 mm \times 99 mm) is around 63 μ m and displayed in the inset of the histograms, shown in figure 3.17(a-e).

3.2 Investigation of sources of error in the single-view fringe projection system

In commercially available DFP systems, the nonlinear response of the digital video projector causes deviation of the projected input intensity from the detected output intensity (called the non-linear gamma effect). Therefore, to understand the nature of the sources of error, we compared a low-cost DLP and a laser pico projector in terms of non-linear gamma effect and DOF performance for use in fringe projection applications.

3.2.1 Principle of gamma effect and DOF

3.2.1.1 Non-linear gamma effect in fringe projection systems

Optical sources of error such as lens distortion, defocus, and the non-linear outcome of the projector's projected intensity manifest as phase measurement error in fringe projection systems [143–145]. The non-linear gamma response is not only due to the camera and projector's gamma effect but is also influenced by the object surface reflectivity and the measurement environment [132]. The projector's gamma response is given in equation (3.1).

State-of-the-art research relies on determining the non-linear response of digital fringe projection systems and compensating the phase measurement error. Numerous gamma correction and error compensation methodologies have been proposed, which can broadly be categorized as active and passive approaches. Both methods are equally reliable [145]. The active methods rely on pre-distorting the sinusoidal fringes and projecting linear grayscale intensity values [140, 145, 159, 160]. In contrast to the active method, the passive methods determine the phase error from the acquired gamma curve, and then compensate the error in the phase domain by subtracting the distorted phase from the ideal phase value [139, 144, 161].

we will use the active error compensation approach to account for the phase map error. Zhang also recommended the active method for 3D digital fringe projection sys-

tems due to the vulnerability of the passive approach to the measurement conditions [145]. We will use a convenient look-up-table to alleviate the non-linearity through active error compensation due to the ease of implementation. Moreover, the limited DOF of digital video projectors will be investigated by designing a prototype experimental setup.

3.2.1.2 Look-up-table approach

A look-up-table (LUT) approach is used to eliminate the non-linear effect being introduced by digital video projectors. The desired linear curve (to be projected) can be determined by fitting the gamma curve with least-squares curve-fitting which yields the same straight line for an inverse gamma curve, as shown in figure 3.18(a). A Matlab algorithm is developed to interpolate and relocate all the values from the non-linear gamma curve to the desired linear curve using a 1012-element LUT approach, as depicted in figure 3.18(b). Since the input intensity values in the simulated images are generated by the computer in the range of (0-255) grayscale; therefore, all values in the input grayscale image are required to be replaced by their inverse gamma values. This approach will pre-distort the input grayscale images and eliminate the non-sinusoidal behaviour, which is the active gamma correction approach.

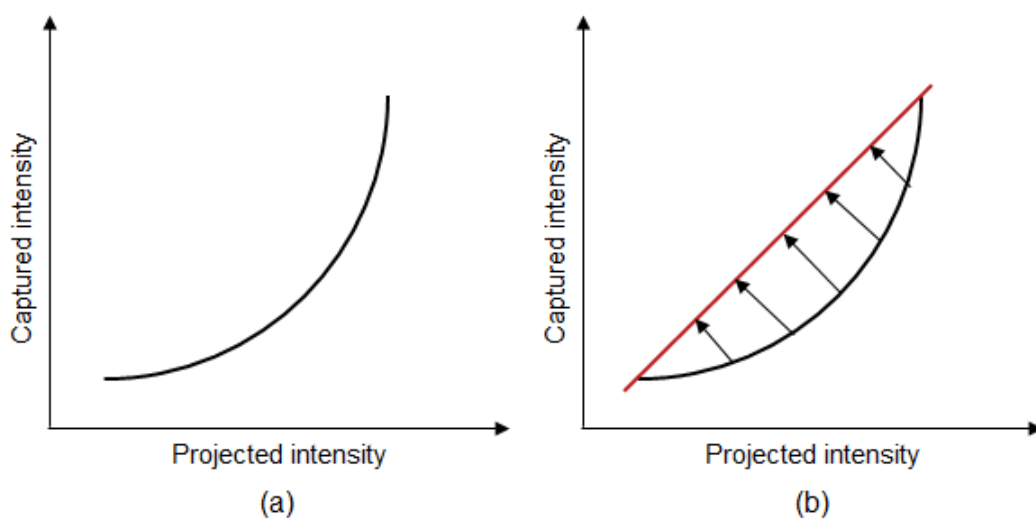


Figure 3.18: Gamma correction approach (a) Schema of the relationship between projected and captured intensity and (b) implementation of the LUT approach.

3.2.1.3 DOF

Commercially available digital video projectors are designed with a large numerical aperture to prevent the loss of light from the light source which significantly limits the DOF of the projector, and introduces blurriness in the projected image [146, 147]. The small DOF can be addressed by extending the DOF of video projectors using the liquid lens technology and modulating the focal length of the projector at a frequency higher than critical flicker fusion CFF, a method proposed by Daisuke et al. [152]. In general, the numerical aperture of a lens and the focal length are related by

$$NA = n \sin \left[\tan^{-1} \frac{D}{2f} \right] \approx \left(\frac{nD}{2f} \right), \quad (3.8)$$

Where n is the refractive index of the medium ($n = 1$ for air), D represents the diameter of the entrance pupil and f is the focal length. For pico DLP projector (ICODIS G-1 Mini projector), the focus is the manual focus and the specifications provided by the manufacturer do not include information about the NA and D of the lens, which makes it difficult to compare the DOF at various distances for the pico DLP projector. In contrast, the laser projector (LaserBeam Pro, C200) is a focus-free (class 1, eye safe laser) projector, and the projected image stays in focus for about 200 cm. Therefore, in order to compare the two projectors (laser and pico DLP) based on a similar approach, the 2D fast Fourier Transform (FFT) of the ROI of projected pattern (checkerboard) is utilised (Den et al. [163]) as a quantitative measure of the DOF.

In order to determine the DOF of digital video projectors, we have performed simulations of a checkerboard pattern and used a checkerboard sample to verify the experimental results afterwards. A number of checkerboard patterns were created in Matlab with different amount of Gaussian noise and pitch sizes (number of pixels/square). The purpose of varying the pitch number and Gaussian filter is to approximate the experimental setup in which the distance between the projector and the imaging target (screen) is varied which introduces blurriness (similar to Gaussian smoothing) and the pitch number changes slightly. Simulations for the same pitch value are also performed. The checkerboard points are detected by which the pitch value is determined and the

ROI is defined. The 2D fast Fourier transform (FFT) of the ROI, as a quantitative measure of DOF is determined, as shown in figure 3.19(b-c). We used a metric which

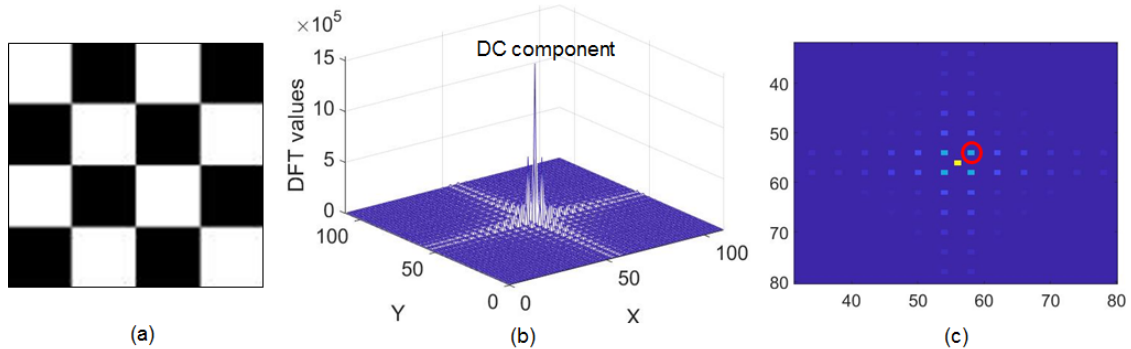


Figure 3.19: Checkerboard pattern. (a) ROI of 4×4 squares area, (b) FFT spectrum of the ROI and (c) FFT spectrum (2-D view) whereby the red circle denotes the periodicity in 45° axis.

uses the maximum of the Fourier transform in the 45° direction, loosely based on the method used by De et al. [165].

This approach is practically implemented on the experimental data where the distance between the imaging target (checkerboard pattern) and the screen is varied at about ≈ 164 cm. The distance variation adds blurriness to the imaging target similar to different Gaussian filters being applied to our simulations. The DOF is determined by finding the maximum value of one the quadrants of 2D FFT of the ROI of imaging target (checkerboard pattern).

3.2.2 Experiments on gamma correction and DOF

For the comparative study, we have used a laser (LaserBeam Pro, C-200) and a pico DLP (ICODIS G-1 Mini projector) projector. A laser projector combines three laser beams of red, green and blue (RGB) colours utilising an optical arrangement. The laser beam creates an image by scanning the area projected pixel by pixel at a fast rate (> 60 Hz). In contrast, the DLP projector uses high power LEDs as a source of illumination. An array of red, green and blue LEDs generates the light that is reflected off the tiny mirrors (digital micro-mirror device, DMD). These tiny mirrors control the brightness of each pixel value by varying the time the mirror is ON within a single frame cycle. The use of LED has also eliminated the use of the colour wheel.

Furthermore, LED projectors consume less energy, run cooler and have a long life as compared to the conventional lamp-based projectors.

3.2.2.1 Non-linear gamma correction

The gamma curve of the projector can be obtained by projecting multiple grayscale images I_{in} onto a flat whiteboard and then capturing the camera response. The experimental assembly consisting of a single projector-camera is depicted in figure 3.20. Matlab software is used to generate an image with a resolution of (600×900) pixels which is sent to the digital video projector (Laser Beam Pro (C-200), ICODIS G1 Mini projector) for projection. A Raspberry-Pi (Module-v1) camera is used to capture the images. The resolution of the projector and camera are (1280×800) pixels, (2592×1944) pixels, respectively. The pixel intensities from a specific ROI (100×100 pixels) is averaged in the captured image, from which we get the output intensity value I_{out} .

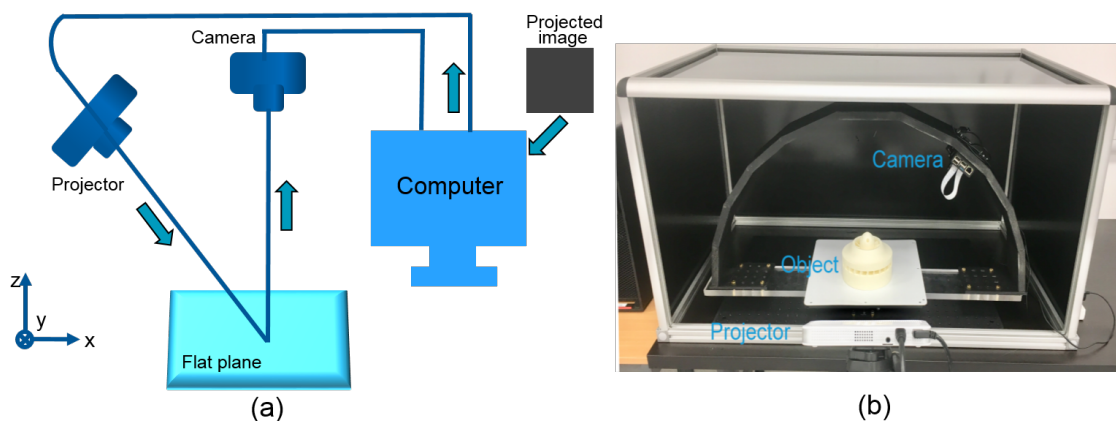


Figure 3.20: Experimental setup. (a) Schema of the setup to acquire the gamma curve and (b) a photograph of the experimental assembly.

Once the gamma curve of the video projector is acquired, then the desired linear curve (to be projected) is determined using a LUT approach. The frequency spectrum of the non-sinusoidal waveform generates higher harmonics, which interrupt the phase distribution and associated with the fundamental frequency component of the frequency spectrum [139, 142]. The Fourier spectrum is obtained by applying Fourier transform to column-1000 of the sinusoidal component of the modulated sinusoidal fringes. Since the gamma correction eliminates the higher harmonics in the frequency spectrum, therefore

it enhances the accuracy of the phase stepping fringe projection system [166, 167].

In order to verify the gamma correction methodology, the three phase-shifted patterns are projected onto a flat whiteboard and the wrapped phase map is obtained. The wrapped phase map is then unwrapped using the differential phase unwrapping algorithm and the root-mean-square values of the gamma correction results for the laser and pico DLP projectors are compared.

3.2.2.2 Experimental results: Gamma correction

The gamma curves of a laser and a pico DLP projector are shown in figure 3.21(a) and figure 3.21(b), respectively. The gamma curve predominantly shows deviation from the ideal linear behaviour. Figures 3.21(a) and 3.21(b) show that the captured intensity covers only a small range of the projected input intensity (0-255 grayscale). The active correction method relies on pre-distortion of the computer-generated fringe patterns and projection of the inverse gamma curve. To incorporate that, we used a 1012-element LUT approach to compensate for the projector's non-linearity.

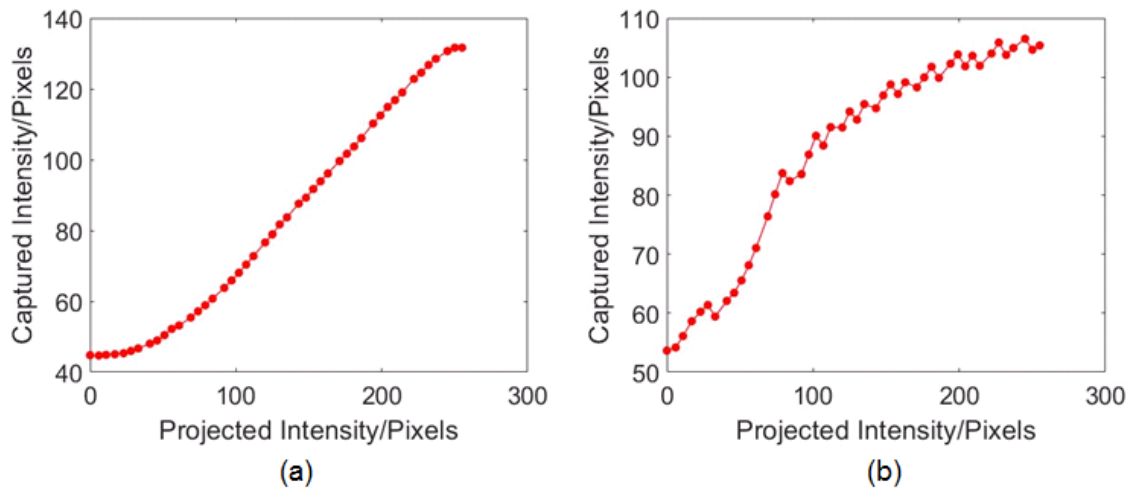


Figure 3.21: Experimental results. (a) The non-linear gamma curve of a laser projector and (b) gamma curve of a pico DLP projector.

Figure 3.22(a) represents the process of linearising the gamma curve of a laser projector. The blue curve represents the real experimental data while the red curve represents the least-square fitted curve. A LUT is used to get the desired linear (red) curve that needs to be projected. The green curve represents the projected range covered by the input grayscale sinusoidal fringe patterns, therefore it is required to

bring down all the input grayscale values (0-255) to the desired range. Likewise, we conducted experiments on a cost-effective pico DLP projector and results are shown in figure 3.22(b).

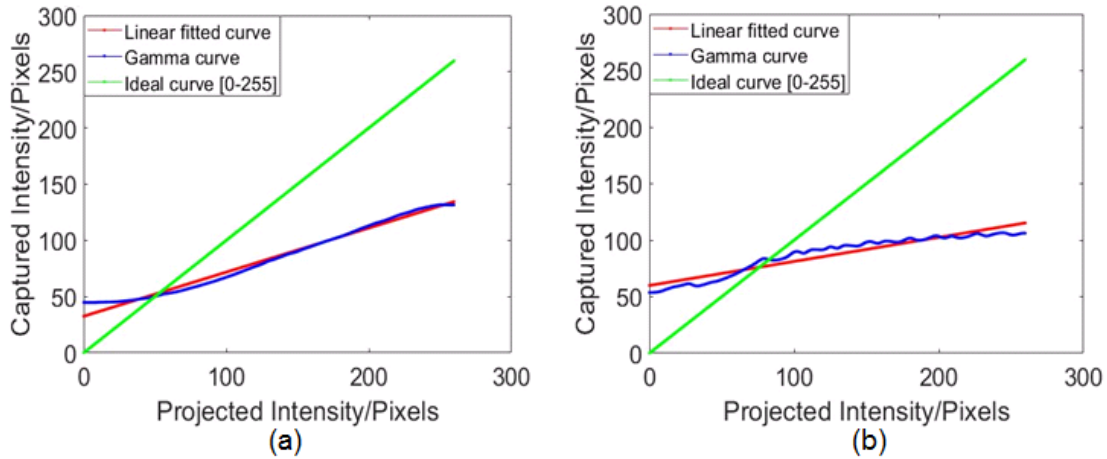


Figure 3.22: Elimination of non-linear gamma distortion by LUT approach. (a) Laser projector and (b) pico DLP projector.

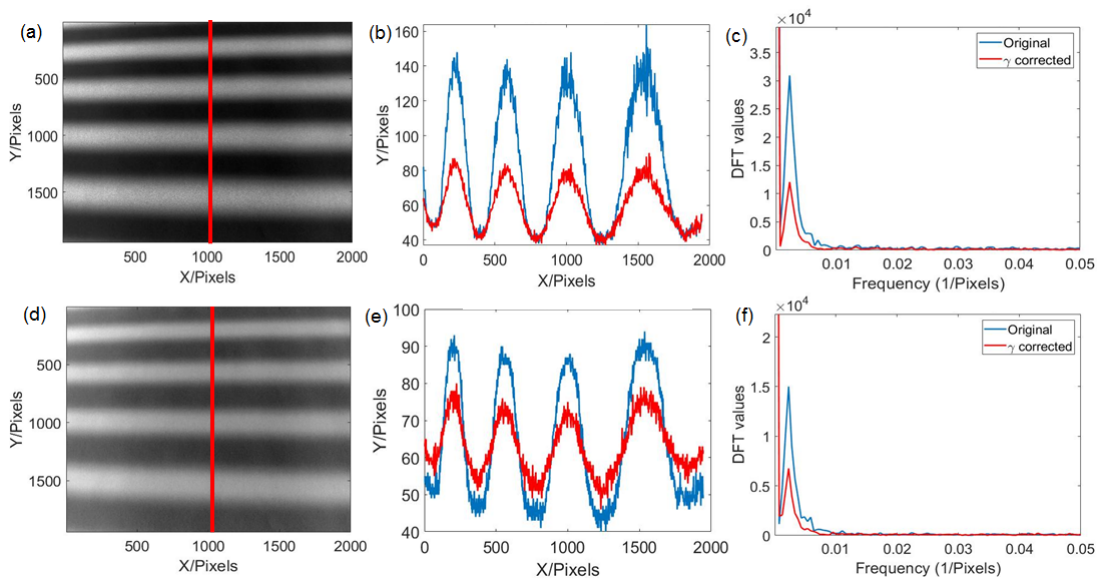


Figure 3.23: Non-linear gamma correction. (a) The original intensity image in grayscale for a laser projector (b) cross-section of column-1000 in (a); blue curve (before correction) and red curve (after correction) for a laser projector (c) the frequency spectrum of the centre of the image column-1000 in (a); blue (before correction) and red curve (after correction) (d) the original intensity image for a pico DLP projector (e) cross-section of column-1000 in (d) blue curve (without correction) and red curve (after correction) for a pico DLP projector and (f) FFT spectrum for a pico DLP projector.

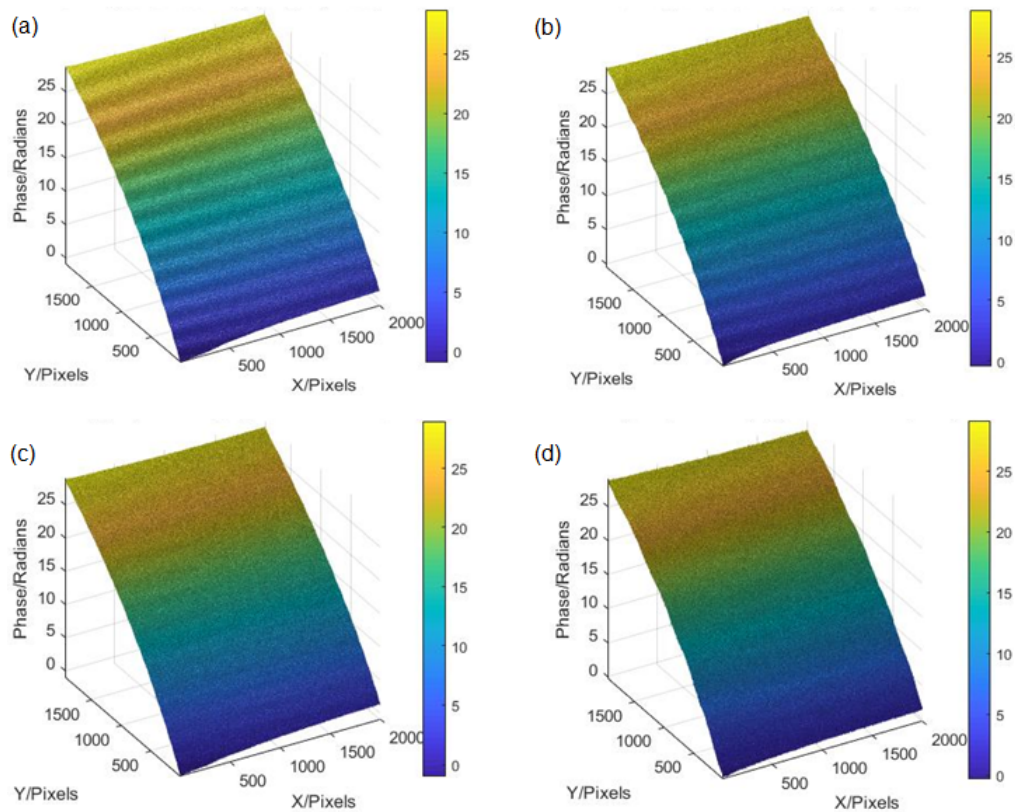


Figure 3.24: Implementation of non-linear gamma correction on laser and pico DLP projectors. (a) Original image as a surface plot (laser projector) (b) original image as a surface plot (pico DLP projector) (c) unwrapped phase image after gamma correction (laser projector) and (d) unwrapped phase image after gamma correction (pico projector).

3.2.2.3 Effect on quality of projected sinusoidal patterns

Figure 3.23(b) depicts the non-sinusoidal waveform (blue) corresponding to column-1000 of the original intensity image in figure 3.23(a). The red curve represents the desired sinusoidal wave which is achieved after gamma correction. The sinusoidal waveform that is achieved after gamma correction shows more sinusoidal behaviour than the waveform (blue curve) without gamma correction and is closer to the projected pattern. The Fourier transform of the projected and corrected sinusoidal waveforms for both projectors was determined and shown in figure 3.23. The red curve indicates the Fourier transform after gamma correction.

Figures 3.24(a-b) indicate the same results for the whole field of view on a flat plane being illuminated by a laser and a pico DLP projector before gamma correction, while figures 3.24(c-d) represent the outcome after implementing the gamma correction. It is worth noticing that the waviness for a laser projector in figure 3.24(a) has been

significantly reduced (with root mean square (RMS) of 0.087 rad) after applying the gamma correction and shown in figure 3.24(c). The gamma-corrected results for a pico DLP projector in figure 3.24 indicate a similar trend of reduction in the waviness error with an RMS of 0.19 rad. The root mean square difference error of the phase value of column-1000 before and after gamma correction for both projectors is shown in figure 3.25.

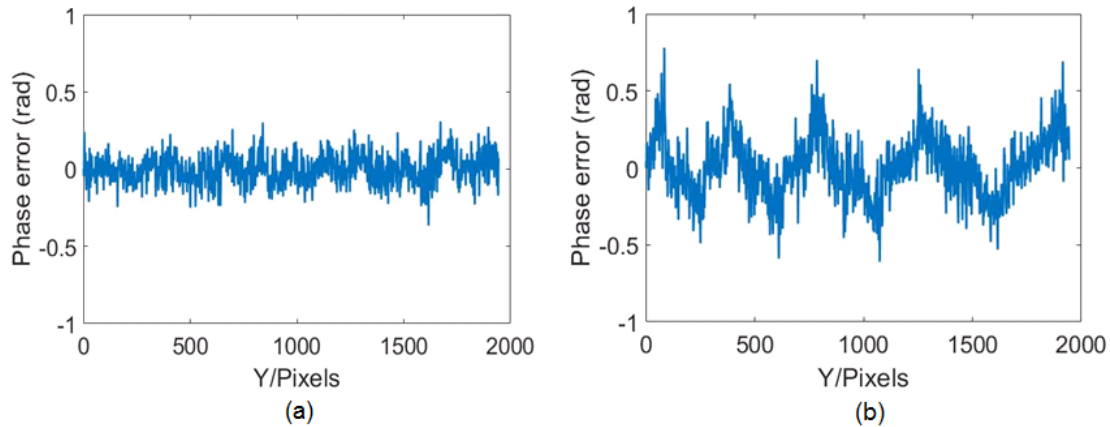


Figure 3.25: The RMS phase difference error of column-1000. (a) Laser projector (RMS= 0.087 rad) and (b) pico DLP projector (RMS= 0.19 rad).

3.2.2.4 DOF: Simulations

In order to test an effective metric to measure the DOF of the projector, we developed a Matlab algorithm to simulate the acquisition of images of a checkerboard pattern projected by the projector onto a flat plane at different distances from the projector by varying the checkerboard pitch (number of pixels/square) and the Gaussian smoothing parameter. The pitch value was varied to simulate the effect of the projected pattern which gets bigger the further away the projector is from the plane. The variation of the Gaussian smoothing parameters introduces different amounts of blurriness in the images. The Gaussian smoothing is a type of image blurring filter that utilizes the Gaussian function and determines the transformation that applies to each individual pixel in the image. The 2D Gaussian function is a product of two Gaussian functions and mathematically represented as

$$G(x, y) = \left(\frac{1}{2\pi\sigma^2} \right) \exp\left(-\frac{x^2 + y^2}{2\sigma^2} \right), \quad (3.9)$$

where x is the distance from origin to the horizontal direction, y is the distance from origin to the vertical direction, σ is the standard deviation. In our simulations, we have changed the σ value to introduce different amount of blurriness.

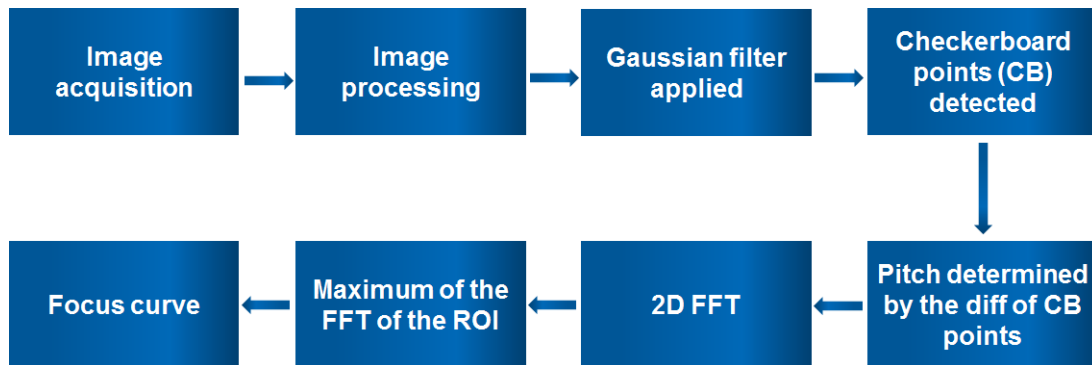


Figure 3.26: The pipeline of the DOF experiment.

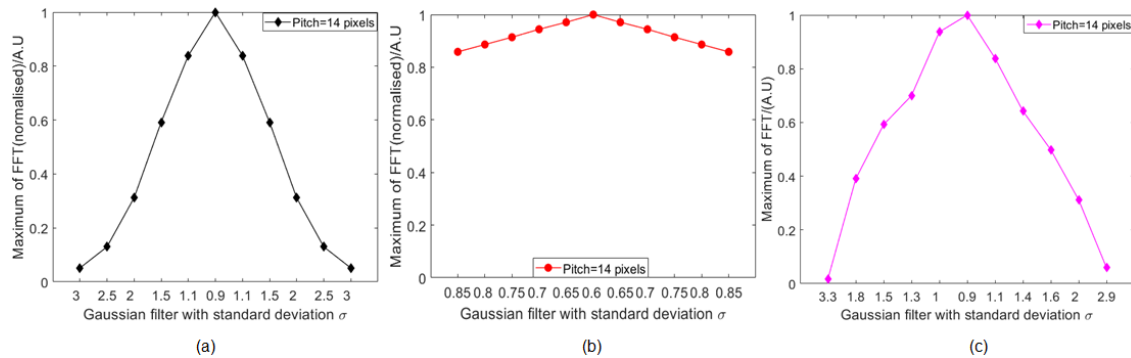


Figure 3.27: Simulated results for DOF. (a) FFT of the ROI (6×6 square) by varying the Gaussian smoothing. The pitch value (14 pixels) remains the same (b) FFT of the ROI (6×6 square) for a very small variation in the Gaussian smoothing ($\sigma = 0.6-0.85$) and (c) FFT of the ROI (6×6 square) when the Gaussian smoothing varies randomly.

The Matlab algorithm detects points on the checkerboard pattern to determine the pitch value. The pitch value is calculated by the difference between the two detected checkerboard points. Once, the pitch value is defined, a ROI is chosen for further image processing. The 2D FFT is performed on the ROI and the normalised maximum value of the Fourier transform is chosen as a quantitative measure of focus [165, 168–170]. The whole pipeline of the process is shown in figure 3.26.

Following the pipeline in figure 3.26, the acquired results are depicted in figure 3.27. Figure 3.27 illustrates the simulated results for the DOF. Eleven different pitch values are used and the different amount of Gaussian filters are introduced. It is obvious that for the same pitch value, the maximum of the FFT follows a Gaussian-like distribution

with the focused image at the centre, whilst, the varying pitch value affects the shape of the Gaussian distribution.

3.2.2.5 DOF: Experiments

The experimental assembly designed to compare the DOF of a cost-effective laser (LaserBeam Pro, C-200) and a pico DLP (ICODIS G-1 Mini projector) projector and it consists of a dolly stand (Hague MCD Micro Camera Dolly), a rail, a projector and a DSLR camera, as depicted in figure 3.28.

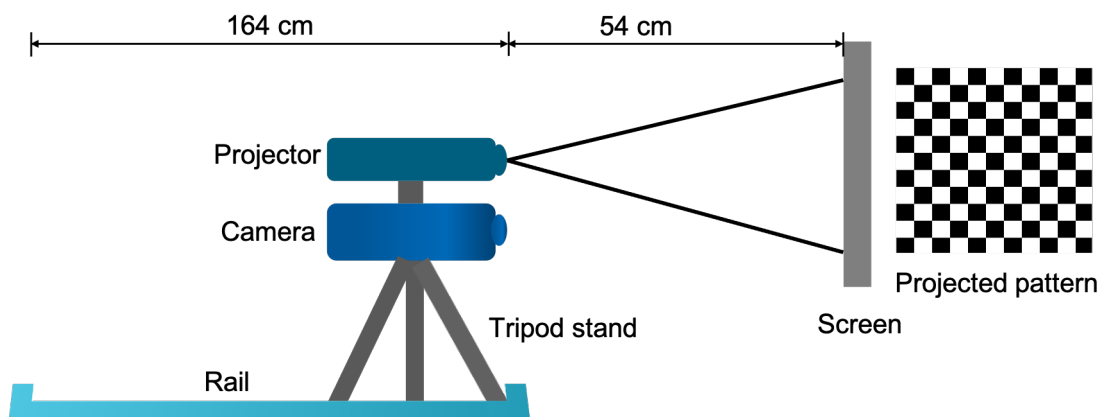


Figure 3.28: Schematic illustration of the DOF setup.

The projector is mounted on top of the camera which is placed on a dolly tripod stand. The projector-camera assembly is then translated on a rail. The wall is used as an imaging target and a checkerboard pattern is projected onto the wall. In total, twelve images were captured by varying the distance (54 cm to 164 cm) between the screen (wall) and the projector-camera assembly [152].

The laser projector is eye-safe class-1 which is harmless to the human eye. It is focus-free, consumes less power, small-sized, has higher projection and contrast ratios (1.3921 : 1, 2000 : 1) as compared to DLP projector (1.19 : 1, 1000 : 1). Figure 3.29(a) shows the results of measuring the focus at 12 distances between a projector (laser/pico DLP) and the screen (wall). The focus value is determined by finding the normalised maximum value of the FFT in the 45° direction. The pico DLP projector has a significant variation between focused and the defocused images, whilst the laser projector's focus remains more stable for the whole distance range measured (200 cm), as shown in figures 3.29(a) and 3.29(b-e).

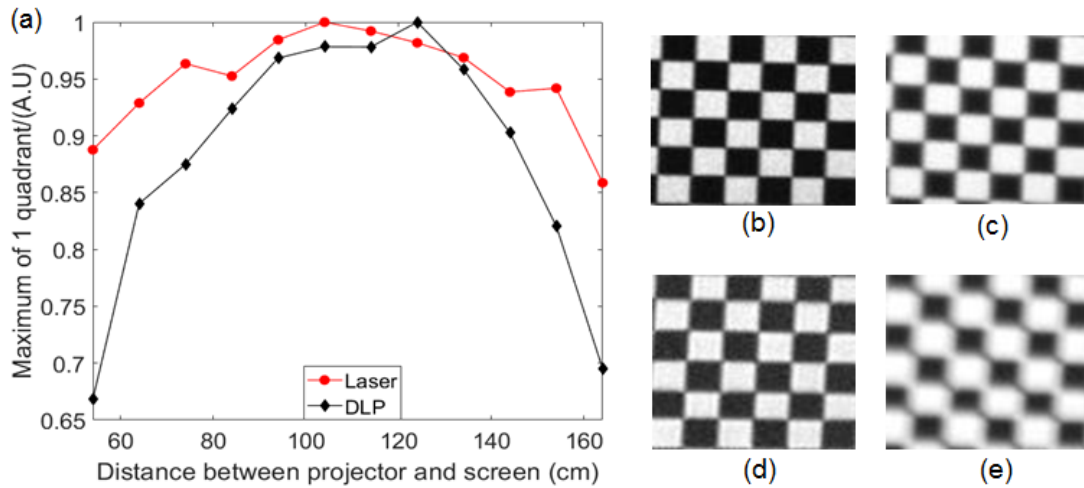


Figure 3.29: DOF results. (a) Comparison of DOF of the pico DLP and laser projectors (b) laser projector's focused image (c) laser projector's defocused image and (d) pico DLP projector's focused image, and (e) pico DLP projector's defocused image.

The deviation of the experimentally acquired results from the simulated results (Gaussian-like distribution in figure 3.27(a) corresponds to the randomly varying Gaussian smoothing as shown in figure 3.27(c). The random variation of Gaussian smoothing is related to the uncertainty in the distance measurement while moving the projector-camera assembly towards the wall, also affected by the camera/projector optics and the ambient conditions. Since the projector is mounted on top of the camera and the whole assembly is translated together, therefore, the pitch number of the projected checkerboard pattern remains the same (pitch = 14 pixels). However, the Gaussian smoothing depends on the DOF of the projector which varies by changing the distance between the projector and the screen (wall).

3.3 Conclusions

The first part of the chapter (section 3.1) presents the development of a single-view fringe projection system using a camera and a projector. All components (optical, electronic, mechanical) are assembled and the system is implemented through a number of steps, mainly by performing the gamma correction, system characterisation and 3D shape measurement of complex geometries of different materials. The second part (section 3.2) takes into account the sources of error in the fringe projection system

by comparing the commercially available cost-effective laser and pico DLP projectors. The comparison is made in terms of the non-linear gamma effect and the DOF.

Experimental results have demonstrated that for the laser projector, the gamma curve is much closer to the linear equation and requires less gamma correction, therefore, it would be more suitable for less critical fringe projection applications where it is impractical to apply the gamma correction. Regarding the DOF, the laser projector outperforms the pico DLP projector as the projected pattern remains in focus for a large distance (≈ 164 cm), also it maximises the signal to noise ratio in the whole measurement volume (for medium to large objects, ≈ 200 cm long) of the fringe projection system.

Chapter 4

Uncertainty evaluation of the form measurement of additively manufactured parts

4.1 Outline

3D shape measurement of complex AM parts has been extensively used in the industrial sector. In general, the inspection process is applied for quality assurance in industrial manufacturing. Before manufacturing, the part is subjected to verification for geometric dimensions and tolerance (GD&T) specifications regarding the design requirements. For this purpose, trustworthy measurement methods with justified uncertainty estimates are essential. The Guide to the Expression of Uncertainty in Measurement (GUM) provides generic rules for establishing and expressing the uncertainty in the measurement [171], ranging from quality control, quality assurance, research and development, science and technology, calibration standards, and the performance verification tests to accomplish traceability according to national standards.

Measurement alone is considered incomplete; therefore, a correspondence between the model and the measurement is essential for the evaluation of measurement uncertainty. Distinctive measurement uncertainty is associated with each individual measurement depending on the measurement environment and practices in the laboratory.

This chapter presents the methodology for the uncertainty evaluation of different features of an industrial test case and a complex shaped artefact (utilised in chapter 5), which are measured by the fringe projection method. An uncertainty budget in accordance with the GUM is specified for the measured features of the AM artefacts. The method incorporates the contribution from different factors which affect the measurement and determines a measurement uncertainty associated with each particular measurement.

4.2 AM artefacts

4.2.1 Mould insert

A mould insert used for the injection moulding of the ABS parts is shown in figure 4.1. The mould insert is supplied by a manufacturer of consumer goods and has been used for the uncertainty evaluation of optical form measurements. The insert has been manufactured by laser powder bed fusion (LPBF) method with maraging steel grade 300 material. The design has been optimised by introducing the conformal cooling channel flowing underneath the mould cavities. The mounting holes and centring holes are the primary features that are designed for the insert with the mould box; therefore, regarded as pivotal features from the perspective of optimisation [1].

The mould insert is designed to minimise the mass of the injection mould and acquiring sufficient thermal transfer simultaneously. The following parameters are considered while formulating the design problem;

- Material: Maraging steel grade 300
- Surface texture inside the cooling channel: as built (as low as possible)
- Injection pressure: 62 MPa to 76 MPa
- Holding pressure: 10 MPa
- Water pressure: 0.3 MPa to 0.6 MPa
- Clamping force: 393 kN

- Cooling medium: Water

Figure 4.1 shows the injection mould part manufactured with maraging steel (grade 300). The dimensions of the sample are 107.50 mm \times 109.99 mm \times 27.60 mm (length \times width \times height). The channels present at the top surface help facilitate the flow of liquid polymer to the moulded elements. There are cooling channels with one inlet and one outlet. Moreover, the design has multiple holes for the ejector pin movement.

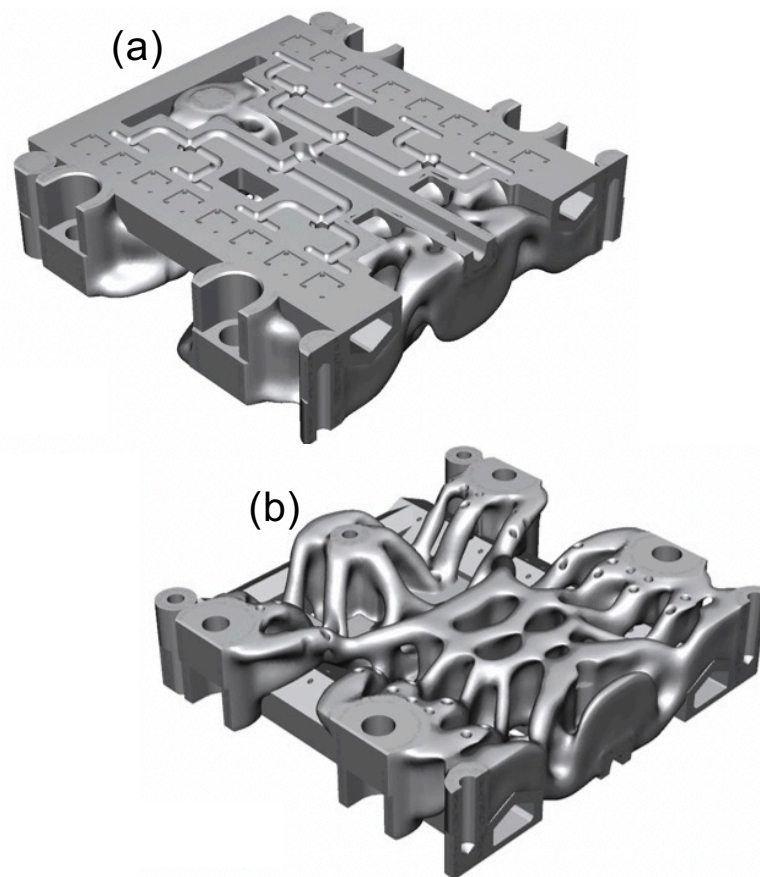


Figure 4.1: Topology optimised mould insert [1]. (a) Top view and (b) bottom view.

4.2.2 Complex shaped artefact

Figure 4.2 shows a complex shaped object (110 mm \times 110 mm \times 50 mm). The artefact is manufactured using the selective laser sintering method with Nylon-12. Various features of interest, such as a hemisphere, spheres, ball bar, and inclination of wedges are chosen for the uncertainty evaluation of optical form measurements.

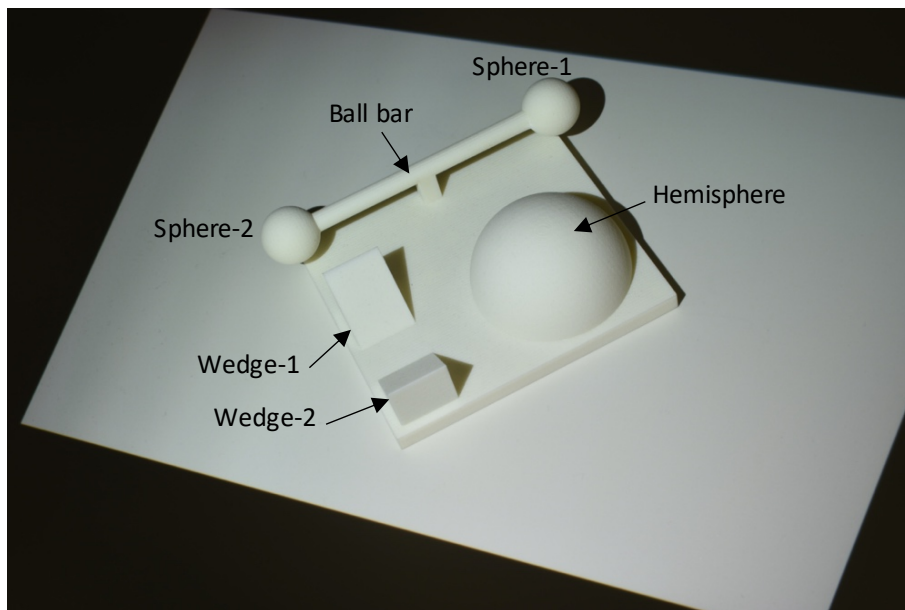


Figure 4.2: Photograph of the complex artefact with labelled features measured by CMM.

4.3 Measurements

The post-process characterisation of different features of an industrial test case and a complex shaped artefact has been performed using contact (CMM) and non-contact (fringe projection) measurement instruments.

4.3.1 Non-contact measurement: Fringe projection

A fringe projection system (GOM ATOS Core 300 [172]) is used for the 3D shape measurement of the AM artefacts. The artefacts are measured in the ambient conditions and each measurement is repeated five times.

4.3.1.1 Methodology for fringe projection

Different features (feature-1, two cooling channels and two supports for the cooling channels shown in figure 4.3) for the industrial test case and features (spheres, sphere-to-sphere spacing, hemisphere and inclined wedge) for the complex shaped artefact are selected. The primitive features (plane, angle between two planes, plane-to-plane distance and cylinder) are fitted in Polyworks [173].

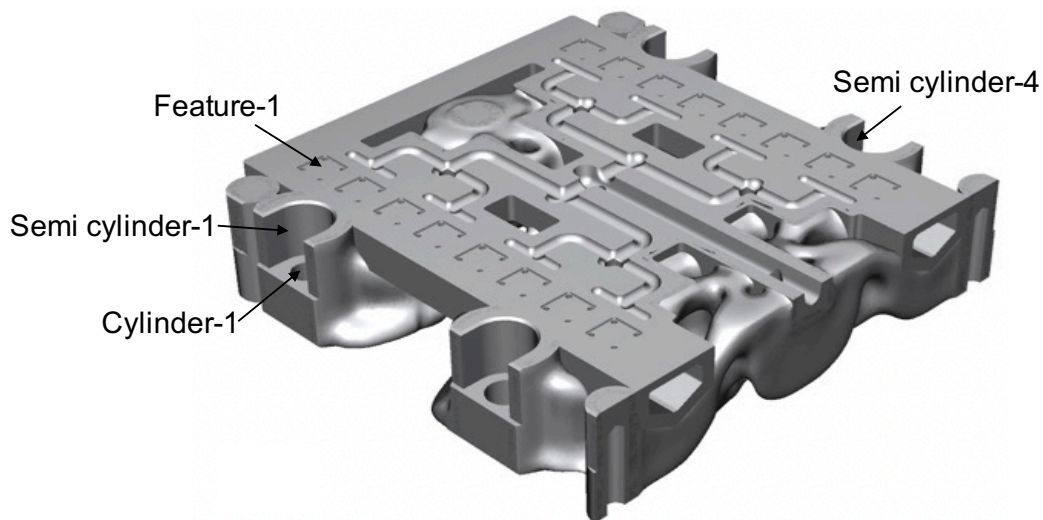


Figure 4.3: Features of interest of the mould insert [1] given in figure 4.1.

4.3.1.2 Uncertainty budget

The GUM explains the method of evaluating the uncertainty in the measurement which is associated with the variance of each component that could possibly contribute to the measurand [171]. Determination of such a variance by statistical methods is categorised as Type-A evaluation, while assessment by any other means is called the Type-B evaluation. Both of these evaluations reside on probability distributions, and the uncertainty contributions acquired from either type are computed from variances or standard deviations.

The uncertainty evaluation comprises many components and, it is performed as follows,

Type-A evaluation: Type-A evaluation is a method of calculating the uncertainty by the statistical evaluation of a sequence of several measurements [174, 175]. For the N number of measurements, the standard uncertainty is calculated as

$$u_m = \frac{s}{\sqrt{N}}, \quad (4.1)$$

where u_m is the standard uncertainty in the mean value of repeat measurements, and s is the standard deviation. For the injection mould, we have scanned the artefact five times and all features of interest have five repeats.

Type-B evaluation: The type-B evaluation incorporates the method of uncer-

tainty evaluation aside from the statistical methods. This includes uncertainty related to the calibration of a physical reference, uncertainty in a physical constant, and the uncertainties in the equations which establish certain quantities [174, 175].

The GOM system (ATOS Core 300 [172]) uses the following parameters for (300 × 230) mm field of view;

- Probing form error (sigma) 0.006 mm
- Probing size error 0.027 mm
- Sphere spacing error 0.020 mm
- Length measurement error 0.047 mm

The u_{MPE} is the type-B uncertainty which is calculated using the maximum permissible error (MPE) value of 0.027 mm (since the probing form error 0.006 mm is 3 times higher than the value provided by GOM system, therefore we will consider the probing size error) as follows

$$u_{\text{MPE}} = \frac{\text{MPE}}{\sqrt{3}}. \quad (4.2)$$

Uncertainty associated with fitting of features: The fitting features include plane-to-plane distance, fitting of a cylinder and angle measurement between two planes. For plane-plane distance, the sphere spacing error is also incorporated.

- Cylinder: probing size error, 0.027 mm (with a rectangular distribution)
- Plane-to-plane distance: probing size error, 0.027 mm (with a rectangular distribution)
- Plane-to-plane distance: sphere spacing error, 0.020 mm (with a rectangular distribution)

Since the angle is measured between two planes, and considering the centre point of the two planes [176], the angle between two points is calculated as

$$\cos \alpha = \frac{(x_2 - x_1)}{\sqrt{(x_2 - x_1)^2 + (y_2 - y_1)^2 + (z_2 - z_1)^2}}, \quad (4.3)$$

$$\cos \beta = \frac{(y_2 - y_1)}{\sqrt{(x_2 - x_1)^2 + (y_2 - y_1)^2 + (z_2 - z_1)^2}}, \quad (4.4)$$

$$\cos \gamma = \frac{(z_2 - z_1)}{\sqrt{(x_2 - x_1)^2 + (y_2 - y_1)^2 + (z_2 - z_1)^2}}, \quad (4.5)$$

where α , β and γ correspond to the angle between the centre point of the two planes along the x , y and z directions, respectively. The uncertainty in the angle measurement is found by determining the sensitivity coefficient [176] which is defined by

$$\frac{d(\cos \alpha)}{dx}, \quad \frac{d(\cos \alpha)}{dy}, \quad \frac{d(\cos \alpha)}{dz}. \quad (4.6)$$

Uncertainty associated with temperature fluctuations: The length of the object depends on temperature. In general, when an object is heated or cooled, the length varies by an amount which is proportional to the original length of the object and the temperature variation, and given by

$$\Delta L = \alpha L \Delta T, \quad (4.7)$$

where L is the original length, ΔT is the temperature variation, α is the coefficient of linear expansion, which depends on the material. For maraging steel, the coefficient of linear expansion is $10.3 \times 10^{-6} \text{ K}^{-1}$, whilst for Nylon-12 is $100 \times 10^{-6} \text{ K}^{-1}$. The ambient temperature in the lab was $(19.5 \pm 0.5)^\circ\text{C}$; and we assume the temperature fluctuation in the surroundings is $\Delta T = 1^\circ\text{C}$; therefore, the uncertainty (with a rectangular distribution) associated with the length change can be expressed as

$$u_{(\Delta L)} = \alpha L \Delta T. \quad (4.8)$$

The uncertainty in the length measurement with temperature fluctuation is incorporated when the distance between the two planes is measured and provided in table 4.1-4.4.

Effective degrees of freedom: The Welch-Satterthwaite expression determines

the effective degrees of freedom for a linear combination of the independent measurand variances [175, 177]. It verifies if the expanded uncertainty with the coverage factor ($k = 2$) truly lies within 95% confidence interval or a larger value is required. In general, when type-A and type-B uncertainties are evaluated, one constraint in combining these uncertainties is how to determine the degrees of freedom, which is calculated from the Welch-Satterthwaite formula.

For type-A evaluation, the standard uncertainty in the mean value is evaluated by equation 4.1, and the associated number of degrees of freedom are ($v = N - 1$). In practice, for type-B uncertainties, the degrees of freedom are provided by the scientific instrument, and for practical purposes, they are considered as an infinite number of degrees of freedom. The mathematical expression for Welch-Satterthwaite [175, 177] is given by

$$v_{\text{eff}} = \frac{u^4(y)}{\sum_{i=1}^N \frac{u_i^4(y)}{v_i}}, \quad (4.9)$$

where u is associated with type-B evaluation, u_i is the standard deviation in the i th value and depicts the uncertainty associated with type-A evaluation, $v_i = N_i - 1$ is the degrees of freedom of type-A evaluation.

Combined uncertainty: The uncertainty mentioned in table 4.1-4.4 is the combined uncertainty, which is calculated by taking the quadrature sum of the uncertainty due to measurement repetitions (type-A evaluation, equation 4.1), type-B evaluation which is probing size error, equation 4.2), uncertainty related to the fitting features provided in equations 4.3-4.5, 4.6, and the uncertainty due to temperature fluctuations, given in equation 4.7. The uncertainty equations for the features of interest would be;

- Cylinder: Quadrature sum of the uncertainty of repeat measurements and probing size error
- Plane-to-plane distance: Quadrature sum of the uncertainty of repeat measurements, probing size error and sphere spacing error

The combined uncertainty for fringe projection is calculated by using the following

expression [16, 178]

$$u_{\text{comb}} = \sqrt{u_{\text{Meas}}^2 + u_{\text{MPE}}^2 + u_{\text{Fitting}}^2 + u_{\alpha}^2}, \quad (4.10)$$

where u_{Meas} is the uncertainty in the measurement repetitions, u_{MPE} is the maximum permissible error of the fringe projection instrument (we will take the probing size error of 0.027 mm), u_{Fitting} is the uncertainty related to the fitting of features and u_{α} is the uncertainty associated with the temperature fluctuations in the length measurement.

Expanded uncertainty: The expanded uncertainty is computed by multiplying the combined uncertainty by a coverage factor, and given by

$$U = k \times u_{\text{comb}}, \quad (4.11)$$

where U is the expanded uncertainty, k is the coverage factor and u_{comb} is the combined uncertainty (given in equation 4.10). The aim of expanded uncertainty is to provide an interval within which the outcome of a measurement lies, and that is expected to comprise a large proportion of the allocation of values that can possibly be attributed to the measurand.

Normalised error: The normalised error compares the measurement result along with the uncertainty (within 95% coverage interval) to the reference measurement along with the uncertainty (within 95% coverage interval) and determines the correlation between the two measurements. Mathematically, the normalised error E_N can be described as

$$E_N = \frac{X_{\text{meas}} - X_{\text{ref}}}{\sqrt{u_{\text{meas}}^2 + u_{\text{ref}}^2}}, \quad (4.12)$$

where X_{meas} is the measurement result, X_{ref} is the reference measurement result, u_{meas} is the expanded uncertainty of the measurement result and u_{ref} is the expanded uncertainty of the reference measurement result.

The comparison to the CAD model and the colourmap for one of the fringe projection data is shown in figure 4.4. CloudCompare is used to analyse the measured

Table 4.1: Features at the front side (top face). FP = Fringe projection, Prob = Probability, dist = distribution, Rect = Rectangular, Norm = Normal, Div = Divisor.

FP mean	Source	Value	Prob dist	Div	Standard uncertainty $u \pm$ units	dof	u_{comb}	Expanded uncertainty $U(k = 2)$
Feature-1 length 4.844 mm	u_{Meas}	0.0106	Norm	1	0.0106 mm	4		
	u_{MPE}	0.027	Rect	$\sqrt{3}$	0.0156 mm	∞	0.022 mm	0.044 mm
	u_{Fitting}	0.020	Rect	$\sqrt{3}$	0.0115 mm	∞	(Normal)	(Normal)
	u_{α}	4.966 $\times 10^{-5}$	Rect	$\sqrt{3}$	2.885 $\times 10^{-5}$ mm	∞		
Feature-1 width 4.794 mm	u_{Meas}	0.0083	Norm	1	0.0083 mm	4		
	u_{MPE}	0.027	Rect	$\sqrt{3}$	0.0156 mm	∞	0.021 mm	0.042 mm
	u_{Fitting}	0.020	Rect	$\sqrt{3}$	0.0115 mm	∞	(Normal)	(Normal)
	u_{α}	4.938 $\times 10^{-5}$	Rect	$\sqrt{3}$	2.851 $\times 10^{-5}$ mm	∞		
Feature-1 angle 151.074°	u_{Meas}	0.3948	Norm	1	0.3948°	4		
	u_{MPE} (u_{sens})	0.027	Rect	$\sqrt{3}$	0.0156	∞	0.395° (Normal)	0.790° (Normal)
	u_{α}	0.151° /mm)				∞		
Diameter cylinder-1 6.627 mm	u_{Meas}	0.0027	Norm	1	0.0027 mm	4		
	u_{MPE}	0.027	Rect	$\sqrt{3}$	0.0156 mm	∞	0.022 mm	0.044 mm
	u_{Fitting}	0.027	Rect	$\sqrt{3}$	0.0156 mm	∞	(Normal)	(Normal)
	u_{α}	6.798 $\times 10^{-5}$	Rect	$\sqrt{3}$	3.925 $\times 10^{-5}$ mm	∞		
Diameter cylinder-4 7.637 mm	u_{Meas}	0.001	Norm	1	0.001 mm	4		
	u_{MPE}	0.027	Rect	$\sqrt{3}$	0.0156 mm	∞	0.022 mm	0.044 mm
	u_{Fitting}	0.027	Rect	$\sqrt{3}$	0.0156 mm	∞	(Normal)	(Normal)
	u_{α}	7.828 $\times 10^{-5}$	Rect	$\sqrt{3}$	4.519 $\times 10^{-5}$ mm	∞		
Diameter semi cylinder-1 12.02 mm	u_{Meas}	0.009	Norm	1	0.009 mm	4		
	u_{MPE}	0.027	Rect	$\sqrt{3}$	0.0156 mm	∞	0.024 mm	0.048 mm
	u_{Fitting}	0.027	Rect	$\sqrt{3}$	0.0156 mm	∞	(Normal)	(Normal)
	u_{α}	12.36 $\times 10^{-5}$	Rect	$\sqrt{3}$	7.136 $\times 10^{-5}$ mm	∞		
Diameter semi cylinder-4 12.02 mm	u_{Meas}	0.005	Norm	1	0.005 mm	4		
	u_{MPE}	0.027	Rect	$\sqrt{3}$	0.0156 mm	∞	0.023 mm	0.046 mm
	u_{Fitting}	0.027	Rect	$\sqrt{3}$	0.0156 mm	∞	(Normal)	(Normal)
	u_{α}	12.3 $\times 10^{-5}$	Rect	$\sqrt{3}$	7.136 $\times 10^{-5}$ mm	∞		

data of the bottom face of the injection mould artefact (depicted in figure 4.1(b)) with reference to the CAD model [173]. The colourmap in figure 4.4 (a) corresponds to the signed point-to-point distance between the CAD model and the scanned data. Figure 4.4 (b) shows the statistical distribution with the mean and standard deviation of

Table 4.2: Features at the rear side (bottom face). FP = Fringe projection, Prob = Probability, dist = distribution, Rect = Rectangular, Norm = Normal, Div = Divisor.

FP mean /mm	Source	Value	Prob dist	Div	Standard uncertainty $u \pm$ units	dof	u_{comb}	Expanded uncertainty $U(k = 2)$
Diameter cylinder-1	u_{Meas}	0.0014	Norm	1	0.0014 mm	4		
	u_{MPE}	0.027	Rect	$\sqrt{3}$	0.0156 mm	∞	0.022 mm	0.044 mm
	u_{Fitting}	0.027	Rect	$\sqrt{3}$	0.0156 mm	∞	(Normal)	(Normal)
6.627	u_{α}	6.79×10^{-5}	Rect	$\sqrt{3}$	3.925×10^{-5} mm	∞		
Diameter cylinder-4	u_{Meas}	0.005	Norm	1	0.005 mm	4		
	u_{MPE}	0.027	Rect	$\sqrt{3}$	0.0156 mm	∞	0.022 mm	0.044 mm
	u_{Fitting}	0.027	Rect	$\sqrt{3}$	0.0156 mm	∞	(Normal)	(Normal)
7.613	u_{α}	7.82×10^{-5}	Rect	$\sqrt{3}$	4.519×10^{-5} mm	∞		

Table 4.3: Dimensions of the sample. FP = Fringe projection, Prob = Probability, dist = distribution, Rect = Rectangular, Norm = Normal, Div = Divisor.

FP mean /mm	Source	Value	Prob dist	Div -sor	Standard uncertainty $u \pm$ units	dof	u_{comb}	Expanded uncertainty $U(k = 2)$
Length	u_{Meas}	0.0107	Norm	1	0.0107 mm	4		
	u_{MPE}	0.027	Rect	$\sqrt{3}$	0.0156 mm	∞	0.022 mm	0.044 mm
	u_{Fitting}	0.020	Rect	$\sqrt{3}$	0.0115 mm	∞	(Normal)	(Normal)
107.85	u_{α}	0.0011	Rect	$\sqrt{3}$	6.351×10^{-4} mm	∞		
Width	u_{Meas}	0.0043	Norm	1	0.0043 mm	4		
	u_{MPE}	0.027	Rect	$\sqrt{3}$	0.0156 mm	∞	0.020 mm	0.040 mm
	u_{Fitting}	0.027	Rect	$\sqrt{3}$	0.0156 mm	∞	(Normal)	(Normal)
109.99	u_{α}	0.0011	Rect	$\sqrt{3}$	4.519×10^{-4} mm	∞		
Height	u_{Meas}	0.048	Norm	1	0.048 mm	4		
	u_{MPE}	0.027	Rect	$\sqrt{3}$	0.0156 mm	∞	0.052 mm	0.104 mm
	u_{Fitting}	0.027	Rect	$\sqrt{3}$	0.0156 mm	∞	(Normal)	(Normal)
27.615	u_{α}	2.844×10^{-4}	Rect	$\sqrt{3}$	1.642×10^{-4} mm	∞		

-0.11 mm and 0.15 mm, respectively.

Figure 4.5 shows the comparison of the CAD model to the scanned fringe projection data using CloudCompare [173]. Figure 4.5 (a) corresponds to the signed point-to-point distance between the CAD model and the scanned fringe projection data, whilst figure 4.5 (b) depicts the statistics with the mean and standard deviation of 0.02 mm and 0.09 mm, respectively.

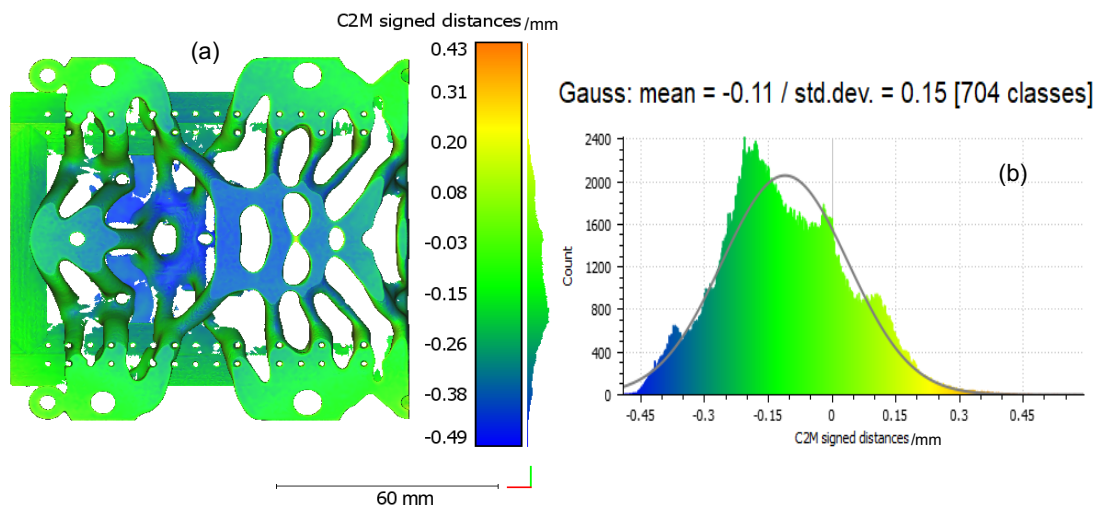


Figure 4.4: A comparison between the fringe projection data of the injection mould and the CAD model. The bottom face of the injection mould (shown in figure 4.1(b)) is chosen to perform the analysis.

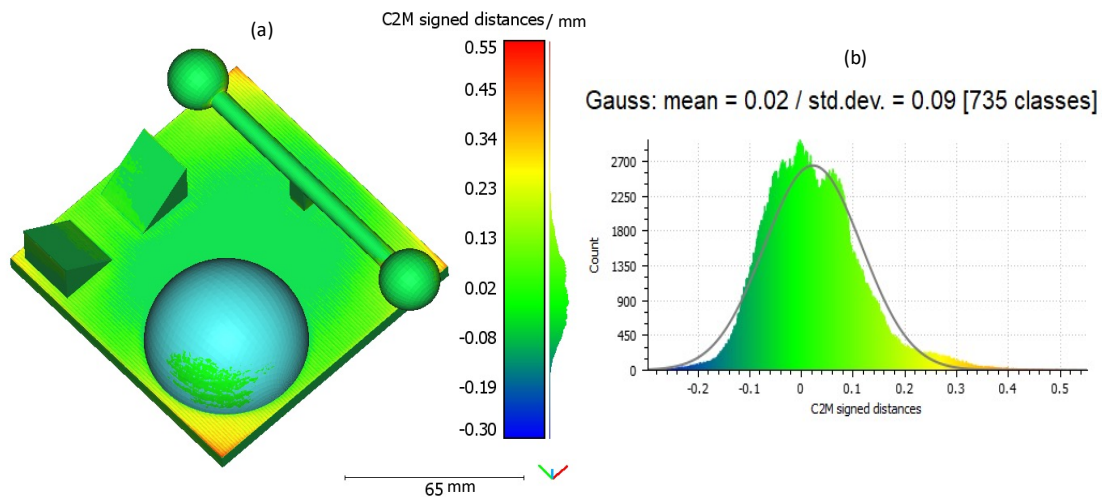


Figure 4.5: Comparison of the fringe projection data of the complex artefact and the CAD model. (a) The difference map and (b) a histogram representing the statistical distribution.

4.3.2 Contact measurement: CMM

A CMM has been used for the dimensional characterisation of the injection mould and the complex shaped artefact, following the National Physical Laboratory (NPL)'s Measurement Good Practice Guide Number 41 on CMM measurement strategies [179].

- Top face of the injection mould was measured which has different complex features (features at an angle, inlet channels for the liquid polymer flow, cooling channels, and multiple holes), whilst for the complex shaped artefact, the features of interest (spheres, sphere spacing between two spheres, hemisphere and

Table 4.4: Complex shaped artefact. FP = Fringe projection, Prob = Probability, dist = distribution, Rect = Rectangular, Norm = Normal, Div = Divisor.

FP mean	Source	Value	Prob dist	Div	Standard uncertainty $u \pm$ units	dof	u_{comb}	Expanded uncertainty $U(k=2)$
Sphere 1 diameter 22.530 mm	u_{Meas}	0.012	Norm	1	0.012 mm	4		
	u_{MPE}	0.027	Rect	$\sqrt{3}$	0.0156 mm	∞	0.025 mm	0.050 mm
	u_{Fitting}	0.027	Rect	$\sqrt{3}$	0.0156 mm	∞	(Normal)	(Normal)
	u_{α}	2.3×10^{-3}	Rect	$\sqrt{3}$	1.3×10^{-3} mm	∞		
Sphere 2 diameter 22.369 mm	u_{Meas}	0.005	Norm	1	0.005 mm	4		
	u_{MPE}	0.027	Rect	$\sqrt{3}$	0.0156 mm	∞	0.023 mm	0.046 mm
	u_{Fitting}	0.027	Rect	$\sqrt{3}$	0.0156 mm	∞	(Normal)	(Normal)
	u_{α}	2.2×10^{-3}	Rect	$\sqrt{3}$	1.3×10^{-3} mm	∞		
Sphere 1 -sphere 2 centre distance 112.467 mm	u_{Meas}	0.005	Norm	1	0.005 mm	4		
	u_{MPE}	0.027	Rect	$\sqrt{3}$	0.0156 mm	∞	0.021 mm	0.042 mm
	u_{Fitting}	0.020	Rect	$\sqrt{3}$	0.0115 mm	∞	(Normal)	(Normal)
	u_{α}	11.2×10^{-3}	Rect	$\sqrt{3}$	6.5×10^{-3} mm	∞		
Hemisphere diameter 59.943 mm	u_{Meas}	0.003	Norm	1	0.003 mm	4		
	u_{MPE}	0.027	Rect	$\sqrt{3}$	0.0156 mm	∞	0.023 mm	0.046 mm
	u_{Fitting}	0.027	Rect	$\sqrt{3}$	0.0156 mm	∞	(Normal)	(Normal)
	u_{α}	6.0×10^{-3}	Rect	$\sqrt{3}$	3.5×10^{-3} mm	∞		
Wedge 1 inclination 44.986°	u_{Meas}	0.009	Norm	1	0.009 mm	4		
	u_{MPE}	0.027	Rect	$\sqrt{3}$	0.0156 mm	∞	0.009 mm	0.018 mm
	$(u_{\text{sens}} / \text{mm})$	0.001°				∞	(Normal)	(Normal)
Wedge 2 inclination 134.780°	u_{Meas}	0.007	Norm	1	0.007 mm	4		
	u_{MPE}	0.027	Rect	$\sqrt{3}$	0.0156 mm	∞	0.007 mm	0.014 mm
	$(u_{\text{sens}} / \text{mm})$	0.001°				∞	(Normal)	(Normal)

wedge inclination) were measured.

- The flat top surface and the two lateral walls were used to establish a coordinate system as shown in figure 4.6 [179]; the corner is occupied by one of the four cooling channels (in case of the injection mould) and the approach is that the probe will avoid these areas.
- More than minimum/recommended number of points (9) were taken for the flat

surface, cylinder, circle, sphere, and straight line following the guidance provided in the good practice guide [179].

Once the minimum (or recommended) number of points for the different features is known for each case, the location of these point needs to be identified. There are two approaches to select the location of the measurement points: an ad hoc approach and a scientific approach that relies on a priori knowledge (CAD data) of the object being measured. Due to the lack of a priori information, this measurement process has followed the ad hoc approach.

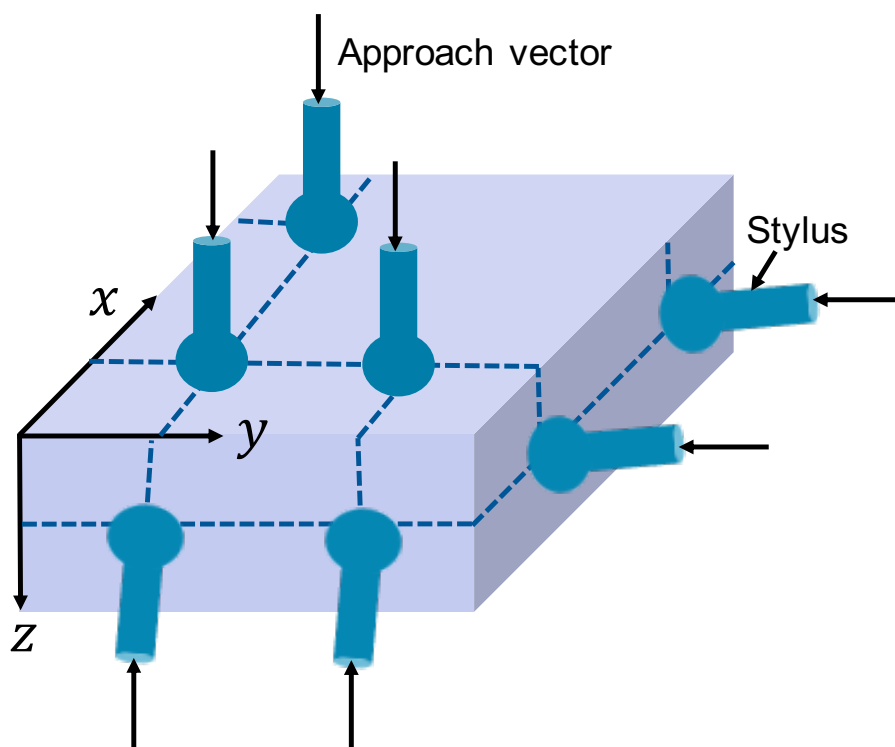


Figure 4.6: CMM coordinate system.

For the top face of the injection mould, shown in figure 4.1, the following features were measured: the feature-1, the length and the width of the feature-1, feature-1 angle, cooling channels (two cylinders) and support channels (two semi-cylinders), whilst for the complex shaped artefact, two spheres, the sphere spacing, hemisphere, and wedge inclination was measured. The measurement of the flat planes and the vertical faces was achieved by obtaining a uniform distribution of N points on the surface [179]. To obtain a quasi-normal distribution, the plane being measured was divided into a grid of N squares (as square as possible), and a point was randomly taken in each

square. A plane was then defined based on a least-squares fit to those points to provide information about the printers ability to produce parallel planes, an important feature in many manufactured parts.

For the injection mould artefact, cylindrical holes were measured by acquiring several points at different heights, whilst for the complex shaped artefact, hemisphere and spheres are measured by taking numerous points. A common problem related to traditional manufacturing is lobing, and more points than the number of lobes are recommended to avoid the loss of information. However, the manufacturing process used in this case does not present lobing; therefore, more than the minimum/recommended approach was followed both for the injection mould and the complex shaped artefact.

In order to achieve a normal distribution using the ad hoc approach, the number of planes n_p , and the number of points distributed in the planes n_c for a cylinder of radius r and height h are given by [179]

$$n_c = \sqrt{\frac{Nh}{2\pi r}}, \quad (4.13)$$

$$n_p = \frac{N}{n_c}. \quad (4.14)$$

Thus, a normal distribution can be obtained using the above equations and the information provided in the good practice guide [179].

4.3.2.1 Comparison of fringe projection and CMM measurements

Table 4.5 depicts different features of the injection mould (shown in figure 4.1) which are measured using a fringe projection system (given in Table 4.1-4.3) and compared with the CMM measurements which serve as a reference. The deviations of the fringe projection measurements from the CMM measurements are listed in column 4 of Table 4.5. The normalised error E_N (given in equation (4.12)) is calculated for all features which lies between -1 to 1.

Likewise, a comparison between the features of interest of the complex artefact (shown in figure 4.2) measured with the fringe projection technique (GOM system, ATOS Core 300 [172]) and CMM is established, as shown in Table 4.6. There are

Table 4.5: Comparison of FP and CMM data for the industrial test case.

Feature	CMM measurement	FP measurement	Deviation of FP data from CMM	Normalised error, E_n
Feature 1 length /mm	(4.836 ± 0.056)	(4.844 ± 0.044)	(0.039 ± 0.071)	0.112
Feature 1 width /mm	(4.805 ± 0.084)	(4.794 ± 0.042)	(-0.011 ± 0.094)	-0.117
Feature 1 angle	$(150.451 \pm 0.232)^\circ$	$(151.074 \pm 0.790)^\circ$	$(-0.377 \pm 0.823)^\circ$	0.757
Diameter cylinder-1 /mm	(6.600 ± 0.046)	(6.627 ± 0.044)	(0.027 ± 0.064)	0.424
Diameter cylinder-4 /mm	(7.592 ± 0.073)	(7.637 ± 0.044)	(0.045 ± 0.085)	0.528
Diameter semi cylinder-1 /mm	(12.009 ± 0.047)	(12.02 ± 0.048)	(0.011 ± 0.067)	0.164
Diameter semi cylinder-4 /mm	(11.977 ± 0.014)	(12.02 ± 0.046)	(0.043 ± 0.048)	0.894

some anomalies present in the E_N value, specifically to sphere 1 diameter and wedge 2 inclination, which corresponds to the measurement uncertainty (type-A and type-B evaluations, uncertainty due to fitting of a feature and ambient conditions). This would be the focus of future work.

4.4 Conclusions

This chapter presents the uncertainty evaluation of the different features of an industrial test case and a complex shaped artefact. The artefacts are measured using contact and non-contact instruments. Since there is no specific standard for fringe projection

Table 4.6: Comparison of FP and CMM data for the complex artefact.

Feature	CMM measurement	FP measurement	Deviation of FP data from CMM	Normalised error, E_n
Sphere 1 diameter /mm	(22.462 ± 0.022)	(22.530 ± 0.050)	(0.068 ± 0.055)	1.245
Sphere 2 diamter /mm	(22.367 ± 0.028)	(22.369 ± 0.046)	(0.002 ± 0.054)	0.037
Sphere 1 to sphere 2 distance /mm	(112.447 ± 0.020)	(112.467 ± 0.042)	(0.020 ± 0.047)	0.430
Hemisphere diameter /mm	(60.194 ± 0.346)	(59.943 ± 0.046)	(-0.251 ± 0.349)	-0.719
Wedge 1 inclination	$(44.964 \pm 0.034)^\circ$	$(44.986 \pm 0.018)^\circ$	$(0.022 \pm 0.039)^\circ$	0.572°
Wedge 2 inclination	$(135.191 \pm 0.036)^\circ$	$(134.780 \pm 0.014)^\circ$	$(-0.411 \pm 0.039)^\circ$	-10.640°

systems, therefore to provide a reference for the dimensional measurements, contact CMM measurements were performed. An uncertainty budget which provides step-by-step guidelines for the uncertainty evaluation of different features of AM artefacts is presented. The process takes into account all types of uncertainties associated with the measurand and the measurement uncertainty is determined. A comparison between the fringe projection and the CMM measurements has been made, and normalised error is computed both for the injection mould and the complex shaped artefacts.

Chapter 5

Multi-view fringe projection system

5.1 Introduction to multi-view fringe projection systems

Commercially available fringe projection systems based on a single camera and projector have restrictions when acquiring the 3D form/shape in one acquisition due to the inadequate field of view of the camera, the frequent presence of occlusions and potentially high slope angles, especially for the freeform geometries of AM parts [6]. A possible solution to overcome these limitations is to introduce multiple cameras and projectors to acquire multiple views. Specifically, multi-view systems have become an emerging research area in 3D form measurement. However, multi-view fringe projection systems are intricate and rely not only on the characterisation of the individual components but also require the global relationship between the cameras and projectors and registering the data from multiple perspectives. In multi-view systems, the characterisation (often called calibration in practice) has a decisive influence on the system performance and for accurate 3D surface reconstruction.

Abedi et al. proposed a method of geometric calibration and rectification of a circular multi-camera system using a pyramid object with symmetric triangles and opposite colours. The method processes all the cameras simultaneously and solved the issue of error accumulation [180]. Liu et al. used a 3D target to characterise a multiple depth camera system using lidar scanning. The method determines the

relative orientation between the cameras with limited overlapping fields of view and unifies the multi-camera coordinates in the same coordinate system [181]. Sun et al. developed a method of global characterisation of a multi-camera system using a group of spherical targets. This one-time operation can globally characterise all the cameras with non-overlapping fields of view and avoids extensive workloads and accuracy loss caused by repeated processes [182]. A flexible method of global characterisation of multiple cameras using a transparent glass checkerboard was proposed by Feng et al. [183]. The method utilises the refractive projection model and the concept of ray tracing to eliminate the error of refraction and to achieve high accuracy.

The characterisation of a multi-view fringe projection system is based on determining both the intrinsic and extrinsic properties of the cameras and projectors and bringing them into the global frame of reference. A common approach to multi-view system characterisation is the extension of the methods for characterising single camera-projector systems, proposed by Tsai, Zhang, and Huang [35–38], where each camera is characterised with an accurately manufactured target (for example, a checkerboard or circle board) and the relationship between the multiple views is obtained by global optimisation of the extrinsic parameters of all the views. Albers et al. presented a flexible characterisation method for a multi-sensor fringe projection system by incorporating the Scheimpflug optics for the cameras and defining a common world coordinate system using a planar target [27]. Gai et al. proposed an easy-to-use characterisation of a multi-view fringe projection system, where the digital fringe projection and phase maps are used to acquire global characterisation [28].

Gdeisat et al. [29] and Deetjen et al. [30] developed the global characterisation methods for multiple camera-projection systems, whereby the cross-talk between multiple camera-projector pairs is avoided by using a particular light bandwidth (RGB optical colour filters). Deetjen et al. also demonstrated the technique for high-speed 3D reconstruction of a flying bird. Servin et al. combined the two techniques: co-phased profilometry and 2-step temporal phase unwrapping, and measured an industrial metallic discontinuous object which is coated with white-matte paint to reduce the specular reflection [184, 185]. A co-phased 2-projector and 1-camera based 360-degree profilome-

ter was proposed which can measure highly discontinuous objects [186]. A plastic skull is measured by rotating it with ϕ rotation steps. In typical fringe projection systems, the projector is modelled as an inverse camera, the camera is used to capture images for the projector and the transformation from the camera image pixels to the projector image pixels is performed by a phase-stepped fringe projection technique [88, 187–189]. However, if the camera pixels are not aligned with the projector pixels, this can lead to mapping error. In general, any error in the camera characterisation is transferred to the projector characterisation, which can significantly affect the performance and accuracy of the fringe projection system.

In this chapter, two different approaches for the characterisation of a multi-view fringe projection system are used. The first method relies on finding the correspondences between the camera and projector pairs. For this purpose, a characterisation target (checkerboard), automated image acquisition and image processing technique are used. The geometric characterisation technique is demonstrated by determining the global world coordinate system and combining the 3D reconstruction results from different perspectives. The characterisation results are implemented, and the multi-view fringe projection system is tested to acquire the three-dimensional shape of a (60 mm \times 60 mm \times 20 mm, Nylon-12) AM part. The 3D reconstructions from different perspectives are aligned with the CAD model and finely registered with an iterative closest point (ICP) algorithm [190].

In the second approach, a novel method to characterise a multi-view fringe projection system is presented which does not require projector characterisation, therefore, the influence of mapping error is removed. The proposed method depends on the stereo matching between rectified unwrapped stereo phase maps based on the epipolar constraint. In general, the stereo vision and fringe projection methodologies are combined to acquire the dense disparity map which is incorporated with the stereo-camera characterisation information for 3D surface reconstruction [31–34]. However, the proposed method relies on determining the correspondences in the phase domain. The absolute phase maps are acquired through the fringe projection method and the matched phase points in the stereo phase maps are triangulated for 3D reconstruction. The effec-

tiveness of the proposed method is determined by finding the point-to-point distance deviations between the point clouds, which are acquired from different views. The results are compared with the contact CMM measurements which serve as a reference for the dimensional measurements. A comparison of the proposed method with the conventional method of characterising the multi-view fringe projection system is also presented.

5.2 Characterisation approach-1: Triangulation

5.2.1 Methods and materials

The multi-view fringe projection system is comprised of multiple sets of cameras and projectors, as shown in figure 5.1 (a). Figure 5.1 (b) depicts the schematic of the multi-view system with eight sets of cameras, however, for experimental purpose, two sets of cameras and projectors are used. The system characterisation is carried out using a checkerboard which is placed at several different orientation in the measurement volume and the images are captured. These images are then used to determine the intrinsic and extrinsic parameters of the cameras. Sinusoidally varying phase-stepped

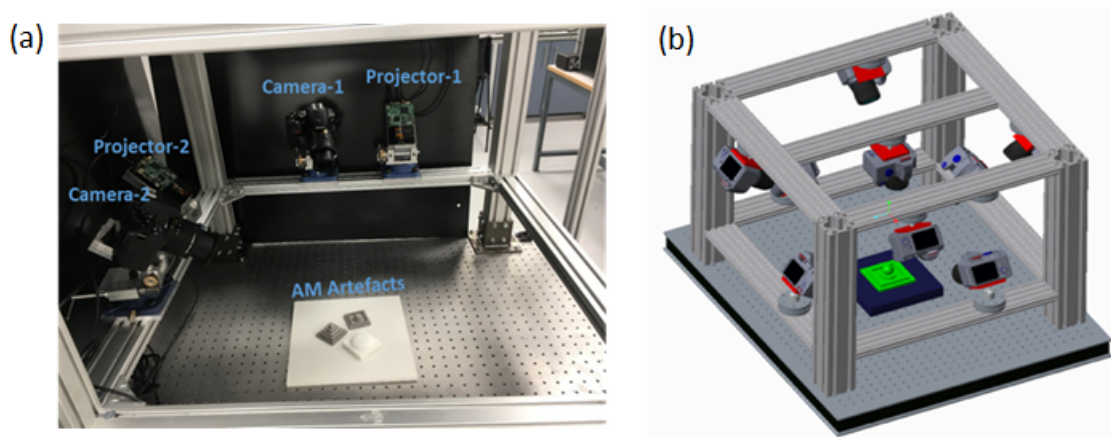


Figure 5.1: Multi-view fringe projection system. (a) A photograph of the multi-view fringe projection system with two sets of cameras and projectors and (b) schematic of the Multi-view fringe projection system.

fringe patterns (10 phase-shifted patterns with a phase shift of $\delta_i = (2\pi i/N)$, where, the phase stepping index is $i = 0, 1, 2 \dots N - 1$, and given in equations (2.15) and (2.16)) are generated using a computer and projected onto the checkerboard. The absolute

Table 5.1: Geometric characterisation results for the cameras and projectors.

Intrinsic parameter	Outcome
Camera 1 (A_1^c)	$\begin{pmatrix} 9326 & 0 & 2282 \\ 0 & 9234 & 1524 \\ 0 & 0 & 1 \end{pmatrix}$
Camera 2 (A_2^c)	$\begin{pmatrix} 10545 & 0 & 2240 \\ 0 & 10833 & 1358 \\ 0 & 0 & 1 \end{pmatrix}$
Projector 1 (A_1^p)	$\begin{pmatrix} 1509 & 0 & 314 \\ 0 & 4856 & 613 \\ 0 & 0 & 1 \end{pmatrix}$
Projector 2 (A_2^p)	$\begin{pmatrix} 863 & 0 & 359 \\ 0 & 1479 & 457 \\ 0 & 0 & 1 \end{pmatrix}$

phase maps are acquired through temporal phase unwrapping method that relies on a combined phase-stepped and binary coded method, described in section 3.1.2.2. The retrieved phase maps are used to determine the parameters of the projectors. The detail of the geometric characterisation procedure is discussed in the following sections.

5.2.1.1 Geometric characterisation

Camera characterisation is a well-developed field [111–115]. A camera is described by the pinhole model [113]. For an arbitrary point in the 3D space, the relationship between a point on the object and its projection on the image sensor is given by equation (2.69). The camera characterisation is performed using a standard checkerboard (checker size, 4 mm) which is placed at several different positions in the measurement volume, and images are captured by projecting a plain white image pattern onto the checkerboard. The intrinsic (A_1^c, A_2^c) parameters for both the cameras are determined using an image processing algorithm. The measured parameters are listed in table (5.1). The extrinsic parameters of the cameras and projectors are determined by projecting fringes and the absolute phase map information (see section 3.1.2.2).

Figure 5.2 shows the fringes projected onto the checkerboard pattern and the corresponding phase maps with square corners detected for one orientation. Figure 5.3 shows the three-dimensional visualisation of the extrinsic parameters for the projectors and cameras. The characterisation patterns (checkerboard) are plotted corresponding

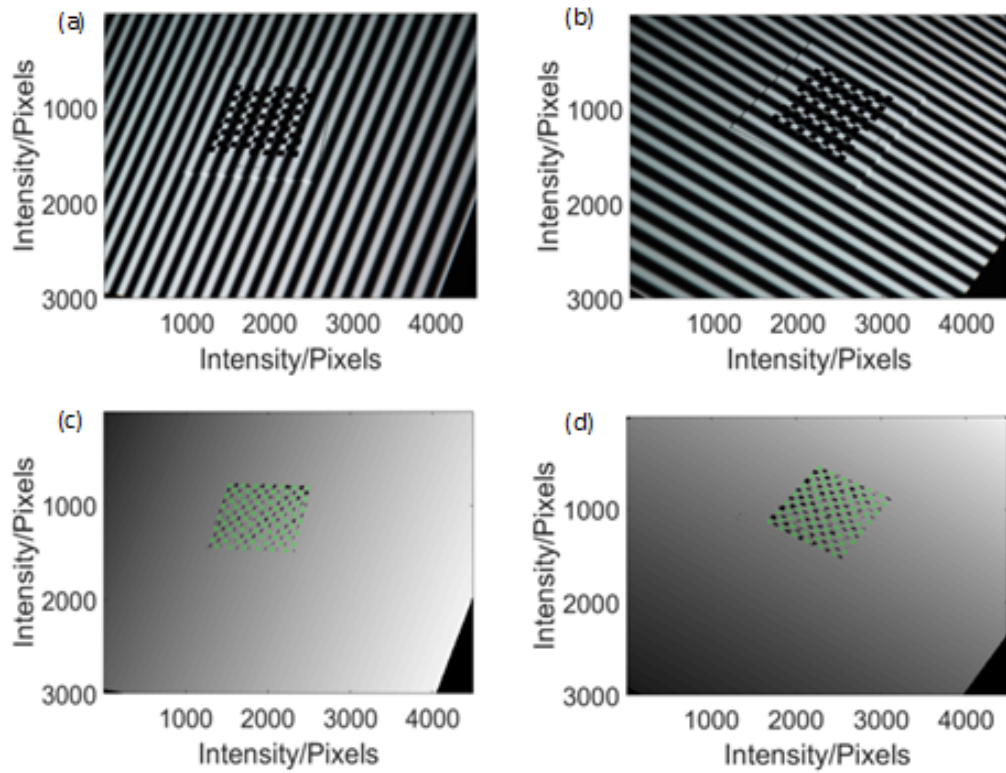


Figure 5.2: Fringes projected on the checkerboard and captured by two different cameras from different perspectives. (a-b) Original images and (c-d) corresponding phase maps with the detected checkerboard points being projected back.

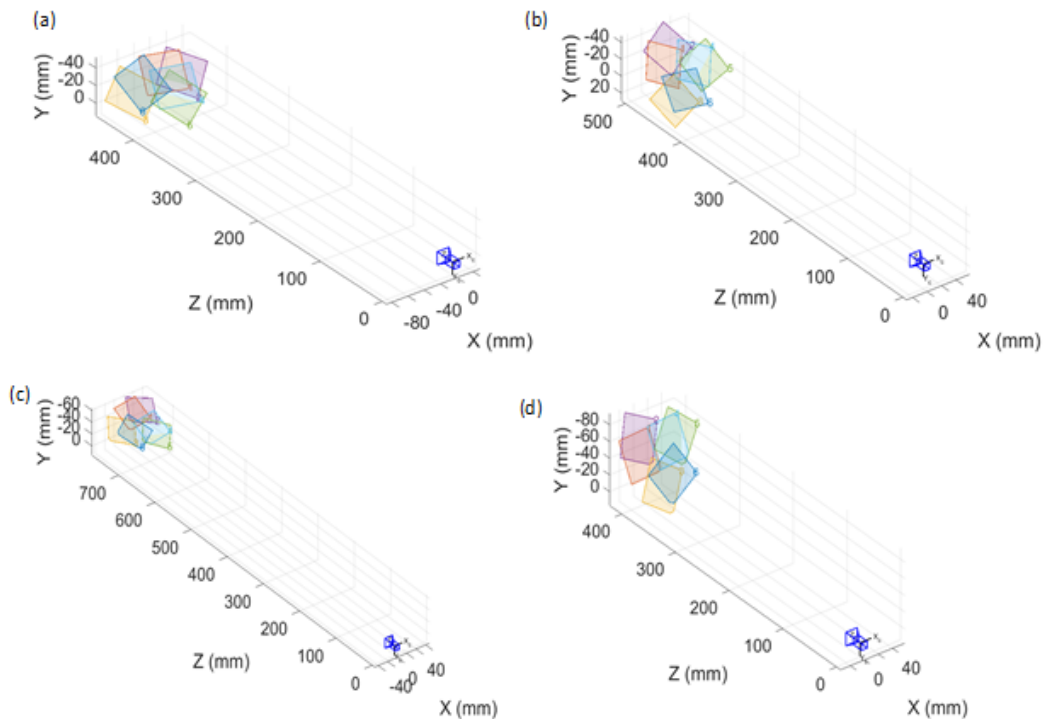


Figure 5.3: Extrinsic parameters. (a) Camera 1 (b) camera 2 (c) projector 1 and (d) projector 2.

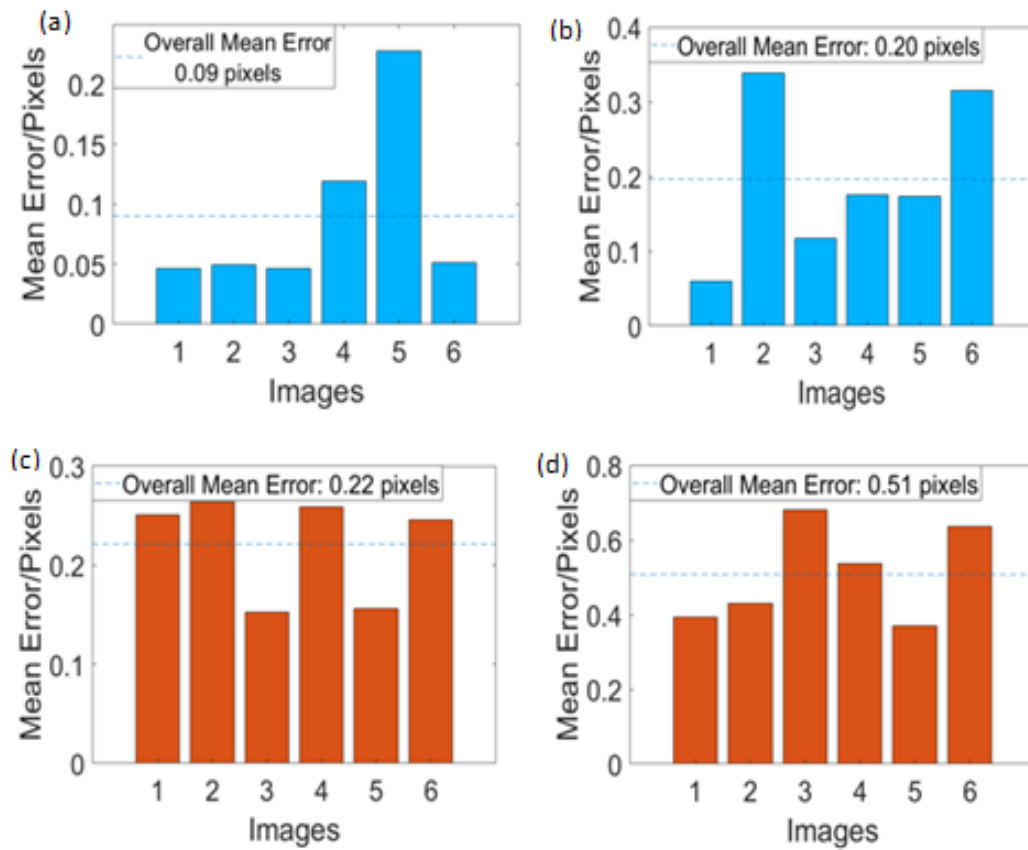


Figure 5.4: Reprojection error per image. (a) Camera 1 (b) camera 2 (c) projector 1 and (d) projector.

to the camera/projector. Figure 5.4 depicts the reprojection error for the cameras and projectors for six different positions. The reprojection error are less than half a pixel, showing that the geometric characterisation was successful.

5.2.1.2 Global frame of reference

The initial steps (mentioned in section 5.2.1.1) determine the intrinsic and extrinsic parameters for each individual camera and projector. The location and orientation of each camera and projector are automatically defined in the same global reference frame. The transformation from the image coordinates to the three-dimensional world coordinates can be achieved through triangulation. Each combination of camera and projector is considered as a stereo pair, with the transformation relationship given by equations (3.3) and (3.4). The global relationship between the camera and projector views is obtained by a plane in the common field-of-view of both the cameras and projectors. The world coordinates can be acquired based on the triangulation (equation

3.7).

5.2.2 Experiments on approach-1

5.2.2.1 Experimental setup

The experimental setup for the multi-view fringe projection system (figure 5.1(a)) is comprised of two DSLR cameras (Nikon D3500, 4496×3000 pixels), two digital light processing projectors (DLPC300 Texas Instruments) with a digital micromirror device (608×680 pixels). In the multi-view fringe projection system, the two sets of cameras and projectors are mounted on a rigid metal mount to reduce mechanical vibration. The tested object is placed approximately 50 cm from the projectors. The projector's digital micromirror device chip is used to project the images onto the tested object. The overlap between the projectors is overcome by only displaying fringes through a single projector at any one time.

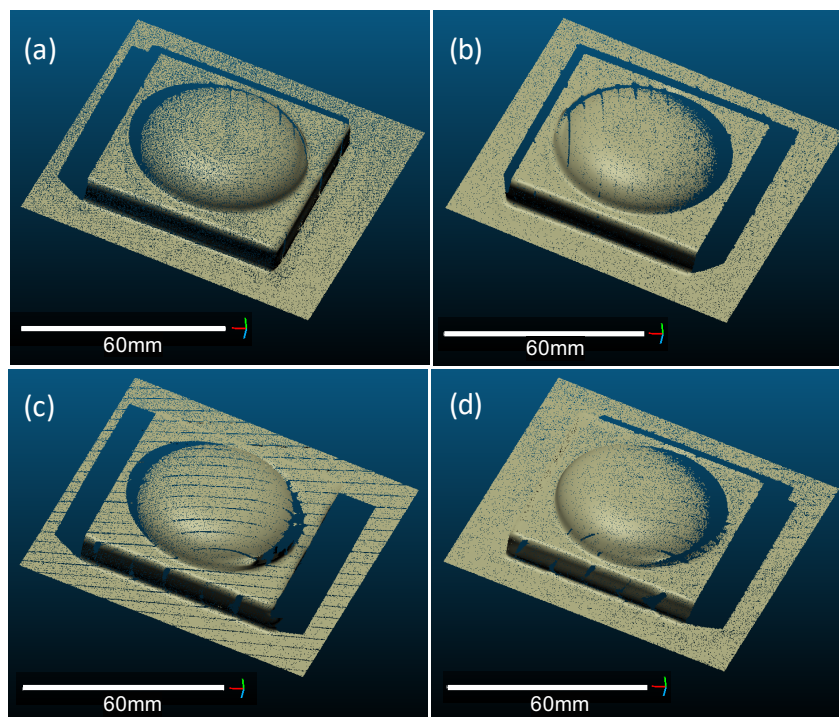


Figure 5.5: 3D reconstruction results from different perspectives. (a) Projector 1-camera 1 (b) projector 1-camera 2 (c) projector 2-camera 1 and (d) projector 2-camera 2.

5.2.2.2 Results of the multi-view system

The geometric characterisation of the multi-view fringe projection system is carried out by using a checkerboard and capturing images at different orientations, as discussed in section 5.2.1.1. To further estimate the system's characterisation accuracy, the 3D measurement of an AM artefact is performed using a set of phase-stepped sinusoidal fringes and binary coded fringes. The multi-view system with two sets of cameras and projectors share the same frame of reference, four individual point clouds have been acquired for two different projections and from two separate perspectives, as shown in figure 5.5 (a-d). Furthermore, figure 5.6 depicts the point clouds for four cameras and three projectors.

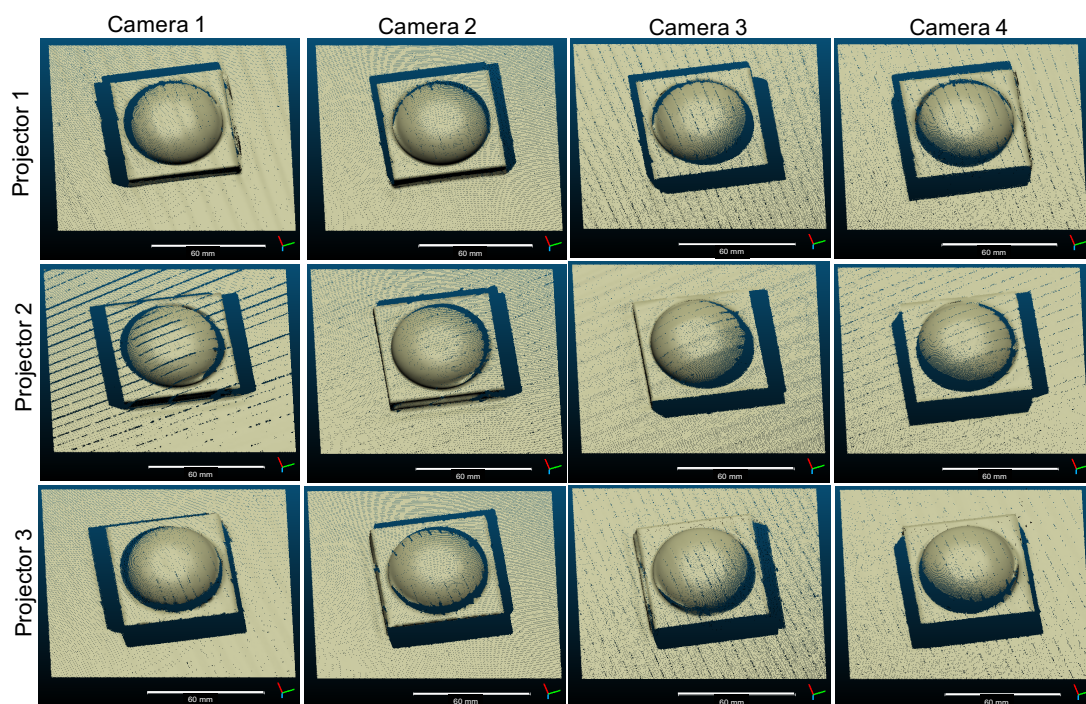


Figure 5.6: 3D reconstruction results for a multi-view fringe projection system with four cameras and three projectors.

Figure 5.7 (a) shows the 3D reconstructed results of a hemisphere artefact (Nylon-12, 60 mm \times 60 mm \times 20 mm) with a single camera-projector based fringe projection system. Figures 5.7 (b) and (c) depict the point cloud by combining the reconstruction results from different perspectives. Compared to the single view system, the multi-view system provides better performance and overcome the self-occlusion and shadowing effect of the AM part. The reconstruction results in figure 5.7 (c) is more complete as

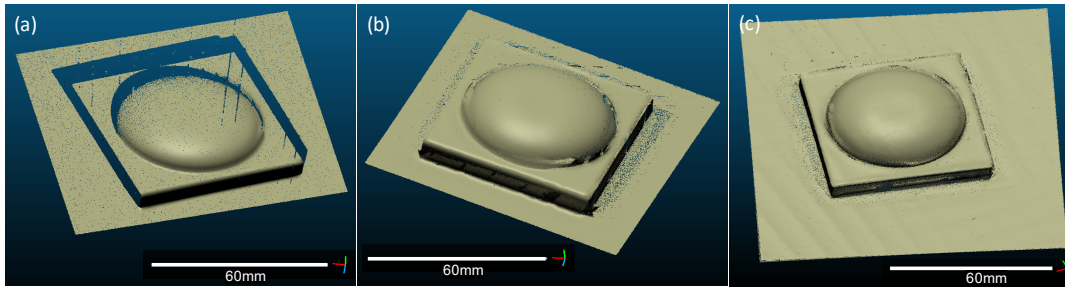


Figure 5.7: 3D reconstruction results for a hemisphere (60 mm \times 60 mm \times 20 mm, Nylon-12) artefact. (a) Point cloud from a single-camera projector (b) point cloud from two sets of cameras and projectors and (c) point cloud from four cameras and three projectors.

there is no gap on the sides of the artefact. There is also no obvious offset between the two views which shows the consistency of the measurement data.

However, the full 3D form of the measured AM artefact requires projections from more positions. The multi-view system fringe projection system is tested with two sets of cameras and projectors and can be generalised for N cameras and projectors using the same algorithmic solution. Future work will focus on the global optimisation of the geometric characterisation for the multi-view fringe projection system and improving its speed and accuracy.

5.3 Characterisation approach-2: Stereo rectification of phase maps

5.3.1 Methodology of approach-2

The methodology of this work falls into five main stages: *Step A - Camera characterisation*, *Step B - Phase map by fringe projection*, *Step C - Rectification of the unwrapped phase maps*, *Step D - Stereo matching of the rectified unwrapped phase maps* and *Step E - Three-dimensional reconstruction*. The schematic is shown in figure (5.8).

Step A - Camera characterisation: The camera characterisation is performed by placing a checkerboard in the field of view of all the cameras (there are four in our example set up - see section 5.3.2). Images of the checkerboard at different orientations are captured by all cameras. Each camera is characterised separately using a pinhole camera model [35–38]. The intrinsic and extrinsic parameters of each camera are

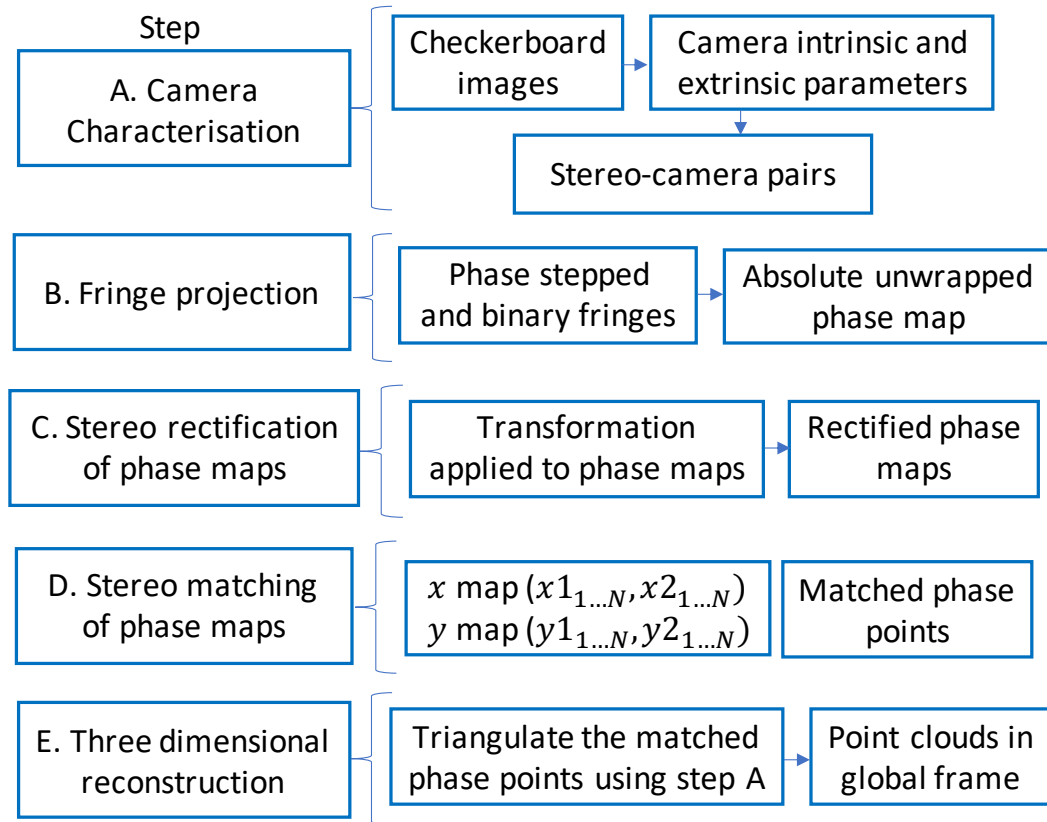


Figure 5.8: Schema of the characterisation method of the multi-view fringe projection system.

determined using a developed image processing algorithm in MATLAB [39].

After characterising each camera individually, the stereo-camera parameters are generated using the camera characterisation information [40–47]. In general, any number of pairs could be used; however, due to the lack of a common field of view and the area illuminated by the structured light, we have considered the adjacent camera pairs and treated the multi-view system as two sets of stereo-camera pairs. The transformation between the stereo-camera pairs is given by [117]

$$R_{2 \rightarrow 1} = R_2(R_1)^T, \quad T_{2 \rightarrow 1} = T_2 - (R_{2 \rightarrow 1}T_1), \quad (5.1)$$

$$R_{4 \rightarrow 3} = R_4(R_3)^T, \quad T_{4 \rightarrow 3} = T_4 - (R_{4 \rightarrow 3}T_3), \quad (5.2)$$

where R and T are the rotation and translation matrices respectively and correspond to the extrinsic parameters that describe the transformation from the world coordinate system to the camera coordinate system. The superscript T in $(R_1)^T$ and $(R_3)^T$ represents the transpose. The relative orientation and location in each stereo-camera pair

are defined with respect to the first checkerboard position, which is in the common field of view of the cameras and corresponds to the same global coordinate system. The first dataset has the checkerboard in the field of view of all cameras, therefore, it removes the need for the checkerboard to be visible to all cameras at all times.

Step B - Phase map by fringe projection: A fringe projection system can be mathematically modelled as a stereo-camera system and relies on triangulation of common points between the projector and the camera. Essentially, one camera in the stereo pair is replaced with a projector and the correspondence is determined by the characteristics of the projected structured light. In this work, the method of phase encoding is based on the phase-stepped fringe projection method [88]. A set of phase-stepped sinusoidal and binary encoded fringe patterns [48] are projected onto the surface of the object being measured. Different phase offsets are applied to the sinusoidal pattern and an image is captured at each step. The phase value at any particular pixel can be determined from the captured N phase-stepped sinusoidal images [88, 187–189]. The retrieved phase has 2π modulation and is unwrapped by removing the 2π discontinuities and acquiring a continuous phase map.

We have used temporal phase unwrapping [49–52] to produce an absolute phase map. In temporal unwrapping, the fringe order is encoded into binary fringes and projected onto the object, and an absolute unwrapped phase map is acquired. A modification to the binary fringes is introduced by converting the binary values to greyscale values, which simplifies the search for 2π discontinuities in the phase map with respect to the neighbouring pixels. The unwrapping errors in the retrieved phase maps are corrected using a filtering algorithm that convolves the unwrapped phase map with a Sobel edge kernel and removes the random spikes and dips in the phase map.

Step C - Rectification of the unwrapped phase maps: One approach to triangulate a large number of points is to rectify the stereo images and estimate the disparity map. Rectification is a transformation applied to the images to project them onto the same plane and can account for camera distortion and the non-coplanar stereo-camera pair [53, 54]. A schematic of the rectification process is shown in figure 5.9, which shows

that the image rectification transforms each image such that the epipolar lines (shown as dotted lines in figure 5.9) are parallel. The epipolar lines are given by

$$l_L = F^T \phi_R, \quad (5.3)$$

$$l_R = F \phi_L, \quad (5.4)$$

where F is the fundamental matrix [54]). The corresponding values on the epipolar lines have the same coordinates in both the phase images based on the epipolar constraint

$$\phi_R^T F \phi_L = 0. \quad (5.5)$$

The advantage of the rectification process is that the search for 2D correspondences reduces to a single line (1D search problem) [117]. The phase maps captured by the

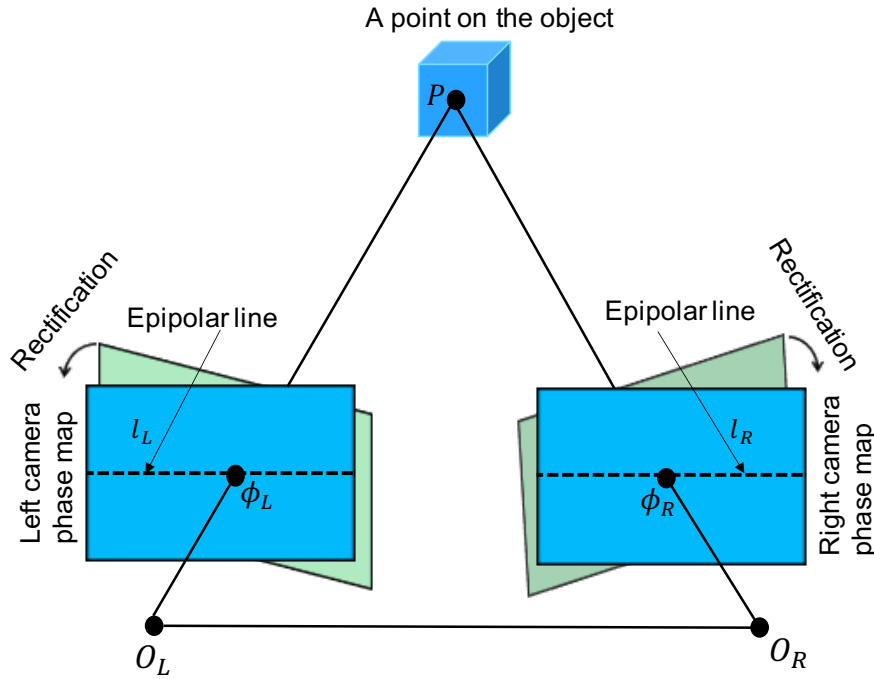


Figure 5.9: Schema of the rectification of the stereo-camera phase images. ϕ_L and ϕ_R are the projections of a 3D point P onto the left and right camera phase images, respectively. l_L and l_R are the epipolar lines of the left and right camera phase images, respectively. O_L and O_R are the left and right cameras' optical centres, respectively.

adjacent cameras (Step B - Phase map by fringe projection) are treated as stereo phase maps (ϕ_L, ϕ_R) , as shown in figure 5.9. An automated algorithm pre-processes the phase maps for denoising (via Gaussian smoothing, a low-pass filter which attenuates the

high frequency components), undistorts the phase maps which accounts for radial and tangential lens distortion and by utilising the stereo parameters information, acquires the rectified version of the left and right phase maps ϕ_L and ϕ_R , respectively (shown as blue coloured phase images in figure 5.9).

Step D - Stereo matching of the rectified unwrapped phase maps: For the stereo matching of the rectified unwrapped phase maps, an automated image processing algorithm was developed. The rectification of the phase images limits the search for correspondences to a single line (epipolar line). By taking the same line in both the rectified unwrapped phase images, the search for correspondences is accomplished by determining the points at which the phase values match. The output of this process is a disparity map. An iterative approach for disparity estimation is used by taking the phase value in the left camera phase image $\phi_{L-rect}(x_{1...N}, y_{1...N})$ and comparing it with the corresponding line (epipolar line) of the right camera phase map $\phi_{R-rect}(x_{2...N}, y_{2...N})$ using a nearest neighbour search. For k -nearest neighbour ($k = 2$), the search for the nearest neighbour (row/line) in the right phase image to each point in the query data (point in the left phase image) is accomplished using an exhaustive search method. This method finds the distance from each query point to every point in the right phase image, arranges them in ascending order, and yields the k points with the smallest distances. The nearest neighbour search returns a numerical matrix representing the indices of the nearest neighbours.

The absolute phase differences in the row coordinate of the rectified phase maps, for the same phase value viewed in the left and right camera phase images, are the disparity values. The disparities are prefiltered to discard phase values outside the expected disparity range. To account for sub-pixel disparity values, the two lowest phase differences from the epipolar line are extracted, and a linear fit between the two phase points and the intercept is determined. In order to access the same phase values in the rectified unwrapped stereo phase maps, location maps $x(x_{1...N}, x_{2...N})$ and $y(y_{1...N}, y_{2...N})$ for N phase values are generated. By incorporating the location map and sub-pixel disparity information, the matched phase points between the rectified images are determined.

Step E - Three-dimensional reconstruction: After determining the correspondences between the rectified stereo phase maps, the 3D points can be obtained based on the triangulation principle. The computation of the scene structure depends on finding the 3D point, which is estimated by the intersection of rays back-projected from the corresponding phase image point pairs (ϕ_L, ϕ_R) through their associated camera projection matrices [54]. For this purpose, the camera projection matrix (3×4), which maps 3D world points in the homogeneous coordinates to the corresponding points in the camera phase image, is retrieved using the camera characterisation information, and the rotation and translation of the camera. The matched phase points in the rectified stereo phase maps are combined with the respective projection matrix of the adjacent cameras (as a stereo-camera pair), and the 3D world coordinates of the object are determined.

5.3.2 Experiments on approach-2

In order to evaluate the effectiveness of the proposed method, a multi-view fringe projection system has been set up, as shown in figure 5.10. The system comprises four DSLR cameras (Nikon D3500, 4496×3000 pixels), and two digital light processing (DLP) projectors (DLPC300 Texas Instruments) with a digital micromirror device (608×680 pixels). All cameras and projectors are mounted on a rigid metal frame to reduce mechanical vibration [137]. The projector's digital micromirror device chip is used to project a series of computer-generated fringe patterns onto the surface of the object, and the cameras capture the distorted fringes. In this set-up, the two cameras and a projector yield one stereo pair, and the multi-view fringe projection system is configured as two sets of stereo pairs. The details of the system characterisation procedure are discussed in the following sections.

5.3.2.1 Camera characterisation results

The camera characterisation is performed using a checkerboard (checker size: 4 mm). The calibration steps are as follows.

1. The position of the cameras is adjusted so that each camera is in the field of view

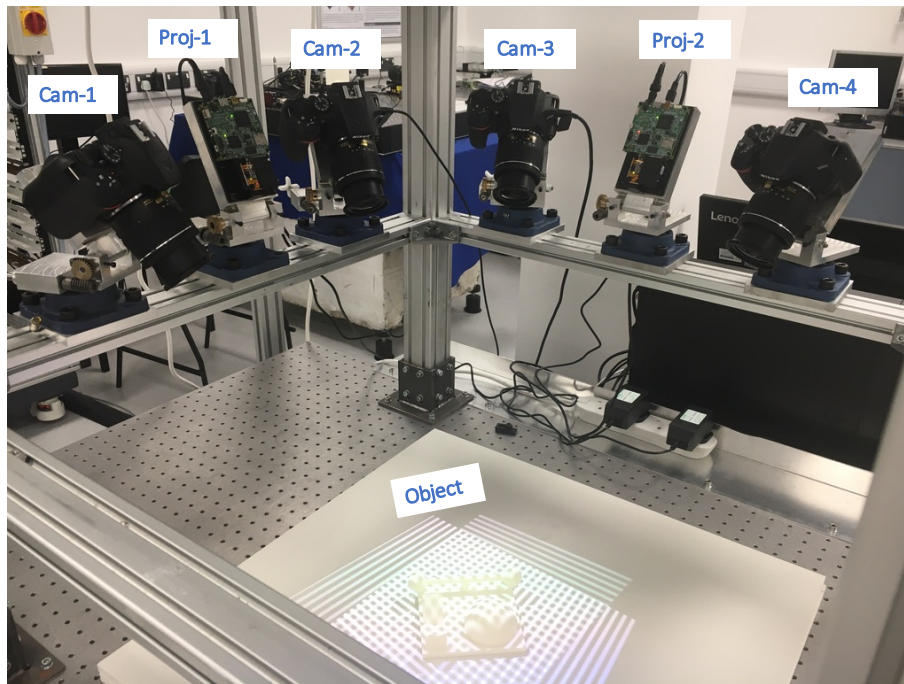


Figure 5.10: Photograph of the multi-view fringe projection system. The system is comprised of four DSLR cameras and two projectors.

and covers the measurement volume.

2. The checkerboard is placed in several positions (46 in our case) in the field of view of the cameras (1 to 4). In each position, images of the checkerboard are captured.
3. The captured images are processed to extract the coordinates of the checkerboard corners - an automated image processing algorithm was developed for this purpose.
4. From the corner information, the intrinsic and extrinsic parameters for each individual camera are determined.
5. After characterising each camera individually, the stereo-camera pairs are generated using the camera characterisation information. The relative orientation and location of each stereo-pair are determined with respect to the first checkerboard position. Figure 5.12(c-d) shows the extrinsic parameter visualisation of the stereo-camera pairs.

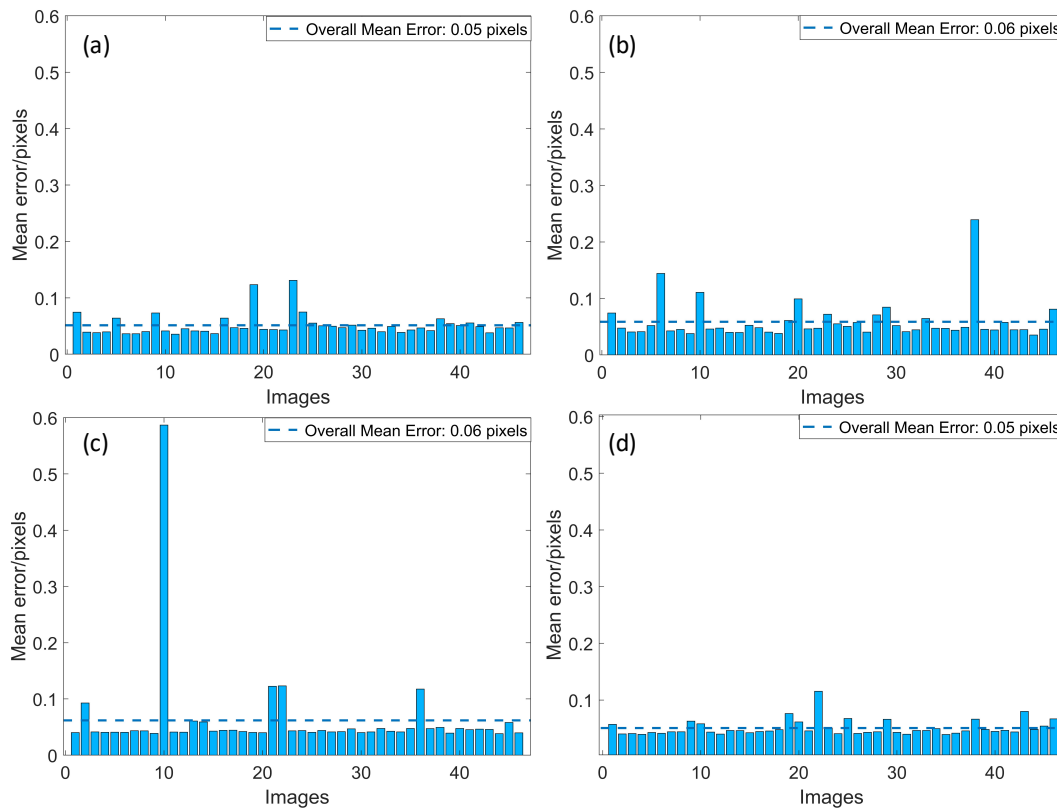


Figure 5.11: Mean reprojection error per image for the camera characterisation. (a) Camera 1 (b) camera 2 (c) camera 3 and (d) camera 4.

We have estimated the quantitative accuracy of the characterisation by determining the reprojection error, which corresponds to the distance between the checkerboard point detected on the characterisation image (checkerboard image) and the corresponding world point projected onto the same image. The mean reprojection errors for individual camera characterisation are 0.052 pixels, 0.059 pixels, 0.062 pixels and 0.051 pixels for camera 1 to 4, respectively. For stereo-camera pairs, the mean reprojection errors are 0.055 pixels and 0.056 pixels, for stereo-camera pairs 1 to 2, respectively. Figures 5.11(a-d) and 5.12(a-b) show the mean reprojection error per image for the individual camera characterisation and the stereo-camera pairs.

5.3.2.2 Rectification of the unwrapped stereo phase maps

Figure 5.13 (a-b) show the captured images of a Nylon-12 complex shaped object (110 mm \times 110 mm \times 50 mm) acquired with the fringe projection method. A set of ten phase-shifted fringe patterns and binary encoded fringes are used. The binary fringes provide the information regarding the fringe order and are used to retrieve

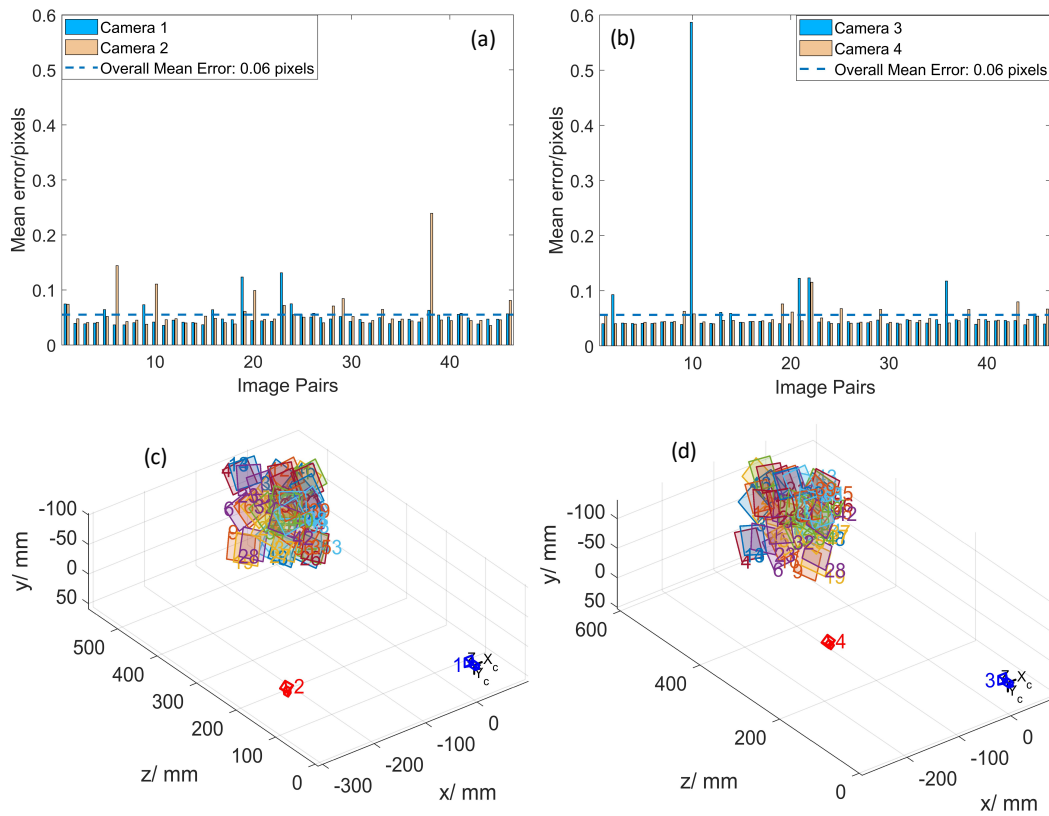


Figure 5.12: Reprojection error per image for stereo-camera pairs (a) stereo-camera pair 1, (b) stereo-camera pair 2, and (c) extrinsic parameter visualisation of stereo-camera pair 1. The region with coloured squares corresponds to the checkerboard patterns detected by the stereo-camera pair 1, and (d) extrinsic parameter visualisation of stereo-camera pair 2.

the absolute unwrapped phase maps from the distorted fringe images. The acquired absolute unwrapped phase maps, after applying the filtering algorithm for one of the stereo-camera pairs are shown in figure 5.13 (c-d).

The image transformation is applied to the filtered phase maps (shown in figure 5.13 (c-d)) and the rectified unwrapped phase maps are shown in figure 5.14 (a-b). The rectification process follows stereo matching in which the phase value in the left phase image is compared with the corresponding row (epipolar line) of the right phase image. The matched phase points in the stereo phase images are triangulated to acquire the 3D coordinates of the object.

5.3.2.3 3D reconstruction results

We validated the proposed method by implementing the characterisation method on the multi-view fringe projection system and acquiring the 3D reconstruction results

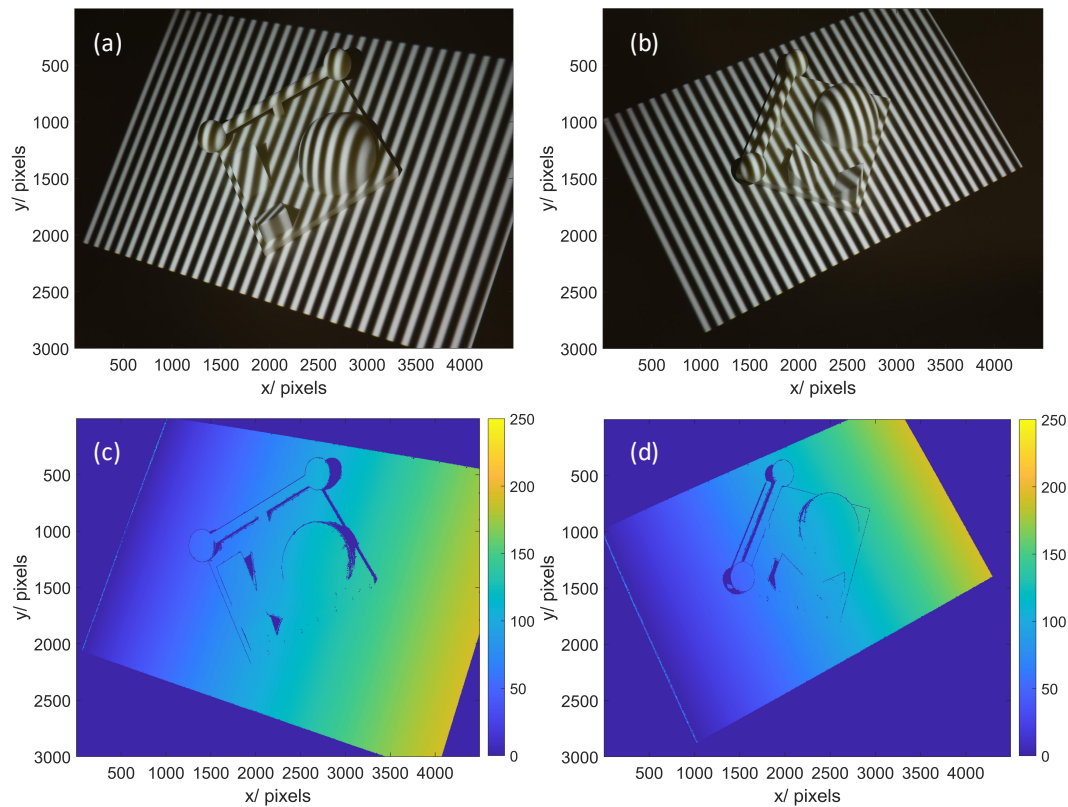


Figure 5.13: Images of a complex shaped object ($110 \text{ mm} \times 110 \text{ mm} \times 50 \text{ mm}$) with fringes projected. The images are captured by two cameras in a stereo configuration (a) Camera-1 and (b) camera-2. Filtered unwrapped phase maps of the object for (c) data shown in (a) and (d) data shown in (b).

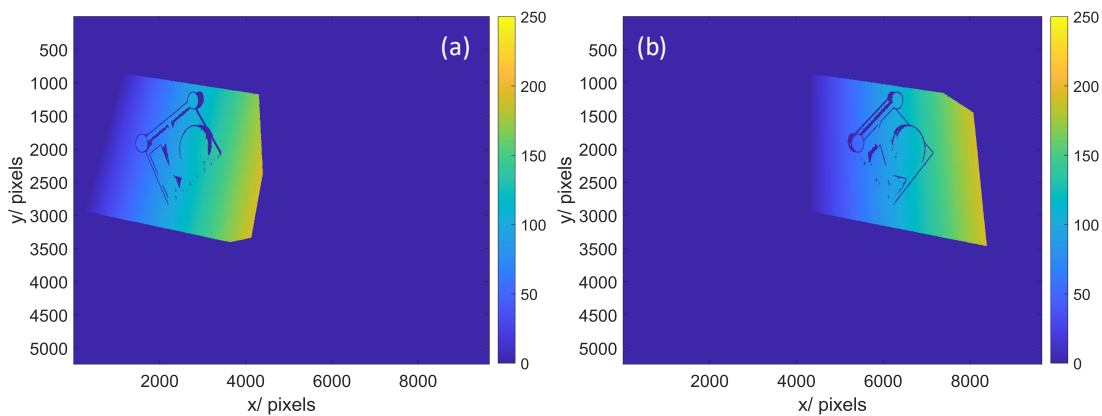


Figure 5.14: Rectified unwrapped phase maps. (a) Rectified phase image for the phase map in figure 5.13 (c) and (b) rectified phase image for the phase map in figure 5.13 (d).

for a complex shaped object ($110 \text{ mm} \times 110 \text{ mm} \times 50 \text{ mm}$, Nylon-12). Following the steps in section 5.3.1 and using the stereo matching of the rectified unwrapped phase maps, the 3D reconstruction results for the complex artefact were acquired, shown in figure 5.15 (a-c). The point clouds from two views are in the global coordinate system, and do not require any further registration. By combining the point clouds (shown in

figure 5.15 (a-b)), a dense point cloud is retrieved, as shown in figure 5.15 (c).

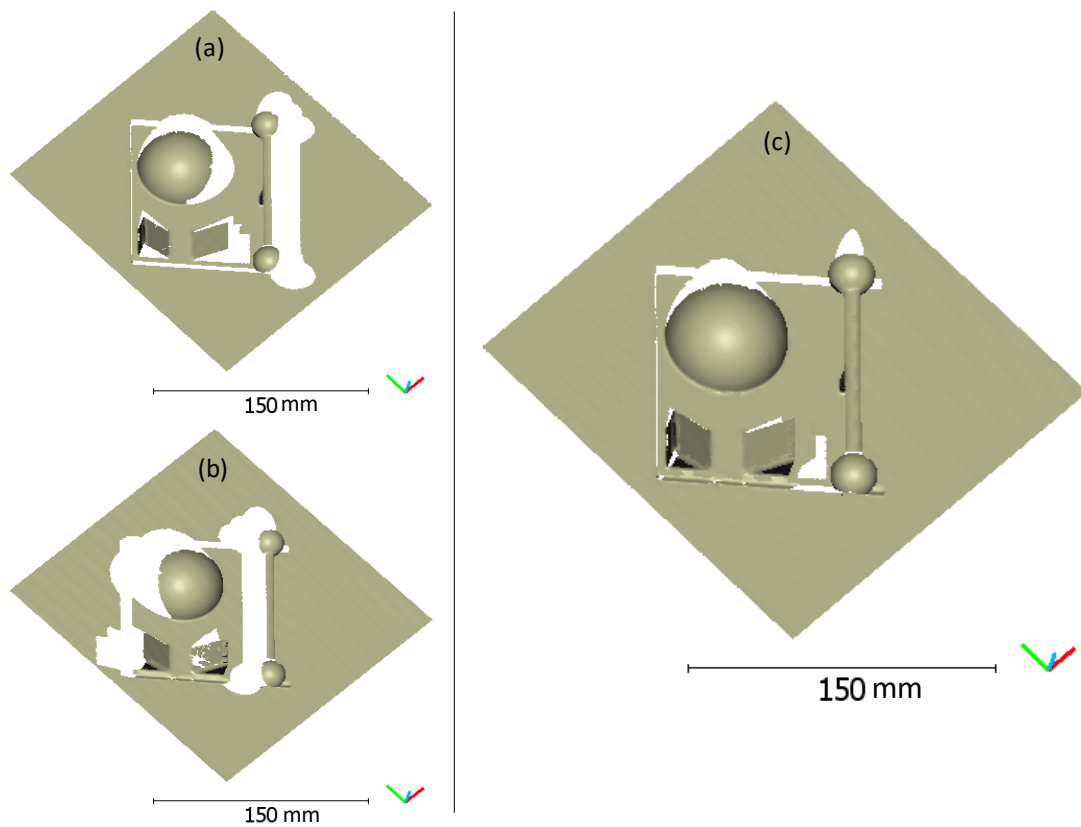


Figure 5.15: 3D reconstruction results for a complex artefact ($110 \text{ mm} \times 110 \text{ mm} \times 50 \text{ mm}$). On the left side, two point clouds acquired from stereo-camera (a) pair 1 (b) pair 2, respectively and on the right side (c) a consolidated point cloud after combining the two views (a-b).

We determined the signed point-to-point distance of the two-point clouds in the overlapping region between them using the CloudCompare [173], and the distances are determined between a point cloud regarded as a reference and a target point cloud [2]. A small region-of-interest (ROI) is chosen between the point clouds from two sets of stereo-camera pairs, and a comparison of the point cloud from stereo-pair 1 (reference point cloud) was made against the other stereo-pair 2 (target point cloud), shown in figure 5.16. Based on the least-squares fitting methods in CloudCompare [173] which relies on nearest-neighbour distances, the distribution of the distance deviations is shown in figure 5.16 (b-c). The colour map corresponds to the Euclidean distance between each point in the reference point cloud (stereo-camera pair-1) and its closest point located in the compared point cloud (stereo-camera pair 2). The statistics for the pairs are shown in figure 5.16 (c). The standard deviation of the ROI of the two

point clouds is $48 \mu\text{m}$ and the point clouds acquired from two orthogonal perspectives are in the global frame.

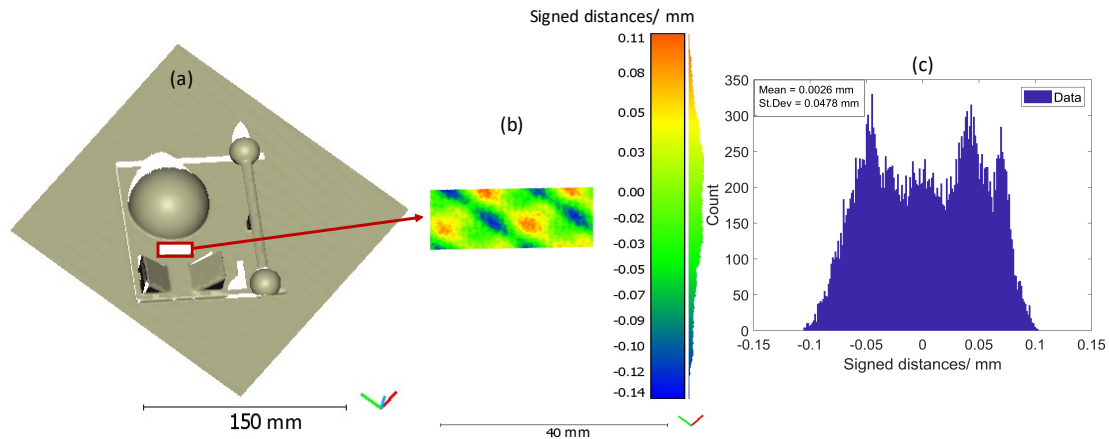


Figure 5.16: Results for the deviation of two point clouds for the complex artefact. (a) Point cloud showing the ROI as a red box, (b) a colour map indicating the signed point-to-point distance of the two point clouds from stereo-camera pairs 1 and 2, and the distances are determined between a reference point cloud (stereo-camera pair 1) and a target point cloud (stereo-camera pair 2) [2], and (c) a histogram depicting the statistics of the signed point-to-point distance of the two point clouds shown in (b), the standard deviation (St.Dev) of the distribution is $48 \mu\text{m}$.

The structured pattern and waviness seen in figure 5.16 (a-b) are associated with systematic effects (offsets in the intrinsic and extrinsic parameters which exhibits complex distortions in the triangulated point clouds) in the measurement process, noise in the phase maps and the accuracy of the system characterisation. These deviations may be considered as a combined effect of projector's non-linear gamma effects (in case the system is not perfectly characterised), non-linear offsets between the DSLR cameras (as four cameras were used), vibration due to the mechanical shutter of DSLRs, and the camera's internal sensor noise.

A Mitutoyo Crysta Apex S7106 CMM (available at University of Nottingham) was used to perform the dimensional measurements which are used as a reference [191]. Specific features were measured using the CMM (21 mm long, 3 mm diameter ball-tipped stylus with SP25 Probe, $\Phi 4 \text{ mm} \times 50 \text{ mm}$) according to the National Physical Laboratory (NPL) good practice guide No. 41 [192]. As per the manufacturer specification, the CMM has a volumetric length measurement accuracy $E_0 = (1.7 + 3L/1000) \mu\text{m}$ (L is the length of the measured object in millimetres) and maximum permissible probing error $P_{\text{FTU}} = 1.7 \mu\text{m}$. The features compared with CMM (four

repeat measurements) are shown in figure 4.2 and listed in table 5.2. The value after the \pm sign in table 5.2 is the standard deviation of the repeat measurements. Each measurement from multi-view system has three repeats. Commercial software (GOM Inspect [172]) was used for inspection of the 3D reconstruction results acquired from the multi-view fringe projection system (shown in figure 5.15).

Table 5.2: Dimensional measurements of the complex artefact.

Feature measured	CMM measurement	Multi-view measurement	Deviation of multi-view data from CMM	Normalised error, E_n
Sphere-1 diameter /mm	(22.462 ± 0.022)	(22.580 ± 0.121) $u_{\text{meas}} = 0.007$ $P_F = 0.104$	(0.118 ± 0.123)	0.960
Sphere-2 diameter /mm	(22.367 ± 0.028)	(22.386 ± 0.120) $u_{\text{meas}} = 0.001$ $P_F = 0.104$	(0.019 ± 0.123)	0.151
Sphere-1 to sphere-2 centre distance /mm	(112.447 ± 0.020)	(112.534 ± 0.121) $u_{\text{meas}} = 0.005$ $P_F = 0.104$	(0.087 ± 0.123)	0.698
Hemisphere diameter /mm	(60.194 ± 0.346)	(60.063 ± 0.120) $u_{\text{meas}} = 0.003$ $P_F = 0.104$	(-0.131 ± 0.366)	-0.358
Wedge-1 inclination	$(44.964 \pm 0.034)^\circ$	$(45.052 \pm 0.008)^\circ$ $u_{\text{meas}} = 0.004^\circ$ $P_F = 0.104$ mm $u_{\text{sens}} = (3.6249 \times 10^{-4})^\circ/\text{mm}$	$(0.088 \pm 0.035)^\circ$	2.519°
Wedge-2 inclination	$(135.191 \pm 0.036)^\circ$	$(135.317 \pm 0.006)^\circ$ $u_{\text{meas}} = 0.003^\circ$ $P_F = 0.104$ mm $u_{\text{sens}} = (3.4249 \times 10^{-4})^\circ/\text{mm}$	$(0.126 \pm 0.037)^\circ$	3.452°

Table 5.2 shows the deviation of the specific features measured by the multi-view fringe projection system and compared them with CMM data. The probing form error (P_F) of the multi-view fringe projection system is incorporated in the uncertainty computation, and the normalised error (described in chapter 4, section 4.3.1.2) is de-

terminated (given in Table 5.2). From the table, we can see a deviation between the multi-view fringe projection data and that from the CMM between $19\ \mu\text{m}$ and $131\ \mu\text{m}$. The influence factors causing the deviations between the features of interest in (table 5.2) can be summarised as follows. Firstly, the scanned data from the multi-view system contains information only on the two visible sides. Generally, in a stereo-camera system, the origin is at the optical centre of camera-1 and the 3D reconstructed points are generated with the origin at the optical centre of camera-1. In our multi-view fringe projection system, camera-1 and camera-3 are considered as the origin for stereo-camera pair 1 and stereo-camera pair 2, respectively and 3D reconstructions are made accordingly. Secondly, the other two sides have voids that affect the comparison analysis. This limitation can be overcome by adding two more stereo-camera pairs in the other two quadrants. Essentially, one stereo-camera pair is needed in each quadrant to reconstruct the full form. Furthermore, to make an impartial comparison with CMM results, it is better to take less points with the CMM and measure features partially, so that results from the two systems can be compared. Thirdly, the systematic errors causing the waviness and structured pattern, shown in figure 5.16 (a-b), contribute to the deviation of the measured features from the CMM data as shown in table 5.2. The above mentioned factors contribute towards the larger deviation of sphere-1 and the higher values of the normalised error for Wedge-1 and Wedge-2 inclinations.

The multi-view stereo-camera fringe projection system provides higher point densities and addresses the issues of occlusions and shadowing effects with the object, which are typically seen in a single view fringe projection systems. The reconstructed point clouds from multiple perspectives are in the same coordinate system and do not depend on point cloud coarse/fine registration methods. The point cloud in figure 5.15(c) contains more information and have a higher number of data points compared to the acquisition from a single-view, as shown in figure 5.15 (a-b). The point-to-point distances for a small ROI between the two-point clouds of the measured object is around $24\ \mu\text{m}$ (see figure 5.16 (a-c)) which will further be optimised in the future work to achieve a higher accuracy of the system characterisation. The future work will focus on introducing more robust optical components (high-speed machine vision cameras

and projectors with high frame rates), investigating the dependence of the structured pattern on the system characterisation accuracy and the correspondence method, and incorporating the information rich metrology (IRM) to make it smart optical form measurement system.

5.4 Comparison with the conventional method

We compared our proposed method with a conventional method. The multi-view fringe projection system consists of two projectors (DLPC300 Texas Instruments) and two cameras (Nikon D3500, 4496×3000 pixels), the arrangement is shown in figure 5.17 (a). The conventional method of characterising a multi-view fringe projection system relies on capturing several positions of a standard checkerboard (checker width is 4 mm) in the measurement volume and determining the intrinsic parameters of the cameras [193]. The projector is incapable of capturing images, therefore, the camera captures the images for the projector and the one-to-one correspondences between the camera and the projector image pixel coordinates are determined using a phase-stepped fringe projection method. The absolute phase is obtained through temporal phase unwrapping that utilises a combined phase-stepped and binary coded method [48, 88]. The retrieved phase maps are used to determine the extrinsic parameters and the global frame of reference.

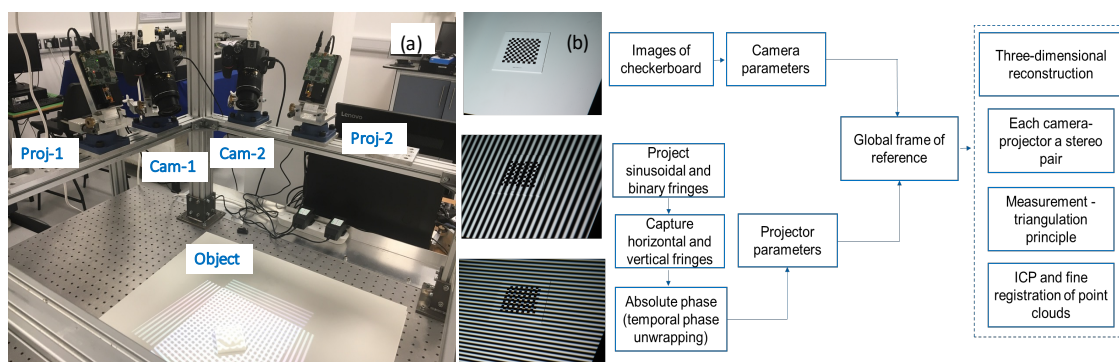


Figure 5.17: Conventional method. (a) Photograph of the multi-view fringe projector system with two cameras and projectors considered for the conventional approach, (b) schematic diagram of the characterisation of the multi-view fringe projection system.

Following the pipeline shown in figure 5.17 (b), a set of horizontal and vertical phase-stepped fringe patterns are projected onto the checkerboard and images are

captured at different positions. The checkerboard was moved manually in the measurement volume. By incorporating the absolute phase maps, the projector coordinates are determined from the camera coordinates using the one-to-one correspondence established through the phase maps [88, 187–189]. The transformation relation is given in equations (2.108) and (2.109).

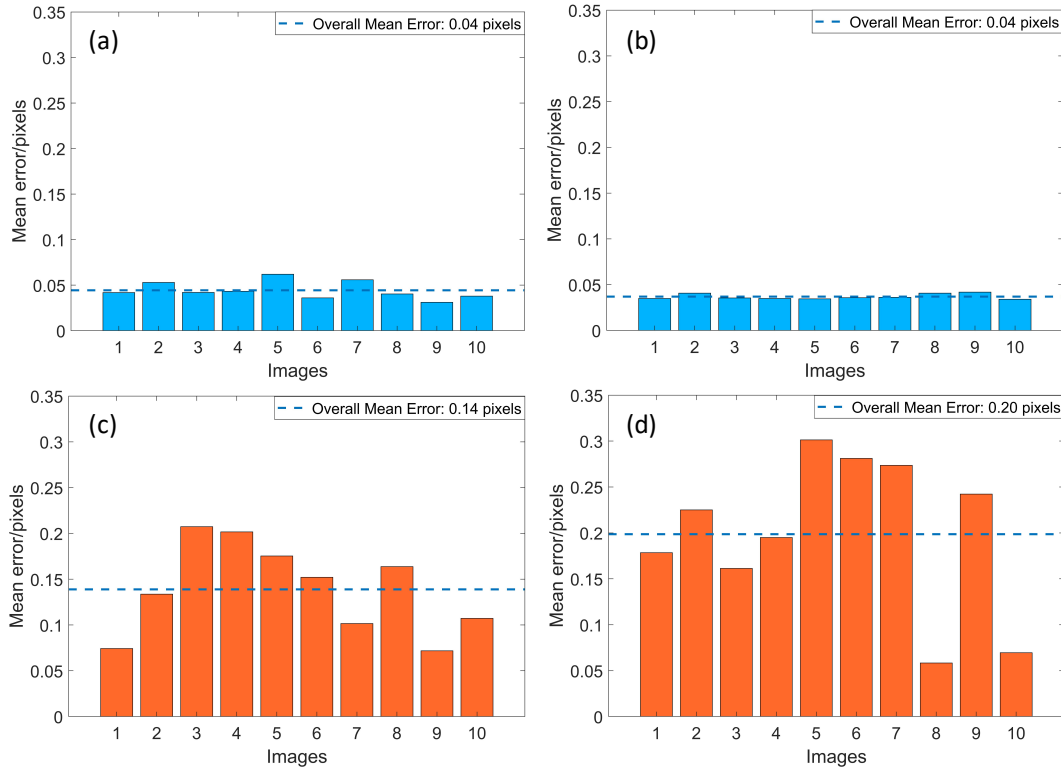


Figure 5.18: Mean reprojection error per image for the camera characterisation. (a) Camera 1 (b) camera 2 (c) projector 1 and (d) projector 2.

The coordinates of the checkerboard corners were detected using a developed image processing algorithm[39]. The intrinsic and extrinsic parameters of all the cameras were determined based on a pinhole camera model as explained in section 5.3.1 (Step A - Camera characterisation). The absolute phase maps are used to find the one-to-one correspondence between the camera and projector intensity pixels and to estimate the projector parameters. Figure 5.18 shows the reprojection errors for the cameras and projectors. The mean reprojection error per image for the cameras is 0.04 pixels, however, the error in the projector characterisation is around 0.20 pixels. The accuracy of the system characterisation is highly dependent on the characterisation of the individual optical components (cameras and projectors) and has a significant influence on the system performance.

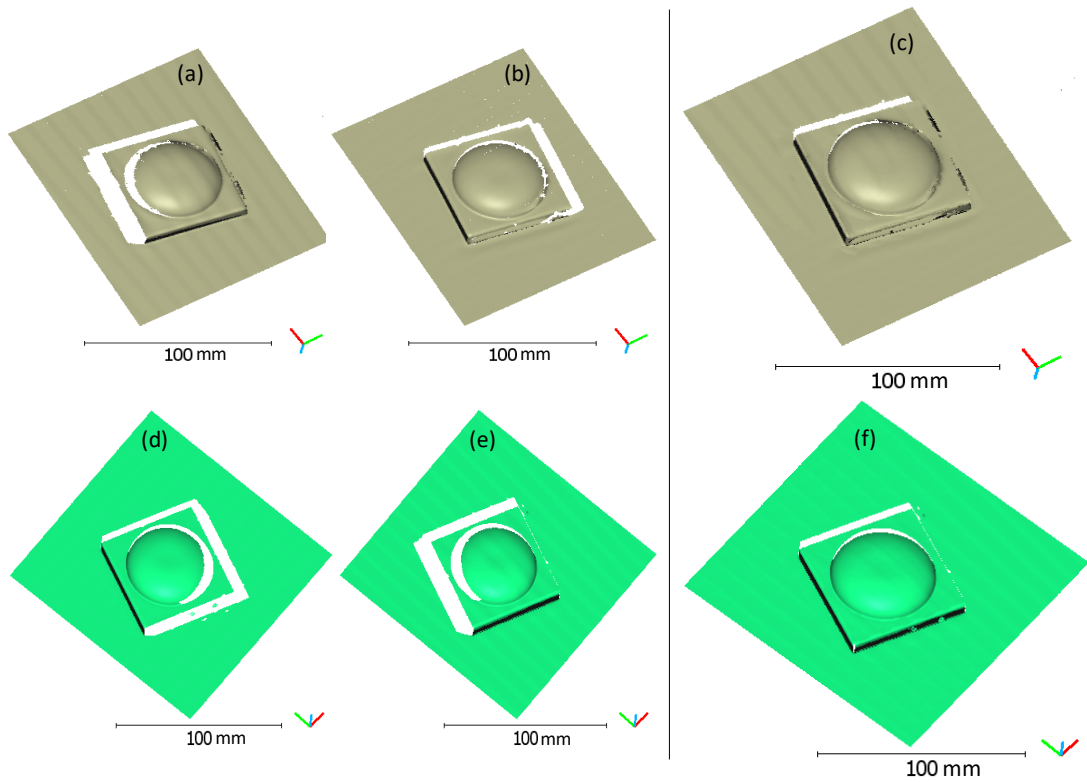


Figure 5.19: 3D reconstruction results of a hemisphere shaped AM artefact ($60 \text{ mm} \times 60 \text{ mm} \times 20 \text{ mm}$). Top row: Conventional method. (a-b) Point clouds acquired from camera-projector pair 1 and 2, respectively (c) combined point cloud of the data shown in (a-b). Bottom row: Proposed method. (d-e) Point clouds from two sets of stereo-camera pairs and (f) the combination of two point clouds shown in (d-e).

Each camera and projector is regarded as a stereo pair and the transformation relationship is given in equations (3.3) and (3.4). The global frame is defined by taking a plane in the common field of view of all the cameras and projectors. The world coordinates between each camera-projector pair are established by triangulation given in equation (3.7).

Using the triangulation principle (equation 3.7), the correspondences between each camera-projector pair are generated and 3D point clouds are acquired. Figure 5.19 shows the 3D reconstructions results of a hemisphere shaped AM artefact. The top row (figure 5.19 (a-c)) depicts the results for the conventional method acquired using two sets of cameras and projectors. The correspondences between each camera-projector pair are established based on the triangulation principle, and the outcome is two separate point clouds from orthogonal perspectives. Figure 5.19 (c) corresponds to the combined point cloud of figure 5.19 (a-b) based on the conventional approach. The

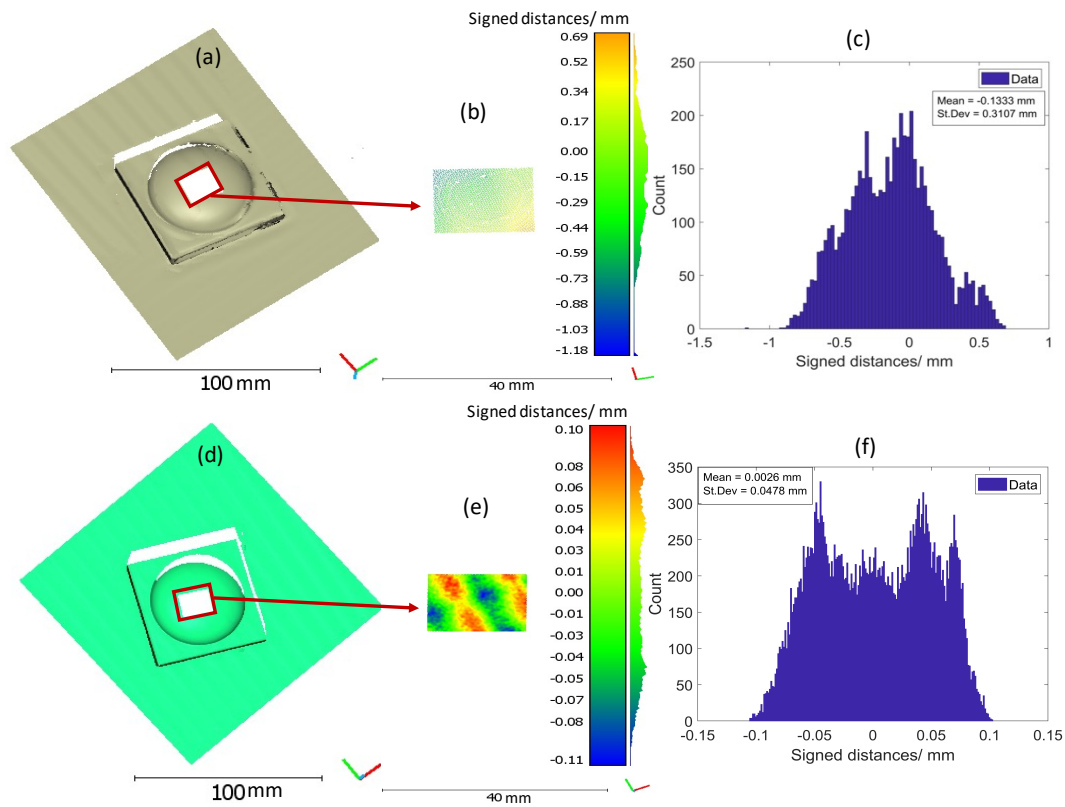


Figure 5.20: Results for the deviation of two point clouds of a hemisphere shaped AM artefact. Top row: Conventional method. (a) Point cloud showing the ROI as a red box, (b) colour map indicating the signed point-to-point distance of the two point clouds from camera-projector pairs 1 and 2, and the distances are determined between a reference point cloud (stereo-camera pair 1) and a target point cloud (stereo-camera pair 2) [2] and (c) histogram depicting the statistics of the signed point-to-point distance of the two point clouds shown in (b). Bottom row: Proposed method. (d) ROI shown as a red box, (e) signed point-to-point distance between the two point clouds from stereo-pair 1 and 2 and (f) statistical distribution of the data shown in (e).

bottom row (figure 5.19 (d-f)) shows the results of the same hemisphere shaped AM artefact but 3D surface reconstruction is achieved based on the stereo rectification approach (explained in sections 5.3.1 and 5.3.2). The CMM measurements (four repeats) and the deviations of the multi-view results from the CMM are listed in table 5.3. In contrast to the proposed method, the hemisphere height measurement has larger deviations ($134 \mu\text{m}$) for the conventional method (table 5.3).

In order to evaluate the effectiveness of the two approaches, a small ROI was chosen in the overlapping region between the two point clouds. The signed point-to-point distances are determined and shown as a deviation map in figure 5.20 (b) for the conventional method and figure 5.20 (e) for the proposed approach. The statistical distributions of the deviation map are depicted in figure 5.20 (c) and figure 5.20

Table 5.3: Dimensional measurements of a hemisphere shaped AM artefact. Each measurement has three repeats. The hemisphere height measured by CMM (four repeat measurements) is (9.6830 ± 0.0004) mm.

Hemisphere height (Ref: Top plane of the base)	Multi-view measurement /mm	Deviation of multi-view data from CMM data /mm
Proposed method	(9.671 ± 0.009)	(0.012 ± 0.009)
Conventional method	(9.549 ± 0.015)	(0.134 ± 0.015)

(f) for the conventional and the proposed approaches, respectively. The conventional method has a mean value of $-133 \mu\text{m}$ and a standard deviation of $311 \mu\text{m}$. The conventional method struggles with mapping errors; the point clouds comprise more noise and require further registration using iterative-closest-point and fine registration algorithms. However, with our proposed method, the mean (figure 5.20 (f)) is $3 \mu\text{m}$ and the deviation for the overlapping ROI is $48 \mu\text{m}$.

5.5 Conclusions

This chapter presents two approaches to characterise a multi-view fringe projection system. In the first method, an automated geometric characterisation has been used which uses a checkerboard to characterise the system and determine the intrinsic and extrinsic parameters of all the cameras and projectors. The phase information from the phase-stepped fringes is used to establish the global reference frame by automated image processing algorithm. The multi-view system has been used to measure an AM artefact. The 3D reconstruction results from the different views are registered with the ICP algorithm. The reconstructed results for a multi-view system have alleviated the limitations of a single view system, mainly associated with occlusions, shading and high slope angles.

In the second approach, a novel characterisation method for a multi-view fringe projection system is presented. The method relies on finding the correspondences between the rectified unwrapped stereo phase maps, and the matched phase values between the stereo phase images are triangulated to acquire 3D form. In contrast to the existing methods of determining the correspondences between the camera and projector

in multi-view fringe projection systems, the benefit of this method is that it does not depend on the projector's characterisation (does not require multiple characterisations, presented in approach-1) as the stereo cameras would have the same phase value for the same point, irrespective of the projector. However, the effectiveness of this method is highly depended on the system's characterisation, and any offset in the stereo-camera pairs will affect the robustness of the method.

The characterisation method has been implemented, and the system has been used for the form measurement of complex AM artefacts. The 3D reconstruction results from multiple perspectives are effectively in a global frame and do not require further registration. Furthermore, the reconstructed results have addressed some of the limitations of a single view system, primarily associated with occlusions, shadowing and complex freeform geometries. The proposed method is also compared with a conventional method and achieved improved performance. The future work will focus on introducing machine vision cameras and to investigate the relationship of the structured deviations with the characterisation accuracy and the proposed correspondence method. This investigation will help to address the current issues with the DSLR's camera (camera's internal sensor noise, vibration due to mechanical shutter), and to achieve improved accuracy of the extrinsic properties of the stereo-camera pairs.

Chapter 6

Performance verification of a multi-view fringe projection system

6.1 Introduction to performance verification

A conventional way of establishing the precise dimensional characterisation of AM parts is to use the contact CMM which can yield the most accurate measurement results with accuracy down to a micrometre [7–10]. However, such systems strive to measure objects with complex freeform geometries. Therefore, non-contact 3D imaging systems, such as fringe projection systems are more often used due to the inherent benefits of fast reconstruction of complex shaped objects with high resolution, generating highly dense data, avoiding any damage to the part due to non-contact and non-destructive in nature [20, 21, 23–25]. Regardless of significant advantages and substantial use in the industrial sector, the metrological characterisation of optical systems poses a challenge as there is no specific calibration standard for traceable measurements of optical imaging systems. The lack of international standards for the calibration of optical form measurement systems has governed various guidelines and to date, there is no specific reference standard for evaluating the accuracy and traceability of optical imaging systems.

In general, German standard VDI/VDE 2634 have been actively used in the acceptance and performance verification of optical coordinate measuring systems. The

standard VDI/VDE 2634 is categorised into three main parts: part-1 is mainly designed for optical 3D imaging systems that require point-by-point probing [194]. However, the verification standards VDI/VDE 2634 part-2 and part-3 are employed for evaluating the precision and accuracy of the optical coordinate measurement systems based on structured light (fringe projection system) or triangulation (photogrammetry [16]) [3, 195]. Specifically, VDI/VDE 2634 part-2 is based on area scanning of a single-view while VDI/VDE 2634 part-3 is suitable for multi-view systems in which the object is scanned from multiple perspectives. Essentially, the quality parameters, such as probing error and sphere spacing error defined in VDI/VDE 2634 parts-2 and part-3 are adapted from ISO 10360 part-8 with an additional quality parameter of flatness measurement error which evaluates the flatness deviation of the optical system. In general, ISO 10360 part-8 summarises the verification tests for CMMs with optical sensors based on a single-view [196].

With the ever-increasing demand and utilisation of 3D imaging systems, the metrological characteristics of optical systems have become an active research area. Radomir evaluated the measurement accuracy of 3D optical scanner based on the verification standard VDI/VDE 2634 part-3 [197]. A calibration etalon was designed, manufactured and used to inspect the key quality parameters, and the accuracy of the 3D scanner has been determined. Thomas et al. conducted a comparative investigation by determining the geometrical accuracy of different handheld scanners and comparing against a reference data acquired by two structured light systems [198]. The guidelines of VDI/VDE 2634 part-3 have been followed and geometrically stable reference objects were used. Michaela et al. developed a new methodology for the metrological characterisation for 3D multi-camera systems [199]. For this purpose, an adaptable artefact with several geometrical shapes has been used. The method is flexible, easily adjustable with respect to the tested device by incorporating some necessary modifications. Tiscareno et al. developed a distinct measurement procedure for a white light scanner [200]. The method depends on the parameters mentioned in VDI/VDE 2634 parts-3 and ISO 10360 part-8.

This chapter addresses the metrological characterisation of the developed multi-

view fringe projection system based on the verification standard VDI/VDE 2634 parts-3 [3]. The novel methodology developed in chapter 5 (section 5.3.2) has been utilised for evaluating the accuracy of the multi-view fringe projection system.

6.2 Multiple view system verification

Optical 3D instruments require standard acceptance criteria to evaluate the accuracy of the system and to ensure the maximum permissible error should not be exceeded. The verification tests are performed using some standard calibrated artefacts and comparing the manufacturer provided values against the experimental results of the verification. In practice, quality parameters such as probing form error, probing size error and sphere spacing error are used to quantitatively evaluate the accuracy of the optical form measurement systems. The following sections will provide more details on the quality parameters.

6.2.1 Probing form error

The probing error represents the distinctive error of the optical form measurement system based on area scanning in the measurement volume. The probing error is described in two different parameters; probing form error (P_F) and probing size error (P_S). The probing error is measured using spheres of various sizes. The probing form error is defined as a range of radial distance between the measured data and the best-fit sphere, which is determined by the least-squares method with free radius. The probing error is influenced by a number of factors, such as phase error, pixel error, digitising error, and spatial resolution; therefore, it is necessary to state the operating mode when determining the probing error.

Figure 6.1 shows the required positions of the sphere in the measurement volume. There is a specific requirement for the calibrated sphere for measuring the probing error, and the diameter should be

$$(0.02 L_0 \leq D_P \leq 0.2 L_0), \quad (6.1)$$

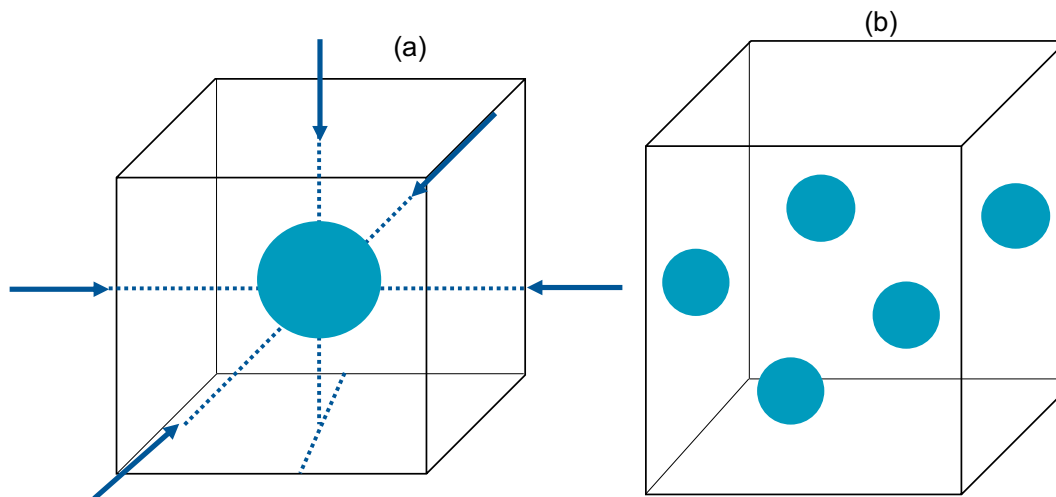


Figure 6.1: Probing error according to VDI/VDE 2634 part-3 [3]. (a) Sensor position for capturing the form of the calibrated test sphere and (b) different orientations of the calibrated test sphere in the measurement volume.

where L_0 is the body diagonal of the measurement volume and D_P is the diameter of the sphere. Therefore, the diameter of the calibrated tested sphere should be between 0.02 and 0.2 of the body diagonal of the measurement volume, hence for $L_0 = 217.5$ mm (body diagonal of the measurement volume of the multi-view fringe projection system) it is given by

$$(4.35 \text{ mm} \leq D_p \leq 43.5 \text{ mm}). \quad (6.2)$$

In VDI/VDE 2634 part-2, the probing error is calculated by measuring ten arbitrary positions of the calibrated artefact in the measurement volume [195]. However, in VDI/VDE 2634 part-3, the quality parameter is determined by measuring the calibrated sphere from three arbitrary positions in the measurement volume [3]. Each sphere position should be captured from five different views which can be done either repositioning the sensor or the tested object (calibrated sphere). It is important that the calibrated sphere surface must be measured completely by acquiring data from different sides. After measuring the calibrated test artefact, a least-squares sphere is implemented on each measured point cloud, and it is recommended that a maximum of 3% of the measured points may be excluded. In general, the probing error is affected by two key factors: error in a single measurement of the measuring instrument and

error due to the registration of many single views.

6.2.2 Probing size error

The quality parameter probing size error is the difference between the measured diameter and the calibrated diameter of the sphere and given by

$$P_S = D_M - D_P, \quad (6.3)$$

where D_M is the measured diameter of the tested artefact. The requirements for the sphere diameter is the same as given in equations 6.1 and 6.3.

6.2.3 Sphere spacing error

The sphere spacing error (SD) represents the capacity of the measuring system to accurately accomplish the length measurement. The sphere spacing error is determined by measuring the centre-to-centre distance between two spheres of a ball bar. The ball bar must be measured in seven different positions in the measurement volume according to VDI/VDE 2634 part-3 as shown in figure 6.2. The arrangement of the ball bar is equivalent to VDI/VDE 2634 part-2 [195]. In order to determine the sphere spacing

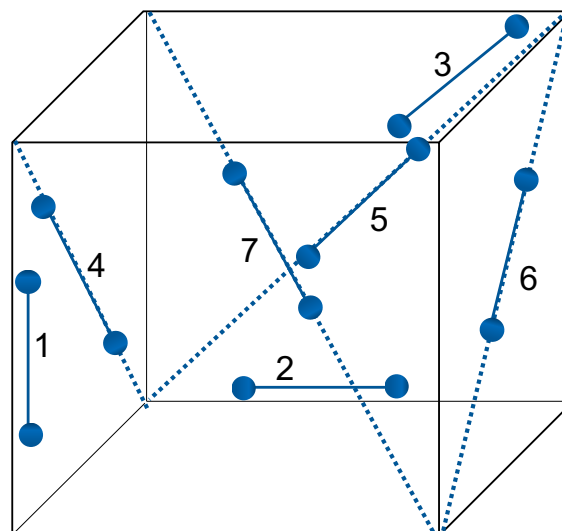


Figure 6.2: Different orientations of the ball bar in the measurement volume for sphere spacing error as recommended in VDI/VDE 2634 part-3.

error, the greatest length of the ball bar must be $2/3$ the length of the body diagonal

of the measurement volume and the smallest length should not be smaller than the shortest length of the measurement volume and given by

$$L_{\max} \geq (2/3) L_0, \quad (6.4)$$

$$L_{\min} \geq (2/3) L_{\min}, \quad (6.5)$$

where L_{\min} is the shortest side length of the measurement volume. Therefore, L_{\max} should be greater or equal 145 mm, while the L_{\min} should be greater or equal to 60 mm.

The sphere spacing error can be calculated

$$SD = L_M - L_S, \quad (6.6)$$

where L_M is the measured length and L_S is the calibrated centre-to-centre length between the two spheres. The measured length is determined by fitting each sphere with a least-squares fit and maximum 3% measured points can be excluded when performing the fitting on the sphere.

6.3 The methodology of performance verification

As described in section 5.3.2 of chapter 5, the methodology of stereo matching of the unwrapped phase maps is used for 3D surface reconstructions.

6.3.1 Artefacts for verification test

A number of key aspects need to be taken into account while choosing the artefact. Specifically, the deviation of the measured features from the nominal values must be negligibly small, the material should be opaque so that sub-surface reflections can be avoided and the measured features should not touch the mounting fixtures to keep the stress level minimal. Two calibrated standard artefacts are used for the metrological characteristics of the multi-view fringe projection system. Further detail of the artefacts is provided in the following sections.



Figure 6.3: Artefacts used for the verification test. (a) A ball bar and (b) a ball beam.

6.3.1.1 Ball bar

A ball bar shaped (two spheres at the end of a rod, shown in figure 6.3(a)) artefact is used for measuring the probing form error and probing size error. The material chosen for the rod is unidirectional carbon fibre in order to maximise stiffness and minimise the thermal expansion. The spheres have a matte finish as fringe projection systems struggle to measure the polished surfaces which restrict the material choice. The spheres have small sphericity (deviation from the mathematical sphere). The spheres are measured by probing 26 equally distributed points of a hemisphere using a CMM. The diameter of sphere-1 is 20.00137 mm (provided in the calibration certificate) with the deviation from the ideal (Gaussian) sphere surface $[-0.00088, 0.00107]$ mm, whilst sphere-2 has a diameter value 20.00146 mm (given in the calibration certificate) with deviations $[-0.00077, 0.00103]$ mm. The sphere spacing (a centre-to-centre distance of the spheres) is 200.10380 mm (according to calibration certificate). Only sphere-1 is used for determining the probing error form and size.

6.3.1.2 Ball beam

A ball beam shown in figure 6.3(b) is used for sphere spacing error. Unidirectional carbon fibre is used for the rod to limit the thermal expansion and enhancing the stiffness. The ball beam has six spheres with a matte finish. The rod has two metallic

fixtures at either end to prevent slipping when placed on the surface. The spheres are measured by CMM and probing each sphere with 18 points which are uniformly distributed over the hemisphere. Two spheres (next from a sphere close to the fixture) are used for determining the sphere spacing error. The length in the x-direction and the diameter of sphere-1 are 480.39842 mm and 20.00073 mm with the deviation $[-0.46, 0.25] \mu\text{m}$, while for sphere-2 the values are 360.34333 mm, 20.00130 mm with deviation $[-0.36, 0.41] \mu\text{m}$. Therefore, the centre-to-centre sphere spacing is 120.05509. Furthermore, the length and the diameter values along with their deviations are listed as mentioned in the calibration certificate.

6.4 Experiments on performance verification

A multi-view fringe projection system (shown in figure 5.10) with four DSLR (Nikon D3500, 4496×3000 pixels) cameras and two DLP projectors (DLPC300 Texas Instruments with a digital micromirror device, 608×680 pixels) are used for the performance verification. The measurement volume of the multi-view fringe projection is calculated by considering it as a parallelepiped (square cuboid) and given by

$$\text{Measurement volume} = (140 \text{ mm} \times 140 \text{ mm} \times 90 \text{ mm}).$$

The body diagonal and the length of the shortest side are given by

$$\text{Body diagonal } (L_0) = \sqrt{(140^2 + 140^2 + 90^2)} = 217.5 \text{ mm}, \quad (6.7)$$

$$\text{Shortest length of the measurement volume } (L_{\min}) = 90 \text{ mm}. \quad (6.8)$$

Using the methodology explained in section 5.3.2 and following the guidelines provided in VDI/VDE 2634 part-3 [3], the quality parameters are determined. For probing form and size errors, a sphere of the calibrated ball bar (shown in figure 6.3 (a)) is measured for three different heights in the measurement volume. Each position

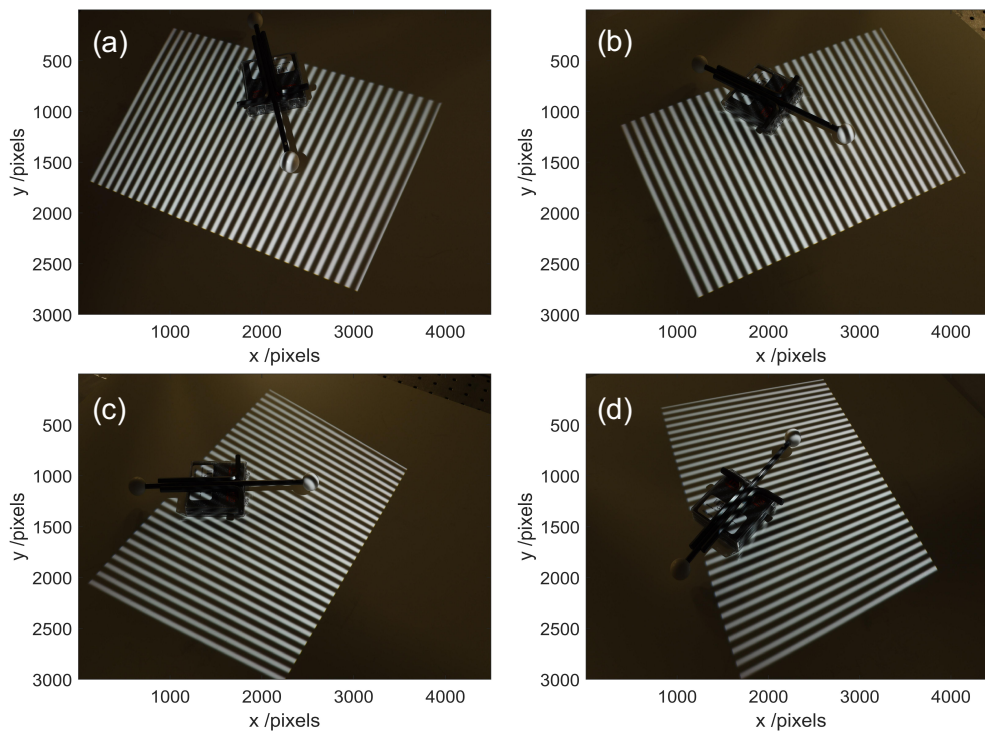


Figure 6.4: A dumbbell shaped ball bar with fringes projected. The orientation for one of the measured positions as seen by (a) camera-1 (b) camera-2 (c) camera-3 and camera-4.

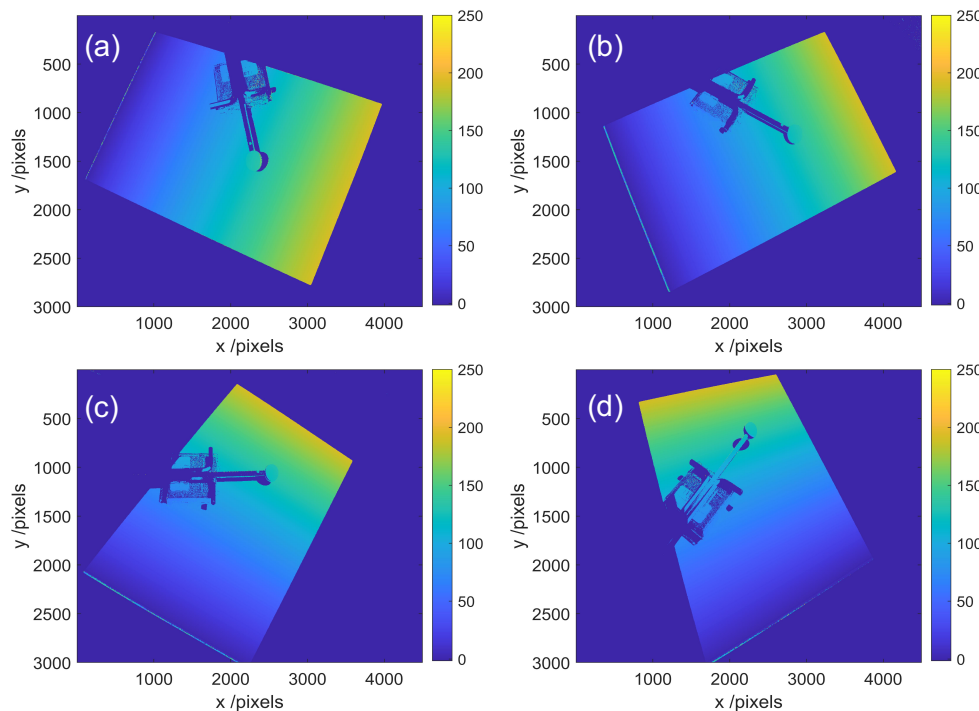


Figure 6.5: Unwrapped phase map for the data shown in figure 6.4 for (a) camera-1 (b) camera-2 (c) camera-3 and camera-4.

is measured from five different perspectives (VDI/VDE 2634 part-3 says three different positions and each position should have five different views [3]), which is achieved by moving the tested object in the measurement volume. The measurement for each view

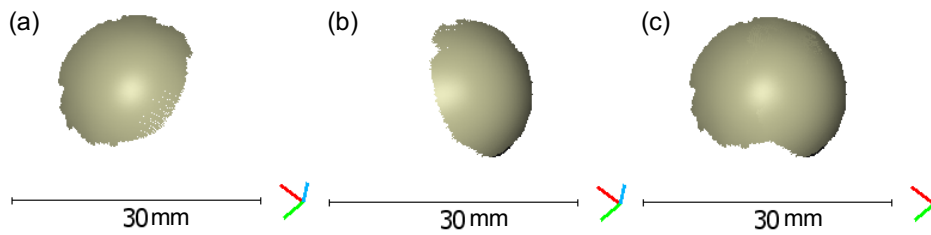


Figure 6.6: 3D surface reconstructions for one of the spheres of a ball bar using the stereo matching of unwrapped phase maps approach as mentioned in section 5.3.2. (a) Stereo-camera pair 1 (b) stereo-camera pair 2 and (c) combined point cloud of the data shown in (a) and (b).

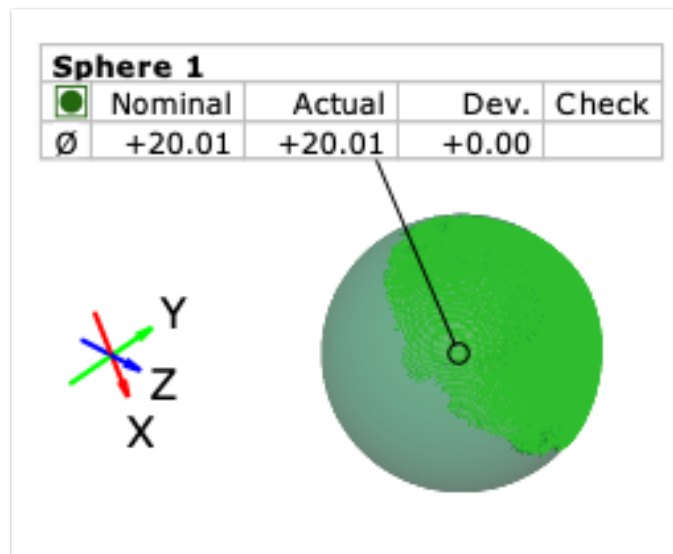


Figure 6.7: Reconstructed point cloud for one of the measured spheres of ball bar. Measured data is fitted with a primitive feature of a sphere.

is repeated three times.

Figure 6.4(a-d) shows one of the measured positions of the tested sphere which is seen by all four cameras whilst figure 6.5(a-d) depicts the corresponding phase maps for the data shown in figure 6.4. The 3D reconstructed results are acquired by considering one projector and two cameras as one stereo pair, and the system is configured as two sets of stereo-camera pairs. Figure 6.6(a-b) shows the individual point clouds obtained from the two stereo-camera pairs while figure 6.6(c) depicts a point cloud which is a combination of the two-point clouds displayed in figure 6.6(a-b).

In order to acquire the probing form and size errors, the measured sphere's data is fitted with a primitive feature using the least-squares method and commercial software (GOM Inspect [172]) is used for this purpose. Figures 6.7 shows the fitting of a measured sphere for the determination of the probing form and size errors. Table

Table 6.1: Probing form and size errors for a calibrated tested sphere. The diameter of the sphere is 20.00137 mm.

Position number	Fitted diameter of the measured sphere /mm	Fitting deviation /mm
1	[20.117, 20.054, 20.058]	[0.0365, 0.0414, 0.0384]
2	[19.988, 19.970, 19.923]	[0.1166, 0.0998, 0.1018]
3	[20.043, 20.007, 20.094]	[0.0246, 0.0348, 0.0156]
4	[20.091, 20.078, 20.056]	[0.0656, 0.0603, 0.0622]
5	[20.083, 20.064, 20.082]	[0.0210, 0.0150, 0.0250]
6	[20.009, 19.985, 20.019]	[0.0520, 0.0504, 0.0518]
7	[20.037, 20.044, 20.056]	[0.0413, 0.0469, 0.0417]
8	[20.016, 19.993, 20.059]	[0.0195, 0.0274, 0.0326]
9	[19.987, 20.000, 19.914]	[0.0906, 0.0975, 0.0940]
10	[19.953, 19.990, 19.997]	[0.0218, 0.0139, 0.0126]
11	[19.996, 20.009, 19.991]	[0.0771, 0.0777, 0.0793]
12	[20.029, 20.024, 19.997]	[0.0263, 0.0277, 0.0255]
13	[19.926, 19.935, 19.867]	[0.0473, 0.0546, 0.0579]
14	[20.068, 19.988, 20.042]	[0.0286, 0.0213, 0.0236]
15	[19.822, 19.772, 19.802]	[0.1137, 0.1099, 0.1104]
Mean /mm	20.001	0.052
Standard deviation /mm	0.076	0.032

6.1 shows the fitted diameter of the measured sphere and the standard deviation of the fitting Gaussian distribution. The mean value, standard deviation and standard uncertainty is also shown in the table 6.1.

As depicted in table 6.1, the system is capable to produce a point cloud with the probing form uncertainty of around $52 \mu\text{m}$ whilst the probing size error of around $76 \mu\text{m}$ on a calibrated tested sphere of diameter 20.00137 mm. The expanded uncertainty within 95% coverage interval is calculated by using a coverage factor of two, therefore the probing form and size expanded uncertainties are $104 \mu\text{m}$ and $152 \mu\text{m}$, respectively.

Likewise, a ball beam is used to determine the sphere spacing error as described in the VDI/VDE 2634 part-3 [3]. Figure 6.8(a-d) shows one orientation of ball beam which is captured by four cameras for one position and figure 6.9(a-d) represents the unwrapped phase maps which are further utilised for acquiring the 3D reconstructed results. The retrieved point clouds for the ball beam (depicted in figure 6.8) from

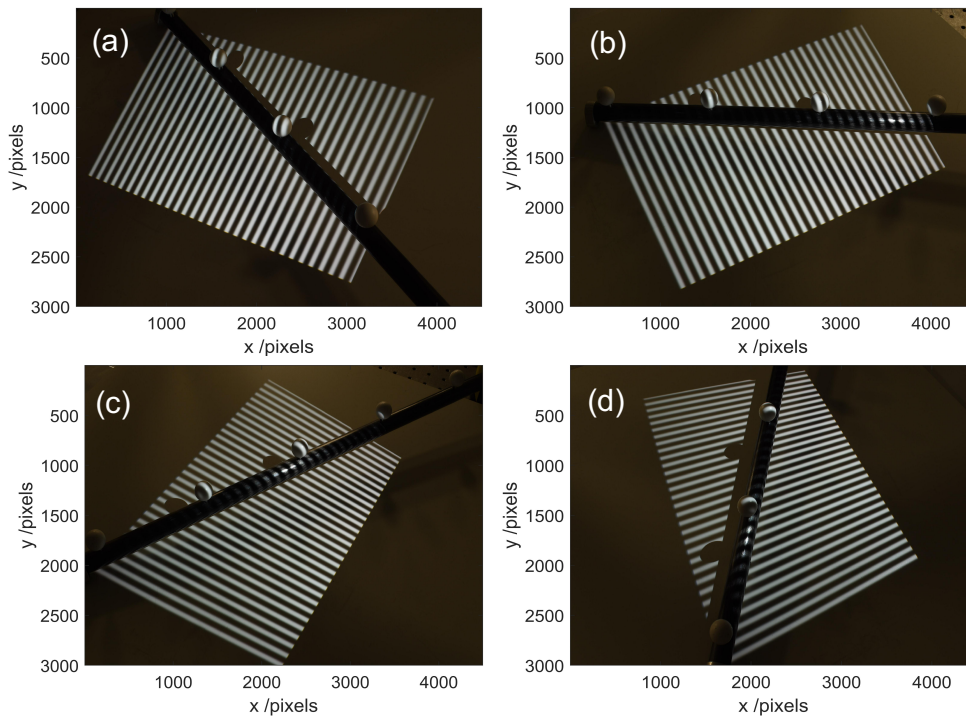


Figure 6.8: A ball beam with fringes projected. The orientation for one of the measured positions as seen by (a) camera-1 (b) camera-2 (c) camera-3 and camera-4.

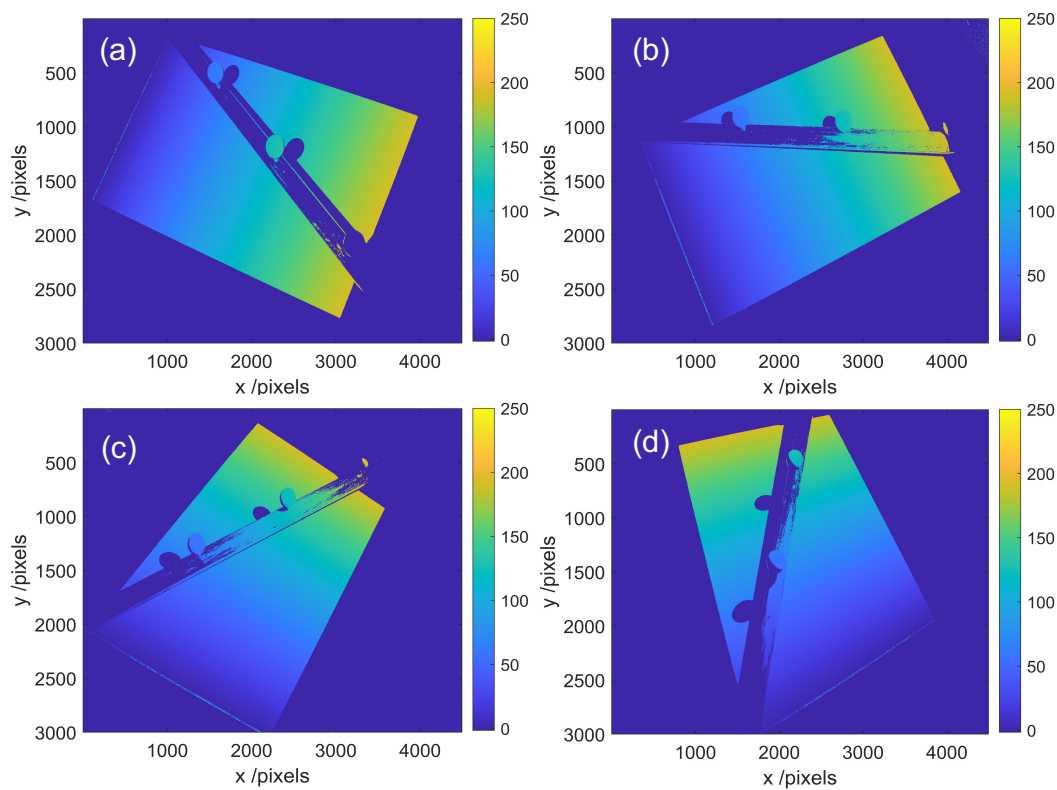


Figure 6.9: Unwrapped phase map for the data shown in figure 6.8 for (a) camera-1 (b) camera-2 (c) camera-3 and camera-4.

single-views and the merged form are shown in figure 6.10(a-c).

Figure 6.11 depicts the fitting of two spheres and an illustration of the sphere

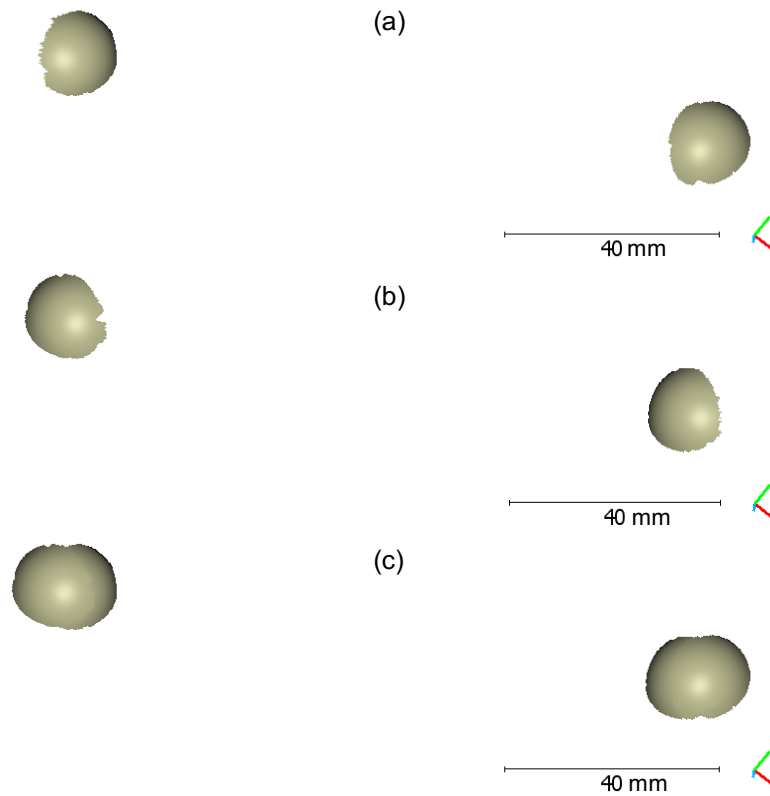


Figure 6.10: 3D surface reconstructions for ball beam using the stereo matching of unwrapped phase maps approach as mentioned in section 5.3.2. (a) Stereo-camera pair 1 (b) stereo-camera pair 2 and (c) combined results of the data shown in (a) and (b).

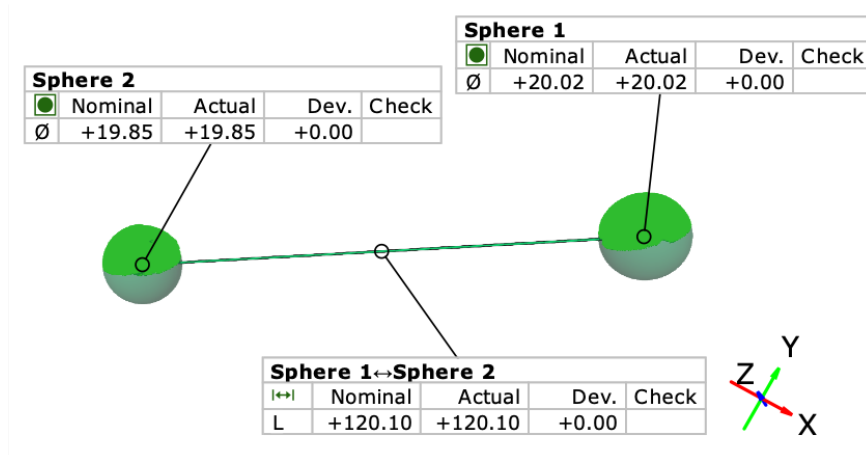


Figure 6.11: Reconstructed point cloud for ball beam. Measured sphere points are fitted with a primitive feature of a sphere and the distance between the centres of two spheres is measured.

centre-to-centre distance which indicates the sphere spacing error. The sphere fitting is performed using the least-squares method. The fitting of the data shown in figure 6.11 is only for the point clouds shown in figures 6.6 and 6.10, respectively. Table 6.2 shows the fitted sphere's diameters and the sphere centre-to-centre distance for the

Table 6.2: Sphere spacing error using a ball beam. The nominal values of sphere-1, sphere-2 and centre-to-centre spacing error are 20.00073, 20.00130 and 120.05509, respectively.

Position number	Sphere-1 diameter /mm	Sphere-2 diameter /mm	Sphere spacing /mm
1	19.871	19.588	119.799
	19.932	19.707	119.826
	19.941	19.716	119.830
2	19.995	19.936	120.332
	19.994	19.920	120.334
	19.954	19.998	120.298
3	19.956	19.809	119.939
	19.877	19.875	119.871
	19.917	19.826	119.921
4	20.029	19.896	120.206
	20.024	19.907	120.206
	20.051	19.896	120.226
5	20.023	19.851	120.100
	20.039	19.821	120.103
	20.048	19.835	120.109
6	20.007	19.976	119.850
	20.057	20.034	119.862
	20.038	20.060	119.884
7	20.043	19.878	120.484
	20.050	19.899	120.474
	20.050	19.858	120.486
Mean /mm	19.995	19.871	120.102
Standard deviation /mm	0.059	0.110	0.238

seven different orientations of the ball beam as given in figure 6.2. The sphere spacing uncertainty is around 238 μm and an expanded uncertainty within 95% of coverage interval is around 476 μm .

6.5 Conclusions

In this chapter, the performance verification of a multi-view fringe projection system has been established based on the verification standard VDI/VDE 2634 part-3. The methodology of the novel approach (discussed in section 5.3.2) of stereo matching of the unwrapped phase maps have been used. A set of calibrated artefacts have been utilised for performing the verification tests and quality parameters such as probing error form,

probing error size and sphere spacing error have been determined. The results have shown that the expanded uncertainties (within 95% confidence of interval) for the probing form, probing size and sphere spacing error were found 104 μm , 152 μm and 476 μm , respectively. The large uncertainties observed are effectively associated with the systematic errors which are influenced by non-linear offsets between the multiple cameras, ambient noise, vibration, and camera sensor noise. These errors will be addressed by using machine vision cameras in the proposed future work and improving the characterisation method.

Chapter 7

Conclusions and future work

7.1 Conclusions

The work presented in this thesis is based on the development of a multi-view fringe projection system for coordinate metrology. A novel methodology is developed for the characterisation of the multi-view fringe projection system, and the developed method is compared with the conventional approach. The accuracy of the multi-view fringe projection is evaluated by performing the metrological characterisation based on the existing verification standards for optical form measurement systems. In general, multi-view fringe projection systems are considered as a potential and effective solution to existing single-view fringe projection systems; therefore, the research is conducted to improve the measurement pipeline. In practice, single-view fringe projection systems are extensively used in the industrial sector for high-speed 3D form measurement; however, such systems encounter issues associated with the line of sight, restricted depth of field, shadowing and occlusions due to complex freeform geometry of AM objects. Additionally, the commercially available systems require a rotation table that rotates the object up to 360° for acquiring the full form/shape of the measuring object, and the entire process consumes time.

The constraints of the existing fringe projection systems are investigated by designing and featuring a single-view fringe projection system (presented in chapter 3). The first part of the chapter 3 (section 3.1) deals with the development of a single-view

fringe projection system using a camera and a digital video projector. The principle of the system is based on the digital fringe projection (DFP) method, which has the benefit of high resolution, fast data acquisition and high measurement accuracy. All optical, electrical, and mechanical components are assembled, and the system is demonstrated by performing the gamma correction, system characterisation and 3D shape measurement of complex geometries. In principle, the gamma correction alleviates the non-linearity of the digital video projector. System characterisation is an important step that determines the transformational relationship between the 3D world coordinate system and the image coordinate system. Specifically, the system characterisation determines the intrinsic and extrinsic properties of the camera and the projector. The developed fringe projection system is demonstrated by measuring complex AM parts of different materials (mentioned in section 3.1.3.3).

The flatness deviation is evaluated by measuring a flat surface five times and fitting a primitive feature of a flat plane on the chosen ROI (119 mm \times 99 mm); the outcome is around 63 μm (given in figure 3.17(a-e)). Nevertheless, the accuracy of the system characterisation can further be improved by using a standard checkerboard and placing the measuring object on a flat surface. Another study, based on the sources of error in the single-view fringe projection system (section 3.2), is performed by comparing the commercially available cost-effective laser and pico DLP projectors in terms of the non-linear gamma effect and the DOF. The experimental results have shown that the gamma curve for the laser projector follows a linear behaviour (figure 3.21); therefore, it needs less gamma correction and recommended for less critical fringe projection applications where it is not feasible to employ the gamma correction. In terms of DOF, the projected pattern of the laser projector stays in focus for a relatively large distance (≈ 164 cm, shown in figure 3.29), and increases the signal to noise ratio in the measurement volume (medium to large objects, ≈ 200 cm long) of the fringe projection system. Thus, the laser projector outperforms the pico DLP projector.

In general, a measurement alone is regarded as incomplete and requires comparison with the model, which can be provided through the uncertainty evaluation. Chapter 4 provides a complete guideline for the uncertainty evaluation of different features of

an industrial AM artefact. The contact (CMM) and non-contact (fringe projection) methods were used to measure the key features of the metal AM artefact (maraging steel grade 300). An uncertainty budget, based on GUM, is established for the measured features of the AM artefact (features on the front side in table 4.1 and the rear side in table 4.2, and the dimensions in table 4.3). The method resides on incorporating the key factors (type-A, type-B, uncertainty associated with temperature fluctuations) affecting the measurement accuracy and establishes a measurement uncertainty related to each specific measurement. In practice, the optical form measurements do not have a specific standard for traceable measurements; therefore, contact CMM measurements were performed to provide a reference for the dimensional measurements.

Chapter 5 presents the development of the multi-view fringe projection system and the methodologies developed in this project. In principle, multi-view fringe projection systems are complex and require to characterise each individual optical component (camera and projector), the structural and global relationship between all cameras and projectors and strategies to combine data from different views. The first part of the chapter (section 5.2) describes the conventional method of system characterisation where each camera and projector is characterised separately and bring in the global frame following the 3D form measurement process, and further improvised by introducing the registration using ICP algorithm. The approach utilises a standard checkerboard to determine the intrinsic and extrinsic parameters of all the cameras and projectors (given in section 5.2.1.1), and accomplishes the transformational relationship between the 3D real-world coordinate system and the image coordinate system. The system characterisation follows the measurement process, in which each camera and projector is considered as a stereo pair, and the correspondences between the camera and the projector coordinates are determined based on the triangulation principle and utilising the system characterisation information. The point clouds for a hemisphere shaped AM artefact (Nylon-12, 60 mm \times 60 mm \times 20 mm) are achieved by configuring the multi-view fringe projection system as two sets of stereo pairs, and by increasing the number of cameras and projectors (given in section 5.2.2). A comparison of the same artefact from a single-view and multiple-views shows that the multi-view

fringe projection system is capable of acquiring a dense point cloud and has addressed some of the limitations of the single-view fringe projection system. Nevertheless, the mapping and triangulation errors affect the 3D surface reconstructions, which can be improved by introducing high-speed cameras and projectors and enclosing the system into a black box to prevent interferences from background light.

The second method (given in section 5.3) resides on a novel approach for the system characterisation of a multi-view fringe projection system. The method relies on establishing the correspondences between the rectified unwrapped stereo phase maps, and the matched phase values between the stereo phase images are triangulated for 3D form measurement. In contrast to the conventional approach that determines the correspondences between the camera and projector (configured as a stereo pair), the benefit of this method is that it does not require the projector's characterisation; therefore, it does not need multiple characterisations (section 5.2). Additionally, the stereo cameras would have the same phase value for the same point, regardless of the projector. Likewise the conventional approach, the first and foremost important step in the developed approach is the system characterisation, which is performed by characterising each camera individually, and then generating the stereo-camera pairs. A continuous phase map is obtained using a set of phase-stepped sinusoidal and binary-encoded fringe patterns [48], and removing the 2π discontinuities using the temporal phase unwrapping algorithm. The acquired phase maps are further rectified followed by stereo matching, and by incorporating the system characterisation information, the 3D reconstructed results of the complex object are acquired (Nylon-12, 110 mm \times 110 mm \times 50 mm, figure 5.15). As the system is configured into two sets of stereo-camera pairs; therefore, two individual point clouds from two different perspectives are obtained, which are already in a global coordinate system. The standard deviation between the two point clouds is 24 μm (figure 5.16), which is computed by considering a small overlapping ROI between the two point clouds.

As mentioned in chapter 4, the optical form measurement systems lack specific standards of calibration; therefore, to provide a reference to the measured data, CMM measurements for different features were carried out. The deviation of the specific fea-

tures measured by the multi-view fringe projection system and compared with CMM data ranges between $19\ \mu\text{m}$ and $131\ \mu\text{m}$ (provided in table 5.2). The factors contributing to these deviations are associated with the scanned data being visible from the two sides and having voids on the other two sides. This limitation can be resolved by introducing more stereo-camera pairs. The systematic error triggering the waviness and structured pattern affect the measurement accuracy. The structured pattern and waviness arise due to offsets in the intrinsic and extrinsic parameters yielding complex distortions in the triangulated point clouds, noise in the phase maps and the accuracy of the system characterisation. These deviations may be regarded as a combined effect of the non-linearities originating due to offsets between multiple cameras and the projector's gamma effect, vibration and the camera's internal sensor noise. In conclusion, the 3D reconstructed results from the multi-view fringe projection system (using the novel approach) have addressed some of the limitations of a single-view fringe projection system, such as complex freeform geometries, multiple occlusions and shadowing effects. Additionally, the developed method is compared with a conventional method, and enhanced performance has been achieved (figure 5.20).

In general, the metrological characterisation of optical imaging systems is challenging due to the lack of a specific calibration standard for estimating the accuracy and traceability. In practice, German standard VDI/VDE 2634 have been used for the performance verification of optical coordinate measuring systems. Chapter 6 describes the metrological characteristics of the multi-view fringe projection system based on the verification standard VDI/VDE 2634 part-3. The developed novel approach (described in section 5.3) of stereo matching of the rectified unwrapped phase maps has been utilised for the performance verification. The quality parameters such as probing form error, probing size error and spere spacing error have been determined using calibrated artefacts. The computed expanded uncertainties (within 95% confidence of interval) for the probing form, probing size and spere spacing error were determined $104\ \mu\text{m}$, $152\ \mu\text{m}$ and $476\ \mu\text{m}$, respectively (given in table 6.1 and table 6.2). The reason for large uncertainties is thought to be associated with the systematic error which arise due to non-linear offsets between the multiple cameras, ambient noise, interfer-

ence from the background light, vibration, and camera sensor noise. These issues will be addressed in the proposed future work using machine vision cameras and improving the characterisation method.

7.2 Future work

The future work will focus on addressing the practical issues of waviness and investigating the dependence of the structured pattern on the system characterisation accuracy and the correspondence approach. The observed waviness and structured patterns in the 3D reconstructed results are considered to be related to systematic effects, unwrapping error in the phase maps, and the accuracy of the system characterisation, which needs further investigation. Therefore, by introducing more robust optical components such as high-speed machine vision cameras and projectors with high frame rates, the potential cause of waviness modulation and the periodic structured pattern can be investigated. In addition, the preliminary phase of the developed method occasionally require the position of the cameras and projectors to be altered; therefore, the manual adjustment of the orientations of the mounted optical components was adequate for the scope of the research work. Essentially, the main emphasis resided on getting the basic system working for the proposed method using suitable and cost-effective hardware, software for interfacing the optical components, and a flexible, easy-to-use system characterisation strategy. However, there is room for introducing the automation of the positioning of the mounted cameras and projectors according to the a-priori information such as the CAD data.

The current system with the developed methodology signifies a vital step towards advancing the multi-view fringe projection system. Whilst primarily developed for proof-of-concept and configured as two sets of stereo-camera pairs in the two quadrants, which yielded a 180° coverage of the measured AM objects. However, with the increasing demand of the manufacturing industry to measure the full-form, the need for measuring the complete 360° form of the AM objects arises and is possible by introducing more cameras and projectors in all four quadrants. A potential solution to acquire

the complete form is incorporating the information-rich metrology, pose estimation, shadow prediction, and machine learning to make it an intelligent optical form measurement system that is capable of measuring the 3D shape of complex geometries in *one shot*. In general, the background/global illumination introduces strong biases in the 3D reconstructed results; therefore, methods that are resistant to global illumination need to be incorporated, and the modified version of the multi-view fringe projection system would be enclosed in a box to prevent interference from the background light. Furthermore, an imperative area of work is towards accomplishing the complete traceability of the multi-view form measurement system using calibrated traceable reference artefacts and verification standards. A traceable calibration method with a rigorous uncertainty budget would account for all the sources of error, thus enhancing the measurement accuracy.

The ultimate regime of future work relies on the fusion of different methodologies, which provides a way of developing a hybrid form measurement system. Thus, by combining the fringe projection method with photogrammetry and deflectometry, a variety of complex surfaces with various surface textures can be measured. However, hybrid systems are complex and require a global coordinate system that can be achieved by using specific targets (checkerboard, dot/circles) being visible and in the field-of-view of all the optical components. An improved and automated method for better estimation of the camera properties will improve the measurement accuracy. Additionally, the introduction of machine learning will further aid to predict the shadowing and occlusions, estimate the pose of the cameras and projectors beforehand, and trigger them in reliance on the measured object. Thus, a potential outcome will be a *one shot* intelligent optical form measurement system for coordinate metrology.

Bibliography

- [1] M. Sinico, R. Ranjan, M. Moshiri, C. Ayas, M. Langelaar, A. Witvrouw, F. Keulen, and W. Dewulf, “A mold insert case study on topology optimized design for additive manufacturing,” in *Proceedings of the Solid Freeform Fabrication Symposium*, 2019.
- [2] D. Lague, N. Brodu, and J. Leroux, “Accurate 3D comparison of complex topography with terrestrial laser scanner: Application to the Rangitikei canyon (N-Z),” *ISPRS Journal of Photogrammetry and Remote Sensing*, vol. 82, pp. 10–26, 2013.
- [3] VDI/VDE 2634 part 3, “Optical 3D-Measuring Systems: Multiple View Systems Based on Area Scanning - Part 3 (Berlin: VDI/VDE),” 2008.
- [4] H. D. Vora and S. Sanyal, “A comprehensive review: metrology in additive manufacturing and 3D printing technology,” *Progress in Additive Manufacturing*, vol. 5, pp. 319–353, 2020.
- [5] R. K. Leach, *Advances in optical form and coordinate metrology*. IOP Publishing, 2020.
- [6] R. K. Leach, D. Bourell, S. Carmignato, A. Donmez, N. Senin, and W. Dewulf, “Geometrical metrology for metal additive manufacturing,” *CIRP Annals*, vol. 68, no. 2, pp. 677–700, 2019.
- [7] H. Zhao, J.-P. Kruth, N. Van Gestel, B. Boeckmans, and P. Bleys, “Automated dimensional inspection planning using the combination of laser scanner and tactile probe,” *Measurement*, vol. 45, no. 5, pp. 1057–1066, 2012.
- [8] B. Acko, M. McCarthy, F. Haertig, and B. Buchmeister, “Standards for testing freeform measurement capability of optical and tactile coordinate measuring machines,” *Measurement Science and Technology*, vol. 23, no. 9, p. 094013, 2012.
- [9] J.-j. Park, K. Kwon, and N. Cho, “Development of a coordinate measuring machine (CMM) touch probe using a multi-axis force sensor,” *Measurement Science and Technology*, vol. 17, no. 9, pp. 2380–2386, 2006.
- [10] I. Puertas, C. J. L. Pérez, D. Salcedo, J. León, R. Luri, and J. P. Fuertes, “Precision study of a coordinate measuring machine using several contact probes,” *Procedia Engineering*, vol. 63, pp. 547–555, 2013.
- [11] R. Thalmann, F. Meli, and A. Küng, “State of the art of tactile micro coordinate metrology,” *Applied Sciences*, vol. 6, no. 5, p. 150, 2016.

- [12] J. D. Claverley and R. K. Leach, "A review of the existing performance verification infrastructure for micro-CMMs," *Precision Engineering*, vol. 39, pp. 1–15, 2015.
- [13] E. J. C. Bos, "Aspects of tactile probing on the micro scale," *Precision Engineering*, vol. 35, no. 2, pp. 228–240, 2011.
- [14] J.-H. Wu, R.-S. Chang, and J.-A. Jiang, "A novel pulse measurement system by using laser triangulation and a CMOS image sensor," *Sensors*, vol. 7, no. 12, pp. 3366–3385, 2007.
- [15] P. I. Stavroulakis and R. K. Leach, "Invited Review Article: Review of post-process optical form metrology for industrial-grade metal additive manufactured parts," *Review of Scientific Instruments*, vol. 87, no. 4, p. 041101, 2016.
- [16] D. Sims-Waterhouse, S. Piano, and R. K. Leach, "Verification of micro-scale photogrammetry for smooth three-dimensional object measurement," *Measurement Science and Technology*, vol. 28, no. 5, p. 055010, 2017.
- [17] C. S. Fraser, "Photogrammetric measurement to one part in a million," *Photogrammetric Engineering and Remote Sensing*, vol. 58, pp. 305–310, 1992.
- [18] D. Scharstein and R. Szeliski, "A taxonomy and evaluation of dense two-frame stereo correspondence algorithms," *International Journal of Computer Vision*, vol. 47, no. 1-3, pp. 7–42, 2002.
- [19] U. R. Dhond and J. K. Aggarwal, "Structure from stereo—A review," *IEEE Transactions on Systems, Man, and Cybernetics*, vol. 19, no. 6, pp. 1489–1510, 1989.
- [20] Z. H. Zhang, "Review of single-shot 3D shape measurement by phase calculation-based fringe projection techniques," *Optics and Lasers in Engineering*, vol. 50, no. 8, pp. 1097–1106, 2012.
- [21] S. Zhang, "Recent progresses on real-time 3D shape measurement using digital fringe projection techniques," *Optics and Lasers in Engineering*, vol. 48, no. 2, pp. 149–158, 2010.
- [22] Ø. Skotheim and F. Couwleers, "Structured light projection for accurate 3D shape determination," in *Proceedings of the 12th International Conference on Experimental Mechanics*, 2004, pp. 536–541.
- [23] S. Zhang and S.-T. Yau, "High-resolution, real-time 3D absolute coordinate measurement based on a phase-shifting method," *Optics Express*, vol. 14, no. 7, pp. 2644–2649, 2006.
- [24] V. Srinivasan, H.-C. Liu, and M. Halioua, "Automated phase-measuring profilometry of 3-D diffuse objects," *Applied Optics*, vol. 23, no. 18, pp. 3105–3108, 1984.
- [25] Y. Fu and Q. Luo, "Fringe projection profilometry based on a novel phase shift method," *Optics Express*, vol. 19, no. 22, pp. 21 739–21 747, 2011.
- [26] GOM - Precise Industrial 3D Metrology, <https://www.gom.com/>.

- [27] O. Albers, A. Poesch, and E. Reithmeier, “Flexible calibration and measurement strategy for a multi-sensor fringe projection unit,” *Optics Express*, vol. 23, no. 23, pp. 29 592–29 607, 2015.
- [28] S. Gai, F. Da, and M. Tang, “A flexible multi-view calibration and 3D measurement method based on digital fringe projection,” *Measurement Science and Technology*, vol. 30, no. 2, p. 025203, 2019.
- [29] M. Gdeisat, M. Qudeisat, M. AlSa’d, D. Burton, F. Lilley, and M. M. M. Ammous, “Simple and accurate empirical absolute volume calibration of a multi-sensor fringe projection system,” *Optics and Lasers in Engineering*, vol. 80, pp. 32–44, 2016.
- [30] M. E. Deetjen and D. Lentink, “Automated calibration of multi-camera-projector structured light systems for volumetric high-speed 3D surface reconstructions,” *Optics Express*, vol. 26, no. 25, pp. 33 278–33 304, 2018.
- [31] W. Jang, C. Je, Y. Seo, and S. W. Lee, “Structured-light stereo: Comparative analysis and integration of structured-light and active stereo for measuring dynamic shape,” *Optics and Lasers in Engineering*, vol. 51, no. 11, pp. 1255–1264, 2013.
- [32] M.-G. Park, J. Park, Y. Shin, E.-G. Lim, and K.-J. Yoon, “Stereo vision with image-guided structured-light pattern matching,” *Electronics Letters*, vol. 51, no. 3, pp. 238–239, 2015.
- [33] K. Liu, C. Zhou, S. Wei, S. Wang, X. Fan, and J. Ma, “Optimized stereo matching in binocular three-dimensional measurement system using structured light,” *Applied Optics*, vol. 53, no. 26, pp. 6083–6090, 2014.
- [34] D. Scharstein and R. Szeliski, “High-accuracy stereo depth maps using structured light,” in *2003 IEEE Computer Society Conference on Computer Vision and Pattern Recognition, Proceedings.*, vol. 1. IEEE, 2003, pp. I–I.
- [35] R. Y. Tsai, “An efficient and accurate camera calibration technique for 3D machine vision,” *Proceedings of Computer Vision and Pattern Recognition*, pp. 364–374, 1986.
- [36] Z. Zhang, “A flexible new technique for camera calibration,” *IEEE Transactions on Pattern Analysis and Machine Intelligence*, vol. 22, no. 11, pp. 1330–1334, 2000.
- [37] S. Zhang and P. S. Huang, “Novel method for structured light system calibration,” *Optical Engineering*, vol. 45, no. 8, p. 083601, 2006.
- [38] Z. Huang, J. Xi, Y. Yu, and Q. Guo, “Accurate projector calibration based on a new point-to-point mapping relationship between the camera and projector images,” *Applied Optics*, vol. 54, no. 3, pp. 347–356, 2015.
- [39] J. Y. Bouguet, “Camera calibration toolbox for MATLAB, Computational Vision Group, California Institute of Technology, Pasadena, CA, USA,” 2001.

- [40] S.-E. Shih and W.-H. Tsai, "A two-omni-camera stereo vision system with an automatic adaptation capability to any system setup for 3-D vision applications," *IEEE Transactions on Circuits and Systems for Video Technology*, vol. 23, no. 7, pp. 1156–1169, 2013.
- [41] M. Z. Brown, D. Burschka, and G. D. Hager, "Advances in computational stereo," *IEEE Transactions on Pattern Analysis and Machine Intelligence*, vol. 25, no. 8, pp. 993–1008, 2003.
- [42] H. Hirschmuller, "Stereo processing by semiglobal matching and mutual information," *IEEE Transactions on Pattern Analysis and Machine Intelligence*, vol. 30, no. 2, pp. 328–341, 2007.
- [43] M. Shimizu and M. Okutomi, "Calibration and rectification for reflection stereo," in *2008 IEEE Conference on Computer Vision and Pattern Recognition*. IEEE, 2008, pp. 1–8.
- [44] R. Tsai, "A versatile camera calibration technique for high-accuracy 3D machine vision metrology using off-the-shelf tv cameras and lenses," *IEEE Journal on Robotics and Automation*, vol. 3, no. 4, pp. 323–344, 1987.
- [45] Z. Zhang, "Flexible camera calibration by viewing a plane from unknown orientations," in *Proceedings of the Seventh IEEE International Conference on Computer Vision*, vol. 1. IEEE, 1999, pp. 666–673.
- [46] J. Gühring, "Dense 3D surface acquisition by structured light using off-the-shelf components," in *Videometrics and Optical Methods for 3D Shape Measurement*, vol. 4309. International Society for Optics and Photonics, 2000, pp. 220–231.
- [47] R. Yang, S. Cheng, and Y. Chen, "Flexible and accurate implementation of a binocular structured light system," *Optics and Lasers in Engineering*, vol. 46, no. 5, pp. 373–379, 2008.
- [48] X. Chen, S. Chen, J. Luo, M. Ma, Y. Wang, Y. Wang, and L. Chen, "Modified gray-level coding method for absolute phase retrieval," *Sensors*, vol. 17, no. 10, p. 2383, 2017.
- [49] X. He and Q. Kemao, "A comparison of n-ary simple code and n-ary gray code phase unwrapping in high-speed fringe projection profilometry," *Optics and Lasers in Engineering*, vol. 128, p. 106046, 2020.
- [50] M. A. Herráez, D. R. Burton, M. J. Lalor, and M. A. Gdeisat, "Fast two-dimensional phase-unwrapping algorithm based on sorting by reliability following a noncontinuous path," *Applied Optics*, vol. 41, no. 35, pp. 7437–7444, 2002.
- [51] C. Zuo, L. Huang, M. Zhang, Q. Chen, and A. Asundi, "Temporal phase unwrapping algorithms for fringe projection profilometry: A comparative review," *Optics and Lasers in Engineering*, vol. 85, pp. 84–103, 2016.
- [52] H. O. Saldner and J. M. Huntley, "Temporal phase unwrapping: application to surface profiling of discontinuous objects," *Applied Optics*, vol. 36, no. 13, pp. 2770–2775, 1997.

- [53] D. Scharstein and R. Szeliski, "A taxonomy and evaluation of dense two-frame stereo correspondence algorithms," *International Journal of Computer Vision*, vol. 47, no. 1-3, pp. 7–42, 2002.
- [54] R. Hartley and A. Zisserman, *Multiple view geometry in computer vision*. Cambridge University Press, 2004.
- [55] A. Kolb, E. Barth, R. Koch, and R. Larsen, "Time-of-flight cameras in computer graphics," in *Computer Graphics Forum*, vol. 29, no. 1. Wiley Online Library, 2010, pp. 141–159.
- [56] S. Foix, G. Alenya, and C. Torras, "Lock-in time-of-flight (ToF) cameras: A survey," *IEEE Sensors Journal*, vol. 11, no. 9, pp. 1917–1926, 2011.
- [57] S. Lei and S. Zhang, "Flexible 3-D shape measurement using projector defocusing," *Optics Letters*, vol. 34, no. 20, pp. 3080–3082, 2009.
- [58] X.-Y. Su, W.-S. Zhou, G. Von Bally, and D. Vukicevic, "Automated phase-measuring profilometry using defocused projection of a ronchi grating," *Optics Communications*, vol. 94, no. 6, pp. 561–573, 1992.
- [59] M. Takeda, H. Ina, and S. Kobayashi, "Fourier-transform method of fringe-pattern analysis for computer-based topography and interferometry," *Journal of the Optical Society of America*, vol. 72, no. 1, pp. 156–160, 1982.
- [60] M. Takeda and K. Mutoh, "Fourier transform profilometry for the automatic measurement of 3-D object shapes," *Applied Optics*, vol. 22, no. 24, pp. 3977–3982, 1983.
- [61] M. Takeda, Q. Gu, M. Kinoshita, H. Takai, and Y. Takahashi, "Frequency-multiplex Fourier-transform profilometry: a single-shot three-dimensional shape measurement of objects with large height discontinuities and/or surface isolations," *Applied Optics*, vol. 36, no. 22, pp. 5347–5354, 1997.
- [62] S. Li, X. Jia, M. Chen, and Y. Yang, "Error analysis and correction for color in laser triangulation measurement," *Optik*, vol. 168, pp. 165–173, 2018.
- [63] C. Dong, "A regression model for analysing the non-linearity of laser triangulation probes," *The International Journal of Advanced Manufacturing Technology*, vol. 59, no. 5-8, pp. 691–695, 2012.
- [64] T. Luhmann, S. Robson, S. Kyle, and I. Harley, *Close range photogrammetry: Principles, techniques and applications*, 2011.
- [65] F. Bruno, G. Bianco, M. Muzzupappa, S. Barone, and A. V. Razionale, "Experimentation of structured light and stereo vision for underwater 3D reconstruction," *ISPRS Journal of Photogrammetry and Remote Sensing*, vol. 66, no. 4, pp. 508–518, 2011.
- [66] M. Idesawa, T. Yatagai, and T. Soma, "Scanning moiré method and automatic measurement of 3-D shapes," *Applied Optics*, vol. 16, no. 8, pp. 2152–2162, 1977.
- [67] Q. Kemao, "Windowed fourier transform for fringe pattern analysis," *Applied Optics*, vol. 43, no. 13, pp. 2695–2702, 2004.

- [68] A. Dursun, S. Özder, and F. N. Ecevit, “Continuous wavelet transform analysis of projected fringe patterns,” *Measurement Science and Technology*, vol. 15, no. 9, pp. 1768–1772, 2004.
- [69] D. C. Ghiglia and L. A. Romero, “Robust two-dimensional weighted and unweighted phase unwrapping that uses fast transforms and iterative methods,” *Journal of the Optical Society of America A*, vol. 11, no. 1, pp. 107–117, 1994.
- [70] J. Huntley, “Noise-immune phase unwrapping algorithm,” *Applied Optics*, vol. 28, no. 16, pp. 3268–3270, 1989.
- [71] J. A. Quiroga and E. Bernabeu, “Phase-unwrapping algorithm for noisy phase-map processing,” *Applied Optics*, vol. 33, no. 29, pp. 6725–6731, 1994.
- [72] J. A. Quiroga, A. Gonzalez-Cano, and E. Bernabeu, “Phase-unwrapping algorithm based on an adaptive criterion,” *Applied Optics*, vol. 34, no. 14, pp. 2560–2563, 1995.
- [73] W. Xu and I. Cumming, “A region-growing algorithm for InSAR phase unwrapping,” *IEEE Transactions on Geoscience and Remote Sensing*, vol. 37, no. 1, pp. 124–134, 1999.
- [74] K. M. Hung and T. Yamada, “Phase unwrapping by regions using least-squares approach,” *Optical Engineering*, vol. 37, no. 11, pp. 2965–2970, 1998.
- [75] S. Zhang, “High-resolution 3D profilometry with binary phase-shifting methods,” *Applied Optics*, vol. 50, no. 12, pp. 1753–1757, 2011.
- [76] L. Ekstrand and S. Zhang, “Three-dimensional profilometry with nearly focused binary phase-shifting algorithms,” *Optics Letters*, vol. 36, no. 23, pp. 4518–4520, 2011.
- [77] M. A. Schofield and Y. Zhu, “Fast phase unwrapping algorithm for interferometric applications,” *Optics Letters*, vol. 28, no. 14, pp. 1194–1196, 2003.
- [78] S. Chavez, Q.-S. Xiang, and L. An, “Understanding phase maps in MRI: A new cutline phase unwrapping method,” *IEEE Transactions on Medical Imaging*, vol. 21, no. 8, pp. 966–977, 2002.
- [79] M. D. Pritt, “Phase unwrapping by means of multigrid techniques for interferometric SAR,” *IEEE Transactions on Geoscience and Remote Sensing*, vol. 34, no. 3, pp. 728–738, 1996.
- [80] J. M. Tribolet, “A new phase unwrapping algorithm,” *IEEE Transactions on Acoustics, Speech, and Signal Processing*, vol. 25, no. 2, pp. 170–177, 1977.
- [81] A. Momose, “Recent advances in x-ray phase imaging,” *Japanese Journal of Applied Physics*, vol. 44, no. 9A, pp. 6355–6367, 2005.
- [82] D. C. Ghiglia and M. D. Pritt, *Two-dimensional phase unwrapping: theory, algorithms, and software*. Wiley New York, 1998, vol. 4.
- [83] S. Zhang, *High-speed 3D imaging with digital fringe projection techniques*. CRC Press, 2016.

- [84] D. J. Bone, "Fourier fringe analysis: the two-dimensional phase unwrapping problem," *Applied Optics*, vol. 30, no. 25, pp. 3627–3632, 1991.
- [85] M. A. Herraez, D. R. Burton, M. J. Lalor, and D. B. Clegg, "Robust, simple, and fast algorithm for phase unwrapping," *Applied Optics*, vol. 35, no. 29, pp. 5847–5852, 1996.
- [86] B. R. Hunt, "Matrix formulation of the reconstruction of phase values from phase differences," *Journal of the Optical Society of America*, vol. 69, no. 3, pp. 393–399, 1979.
- [87] K. Creath, "Step height measurement using two-wavelength phase-shifting interferometry," *Applied Optics*, vol. 26, no. 14, pp. 2810–2816, 1987.
- [88] G. Sansoni, M. Carocci, and R. Rodella, "Three-dimensional vision based on a combination of gray-code and phase-shift light projection: analysis and compensation of the systematic errors," *Applied Optics*, vol. 38, no. 31, pp. 6565–6573, 1999.
- [89] J. M. Huntley and H. Saldner, "Temporal phase-unwrapping algorithm for automated interferogram analysis," *Applied Optics*, vol. 32, no. 17, pp. 3047–3052, 1993.
- [90] J. C. Wyant, "Testing aspherics using two-wavelength holography," *Applied Optics*, vol. 10, no. 9, pp. 2113–2118, 1971.
- [91] Y.-Y. Cheng and J. C. Wyant, "Two-wavelength phase shifting interferometry," *Applied Optics*, vol. 23, no. 24, pp. 4539–4543, 1984.
- [92] H. Zhao, W. Chen, and Y. Tan, "Phase-unwrapping algorithm for the measurement of three-dimensional object shapes," *Applied Optics*, vol. 33, no. 20, pp. 4497–4500, 1994.
- [93] L. Kinell and M. Sjö Dahl, "Robustness of reduced temporal phase unwrapping in the measurement of shape," *Applied Optics*, vol. 40, no. 14, pp. 2297–2303, 2001.
- [94] X. Peng, Z. Yang, and H. Niu, "Multi-resolution reconstruction of 3-D image with modified temporal unwrapping algorithm," *Optics Communications*, vol. 224, no. 1-3, pp. 35–44, 2003.
- [95] J. Tian, X. Peng, and X. Zhao, "A generalized temporal phase unwrapping algorithm for three-dimensional profilometry," *Optics and Lasers in Engineering*, vol. 46, no. 4, pp. 336–342, 2008.
- [96] J. Zhong and M. Wang, "Phase unwrapping by lookup table method: application to phase map with singular points," *Optical Engineering*, vol. 38, pp. 2075–2080, 1999.
- [97] C. E. Towers, D. P. Towers, and J. D. Jones, "Time efficient chinese remainder theorem algorithm for full-field fringe phase analysis in multi-wavelength interferometry," *Optics Express*, vol. 12, no. 6, pp. 1136–1143, 2004.

- [98] M. Zhang, Q. Chen, T. Tao, S. Feng, Y. Hu, H. Li, and C. Zuo, "Robust and efficient multi-frequency temporal phase unwrapping: optimal fringe frequency and pattern sequence selection," *Optics Express*, vol. 25, no. 17, pp. 20 381–20 400, 2017.
- [99] Y. Wan, Y. Cao, and J. Kofman, "High-accuracy 3D surface measurement using hybrid multi-frequency composite-pattern temporal phase unwrapping," *Optics Express*, vol. 28, no. 26, pp. 39 165–39 180, 2020.
- [100] C. Zuo, Q. Chen, G. Gu, S. Feng, F. Feng, R. Li, and G. Shen, "High-speed three-dimensional shape measurement for dynamic scenes using bi-frequency tripolar pulse-width-modulation fringe projection," *Optics and Lasers in Engineering*, vol. 51, no. 8, pp. 953–960, 2013.
- [101] J. M. Huntley and H. O. Saldner, "Error-reduction methods for shape measurement by temporal phase unwrapping," *Journal of the Optical Society of America A*, vol. 14, no. 12, pp. 3188–3196, 1997.
- [102] J. M. Huntley and H. O. Saldner, "Shape measurement by temporal phase unwrapping: comparison of unwrapping algorithms," *Measurement Science and Technology*, vol. 8, no. 9, pp. 986–992, 1997.
- [103] V. I. Gushov and Y. N. Solodkin, "Automatic processing of fringe patterns in integer interferometers," *Optics and Lasers in Engineering*, vol. 14, no. 4-5, pp. 311–324, 1991.
- [104] J. Zhong and Y. Zhang, "Absolute phase-measurement technique based on number theory in multifrequency grating projection profilometry," *Applied Optics*, vol. 40, no. 4, pp. 492–500, 2001.
- [105] E. Lilienblum and B. Michaelis, "Optical 3D surface reconstruction by a multi-period phase shift method," *Journal of Computers*, vol. 2, no. 2, pp. 73–83, 2007.
- [106] T. Pribanić, S. Mrvoš, and J. Salvi, "Efficient multiple phase shift patterns for dense 3D acquisition in structured light scanning," *Image and Vision Computing*, vol. 28, no. 8, pp. 1255–1266, 2010.
- [107] Y. Ding, J. Xi, Y. Yu, and J. Chicharo, "Recovering the absolute phase maps of two fringe patterns with selected frequencies," *Optics Letters*, vol. 36, no. 13, pp. 2518–2520, 2011.
- [108] Y. Ding, J. Xi, Y. Yu, and F. Deng, "Absolute phase recovery of three fringe patterns with selected spatial frequencies," *Optics and Lasers in Engineering*, vol. 70, pp. 18–25, 2015.
- [109] J. L. Posdamer and M. D. Altschuler, "Surface measurement by space-encoded projected beam systems," *Computer Graphics and Image processing*, vol. 18, no. 1, pp. 1–17, 1982.
- [110] S. Zhang, "Composite phase-shifting algorithm for absolute phase measurement," *Optics and Lasers in Engineering*, vol. 50, no. 11, pp. 1538–1541, 2012.

- [111] Z. Zhang, "Camera calibration with one-dimensional objects," *IEEE Transactions on Pattern Analysis and Machine Intelligence*, vol. 26, no. 7, pp. 892–899, 2004.
- [112] S. Gai, F. Da, and X. Fang, "A novel camera calibration method based on polar coordinate," *PLoS ONE*, vol. 11, no. 10, 2016.
- [113] F. Gu, H. Zhao, Y. Ma, and P. Bu, "Camera calibration based on the back projection process," *Measurement Science and Technology*, vol. 26, no. 12, p. 125004, 2015.
- [114] R. S. Lu and Y. F. Li, "A global calibration method for large-scale multi-sensor visual measurement systems," *Sensors and Actuators A: Physical*, vol. 116, no. 3, pp. 384–393, 2004.
- [115] Z. Liu, G. Zhang, Z. Wei, and J. Sun, "Novel calibration method for non-overlapping multiple vision sensors based on 1D target," *Optics and Lasers in Engineering*, vol. 49, no. 4, pp. 570–577, 2011.
- [116] B. Cyganek and J. P. Siebert, *An Introduction to 3D Computer Vision Techniques and Algorithms*. Wiley, 2009.
- [117] G. Bradski and A. Kaehler, *Learning OpenCV: Computer vision with the OpenCV library*. " O'Reilly Media, Inc.", 2008.
- [118] D. He, X. Liu, X. Peng, Y. Ding, and B. Z. Gao, "Eccentricity error identification and compensation for high-accuracy 3D optical measurement," *Measurement Science and Technology*, vol. 24, no. 7, p. 075402, 2013.
- [119] X. Yang and S. Fang, "Eccentricity error compensation for geometric camera calibration based on circular features," *Measurement Science and Technology*, vol. 25, no. 2, p. 025007, 2014.
- [120] W. Zhang, W. Li, L. Yu, H. Luo, H. Zhao, and H. Xia, "Sub-pixel projector calibration method for fringe projection profilometry," *Optics Express*, vol. 25, no. 16, pp. 19 158–19 169, 2017.
- [121] R. Chen, J. Xu, H. Chen, J. Su, Z. Zhang, and K. Chen, "Accurate calibration method for camera and projector in fringe patterns measurement system," *Applied Optics*, vol. 55, no. 16, pp. 4293–4300, 2016.
- [122] A. Gonzalez and J. Meneses, "Accurate calibration method for a fringe projection system by projecting an adaptive fringe pattern," *Applied Optics*, vol. 58, no. 17, pp. 4610–4615, 2019.
- [123] S. Huang, L. Xie, Z. Wang, Z. Zhang, F. Gao, and X. Jiang, "Accurate projector calibration method by using an optical coaxial camera," *Applied Optics*, vol. 54, no. 4, pp. 789–795, 2015.
- [124] Z. Li, Y. Shi, C. Wang, and Y. Wang, "Accurate calibration method for a structured light system," *Optical Engineering*, vol. 47, no. 5, p. 053604, 2008.
- [125] S. Xing and H. Guo, "Correction of projector nonlinearity in multi-frequency phase-shifting fringe projection profilometry," *Optics Express*, vol. 26, no. 13, pp. 16 277–16 291, 2018.

- [126] F. Lü, S. Xing, and H. Guo, “Self-correction of projector nonlinearity in phase-shifting fringe projection profilometry,” *Applied Optics*, vol. 56, no. 25, pp. 7204–7216, 2017.
- [127] Z. Song and R. Chung, “Use of LCD panel for calibrating structured-light-based range sensing system,” *IEEE Transactions on Instrumentation and Measurement*, vol. 57, no. 11, pp. 2623–2630, 2008.
- [128] J. Lu, R. Mo, H. Sun, and Z. Chang, “Flexible calibration of phase-to-height conversion in fringe projection profilometry,” *Applied Optics*, vol. 55, no. 23, pp. 6381–6388, 2016.
- [129] X. Zhang and L. Zhu, “Projector calibration from the camera image point of view,” *Optical Engineering*, vol. 48, no. 11, p. 117208, 2009.
- [130] P. F. Meilan and M. Garavaglia, “Rayleigh criterion of resolution and light sources of different spectral composition,” in *Fifth International Topical Meeting on Education and Training in Optics*, vol. 3190. International Society for Optics and Photonics, 1997, pp. 296–303.
- [131] E. Hecht, *Optics, 5e*. Pearson Education India, 2002.
- [132] J. Yao, X. Chen, Y. Zhou, H. Miao, and J. Chen, “Phase error elimination considering gamma nonlinearity, system vibration, and noise for fringe projection profilometry,” *Optical Engineering*, vol. 53, no. 9, p. 094102, 2014.
- [133] J. Deng, J. Li, H. Feng, S. Ding, Y. Xiao, W. Han, and Z. Zeng, “Efficient intensity-based fringe projection profilometry method resistant to global illumination,” *Optics Express*, vol. 28, no. 24, pp. 36 346–36 360, 2020.
- [134] M. Gupta, A. Agrawal, A. Veeraraghavan, and S. G. Narasimhan, “Structured light 3D scanning in the presence of global illumination,” in *CVPR 2011*. IEEE, 2011, pp. 713–720.
- [135] A. K. Boyat and B. K. Joshi, “A review paper: noise models in digital image processing,” *arXiv preprint arXiv:1505.03489*, 2015.
- [136] G. Kaur, R. Kumar, and K. Kainth, “A review paper on different noise types and digital image processing,” *International Journal of Advanced Research in Computer Science and Software Engineering*, vol. 6, no. 6, pp. 562–565, 2016.
- [137] P. Bointon, L. Todhunter, P. Stavroulakis, A. Clare, and R. K. Leach, “The effects of vibration on fringe projection systems,” in *Proc. 18th Int. euspen Conf.*, 2018, pp. 119–120.
- [138] Y. Fu, “Low-frequency vibration measurement by temporal analysis of projected fringe patterns,” *Optics and Lasers in Engineering*, vol. 48, no. 2, pp. 226–234, 2010.
- [139] B. Pan, Q. Kemao, L. Huang, and A. Asundi, “Phase error analysis and compensation for nonsinusoidal waveforms in phase-shifting digital fringe projection profilometry,” *Optics Letters*, vol. 34, no. 4, pp. 416–418, 2009.

- [140] T. Hoang, B. Pan, D. Nguyen, and Z. Wang, "Generic gamma correction for accuracy enhancement in fringe-projection profilometry," *Optics Letters*, vol. 35, no. 12, pp. 1992–1994, 2010.
- [141] P. S. Huang, Q. J. Hu, and F.-P. Chiang, "Double three-step phase-shifting algorithm," *Applied Optics*, vol. 41, no. 22, pp. 4503–4509, 2002.
- [142] X.-Y. Su, W.-S. Zhou, G. Von Bally, and D. Vukicevic, "Automated phase-measuring profilometry using defocused projection of a ronchi grating," *Optics Communications*, vol. 94, no. 6, pp. 561–573, 1992.
- [143] P. Zhou, X. Liu, Y. He, and T. Zhu, "Phase error analysis and compensation considering ambient light for phase measuring profilometry," *Optics and Lasers in Engineering*, vol. 55, pp. 99–104, 2014.
- [144] C. Zhang, H. Zhao, L. Zhang, and X. Wang, "Full-field phase error detection and compensation method for digital phase-shifting fringe projection profilometry," *Measurement Science and Technology*, vol. 26, no. 3, p. 035201, 2015.
- [145] S. Zhang, "Comparative study on passive and active projector nonlinear gamma calibration," *Applied Optics*, vol. 54, no. 13, pp. 3834–3841, 2015.
- [146] O. Bimber and A. Emmerling, "Multifocal projection: A multiprojector technique for increasing focal depth," *IEEE Transactions on Visualization and Computer Graphics*, vol. 12, no. 4, pp. 658–667, 2006.
- [147] O. Packer, L. C. Diller, J. Verweij, B. B. Lee, J. Pokorny, D. R. Williams, D. M. Dacey, and D. H. Brainard, "Characterization and use of a digital light projector for vision research," *Vision Research*, vol. 41, no. 4, pp. 427–439, 2001.
- [148] J. E. Greivenkamp, "Field guide to geometrical optics." SPIE Bellingham, WA, 2004.
- [149] J. Kim, R. Horstmeyer, I.-J. Kim, and R. Raskar, "Highlighted depth-of-field photography: Shining light on focus," *ACM Transactions on Graphics (TOG)*, vol. 30, no. 3, pp. 1–9, 2011.
- [150] M. S. Brown, P. Song, and T.-J. Cham, "Image pre-conditioning for out-of-focus projector blur," in *2006 IEEE Computer Society Conference on Computer Vision and Pattern Recognition (CVPR'06)*, vol. 2. IEEE, 2006, pp. 1956–1963.
- [151] L. Zhang, Y. Yang, X. Zhao, Z. Fang, and X. Yuan, "Enhancement of depth-of-field in a direct projection-type integral imaging system by a negative lens array," *Optics Express*, vol. 20, no. 23, pp. 26 021–26 026, 2012.
- [152] D. Iwai, S. Mihara, and K. Sato, "Extended depth-of-field projector by fast focal sweep projection," *IEEE Transactions on Visualization and Computer Graphics*, vol. 21, no. 4, pp. 462–470, 2015.
- [153] M. Grosse, G. Wetzstein, A. Grundhöfer, and O. Bimber, "Coded aperture projection," *ACM Transactions on Graphics (TOG)*, vol. 29, no. 3, pp. 1–12, 2010.
- [154] O. Cossairt, C. Zhou, and S. Nayar, "Diffusion coded photography for extended depth of field," in *ACM SIGGRAPH 2010 papers*, 2010, pp. 1–10.

- [155] E. R. Dowski and W. T. Cathey, "Extended depth of field through wave-front coding," *Applied Optics*, vol. 34, no. 11, pp. 1859–1866, 1995.
- [156] A. Levin, R. Fergus, F. Durand, and W. T. Freeman, "Image and depth from a conventional camera with a coded aperture," *ACM Transactions on Graphics (TOG)*, vol. 26, no. 3, pp. 70–es, 2007.
- [157] W.-S. Sun, Y.-C. Chiang, and C.-H. Tsuei, "Optical design for the dlp pocket projector using led light source," *Physics Procedia*, vol. 19, pp. 301–307, 2011.
- [158] C. Xiong, J. Yao, J. Chen, and H. Miao, "A convenient look-up-table based method for the compensation of non-linear error in digital fringe projection," *Theoretical and Applied Mechanics Letters*, vol. 6, no. 1, pp. 49–53, 2016.
- [159] H. Cui, Z. Zhao, Y. Wu, N. Dai, X. Cheng, and L. Zhang, "Digital fringe image gamma modeling and new algorithm for phase error compensation," *Optik*, vol. 125, no. 24, pp. 7175–7181, 2014.
- [160] K. Liu, Y. Wang, D. L. Lau, Q. Hao, and L. G. Hassebrook, "Gamma model and its analysis for phase measuring profilometry," *Journal of the Optical Society of America A*, vol. 27, no. 3, pp. 553–562, 2010.
- [161] H. Guo, H. He, and M. Chen, "Gamma correction for digital fringe projection profilometry," *Applied Optics*, vol. 43, no. 14, pp. 2906–2914, 2004.
- [162] S. Zhang and S.-T. Yau, "Generic nonsinusoidal phase error correction for three-dimensional shape measurement using a digital video projector," *Applied Optics*, vol. 46, no. 1, pp. 36–43, 2007.
- [163] Z. Cai, X. Liu, X. Peng, Z. Zhang, H. Jiang, Y. Yin, and S. Huang, "Phase error compensation methods for high-accuracy profile measurement," *Measurement Science and Technology*, vol. 27, no. 4, p. 045201, 2016.
- [164] J.-Z. Peng, H.-K. Ouyang, Q. Yu, Y.-J. Yu, and K.-S. Wang, "Phase error correction for fringe projection profilometry by using constrained cubic spline," *Advances in Manufacturing*, vol. 2, no. 1, pp. 39–47, 2014.
- [165] K. De and V. Masilamani, "Image sharpness measure for blurred images in frequency domain," *Procedia Engineering*, vol. 64, pp. 149–158, 2013.
- [166] X. Su and L. Xue, "Phase unwrapping algorithm based on fringe frequency analysis in fourier-transform profilometry," *Optical Engineering*, vol. 40, no. 4, pp. 637–643, 2001.
- [167] D. Zheng and F. Da, "Gamma correction for two step phase shifting fringe projection profilometry," *Optik*, vol. 124, no. 13, pp. 1392–1397, 2013.
- [168] S.-H. Lu and H. Hua, "Imaging properties of extended depth of field microscopy through single-shot focus scanning," *Optics Express*, vol. 23, no. 8, pp. 10714–10731, 2015.
- [169] A. Levin, R. Fergus, F. Durand, and W. T. Freeman, "Image and depth from a conventional camera with a coded aperture," *ACM Transactions on Graphics (TOG)*, vol. 26, no. 3, pp. 70–es, 2007.

- [170] O. Packer, L. C. Diller, J. Verweij, B. B. Lee, J. Pokorny, D. R. Williams, D. M. Dacey, and D. H. Brainard, "Characterization and use of a digital light projector for vision research," *Vision research*, vol. 41, no. 4, pp. 427–439, 2001.
- [171] JCGM 2008 GUM 1995 with Minor Corrections, Evaluation of Measurement Data - Guide to the Expression of Uncertainty in Measurement JCGM 100 (Svres: BIPM), 2008.
- [172] ATOS process description 2014 GOM Acceptance Test with reference to the Guideline VDI/VDE 2634 Part 3.
- [173] CloudCompare (version 2.11.1) [GPL software] (2020), <http://www.cloudcompare.org/>.
- [174] R. K. Leach and S. T. Smith, *Basics of precision engineering*. CRC Press, 2018.
- [175] R. Willink, "An improved procedure for combining type a and type b components of measurement uncertainty," *International Journal of Metrology and Quality Engineering*, vol. 4, no. 1, pp. 55–62, 2013.
- [176] K. Dhoska, T. Kübarsepp, and A. Hermaste, "Uncertainty evaluation of angle measurements by using 3D coordinate measuring machine," in *DAAAM Proceedings, 9th International DAAAM Baltic Conference, Industrial Engineering., Tallinn*, 2014, pp. 221–225.
- [177] R. Willink, "A generalization of the welch–satterthwaite formula for use with correlated uncertainty components," *Metrologia*, vol. 44, no. 5, p. 340, 2007.
- [178] D. Flack, "Measurement good practice guide No. 130 Co-ordinate measuring machine task-specific measurement uncertainties (National Physical Laboratory: London)," 2013.
- [179] D. Flack, "Measurement good practice guide No. 41 CMM measurement strategies (National Physical Laboratory: London)," 2014.
- [180] F. Abedi, Y. Yang, and Q. Liu, "Group geometric calibration and rectification for circular multi-camera imaging system," *Optics Express*, vol. 26, no. 23, pp. 30 596–30 613, 2018.
- [181] Z. Liu, Z. Meng, N. Gao, and Z. Zhang, "Calibration of the relative orientation between multiple depth cameras based on a three-dimensional target," *Sensors*, vol. 19, no. 13, p. 3008, 2019.
- [182] J. Sun, H. He, and D. Zeng, "Global calibration of multiple cameras based on sphere targets," *Sensors*, vol. 16, no. 1, p. 77, 2016.
- [183] M. Feng, X. Jia, J. Wang, S. Feng, and T. Zheng, "Global calibration of multi-cameras based on refractive projection and ray tracing," *Sensors*, vol. 17, no. 11, p. 2494, 2017.
- [184] M. Servin, M. Padilla, G. Garnica, and A. Gonzalez, "Profilometry of three-dimensional discontinuous solids by combining two-steps temporal phase unwrapping, co-phased profilometry and phase-shifting interferometry," *Optics and Lasers in Engineering*, vol. 87, pp. 75–82, 2016.

- [185] M. Servin, G. Garnica, J. C. Estrada, and A. Quiroga, “Coherent digital demodulation of single-camera N-projections for 3D-object shape measurement: Co-phased profilometry,” *Optics Express*, vol. 21, no. 21, pp. 24 873–24 878, 2013.
- [186] M. Servin, G. Garnica, and J. M. Padilla, “Co-phased 360-degree profilometry of discontinuous solids with 2-projectors and 1-camera,” in *Latin America Optics and Photonics Conference*. Optical Society of America, 2014, pp. LTh2B–2.
- [187] S. Xiao, W. Tao, H. Yan, and H. Zhao, “A new geometrical model and mathematical method for three-dimensional surface reconstruction based on phase-shifting structured light technique,” in *Optical Metrology and Inspection for Industrial Applications III*, vol. 9276. International Society for Optics and Photonics, 2014, p. 92761Z.
- [188] P. Lu, C. Sun, B. Liu, and P. Wang, “Accurate and robust calibration method based on pattern geometric constraints for fringe projection profilometry,” *Applied Optics*, vol. 56, no. 4, pp. 784–794, 2017.
- [189] C. Zhang, H. Zhao, and K. Jiang, “Fringe-period selection for a multifrequency fringe-projection phase unwrapping method,” *Measurement Science and Technology*, vol. 27, no. 8, p. 085204, 2016.
- [190] S. Du, Y. Xu, T. Wan, H. Hu, S. Zhang, G. Xu, and X. Zhang, “Robust iterative closest point algorithm based on global reference point for rotation invariant registration,” *PLOS ONE*, vol. 12, no. 11, 2017.
- [191] Mitutoyo Crysta Apex: S7106 CMM, www.mitutoyo.co.uk.
- [192] D. Flack, “NPL Good Practice Guide No. 41 CMM Measurement Strategies,” 2014.
- [193] A. Shaheen, D. Sims-Waterhouse, P. Bointon, S. Piano, and R. K. Leach, “Automated characterisation of multi-view fringe projection system for three-dimensional measurement of additively manufactured parts,” in *Proc. euspen/ASPE Advancing Precision in Additive Manufacturing*, 09 2019, pp. 19–22.
- [194] VDI/VDE 2634, part 1, “Optical 3d measuring systems, imaging systems with point-by-point probing,” pp. 1–10, 2002.
- [195] VDI/VDE 2634 Part 2, “Optical 3D-measuring systems-Optical systems based on area scanning - Part 2 (Berlin: VDI/VDE),” 2012.
- [196] ISO 10360, “Geometrical Product Specifications (GPS)Acceptance and Reverification Tests for Coordinate Measuring Systems (CMS)Part 8: CMMs with Optical Distance Sensors,” 2013.
- [197] R. Mendricky, “Determination of measurement accuracy of optical 3D scanners,” *MM Science Journal*, pp. 1565–1572, 2016.
- [198] T. P. Kersten, H.-J. Przybilla, and M. Lindstaedt, “Investigations of the geometrical accuracy of handheld 3D scanning systems,” *Photogrammetrie-Fernerkundung-Geoinformation*, vol. 2016, no. 5-6, pp. 271–283, 2016.

- [199] M. Servi, F. Buonamici, L. Puggelli, and Y. Volpe, “A new metrological characterization strategy for 3D multi-camera systems,” *International Journal on Interactive Design and Manufacturing (IJIDeM)*, pp. 1–4, 2020.
- [200] J. Tiscareño, J. Santolaria, and J. A. Albajez, “Measurement procedure for application of white light scanner in the automotive sector,” *Procedia Manufacturing*, vol. 13, pp. 565–572, 2017.